Research Frontiers 2019

SPring-8
SACLA

ISSN 2433-5126
SPring-8 Document D2020-008

SPring-8/SACLA Research Frontiers 2019

CONTENTS

Preface 5

Editor's Note 6

Scientific Frontiers 7

Review

Synchrotron radiation-based X-ray analysis for cultural heritage and art 8
Y. Abe

Life Science

Serial femtosecond crystallography: Oxyl/oxo coupling mechanism for dioxygen formation in photosystem II 12
M. Suga and J.-R. Shen

High-resolution protein crystallography: Charge-density analysis of green fluorescent protein at ultra-high resolution 14
K. Takaba and K. Takeda

Protein crystallography: Crystal structure of heliorhodopsin 16
W. Shihoya

Protein crystallography: Discovery of cap-specific adenosine-N^6-methyltransferase (CAPAM) 18
S. Akichika, S. Hirano, O. Nureki and T. Suzuki

Protein crystallography: *In crystallo* thermodynamic analysis of catalytic reaction in bacterial copper amine oxidase 20
T. Murakawa, S. Baba and T. Okajima

Protein crystallography: Mechanism of stress-induced inhibition of eukaryotic translation initiation factor 2B 22
K. Kashiwagi and T. Ito

Protein hydration: Sugars can protect hydration shell of proteins and stabilize their native structures in crowded molecular environment: clarified by complemental use of X-rays and neutrons 24
M. Hirai

Neurology: Parkinson's disease is a type of amyloidosis characterized by accumulation of amyloid fibrils of α-synuclein 26
K. Araki, N. Yagi and H. Mochizuki

Ophthalmology: Gradient of index and moduli is essential for optimal function of the eye lens 28
K. Wang, M. Hoshino and B. K. Pierscionek

Physical Science

Nuclear clock: Active pumping of ^{229}Th nuclear clock isomer by synchrotron radiation-based nuclear resonant scattering 30
T. Masuda, T. Hiraki, A. Yoshimi and K. Yoshimura

Barocaloric effect: Pressure-induced phase transition in plastic crystal neopentylglycol with colossal barocaloric effects 32
B. Li, T. Sugahara and K. Li

Martensitic transformation: Discovery of simple variant selection effect during stress-driven martensitic transformation 34
B. Yue, F. Hong and B. Chen

SACLA **Ultrafast dislocation behavior:** Studying ultrafast dynamics of temperature-dependent dislocation in Fe-0.1mass%C using femtosecond X-ray diffraction 36
M. Yonemura

Spin dynamics: Direct evidence of Co-3*d* orbital change associated with spin crossover in $LaCoO_3$ obtained by X-ray Compton scattering 38
Y. Kobayashi

Solid oxygen: Oxygen *K*-edge X-ray Raman spectroscopy for solid oxygen up to 140 GPa with hard X-rays 40
H. Fukui

Magnetic anisotropy: The magnetic anisotropy of graphene-covered cobalt on silicon carbide 42
R. Hönig, T. Ohkochi and C. Westphal

Antiferromagnetic domain motion: Magnetoelectric-effect-driven antiferromagnetic domain motion revealed by scanning soft X-ray magnetic circular dichroism microscopy 44
Y. Shiratsuchi

Inelastic scattering: Signature of rigidity transition in liquid As_2Se_3 observed by inelastic X-ray scattering 46
M. Inui, A. Q. R. Baron and Y. Kajihara

SACLA **Superfluorescence:** First observation of 'superfluorescence' at extreme ultra-violet wavelengths 48
J. R. Harries, H. Iwayama and S. Kuma

Chemical Science

Photoactuator molecule: Object transport system mimicking the cilia of *Paramecium Aurelia*, making use of the light-controllable crystal bending behavior of photochromic diarylethene 50
K. Uchida, R. Nishimura and A. Fujimoto

Multifunctional liquid crystal: Supramolecular polymerization in liquid crystalline media enables modular approach to multifunctional core–shell columnar coassembly 52
K. Yano, Y. Itoh and T. Aida

Crystal-like droplet: Single-crystal-like chiral organic droplets exhibiting unidirectional rotating sliding 54
T. Kajitani

Diamond semiconductor: Determination of the 3D local structures of dopant in heavily phosphorus-doped diamond 56
T. Yokoya, H. Kato and T. Matsushita

Ultrafast X-ray spectroscopy: Tracking multiple components of a nuclear wavepacket in photexcited Cu(I)-phenanthroline complex using ultrafast X-ray spectroscopy 58
T. Katayama

Hydrogen bonds: Environmental effects on the nature of hydrogen bonding detected by synchrotron FTIR microspectroscopy 60
M. Takahashi

Catalytic converter: Dynamic behavior of Rh species in Rh/Al_2O_3 model catalyst during three-way catalytic reaction: An *operando* X-ray absorption spectroscopy study 62
H. Asakura, S. Hosokawa, K. Teramura and T. Tanaka

Fuel cells: *Operando* observation of sulfur species that poison polymer electrolyte fuel cell studied by near ambient pressure hard X-ray photoelectron spectroscopy 64
T. Yokoyama and Y. Iwasawa

Fuel cells: *Operando* three-dimensional imaging of distribution and degradation process of Pt-Co cathode catalyst in polymer electrolyte fuel cell 66
H. Matsui, Y. Tan and M. Tada

PEFC catalyst: Electrical double layer structure that activates the oxygen reduction reaction 68
T. Kumeda, O. Sakata and M. Nakamura

Spectro-ptychography: Oxygen-diffusion-driven oxidation behavior and tracking areas visualized by X-ray spectro-ptychography with unsupervised learning 70
Y. Takahashi, H. C. Dam and M. Tada

Soil science: Speciation of phosphorus and zinc in soils receiving swine manure compost for nearly a quarter of a century 72
Y. Hashimoto, K. Yamamoto and J. Kang

Earth & Planetary Science

Mantle dynamics: Sharp 660-km seismic discontinuity explained by extremely narrow binary post-spinel transition 74
T. Ishii and T. Katsura

Mantle dynamics: Laboratory measurements of sound velocities of $CaSiO_3$ perovskite reveal the fate of subducted oceanic crust into the Earth's deep interior 76
S. Gréaux and T. Irifune

Core dynamics: Earth's cooler core inferred from new resistance-heated diamond-anvil-cell experiments 78
R. Sinmyo, K. Hirose and Y. Ohishi

Planetary science: Imaging fossil asteroidal ice in primitive meteorite by synchrotron radiation-based X-ray computed nanotomography 80
M. Matsumoto

Industrial Applications

Piezoelectric device: Investigation of crystallographic deformation by converse piezoelectric effect of piezoelectric thin films 82
G. Tan and I. Kanno

Metal/polymer interface: Revealing interfacial chemistry between metal and polymer by hard X-ray photoelectron spectroscopy 84
Y. Kubo

Accelerators & Beamlines Frontiers 86

SPring-8
Beam Performance 87

New Apparatus, Upgrades & Methodology

• New highly efficient and fully automatic MX at SPring-8 BL45XU beamline 88
S. Baba, K. Hirata, N. Mizuno and T. Kumasaka

SACLA
Beam Performance 91

New Apparatus, Upgrades & Methodology

• Generation of high-intensity narrowband X-ray Free Electron Laser through reflection self-seeding 92
I. Inoue, T. Osaka and M. Yabashi

Facility Frontiers 94

SPring-8 Facility Status 95

Introduction 95
Machine Operation 96
Beamlines 97
User Program and Statistics 100
Research Outcome 103
Budget and Personnel 103
Research Complex 103
SPring-8 Users Community (SPRUC) 105
Outreach Activities 106

SACLA Facility Status 107

Note: The principal publication(s) concerning each article is indicated with all author's names in italics in the list of references.

Preface

It is my great pleasure to publish SPring-8/SACLA Research Frontier 2019 describing the activities of SPring-8 and SACLA in FY2019. JASRI is responsible for operating two world-leading accelerator-based light sources, SPring-8 and SACLA, located on the same campus, whose synergy produces groundbreaking results.

SPring-8 (Super Photon ring 8 GeV) welcomed 15,970 users in 2019 who came to perform more than 2,000 experiments. Currently, SPring-8 users are publishing over 1,000 research papers per year. SACLA users published over 70 research papers in 2019.

A number of SPring-8 and SACLA users were awarded prestigious prizes in 2019 and 2020 for their achievements in science and technology. To take a few, Professor Shigeyuki Yokoyama (RIKEN, The University of Tokyo) was awarded the Medal with Purple Ribbon in fall 2019 for his achievements in structure biology, to which X-ray crystallography experiments at SPring-8 made major contribution. Professor Junji Sugiyama (Kyoto University, visiting scientist of JASRI) was awarded the Medal with Purple Ribbon in spring 2020 for his achievements in wood science, where the small-angle X-ray scattering (SAXS) and imaging experiments at SPring-8 made major contributions.

In this volume, a comprehensive review is reported by Professor Yoshinari Abe (Tokyo University of Science) on the application of synchrotron-based X-ray analysis to cultural heritages and art.

Active users of SPring-8 have also contributed the essence of their results as review articles in the section of Scientific Frontiers in this volume, which composes Life Science, Physical Science, Chemical Science, Earth & Planetary Science, and Industrial Applications. In addition, the principal activity reports on SPring-8/SACLA facilities are included in the sections of Accelerators & Beamlines Frontiers and Facility Frontiers.

I am very grateful to the many authors and experts who contributed their papers to this volume. Special thanks are due to Dr. Naoto Yagi and the members of the editorial board for their continuous efforts.

Y. Amemiya

Yoshiyuki Amemiya
President
Japan Synchrotron Radiation Research Institute (JASRI)

Editor's Note

This is the 2019 issue of SPring-8/SACLA Research Frontiers that covers outstanding scientific outcomes of SPring-8 and SACLA in 2018 and 2019. The best scientific achievements are collected from more than 1,000 papers published using SPring-8 or SACLA each year. As some open journals claim, it is hard to judge the true value of a scientific paper when it is published. Even so, there are papers that attract strong attention of the researchers in the field and those that surprise specialists. The editors are picking up such papers. In this sense, this is a snapshot of science at SPring-8 and SACLA in 2019 that we will look back in future. Even if some of these papers are forgotten, they may give inspirations to readers.

There is one review in this issue, which is written by Dr. Yoshinari Abe of Tokyo University of Science (recently moved to Tokyo Denki University). SPring-8 ran "The Social Interest Proposals" from 2015 through 2018. This program included many proposals in the field of cultural heritage studies. The objects of the studies spanned widely both in time and space. Results of some of these studies are described by Dr. Abe who, with Prof. Izumi Nakai, is playing a major role in synchrotron-based studies on cultural heritages in Japan.

SPring-8/SACLA Research Frontiers is made of two parts. The first is scientific results (Scientific Frontiers) and the second is additional information on hard and soft infrastructures that support scientific research. Although some important numbers such as the operation time are given in the second part, other information and more complete statistical numbers on the operation of SPring-8 and SACLA are available on the website so that more updated information can be accessed (http://www.spring8.or.jp/en/about_us/spring8data/).

The full text of SPring-8/SACLA Research Frontiers is also available on the SPring-8 website (http://www.spring8.or.jp/en). For the list of publications produced by SPring-8 users and staff, please visit the publication database at http://www.spring8.or.jp/en/science/publication_database/.

On behalf of all the editors, I would like to thank those who helped us by recommending excellent research results suitable for publication in this issue, and the users and staff of SPring-8 who contributed their reports to this issue.

Naoto Yagi
Japan Synchrotron Radiation Research Institute (JASRI)

Editorial Board

Scientific Frontiers

Review Article

Synchrotron radiation-based X-ray analysis for cultural heritage and art

1. Introduction

Today, introduction of scientific techniques has been necessary in the field of the cultural heritage. Various chemical and physical analytical techniques have been applied to archaeological sites and excavated artifacts for many purposes, e.g., identification of material and production techniques, provenancing, dating, investigation of aging degradation, and preservation and restoration. Likewise, these techniques have been utilized aggressively in the field of art as well. This is due to the efforts of curators, conservators, and scientists that we can see masterpieces of art painted hundreds of years ago in museums today. On the other hand, it is not always possible to introduce any scientific techniques into the investigation of cultural heritage and art; because of their high historical and artistic values, it is often required to choose a nondestructive and noncontact analytical technique at ordinary temperatures and pressures. The use of X-rays is a suitable solution to analyze cultural heritage and art under tight restriction. X-rays will be a good decoder for interpreting the provenance information inherent within them nondestructively. Particularly in X-ray fluorescence (XRF) analysis, a handheld XRF spectrometer has been in widespread use as an easy, quick tool for measuring chemical composition of cultural heritage and art in a nondestructive and on-site manner. Today, the application to cultural heritage and art is forming an appreciable market for X-ray instruments and related equipment in both laboratory and on-site uses.

The application of synchrotron radiation (SR) X-rays in the fields of cultural heritage and art dates to the late 1980s, but it has become widespread only recently [1] owing to the continuous development of stable light sources and measurement equipment, and close dialog among researchers in different fields: archaeologists, curators, conservators, and experts on physical and chemical techniques based on the SR. Outstanding features of the SR light sources, such as high brilliance, high directionally, and wide tunability of energy/wavelength, enable us to conduct various X-ray analyses with superior sensitivity, accuracy, and spatial resolution on cultural heritage and art without their destruction, e.g., XRF analysis, X-ray powder diffraction, X-ray absorption fine structure (XAFS) analysis, and computed tomography (CT). In addition, by shaping the size and shape of the SR-X-ray beam using optical elements, any samples from an entire painting as tall as a human to a single microscopic particle of pigment in the painting, can be a target of SR-based X-ray analysis. One of the major reasons behind the wide spread of the SR-based X-ray analytical techniques among researchers of cultural heritage and art was the investigation of a painting by Vincent van Gogh [2]. The SR-based XRF imaging of the painting successfully revealed the hidden image of a woman's head painted under Van Gogh's work "Patch of Grass." Along with a reconstructed image of this hidden face, the results of its study were widely covered by the media.

In this review, the author introduces three SR-based X-ray analytical techniques, XRF analysis, X-ray CT, and X-ray absorption edge radiography, with actual examples of application to cultural heritage and art at SPring-8.

2. High-energy SR-XRF of ceramic and glass

In the case of XRF analysis, utilizing the monochromatic SR-X-ray will improve the lower limits of detection markedly compared with bench-top XRF instruments because of the reduction in background due to the scattering of white X-rays from an X-ray source. In addition, the selection of a suitable energy of excitation X-rays enables the selective excitation of target element(s). In some SR-facilities adapted to hard X-rays, monochromated X-rays with very high energy unattainable in bench-top instruments can be utilized for XRF analysis specialized for heavy elements; this is the so-called high-energy (HE-) SR-XRF analysis. The use of 116 keV monochromated X-rays enables excitation of *K*-edges of all heavy elements up to uranium (*K*-edge: 115.6 keV). Figure 1 shows a HE-SR-XRF spectrum of NIST SRM 613, a certified standard material of soda-lime silicate glass containing 40–50 ppm trace heavy elements [3]. The spectrum was obtained at BL08W, the only wiggler beamline and the highest X-ray energy beamline in SPring-8. Lower limits of detection for elements in the lower background region of the spectrum (25–60 keV), such as Sn,

Ba, and lanthanoids, were estimated to be 1 ppm or less [4]. The benchtop XRF instrument can also detect these elements using L-lines in the lower energy region, but L-line peaks of these elements overlap considerably with K-line peaks of K, Ca, and 3*d* transition metals. HE-SR-XRF analysis, therefore, is the only nondestructive multielement analytical technique for detecting trace amounts of heavy elements with sensitivity as good or better than that of the instrumental neutron activation analysis.

HE-SR-XRF at SPring-8 was originally developed for a forensic application by Nakai *et al*. [5] in the late 1990s. As the first application to a cultural heritage, Miura *et al*. [6] applied this technique to porcelain clay bodies of china wares excavated from old kilns in Kutani and Arita districts in Japan and showed that Kutani and Arita wares can be clearly distinguished on the basis of the trace heavy element composition. The author has recently applied the technique to ancient glass products found in Japan to identify where they were manufactured. Because no evidence of primary glass production from raw materials prior to the late 7th century was previously found in Japan, it is believed that all earlier glass products were imported from overseas. In contrast to the thousands of glass beads excavated from a number of ancient tombs in Japan, only a few glass vessels imported to ancient Japan remain today. The author conducted the HE-SR-XRF analysis of fragments of two glass vessels excavated from a tumulus in Nara prefecture and revealed that these precious glass vessels were originally manufactured at workshops located in the Sasanian Empire (West Asia) and Roman Empire (Mediterranean region) [4,7]. As an example, Fig. 2 shows the chemical compositions of Specimen A, a fragment of a glass bowl excavated from the tumulus, and glassware manufactured in the Sasanian Empire, namely, Sasanian glass; the compositional feature of the fragment closely matches that of one of the three compositional groups identified in Sasanian glass, that is, the Sasanian 2 group. The results of this study thus demonstrated scientifically the extent of East-West trade through the Silk Road in ancient times.

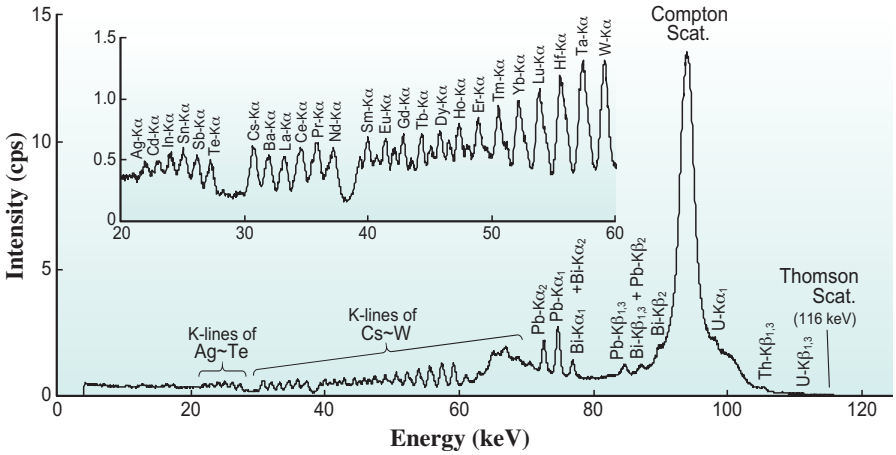

Fig. 1. HE-SR-XRF spectrum of NIST SRM613, a certified standard material of soda-lime silicate glass containing trace heavy elements, obtained by the author using SPring-8 BL08W [3].

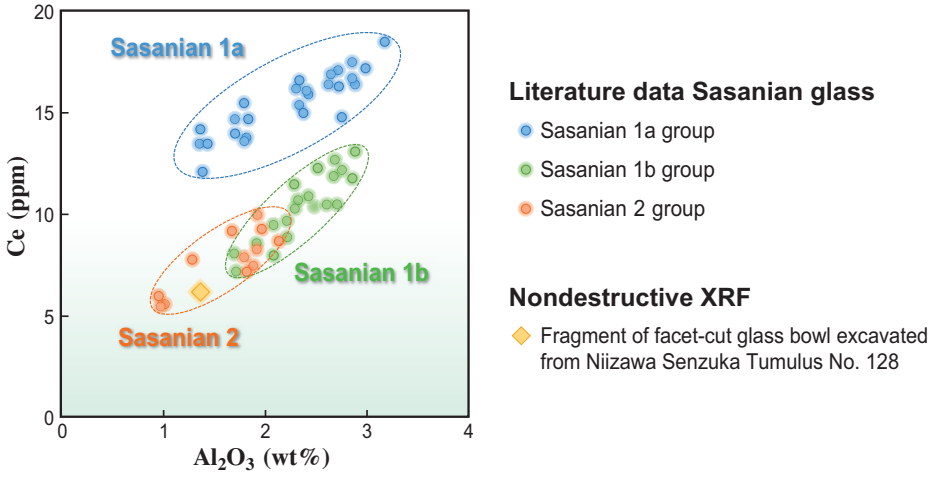

Fig. 2. Chemical composition of a fragment of a facet-cut glass bowl excavated from Niizawa Senzuka Tumulus No. 128 in Nara prefecture and literature data of three compositional groups of Sasanian glass [4,7].

3. SR-X-ray CT of ancient metallic sword

Since humans have long been using metals, there are many historic and archaeological artifacts and works of fine art made of metal. For such studies, X-ray CT is an indispensable tool because it allows us to investigate the inner structure of samples nondestructively. In such studies, high-energy X-rays are required to penetrate a metal object with high density. Hoshino *et al.* [8] applied a CT imaging system using the high-energy (200 keV peak energy) non-monochromatized X-rays from a bending magnet at SPring-8 BL28B2 to visualize the inner structure of an ancient bimetallic sword consisting of both bronze and iron. The sword is part of a collection at Okayama Orient Museum. It is 86 cm long and its blade is bronze. The hilt is also bronze on the surface, but unusual in that it has an iron core, thus bimetallic. It is considered to be from northern Iran dated 10th–8th century BC, which is a transition period from the Bronze Age to the Iron Age. As shown in Fig. 3, the inner structure of this bimetallic sword made of iron and bronze was visualized successfully by SR-based high-energy high-resolution X-ray tomography without destruction. Although the beam hardening of a 2.5% difference in density was observed, inner structures of the ancient sword were clearly visualized. This work demonstrated the feasibility of the high-energy, high-resolution imaging of metallic objects.

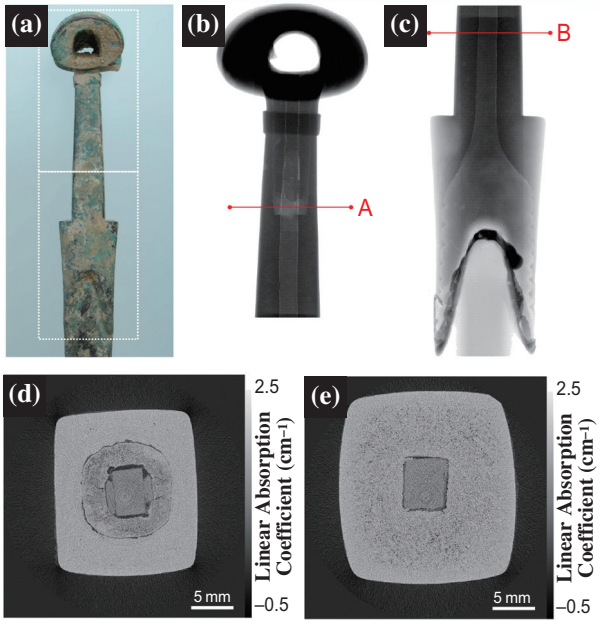

Fig. 3. **(a)** Photograph of a bimetal sword stored at Okayama Orient Museum, Japan. **(b, c)** X-ray projection images of the hilt (handle) and pommel (knob) of the sword indicated by dotted rectangles in (a). **(d)** CT cross section at the solid line A shown in (b). **(e)** CT cross section at the solid line B shown in (c). All data were obtained at SPring-8 BL28B2 and reprinted from the article by Hoshino *et al.* [8].

4. SR-X-ray absorption edge radiography of oil painting

Large-area XRF elemental mapping, the so-called scanning macro (MA)-XRF imaging, is one of the most effective tools for investigating paintings in a nondestructive and noncontact manner, as introduced at the beginning of this review. Although the utilization of the SR-X-ray beam was, in the past, the only way to carry out the MA-XRF imaging of a large painting, some portable analytical instruments specialized for nondestructive on-site MA-XRF imaging have recently been developed and are now in practical use. Today, MA-XRF imaging has become a standard method of investigating paintings nondestructively, but note that a long measurement time is necessary to analyze an entire painting; it sometimes takes all hours of the night. In addition, the same as conventional XRF analysis, the result of MA-XRF imaging will be influenced to no small extent by the presence of other elements that may be present as a major component of the painting.

As a rapid and element-selective imaging technique applicable to cultural heritage and art, SR-based X-ray absorption edge radiography is introduced here. Similarly to conventional X-ray radiography, the technique irradiates a large-area X-ray beam onto the object and records a transmission X-ray image using a two-dimensional (2D) X-ray detector. What is different from the conventional X-ray radiography is that two transmission images are recorded simultaneously using two different energies of monochromatic X-rays above and below the absorption edge energy of the target element. The distribution of only the target element can be visualized by calculating the difference between these two images. Similar X-ray imaging techniques using contrast between above and below the absorption edge were, in principle, utilized since the early stage of the application of SR-X-rays in the healthcare field. For the application to cultural heritage and art, Wallert *et al.* [9] applied the technique to an early modern painting as “dual-energy *K*-edge absorption radiography.” They successfully visualized the distributions of Pb

and Hg on the painting by measuring their *K*-edge absorptions, but only the high-energy X-rays over 80 keV were used in consideration of the strong absorption of X-rays by the pigments containing these heavy elements and the lack of sensitivity of the 2D X-ray detector in the lower energy region.

The author has recently developed this technique for the lower energy region using a large-area monochromatic SR-X-ray beam at BL20B2 in the Medium-length Beamline Facility of SPring-8 with a 2D-flat panel X-ray sensor suitable for the detection of X-rays with an energy higher than 12 keV [10]. The verification using model paintings prepared by the author demonstrated that it is possible to rapidly perform the elemental imaging of paintings by this method: ~5 min per element for an area of 10×10 cm^2. The analysis of a modern oil painting showed that this technique is useful for the elemental imaging of elements with absorption edge energies above 12 keV (see Fig. 4) with a spatial resolution of ~100 μm. Because the technique utilizes the absorption of X-rays, it is expected that the technique will enable the mapping of the difference in the chemical state of the same element by combined use of XAFS analysis. While there is still some room for improvement before practical realization, this new SR-based analytical technique could become an alternative for the investigation of the cultural heritage and art instead of the MA-XRF imaging technique in the future.

5. Conclusion

SR-based X-ray analytical techniques are highly suitable for the investigation of cultural heritage and art because of the strong demand for nondestructive and noncontact techniques. In contrast to the increasing activity concerning cultural heritage and art at SR facilities in the US and Europe, only a few researchers apply SR-X-rays to these fields at a limited number of beamlines available for these fields in Japan. It is hoped that the usefulness of the SR-based X-ray analytical techniques will gain increasing recognition among researchers in the fields of cultural heritage and art in this country. At the same time, we scientists utilizing the techniques based on SR should not forget to make compromises with researchers in different fields. On the other hand, we should understand that there are drawbacks to using the SR-based X-ray analysis in the investigation of cultural heritage and art. Needless to say, to use SR-X-rays, all samples for analysis must be transported into the SR facility. For cultural heritage and art, transport between their depository and the SR facility poses a risk of unnecessary damage or destruction. In particular, in the case of objects designated as important cultural heritage or national treasures by the government, it will be more difficult to remove them from their depository even for scholarly purposes. Thus, for researchers working in the fields of cultural heritage and art, the use of SR-X-rays is a "last resort". In other words, researchers exhaust other options before taking the cultural heritage or art into the SR facility.

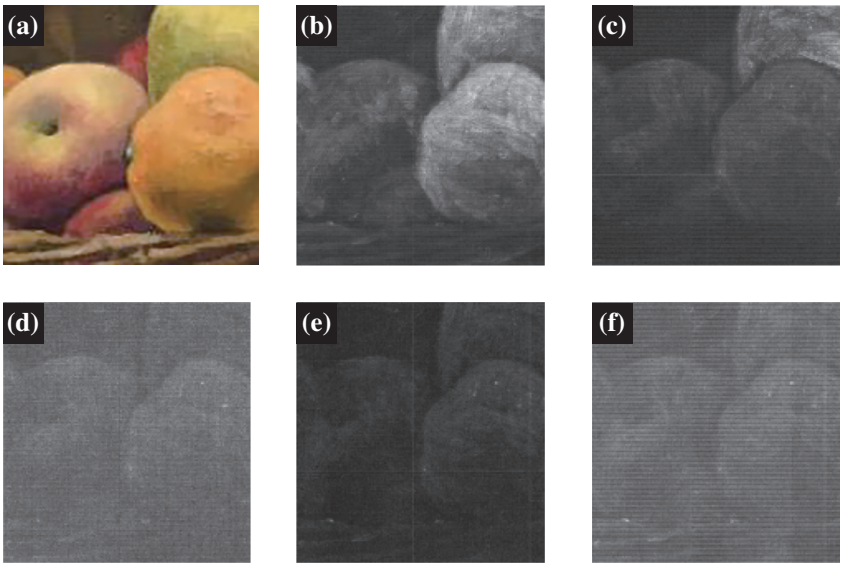

Fig. 4. **(a)** Photograph of modern oil painting analyzed in this study. Representative elemental distributions visualized by SR-X-ray absorption edge radiography: **(b)** Pb L_3-edge, **(c)** Cd *K*-edge, **(d)** Ba *K*-edge, **(e)** Sr *K*-edge, and **(f)** Se-*K* edge. All data were obtained at SPring-8 BL20B2 by the author [10].

Yoshinari Abe[a,b]

[a] Department of Applied Chemistry, Tokyo University of Science
[b] Division of Materials Science and Engineering, Tokyo Denki University

Email: y.abe@mail.dendai.ac.jp

References

[1] S. Mobilio *et al.*: Synchrotron Rad. (2015) Springer.
[2] J. Dik *et al.*: Anal. Chem. **80** (2008) 6436.
[3] Y. Abe: Adv. X-ray Chem. Anal. Jpn. **51** (2020) 1.
[4] Y. Abe *et al.*: J. Archaeol. Sci. Rep. **17** (2018) 212.
[5] I. Nakai *et al.*: Synchrotron Rad. **8** (2001) 1071.
[6] Y. Miura *et al.*: Archaeol. Nat. Sci. Jpn. **46** (2003) 33.
[7] Y. Abe: SPring-8/SACLA Research Frontiers 2017 (2018) 88.
[8] M. Hoshino *et al.*: AIP Advances **7** (2017) 105122.
[9] A. Wallert *et al.*: J. Am. Inst. Conservat. **48** (2009) 159.
[10] I. Nakai *et al.*: Adv. X-ray Chem. Anal. Jpn. **50** (2019) 261.

Oxyl/oxo coupling mechanism for dioxygen formation in photosystem II

Photosynthesis in plants and algae is a process of synthesizing biomass in the form of sugars using light energy from the sun. The initial step of oxygenic photosynthesis is the light-driven water oxidation reaction of photosystem II (PSII), in which four electrons and protons are extracted from two water molecules, and a dioxygen molecule is released into the atmosphere. A manganese complex called the oxygen-evolving center (OEC) catalyzes this reaction through five linear oxidation intermediates of the S_i-state cycle (i = 0–4). Unveiling the mechanism of natural water oxidation is of considerable importance as it may have great potential in applications for developing a sustainable energy source, that is, a framework for the S_i-state cycle may provide structural insights into a rational design for catalysts capable of artificial water oxidation by which clean, renewable energy from the sun may be harvested.

The structure of PSII in the dark-adapted S_1 state was first analyzed at 1.9 Å resolution at SPring-8 **BL41XU** and **BL44XU**, and the detailed organization of the OEC was revealed (Fig. 1) [1]. The OEC is a Mn_4CaO_5 cluster with a shape resembling a distorted chair, located at the lumenal surface of the thylakoid membrane and linked to four hydrogen-bonded water channels [1]. The S_1-state structure was further analyzed using X-ray free electron lasers (XFELs) provided by the SACLA **BL2** and **BL3** to obtain its radiation-damage-free structure [2], which confirmed the presence of a unique, central oxo-bridged oxygen (O5) located between two manganese atoms, Mn1 and Mn4, with unusually long bond distances to the two Mn ions. This feature suggests weak binding of O5 with the nearby Mn ions and therefore possibly a crucial role of O5 in dioxygen formation [2]. Furthermore, pump-probe, time-resolved serial femtosecond crystallography (SFX) at room temperature on the S_3-state structure induced by two-flash illumination at 2.35 Å resolution revealed that the OEC becomes a Mn_4CaO_6 cluster in the S_3 state by incorporating an additional oxygen O6 in the vicinity of O5. This result supports a dioxygen formation mechanism between O5 and O6 [3]. While the insertion of O6 seems reasonable, the chemical structures of O5 and O6 remain controversial because of the uncertainty in the O5-O6 distance of 1.5 Å reported at the limited resolution. Therefore, several possible mechanisms for the O=O bond formation have been under debate.

To reveal detailed structural changes during the water oxidation reaction, we further analyzed the XFEL structures of PSII in the S_1, S_2, and S_3 states by using fixed-target serial femtosecond crystallography with SACLA-XFELs. The S_2 and S_3 states were generated by excitations with one or two flashes at room temperature with PSII microcrystals evenly sprayed on a mesh and trapped immediately at 77 K. Single-shot diffraction images were collected by fixed-target data collection at cryogenic temperature. Compared with the previous SFX approach, this method reduced sample consumption by one order of magnitude and ensured low-background images, allowing us to analyze the structure of multiple intermediate states at 2.15 Å resolution [4].

The results showed that no insertion of water occurs in the S_2 state, but upon transition to the S_3 state, the flipping of D1-Glu189, the only monodendate carboxyl ligand of the OEC, provides a space for incorporating the additional oxygen O6, and the

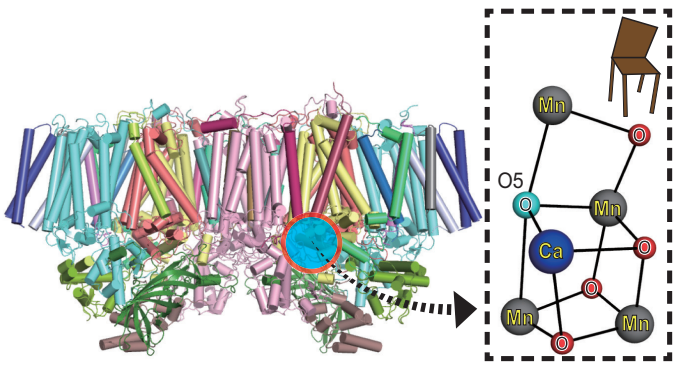

Fig. 1. Overall structure of PSII and an enlarged view of the OEC, the Mn_4CaO_5 cluster. PSII is a large membrane protein-pigment complex consisting of twenty protein subunits and exists in a dimeric form. Red circle indicates the location of the OEC, and its enlarged view on the right side shows the architecture of the OEC, which resembles the form of a distorted chair.

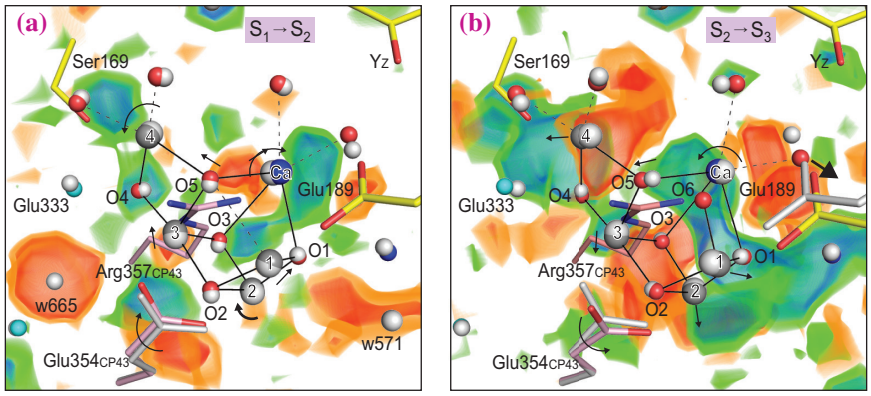

Fig. 2. Structural changes in the vicinity of the OEC during the S_i-state transitions. OEC structures were superposed with the difference Fourier maps of **(a)** S_2 minus S_1 and **(b)** S_3 minus S_2 datasets. Difference maps are contoured at –4σ (red), –3σ (orange), 3σ (green), and 4σ (blue).

Mn_4CaO_5 cluster remains in the open-cubane form (Fig. 2). To determine the exact chemical structure of the species of O5-O6 we examined four possible chemical species, namely, superoxo, peroxo, oxyl/oxo, and oxyl/hydroxo. By altering the O5-O6 distance and examining the residual densities in the difference map, we found that a distance of 1.9 Å between O5 and O6 resulted in the lowest residual density. This finding suggests an oxyl/oxo coupling mechanism for dioxygen formation in the OEC. Moreover, the flipping of Glu-189 induces van der Waals repulsion between the carbonyl oxygen of D1-Glu189 and Ala-411$_{CP43}$, thereby moving a short loop of the CP43 subunit that restricts the size of the O1-water channel, leading to the widening of the O1-channel. This channel thus likely plays a role in delivering the substrate water to the Mn cluster during the S_2 to S_3 transition. Furthermore, O6 is coordinated to the Ca ion in the S_3 state, leading to the change in the coordination number of Ca from 7 in the S_1 state to 8 in the S_3 state. These structural changes revealed the mechanism of photosynthetic water oxidation via the cooperative action of substrate water access, proton release, and O=O bond formation (Fig. 3) [4].

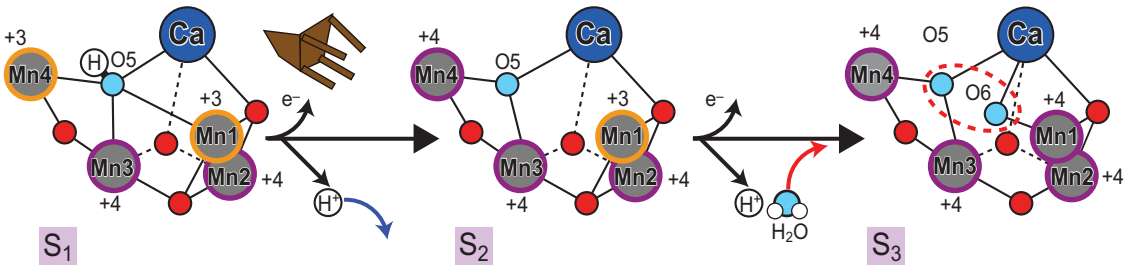

Fig. 3. Summary of structural changes of the OEC and the proposed mechanism of dioxygen formation. The protonated O5 atom in the S_1 state is located between Mn1 and Mn4 atoms and may be deprotonated in the S_2 state. Upon transition to the S_3 state, the OEC incorporates an additional water molecule as the O6 atom into the vicinity of O5 from the O1 channel. The species formed between O5 and O6 is determined to be oxyl/oxo in the S_3 state, which is considered to proceed to the O=O bond formation and dioxygen release upon further transition beyond the S_3 state.

Michihiro Suga[a,b,*] and Jian-Ren Shen[a]

[a] Research Institute for Interdisciplinary Science, Okayama University
[b] JST, PREST

*Email: michisuga@okayama-u.ac.jp

References

[1] Y. Umena *et al.*: Nature **473** (2011) 55.
[2] M. Suga *et al.*: Nature **517** (2015) 99.
[3] M. Suga *et al.*: Nature **543** (2017) 131.
[4] *M. Suga, F. Akita, K. Yamashita, Y. Nakajima, G. Ueno, H. Li, T. Yamane, K. Hirata, Y. Umena, S. Yonekura, L.-J. Yu, H. Murakami, T. Nomura, T. Kimura, M. Kubo, S. Baba, T. Kumasaka, K. Tono, M. Yabashi, H. Isobe, K. Yamaguchi, M. Yamamoto, H. Ago, and J.-R. Shen: Science* ***366*** *(2019) 334.*

Charge-density analysis of green fluorescent protein at ultra-high resolution

Green fluorescent protein (GFP) from the jellyfish *Aequorea victoria* is a light-emitting protein that absorbs blue light and emits green light [1]. The structure consists of an 11-stranded β-barrel plugged by the chromophore (Fig. 1). The chromophore 4-(*p*-hydroxybenzylidene)imidazolin-5-one is formed from three intrinsic residues in the polypeptide chain by post-translational reactions. Two forms of the chromophore, "A" and "B", with different protonated states exist in wild-type GFP. The A and B forms can be individually stabilized by introducing mutations to residues around the chromophore. Many artificial variants with various useful features have been created, and the variants as well as the wild-type GFP are now indispensable as tools in molecular biology. More than 400 structures of related fluorescent proteins, including their variants, have been deposited in the Protein Data Bank (PDB). However, the electron densities of hydrogen atoms and valence electrons, which characterize the chemical states of atoms, are difficult to detect by conventional X-ray analysis. Accordingly, chemical states of atoms constituting the chromophore and the details of the interaction with the surrounding residues in GFP are unclear but indispensable for understanding the fluorescence mechanism. Meanwhile, the charge-density analysis at ultra-high resolution can provide details of the electronic structures of the protein. Recently, we successfully performed the charge density analysis of GFP at ultra-high resolution [2].

The F99S/M153T/V163A/E222Q mutation was introduced to GFP to stabilize the B-form structure of the chromophore. Large (~1.0×0.5×0.5 mm^3) crystals were obtained by the seeding method. A diffraction dataset at 0.78 Å resolution was obtained at SPring-8 **BL41XU** beamline using high-energy X-rays (λ = 0.35 Å, E = 35.4 keV) [3]. The structure was initially refined with the parameters of the conventional independent spherical atom model (ISAM). Almost all the hydrogen atoms of the protein residues were detected and included in the structure model. In addition, more than 20 hydrogen atoms of water molecules were included. Residual densities from the valence electrons were observed around each atom after several cycles of refinement (Fig. 2(a)). Further refinements were performed using the parameters of the multipolar atomic model (MAM) to explain the nonspherical features of the valence electrons. The final R_{work} and R_{free} factors converged to 10.8% and 12.5%, respectively. After the MAM refinement, the residual densities were reproduced in the static deformation map, indicating the success of the MAM refinement (Fig. 2(b)).

We analyzed the features of the refined map of GFP by applying the atoms-in-molecules (AIM) theory to detect hydrogen bonding around the chromophore (Fig. 3(a)). We detected some nonconventional (CH···O type) hydrogen bonds between the chromophore and the protein environment in addition to conventional hydrogen bonds. Another nonconventional (CH···N type) hydrogen bond bridging was also detected between two ring moieties of the chromophore. The planarity of the two ring moieties, which is essential to the high fluorescence activity of GFP, seems to be reinforced by the CH···N type interaction. In addition, weaker attractive and repulsive interactions were visualized by the noncovalent interaction (NCI) analysis of the accurate electron density map. Some attractive CH–π and lone pair–π interactions were detected between the chromophore and

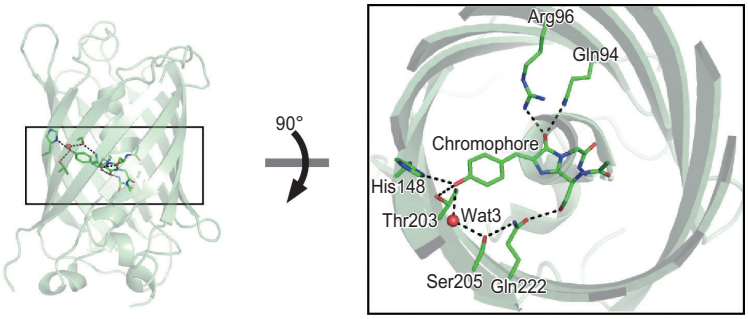

Fig. 1. Structure of GFP. The barrel structure for the F99S/M153T/V163A/E222Q variant is represented as a ribbon model. The chromophore and the surrounding residues are represented as sticks. Conventional hydrogen bonds around the chromophore are indicated as dashed lines.

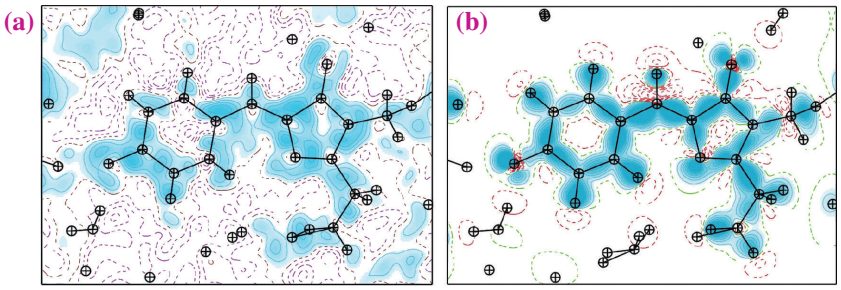

Fig. 2. Contour maps around the chromophore in the GFP. **(a)** Residual ($F_{obs} - F_{calc}$) map after ISAM refinement. The contour intervals are 0.05 e/Å^3. **(b)** Static deformation map after MAM refinement.

Thr62 (Fig. 3(b)). These weak interactions cause electron delocalization in the chromophore from the imidazolinone moiety to the phenolic moiety, which means the phenolate form is more predominant than the quinone form. The resultant electronic structure enhances the transition moment in the excitation reaction for efficient fluorescence.

Interactions in protein molecules have been estimated empirically from geometric parameters such as bond lengths and angles. However, by using the charge density obtained from ultra-high-resolution analysis, intramolecular interactions can be detected quantitatively as features of the experimental electron density. Actually, intramolecular interactions around the active sites have recently been investigated by charge density analyses at ultra-high resolutions for other proteins [4,5]. The information obtained in this work will enable us to perform the rational design of new GFP variants through quantum chemical calculations.

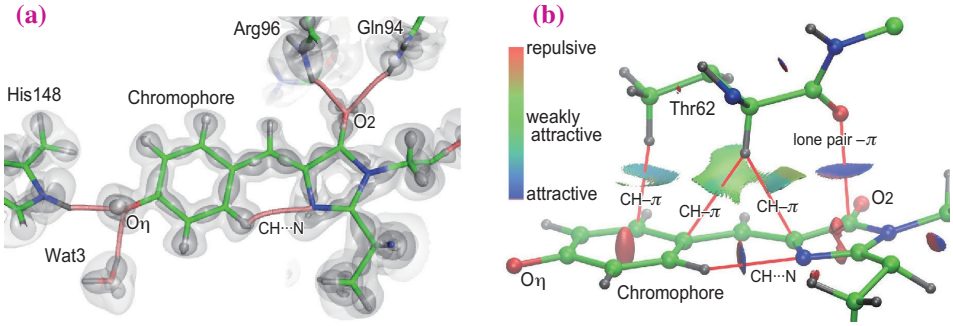

Fig. 3. Interactions between the chromophore and the surrounding residues. **(a)** Hydrogen bonding network revealed by the AIM analysis. The bond paths for conventional and nonconventional hydrogen bonds are represented as pink curves. The gray surfaces represent the deformation electron density at contour levels of +0.01, +0.15 and +0.5 e/Å^3. **(b)** NCI surface around the chromophore. The reduced density gradient isosurface is represented in a blue-green-red scheme. Blue indicates attraction, green indicates very weak attraction and red indicates repulsion.

Kiyofumi Takaba† and Kazuki Takeda*

Department of Chemistry, Kyoto University

*Email: ktakeda@kuchem.kyoto-u.ac.jp

† Present address: RIKEN SPring-8 Center

References

[1] O. Shimomura *et al.*: Cell. Comp. Physiol. **59** (1962) 223.
[2] *K. Takaba, Y. Tai, H. Eki, H.-A. Dao, Y. Hanazono, K. Hasegawa, K. Miki and K. Takeda: IUCrJ **6** (2019) 387.*
[3] K. Hasegawa *et al.*: J. Synchrotron Rad. **20** (2013) 910.
[4] Y. Hirano *et al.*: Nature **534** (2016) 281.
[5] K. Takaba *et al.*: Sci. Rep. **7** (2017) 43162.

Crystal structure of heliorhodopsin

Rhodopsins consist of two distinct protein types, microbial rhodopsins (type-1) and animal rhodopsins (type-2). Type-1 microbial rhodopsins comprise seven transmembrane helices and an all-*trans* retinal chromophore attached to a lysine residue of the protein through a protonated Schiff base linkage and exhibit diverse functions such as pumps, channels, enzymes, and signaling. Recently, a distinct abundant group of microbial rhodopsins, heliorhodopsins (HeRs), were discovered by metagenomics [1] (Fig. 1). HeRs are widely present in bacteria, archaea, algae, and algal viruses. Although HeRs are phylogenetically distant from the type-1 rhodopsins, HeRs are predicted to have seven transmembrane helices and a retinal chromophore linked to lysine at the seventh transmembrane helix through a protonated Schiff base linkage, as in the type-1 rhodopsins. However, the distribution of charged residues and the functional analysis have suggested that HeRs are embedded in the membrane with their N termini facing the cell cytoplasm, which is the opposite orientation to those of the type-1 and type-2 rhodopsins.

HeRs exhibit a photocycle involving the K, M, and O intermediates upon light absorption, and have a long-lived photoactivated state ($\tau \sim 1$ s). HeR photocycles accompany retinal isomerization and proton transfer, as in the type-1 and type-2 rhodopsins, but protons are never released from the protein, even transiently. HeRs lack pump and channel activities, suggesting that HeRs function as light sensors through putative interaction partners. Moreover, the HeR-possessing species lack a retinal biosynthetic pathway in their genomes. Thus, HeRs are considered to work by efficiently binding an exogenous retinal, similar to actinorhodopsin [2]. HeRs and type-1 rhodopsins exhibit distant sequence similarities, and thus little is known about the overall fold and the photoactivation mechanism of HeRs.

We screened multiple HeRs and identified the Thermoplasmatales archaeon SG8-52-1 HeR (TaHeR) as a promising candidate. We purified and crystallized the full-length TaHeR by meso crystallization. We determined the TaHeR structure at 2.4 Å resolution [3]. The diffraction data was collected with an automated data-collection system, ZOO, at SPring-8 **BL32XU**.

The structure comprises seven transmembrane helices (TM), six loops and short N and C termini (Fig. 2(a)). Analysis of HeR 48C12 showed that the N terminus faces the cell cytoplasm [1], and we therefore refer to the loops on the N-terminal side as intracellular loops (ICL) 1–3, and those on the C-terminal side as extracellular loops (ECL) 1–3. ECL1 forms a long loop containing two antiparallel β-strands and ICL1 forms a three-turn α-helix. HeR forms a dimer with the symmetric protomers aligned along the crystallographic two-fold axis. High-speed atomic force microscopy (HS-AFM) images revealed that HeR also forms a dimer in a lipid bilayer, indicating that the dimer reflects the physiological condition (Fig. 2(b)).

To investigate the structural similarity between HeR and type-1 rhodopsin, we compare the structures of TaHeR and bacteriorhodopsin (BR), a representative type-I rhodopsin. The loop structures of HeR are completely different from those of BR (Fig. 2(c)). By contrast, the transmembrane region is more similar, although HeR and BR share only 8% sequence identity. An all-trans retinal is covalently bound to Lys238, forming the Schiff base, as in the type-1 microbial rhodopsins. Overall, HeR shares an essentially common fold with the type-1 rhodopsins. Despite these similarities, HeRs are embedded in the membrane in an inverted orientation relative to the other rhodopsins. The results of immunofluorescent staining analysis supported this inverted topology when HeR was expressed in mammalian cells. The intracellular and extracellular faces are positively and negatively charged, respectively (Fig. 2(d)), consistent with the 'positive-inside' rule.

From the Schiff base to the intracellular side, there are extensive water-mediated hydrogen-bonding interactions that play a key role in the photoactivation of HeR. By contrast, all of the residues directed toward the transmembrane region in the extracellular half are quite hydrophobic (Fig. 3(a)). No carboxylate residue is observed, which is critical for proton transfer in

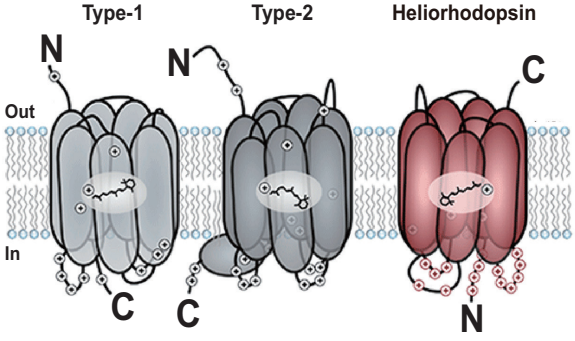

Fig. 1. Schematic of membrane topologies of type-1 rhodopsin, type-2 rhodopsin and heliorhodopsins.

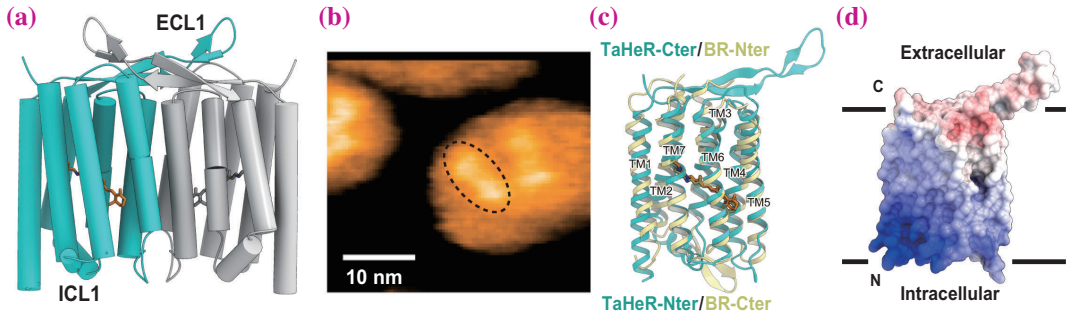

Fig. 2. Overall structure of TaHeR. **(a)** Schematic representation of TaHeR dimer. **(b)** Typical HS-AFM image of TaHeR dimers in the lipid membrane. **(c)** Superimposition of TaHeR and BR. **(d)** Electrostatic surface viewed from the membrane plane.

the proton-pumping rhodopsins. These hydrophobic residues fill the space in the extracellular half, preventing the permeation of protons and ions.

Unexpectedly, a lateral fenestration exists between TM5 and TM6, located above the β-ionone ring of the retinal chromophore, in the surface representation of the TaHeR structure (Fig. 3(b)). The β-ionone ring is exposed to the membrane environment through this fenestration, and the monoolein used in the crystallization fits within the fenestration and directly interacts with the β-ionone ring (Fig. 3(c)). The residue above the β-ionone ring is Gly171, which contributes to the formation of the fenestration. The G171W mutant showed no regeneration of the retinal chromophore in retinal bleaching and regeneration upon hydroxylamine (HA) analysis (Fig. 3(d)), and thus prevented retinal access through the lateral fenestration, suggesting that HeRs efficiently capture the exogenous retinal, which functions as light sensors, from the lipid environment through lateral fenestration.

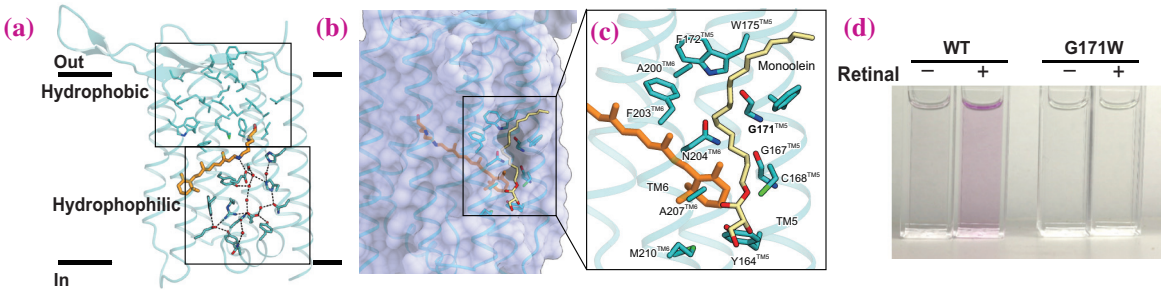

Fig. 3. **(a)** Intramolecular interactions viewed from the membrane plane. **(b)** Surface representation of the TaHeR structure. **(c)** Residues constituting the lateral fenestration and the monoolein are shown as sticks. **(d)** Pictures of TaHeR wild-type and G171W solutions without (–) and with (+) retinal.

Wataru Shihoya

Department of Biological Sciences,
The University of Tokyo

Email: wtrshh9@gmail.com

References

[1] A. Pushkarev *et al.*: Nature **558** (2018) 595.
[2] J.L. Keffer *et al.*: J. Bacteriol. **197** (2015) 2704 .
[3] *W. Shihoya, K. Inoue, M. Singh, M. Konno, S. Hososhima, K. Yamashita, K. Ikeda, A. Higuchi, T. Izume, S. Okazaki, M. Hashimoto, R. Mizutori, S. Tomida, Y. Yamauchi, R. Abe-Yoshizumi, K. Katayama, S.P. Tsunoda, M. Shibata, Y. Furutani, A. Pushkarev, O. Béjà, T. Uchihashi, H. Kandori and O. Nureki: Nature* ***574*** *(2019) 132.*

Discovery of cap-specific adenosine-N^6-methyltransferase (CAPAM)

RNA molecules are enzymatically modified after transcription. To date, about 150 types of chemical modifications have been identified in various RNAs from all domains of life. N^6-methyladenosine (m^6A), one of the most abundant modifications in eukaryotic mRNA, plays critical roles in RNA metabolism and function. Recent advances in deep sequencing technology enable us to map m^6A in a transcriptome-wide manner, highlighting the biological importance of this modification and establishing the concept of "epitranscriptomics" [1]. Most m^6A sites in internal regions of mRNAs are introduced by an m^6A writer, METTL3 methyltransferase, working in conjunction with accessory proteins. m^6A is a reversible modification that can be removed by the eraser proteins ALKBH5 and FTO. m^6A is recognized by several reader proteins, including the YTH family proteins, which have diverse influences on their target mRNAs, affecting processes such as translational regulation and mRNA decay. m^6A is also present at the transcription start site of mRNAs.

The 7-methylguanosine (m^7G) cap, a characteristic 5′-terminal structure of eukaryotic mRNAs, plays extensive roles in mRNA processing, stability, nuclear export, and translation. In addition to the m^7G cap structure, the 5′-terminal regions of the mRNAs of higher eukaryotes are frequently methylated [2]. The first and second nucleotides of mRNAs are 2′-*O*-methylated by CMTR1 and CMTR2, respectively. These modifications serve as molecular markers that distinguish between self and non-self mRNAs by antagonizing RNA sensors, allowing escape from the innate immune system. In vertebrate mRNAs, if the 5′ terminal nucleoside is adenosine, the N^6 position of the A is methylated by an unidentified enzyme to form N^6,2′-*O*-dimethyladenosine (m^6Am) (Fig. 1(a)). Recent studies indicated that m^6Am is involved in mRNA stability and metabolism. However, the biogenesis and functional role of this modification remained elusive.

To identify the enzyme responsible for N^6 methylation of m^6Am, we first established a highly sensitive method for analyzing the 5′-terminal chemical structures of capped mRNAs using RNA mass spectrometry (RNA-MS). We then analyzed the modification status of the 5' cap structure of mRNAs obtained from several strains harboring knockouts of uncharacterized methyltransferases that are conserved in vertebrates but not in yeast. When we knocked out the candidate gene *PCIF1*, m^6Am disappeared completely and was replaced by Am at the first nucleotide, indicating that PCIF1 is responsible for m^6Am formation. We then confirmed that recombinant PCIF1 could form m^6Am on the capped mRNA *in vitro* in the presence of *S*-adenosylmethionine (SAM), demonstrating that PCIF1 is a cap-specific adenosine-N^6-methyltransferase; hence, we renamed the protein CAPAM [3]. Biochemical characterization revealed that CAPAM methylates mRNA containing $m^7GpppAm$ more efficiently than mRNA containing m^7GpppA.

CAPAM/PCIF1 was originally identified as a protein that interacts with the phosphorylated CTD of RNA polymerase II (RNAPII) via its N-terminal WW domain [4]. We also showed that the WW domain of CAPAM specifically interacts with Ser5-phosphorylated CTD, indicating that CAPAM is recruited to the early elongation complex of RNAPII and co-transcriptionally introduces N^6-methylation in nascent transcripts. Our results implied hierarchical formation of

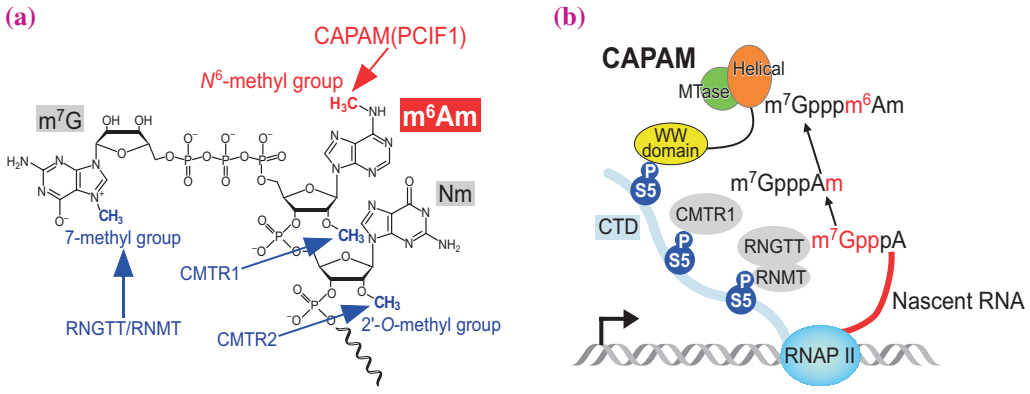

Fig. 1. **(a)** Chemical structure of the 5'-terminus of vertebrate mRNA bearing adenosine at the transcription start site. **(b)** Hierarchical formation of m^7Gpppm^6Am in the early elongation complex of RNA polymerase II.

m^7Gpppm^{6}Am–pppA, GpppA, m^7GpppA, m^7GpppAm, and m^7Gpppm^{6}Am (Fig. 1(b)).

In its C-terminal region, CAPAM has a putative methyltransferase domain that has a topology similar to that of DNA m^{6}A methyltransferase [5]. To elucidate the molecular mechanism of *N*^{6}-methylation, we solved the crystal structures of human and zebrafish CAPAMs with or without ligands. Crystals of CAPAMs in complex with m^7G cap analog and *S*-adenosylhomocysteine (SAH) were obtained by the soaking method. X-ray diffraction data were collected at 100 K at SPring-8 **BL41XU** and PXI at the Swiss Light Source. We determined the crystal structures of CAPAMs at 1.8–2.9 Å resolution. The core region of CAPAM consists of the methyltransferase (MTase) and helical domains (Fig. 2(a)). The MTase domain adopts a canonical Rossmann fold that contains the conserved catalytic NPPF motif. The helical domain contains three-helix bundles, a four-helix bundle, and β sheets, and exhibits no structural similarity with any known protein. SAH is bound to a catalytic site of the MTase domain in a manner similar to what has been observed in class I MTases. The m^7G cap is bound to a pocket formed by the MTase and helical domains, and interacts tightly with the surrounding residues. In mutation studies, we confirmed the importance of these residues for *N*^{6}-methylation. The target adenosine residue adjacent to the m^7G cap is not visible in the electron density map. Hence, we modeled the target Am at the catalytic site of the MTase domain based on the structure of M.TaqI DNA m^{6}A methyltransferase (Fig. 2(b)). Our model suggested that the adenine of Am is recognized by the NPPF motif, while the ribose moiety of Am interacts with the histidine residue, contributing to the strong interaction with the m^7GpppAm cap structure. Notably, the helical domain forms a positively charged groove, suggesting that it serves as a binding surface for the RNA chain (Fig. 2(c)).

Ribosome profiling and RNA-seq experiments suggested that CAPAM-mediated m^{6}Am formation promotes translation of mRNAs starting with A, rather than mRNA stabilization [3]. The molecular mechanism underlying m^{6}Am-mediated translational regulation remains to be determined. Regarding the physiological role of CAPAM, we observed a significant growth defect in *CAPAM*-knockout cells under oxidative stress, suggesting that CAPAM plays a key role in gene expression in response to such conditions. Given that *CAPAM* has been reported as a putative tumor suppressor gene in bladder cancer cells, CAPAM-mediated m^{6}Am modification might have a substantial impact on physiology and pathology in mammals.

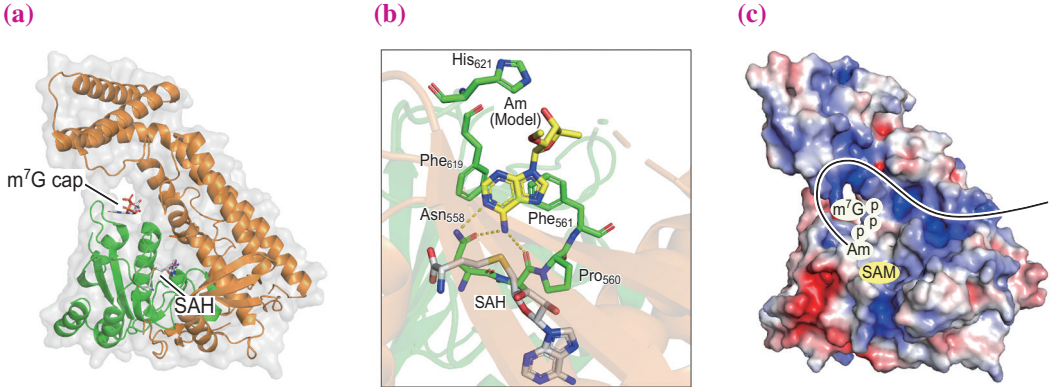

Fig. 2. **(a)** Crystal structure of zebrafish CAPAM in complex with m^7GpppA and SAH (PDB: 6IRZ). **(b)** Model structure of the catalytic site with the target Am residue. **(c)** Electrostatic surface potential of zebrafish CAPAM with a model RNA substrate.

S. Akichika[a], S. Hirano[b], O. Nureki[b] and T. Suzuki[a,*]

[a] Department of Chemistry and Biotechnology, The University of Tokyo
[b] Department of Biological Sciences, The University of Tokyo

*Email: ts@chembio.t.u-tokyo.ac.jp

References

[1] H. Shi *et al.*: Mol. Cell **74** (2019) 640.
[2] A.K. Banerjee: Microbiol. Rev. **44** (1980) 175.
[3] *S. Akichika, S. Hirano, Y. Shichino, Ta. Suzuki, H. Nishimasu, R. Ishitani, A. Sugita, Y. Hirose, S. Iwasaki, O. Nureki and Ts. Suzuki: Science* ***363*** *(2019) eaav0080.*
[4] H. Fan *et al.*: Biochem. Biophys. Res. Commun. **301** (2003) 378.
[5] L.M. Iyer *et al.*: BioEssays **38** (2016) 27.

In crystallo thermodynamic analysis of catalytic reaction in bacterial copper amine oxidase

Currently, protein X-ray structures are usually determined from diffraction data of cryocooled crystals at around 100 K. It is believed that the structures at such cryogenic temperatures are basically identical to those at room temperatures where proteins actually function. However, thermodynamic analyses of conformational changes occurring in protein crystals have been very difficult by cryogenic X-ray crystallography, because the proteins lose their dynamics properties and temperature-dependent information is lost after cryocooling in exchange for protection from X-ray damage. Therefore, there has recently been much interest in the use of X-ray diffraction measurements at non-cryogenic temperatures to obtain dynamic structural information. Copper amine oxidases catalyze the oxidative deamination of various primary amines to produce the corresponding aldehydes (Fig. 1(a)) [1]. The active site contains a Cu^{2+} ion and a protein-derived quinone cofactor, topaquinone (TPQ) (Fig. 1(b)). We have determined the crystal structures of a copper amine oxidase from *Arthrobacter globiformis* (AGAO) that had been reduced with substrate amines under anaerobic coenditions. The determined structures revealed that the reduced cofactor has two distinct states: a semiquinone radical form (TPQ_{sq}) and an aminoresorcinol form (TPQ_{amr}) having the copper-ligated "on-copper" and indirectly copper-contacting "off-copper" conformations, respectively [2]. Previous UV-vis spectral studies in solution revealed that the equilibrium between TPQ_{sq} and TPQ_{amr} is affected significantly by temperature and pH. The structural basis for the temperature- and pH-dependent equilibrium remains unresolved. To address this problem, we applied a temperature-controlled humid air and glue-coating (HAG) method to non-cryocooled crystals of AGAO at SPring-8 **BL38B1** and thermodynamically analyzed the conformational change of TPQ in the crystal [3]. The HAG method was originally developed by JASRI [4] and has recently been improved to allow strict temperature control of protein crystals under anaerobic conditions [5].

To investigate temperature-dependent equilibrium changes of the AGAO crystal structure, we collected

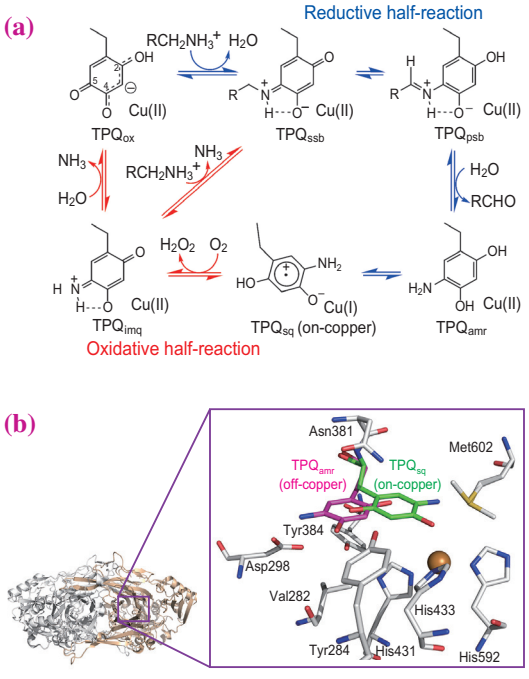

Fig. 1. **(a)** Presumed catalytic mechanism of AGAO. TPQ_{ox}, oxidative form of TPQ; TPQ_{ssb}, substrate Schiff base of TPQ; TPQ_{psb}, product Schiff base of TPQ; TPQ_{amr}, aminoresorcinol form of TPQ; TPQ_{sq}, semiquinone radical form of TPQ; TPQ_{imq}, iminoquinone form of TPQ. **(b)** Overall structure of the AGAO dimer as a ribbon model. Enlarged view: stick model of the active site. The off-copper conformer (TPQ_{amr}) and on-copper conformer (TPQ_{sq}) are drawn in magenta and green, respectively.

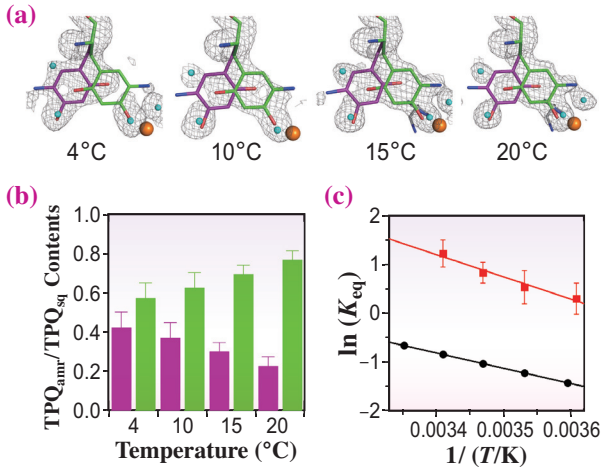

Fig. 2. Temperature dependence of TPQ_{sq}/TPQ_{amr} equilibrium. The TPQ conformation in the ethylamine-reduced AGAO crystal was examined at pH 6.0 by the temperature-controlled HAG method. **(a)** Assigned models of TPQ_{sq} (green sticks) and TPQ_{amr} (magenta sticks) are superimposed on the $F_o - F_c$ omit maps (gray mesh) for residue 382 (TPQ) contoured at 3.5 σ, determined at the indicated temperatures. **(b)** Average occupancies of TPQ_{amr} and TPQ_{sq} at various temperatures are shown by magenta and green bars, respectively, with S.E. ($n \geq 6$), assuming that the sum of occupancies of TPQ_{amr} and TPQ_{sq} is 1.0. **(c)** van't Hoff plots for the TPQ_{sq}/TPQ_{amr} equilibrium in solution (black) and crystal (red).

diffraction data of AGAO crystals anaerobically reduced with ethylamine at 4, 10, 15, and 20°C. Relative occupancies of each conformer provided K_{eq} values (equilibrium constant for TPQ_{sq}/TPQ_{amr}) that clearly indicate that the off-copper TPQ_{amr} shifts to the on-copper TPQ_{sq} as the temperature increases (Fig. 2(a,b)). Thermodynamic parameters obtained from a van't Hoff plot of K_{eq} values (Fig. 2(c)) for both crystalline ($\Delta H°$ = 38 kJ/mol, $\Delta S°$ = 139 J/mol/K) and solution ($\Delta H°$ = 26 kJ/mol, $\Delta S°$ = 83 J/mol/K) states indicated that the transition to TPQ_{sq} is entropy-driven in both crystal and solution states. The *in crystallo* increases of $\Delta H°$ and $\Delta S°$ can be ascribed to the packing effect in the crystal lattice and suggest the reason for an equilibrium shift of TPQ_{sq}/TPQ_{amr} that is directly linkied to structural changes. To clarify pH-dependent equilibrium changes, the structures of 2-phenylethylamine (2-PEA)-reduced crystals were determined at 15°C with various pHs under aerobic conditions. The $F_o - F_c$ omit maps for the TPQ moiety were considerably different depending on pH, indicating the formation of various intermediates (Fig. 3(a)). These differences suggest that the binding of the product aldehyde, phenylacetaldehyde (PAA), to the hydrophobic pocket facilitates the transition to TPQ_{sq} at high pH and the formation of TPQ_{psb} at low pH by the back reaction between TPQ_{amr} and PAA in the crystals. (Fig. 3(b)).

Our study revealed that the temperature-controlled HAG method has great advantages for detecting the equilibrium mixture of catalytic intermediates in protein crystals and will enable the elucidation of '*in crystallo*' thermodynamics of conformational changes. We expect that the temperature-controlled HAG method will provide an important addition to various X-ray crystallographic techniques currently being developed.

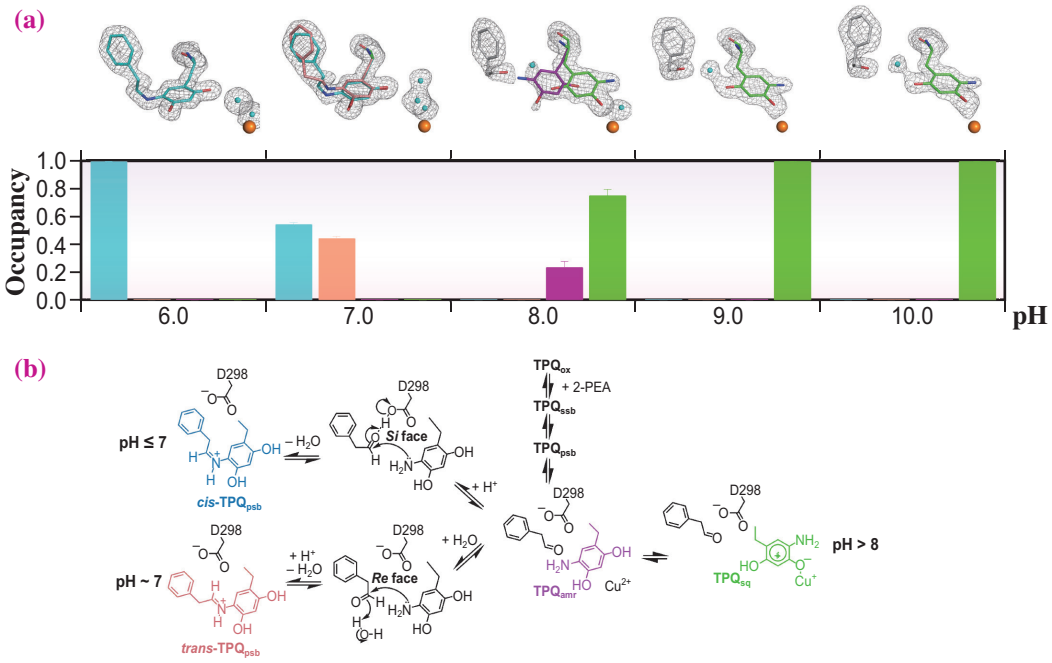

Fig. 3. pH dependence of equilibrium. **(a)** pH profile of 2-PEA-reduced AGAO crystal structures at 15°C at various pH determined by the temperature-controlled HAG method. The determined active-site structures are superimposed on the $F_o - F_c$ omit map (gray mesh) for residue 382 and the product aldehyde contoured at 3.5 σ. Residue 382 is represented by a stick model with the same color scheme as in the bar graph. Average occupancies of the intermediates are shown by bars with S.E. ($n \geq 4$): cyan, *cis*-TPQ_{psb}; brown, *trans*-TPQ_{psb}; purple, TPQ_{amr}; green, TPQ_{sq}. **(b)** Possible mechanism of pH-dependent equilibrium changes in the 2-PEA-reduced AGAO crystal.

Takeshi Murakawa[a,*], Seiki Baba[b] and Toshihide Okajima[c]

[a] Department of Biochemistry, Osaka Medical College
[b] Japan Synchrotron Radiation Research Institute (JASRI)
[c] Institute of Scientific and Industrial Research, Osaka University

*Email: murakawa@osaka-med.ac.jp

References

[1] V.J. Klema *et al.*: Int. J. Mol. Sci. **13** (2012) 5375.
[2] T. Murakawa *et al.*: J. Biol. Chem. **290** (2015) 23094.
[3] *T. Murakawa, S. Baba, Y. Kawano, H. Hayashi, T. Yano, T. Kumasaka, M. Yamamoto, K. Tanizawa, T. Okajima: Proc. Natl. Aca. Sci. USA* ***116*** *(2019) 135.*
[4] S. Baba *et al.*: Acta Crystallogr. D Biol. Crystallogr. **69** (2013) 1839.
[5] S. Baba *et al.*: J. Appl. Cryst. **52** (2019) 699.

Mechanism of stress-induced inhibition of eukaryotic translation initiation factor 2B

The regulation of the eukaryotic initiation factor 2B (eIF2B) is central to the stress-induced control of protein synthesis. eIF2B is the guanine nucleotide exchange factor specific for another initiation factor eIF2, which delivers the methionylated initiator tRNA to the ribosomes in a GTP-dependent manner. eIF2B catalyzes the conversion of inactive GDP-bound eIF2 to active GTP-bound eIF2 [1]. When eukaryotic cells detect stress, eIF2 is rapidly phosphorylated by eIF2 kinases, and this phosphorylation inhibits the activity of eIF2B. As a result, the decreased cellular level of the GTP-bound eIF2 limits the supply of initiator tRNA to the ribosomes and globally attenuates translation. Various types of stress signals, such as nutrient starvation or viral infection, induce this response, and therefore it is called the "integrated" stress response (ISR) [2]. Although the factors involved in ISR are well characterized, the structural basis of this process is largely unknown. In particular, how eIF2B catalyzes the exchange reaction on eIF2 and how this activity is inhibited by the phosphorylation of eIF2 have remained undescribed.

eIF2 and eIF2B, the key factors of ISR, are both multimeric proteins. eIF2 is a heterotrimeric protein (α to γ); the α subunit is phosphorylated under stress, and the γ subunit binds GTP or GDP. eIF2B is a heterodecameric protein composed of two copies each of five different subunits (α to ε). The minimal region required for the nucleotide exchange is the HEAT domain, which resides at the C-terminus of the ε subunit. We prepared the various complexes of eIF2 and eIF2B, and analyzed them by cryo-electron microscopy (cryo-EM) and X-ray crystallography. X-ray diffraction data were collected at SPring-8 **BL41XU** [3].

We determined the cryo-EM structures of eIF2B complexed with phosphorylated or unphosphorylated eIF2. They revealed that the binding mode of eIF2 is completely different depending on its phosphorylation status (Fig. 1), and the catalytic HEAT domain of eIF2B is observed only in the unphosphorylated eIF2•eIF2B complex. Since the HEAT domain is bound to eIF2γ, the nucleotide-binding subunit, this complex seems to represent the "productive" state in which the nucleotide is being exchanged by eIF2B. On the other hand, in the phosphorylated eIF2•eIF2B complex, eIF2γ is located apart from eIF2Bε, representing the "nonproductive" state in which no nucleotide exchange reaction occurs.

The details of the recognition of eIF2 phosphorylation were obtained from the crystal structures of eIF2B complexed with the phosphorylated or unphosphorylated eIF2α subunit. Because of the absence of the interaction mediated by eIF2γ, the binding modes of eIF2α resemble the nonproductive mode regardless of their phosphorylation status (Fig. 2(a)). The difference between these structures is limited to the neighborhood of the phosphorylation residue Ser51. In the complex with the phosphorylated eIF2α, the phosphorylated Ser51 residue itself is not recognized directly by eIF2B, but instead, the loop region adjacent to this residue is inserted toward the eIF2B subunits (Fig. 2(b)). Compared with the unphosphorylated structure, this loop is inserted more deeply and undergoes more interaction with eIF2B subunits. Therefore, this change makes the "nonproductive" binding mode more stable than the productive mode when eIF2 is phosphorylated and prevents the nucleotide exchange from the phosphorylated eIF2.

In addition to the above prevention, the binding of phosphorylated eIF2 appears to have an additional role in the inhibition of eIF2B. Our cryo-EM structures

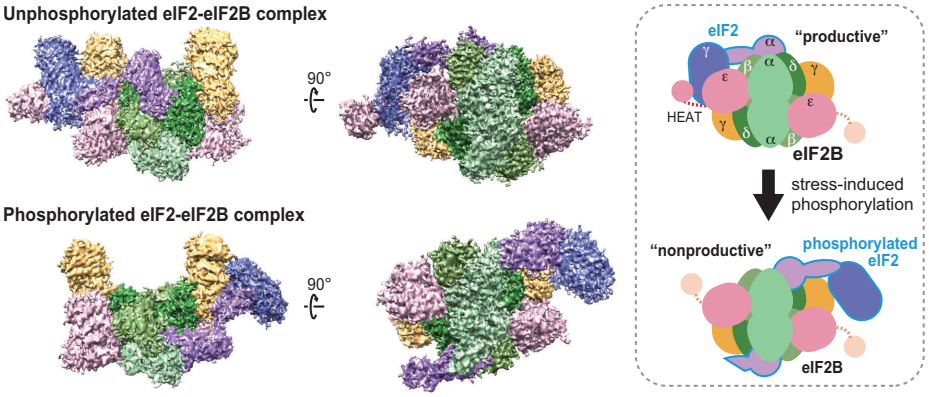

Fig. 1. Cryo-EM structures of eIF2B complexed with unphosphorylated eIF2 (upper) and phosphorylated eIF2 (below), and their schematic representations.

indicate that the simultaneous binding of one phosphorylated eIF2 and one unphosphorylated eIF2 to the opposite sides of eIF2B is impossible owing to the steric clash between the HEAT domain of eIF2Bε and the γ subunit of the phosphorylated eIF2 (Fig. 3(a)). Therefore, the binding of the phosphorylated eIF2 also blocks the nucleotide exchange reaction at the opposite side of eIF2B. On the basis of these findings, we propose the following mechanism of eIF2B inhibition under stress. Under the normal condition, eIF2B forms the productive complex with the unphosphorylated eIF2 and performs nucleotide exchange. Upon stress, the phosphorylated eIF2 appears and binds to eIF2B in the nonproductive manner. Not only does the phosphorylated eIF2 prevent nucleotide exchange by keeping itself away from the catalytic elements of eIF2B, it also hinders the catalysis at the opposite side. Eventually, the phosphorylated eIF2 occupies both sides of eIF2B and completely stops the exchange activity of eIF2B (Fig. 3(b)).

Our structures provide the structural basis for the stress-induced translational control mediated by eIF2B. eIF2B is now attracting growing interest as a potential drug target for traumatic brain injury and neurodegeneration [4,5]. The small molecule called ISRIB, which boosts the catalytic activity of eIF2B and reverses ISR, has shown promising effects in mouse models. Our structures may also provide valuable information for understanding the mechanistic action of ISRIB and the development of a novel treatment for traumatic brain injury and neurodegeneration.

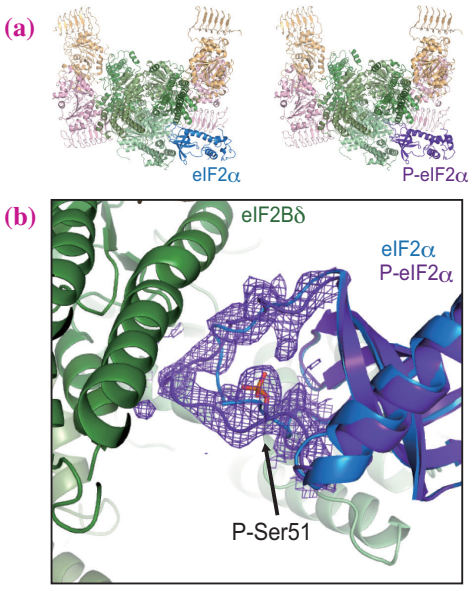

Fig. 2. **(a)** Crystal structures of eIF2B complexed with unphosphorylated eIF2α (left) and phosphorylated eIF2α (P-eIF2α, right). **(b)** Loop regions adjacent to the phosphorylation residue Ser51 (P-Ser51). The electron density in the loop region of phosphorylated eIF2α is also shown.

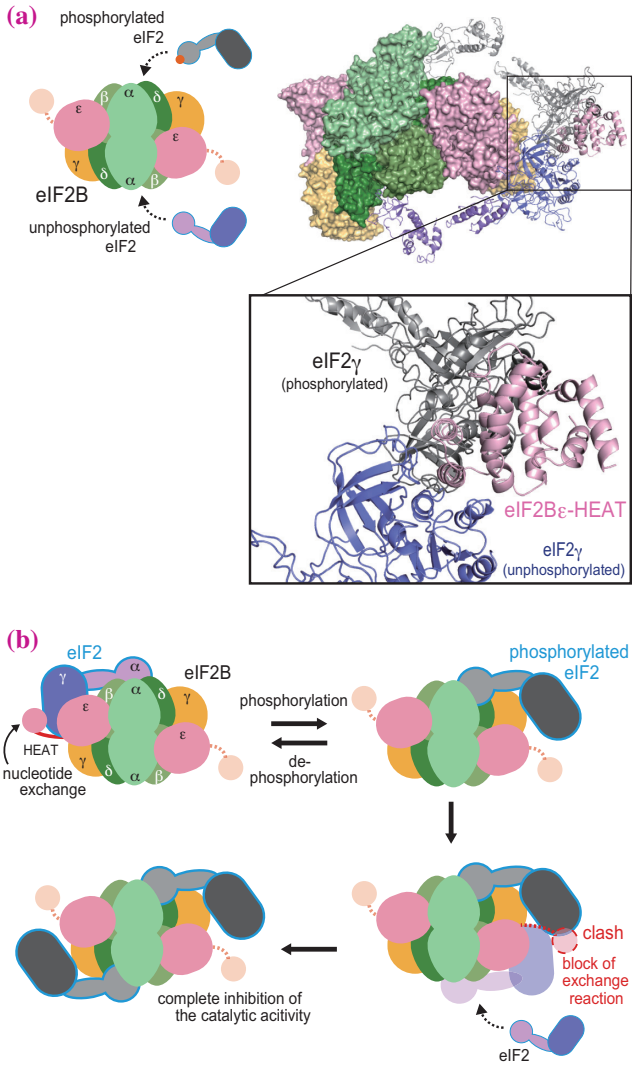

Fig. 3. **(a)** Model in which phosphorylated eIF2 (gray) and unphosphorylated eIF2 (violet) are bound to either side of eIF2B. The position of the eIF2Bε HEAT domain (pink) overlaps with that of the γ subunit of phosphorylated eIF2. **(b)** Proposed model of inhibition of eIF2B by phosphorylated eIF2.

Kazuhiro Kashiwagi and Takuhiro Ito*

RIKEN Center for Biosystems Dynamics Research/Yokohama

*Email: takuhiro.ito@riken.jp

References

[1] A.G. Hinnebusch & J.R. Lorsch: Cold Spring Harb. Perspect. Biol. **4** (2012) a011544.
[2] K. Pakos-Zebrucka *et al.*: EMBO Rep. **17** (2016) 1374.
[3] *K. Kashiwagi, T. Yokoyama, M. Nishimoto, M. Takahashi, A. Sakamoto, M. Yonemochi, M. Shirouzu and T. Ito: Science **364** (2019) 495.*
[4] A. Chou *et al.*: Proc. Natl. Acad. Sci. USA **114** (2017) E6420.
[5] M. Halliday *et al.*: Cell Death Dis. **6** (2015) e1672.

Sugars can protect hydration shell of proteins and stabilize their native structures in crowded molecular environment: clarified by complemental use of X-rays and neutrons

The denaturation and/or deactivation of proteins can be prevented by additives such as sugars and polyols. These additives are widely applied to the storage of living cells, food preservation, and so forth. On the other hand, organisms tolerant to adverse environmental conditions such as desiccation and freezing have been shown to temporarily produce and/or accumulate stress proteins and/or sugars to stop all measurable metabolic processes until environmental conditions return to being favorable. This metabolic state is called cryptobiosis. In particular, the protective actions of sugars and polyols on protein structures have been considered to be related to specific bindings of these additives, changes in solvent viscosity and surface tension, and free energy changes upon addition of proteins into these additive solutions. Clearly, from a previous report, hydration is the key determinant of the isothermal and concentration-dependent effects on protein equilibria, since the dynamics of proteins are surely coupled with and/or governed by surrounding water molecules. Nevertheless, direct observation or characterization of the protein structure and its solvation in solutions where large quantities of additives such as sugars and polyols exist have not been obtained and clarified yet. This is because the crowded molecular environment of these additives significantly interferes with the acquisition of high quality statistical data of a protein owing to a large decrease in the difference between the average scattering densities of the solute and the solvent, so-called contrast.

By the complemental use of small- and wide-angle X-ray scattering (SWAXS) and small- and wide-angle neutron scattering (SWANS), we succeeded in quantitatively clarifying the effect of sugars (mono- and disaccharides) on protein hydration [1] and structural stability against chemical and thermal denaturation [2]. SWAXS experiments were carried out at SPring-8 **BL40B2**. We used glucose and fructose as the monosaccharides, and sucrose and trehalose as the disaccharides. Figure 1 shows examples of the SWAXS curves of myoglobin as a function of sugar concentration (panel 1A, trehalose; panel 1B, glucose). Note that the SWAXS curve covers all structures at different hierarchal levels of the myoglobin structure. Namely, the observed q regions of q < ~0.2 Å^{-1}, ~0.25 Å^{-1} < q < ~0.5 Å^{-1}, ~0.5 Å^{-1} < q < ~0.8 Å^{-1}, and ~1.1 Å^{-1} < q < ~1.9 Å^{-1} respectively correspond to the tertiary structure, the inter- and intradomain

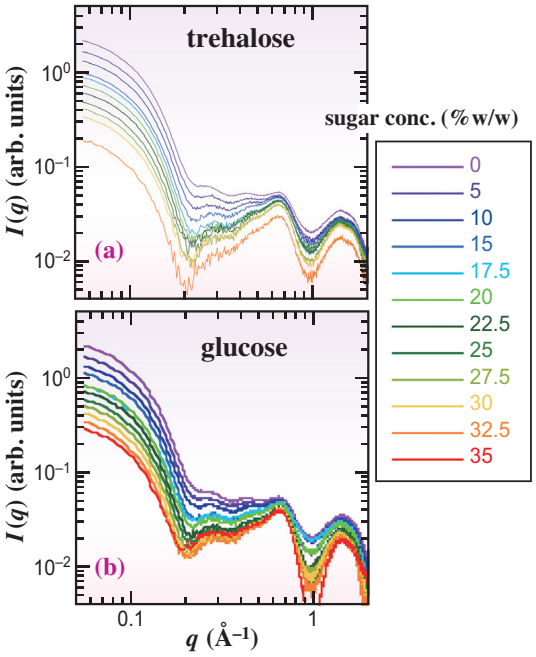

Fig. 1. SWAXS curves of myoglobin as a function of sugar concentration (%w/w). **(a)** trehalose; **(b)** glucose.

structures, and the secondary structure including the closely packed side chains [2]. By comparing experimental data with data obtained by theoretical simulation based on three different solvation models (Model 1, preferential solvation model; Model 2, neutral (non-preferential) solvation model; Model 3, preferential exclusion (preferential hydration) model), we quantitatively describe the observed changes in the zero-angle scattering intensity ($I(0)^{1/2}$) and the radius of gyration (R_g), as shown in Fig. 2. Results indicate that sugar molecules are preferentially or weakly excluded from the protein surface to preserve the native protein hydration shell, and the preferential exclusion shifts gradually to neutral solvation as the concentration increases. The hydration-shell density directly determined by the inverse contrast matching method of neutron scattering using deuterated sugars strongly supported the WAXS results [1]. Owing to such action of sugars, guanidinium chloride-mediated denaturation and thermal denaturation were found to be significantly suppressed by the presence of sugars [3]. Similar protective action of glycerol was observed [4]. On the other hand, myoglobin is known to undergo an amyloidogenic reaction under denaturated conditions. The SWAXS and dynamic

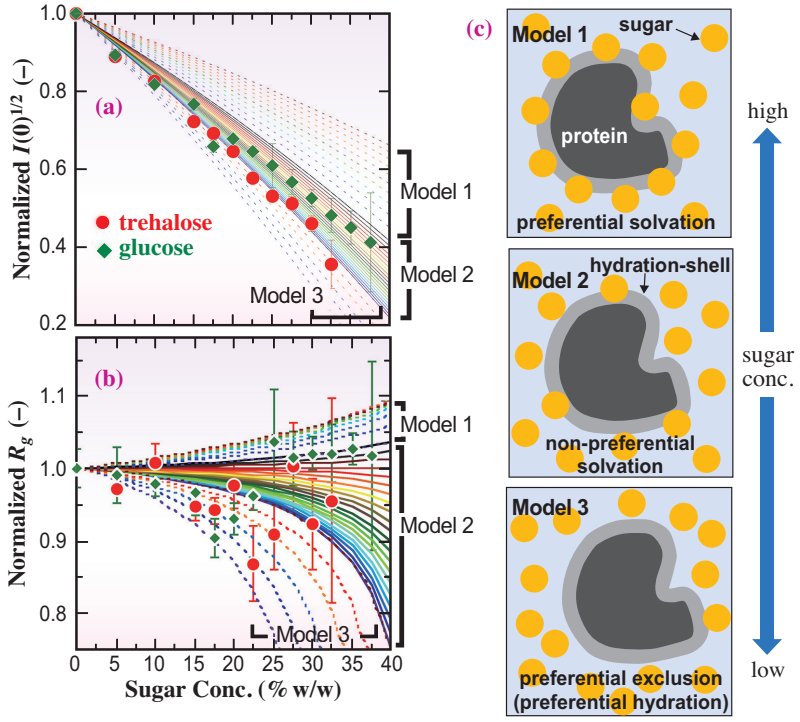

Fig. 2. **(a)** Zero-angle scattering intensity ($I(0)^{1/2}$) and **(b)** radius of gyration (R_g) as a function of sugar concentration. The frames depict the theoretical values in the different solvation models shown in **(c)**. From the top in (c), preferential solvation by sugar (Model 1); neutral (non-preferential) solvation (Model 2); preferential exclusion (preferential hydration) (Model 3).

light scattering measurements indicated that acid-denatured myoglobin in the initial process of the amyloidogenic reaction (helix-to-sheet transition followed by oligomerization) was substantially restored to its native structure by trehalose [5]. Figure 3 shows the restoration of the protein structure from the amyloid state to the native state with increasing trehalose concentration. The hump at q = ~0.58 Å^{-1} and the peak at q = ~1.34 Å^{-1} are the characteristic features emerging during the early stages of amyloid formation, (i.e., the pleated-beta-sheet stacking) and the helix-to-sheet (cross-beta-sheet) transition, respectively. These characteristic profiles reflecting amyloid formation disappeared and returned to those of the native ones.

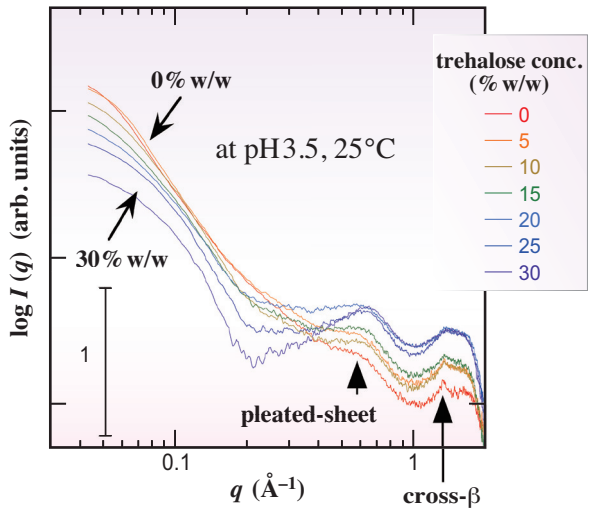

Fig. 3. SWAXS curves showing the restoration of acid-denatured myoglobin (amyloid state) to its native structure by trehalose.

The series of SWAXS and SWANS experiments on the effect of sugars on the protein structure and stability are expected to provide new insight into the molecular mechanism underlying the intrinsic function of sugars in cryptobiosis and amyloidosis.

Mitsuhiro Hirai

Graduate School of Science and Technology,
Gunma University

Email: mhirai@gunma-u.ac.jp

References

[1] S. Ajito *et al.*: Physica B **551** (2018) 249.
[2] M. Hirai *et al.*: J. Synchrotron Rad. **9** (2002) 202; Biochem. **43** (2004) 9036.
[3] S. Ajito *et al.*: Phys. Chem. B **122** (2018) 8685.
[4] *M. Hirai et al.: Biophys. J. **115** (2018) 313.*
[5] *M. Hirai et al.: Phys. Chem. B **122** (2018) 11962.*

Parkinson's disease is a type of amyloidosis characterized by accumulation of amyloid fibrils of α-synuclein

Parkinson's disease (PD) is a progressive neurodegenerative disorder of the central nervous system that mainly affects the motor system with the characteristic symptoms of tremor, rigidity, slowness of movement, and postural instability. It has been known for quite some time that Lewy bodies (LBs), which are abnormal protein aggregates, are formed in the brain of PD patients, and it is thought that LBs play an important role in the onset of the disease. LBs mainly consist of α-synuclein (α-syn), which is a 140-amino acid protein abundant in presynaptic terminals of nerve cells in the brain. Recently, it has been reported that aggregates of α-syn with a cross-β structure (seeds of α-syn amyloid fibrils) are capable of propagating within the brain similarly to prions [1]. However, the presence of cross-β sheet-rich aggregates in LBs of PD patients has not been demonstrated so far (Fig. 1). Nowadays, PD is described as a heterogeneous multisystem neurodegenerative disease because α-syn deposits are not restricted to the central nervous systems; they are also found in the peripheral nerves innervating visceral organs, such as the heart and gut. This observation indicating that α-syn may propagate is interesting.

On the other hand, amyloidosis, a disease in which amyloid fibrils accumulate throughout the body, has been known for a long time. Amyloidosis is incurable because various organs are affected. Because senile plaques of Alzheimer's disease (AD) contain amyloid fibrils, AD is classified as localized amyloidosis. Is PD a type of amyloidosis? By classical histopathological definition, amyloids are Congo Red-stained extracellular proteinaceous deposits with a β-sheet structure. LBs are intracellular deposits and generally not stained by Congo Red. Therefore, PD does not meet the definition of amyloidosis. This seems to contradict the propagation hypothesis of α-syn. Our previous work has demonstrated that LBs are rich in β-sheet structures [4], but it did not provide results that satisfactorily answer the above question. To more accurately answer the above question, the following experiment was performed.

First, we adopted the biophysical definition of amyloid fibrils, that is, amyloid fibrils are fibrillar polypeptide aggregates with a cross-β conformation. We carried out the fine structure analysis of LBs using thin sections of brains of autopsied patients with PD. There are excellent electron microscopy studies that show fibril-like structures in the aggregates. However, they are only morphological observations and do not provide information on the secondary structure of the proteins (Fig. 1). Measurements using real brain tissue are not easy. In addition, LBs are very small with a diameter of 10 μm, so fine structure analysis is very difficult. Therefore, we examined LBs in thin sections of brains of autopsied patients with PD by microbeam X-ray diffraction (XRD) at SPring-8 **BL40XU**.

Brain tissue samples from three patients with neuropathologically confirmed PD were used for our measurements. All samples were collected from the midbrains. The brain samples were fixed in 4% buffered formaldehyde and frozen in accordance with routine tissue processing for histopathological examination. For each sample, 20-μm-thick sections were cut and deposited on Kapton polyimide films. Tissue sections from the PD patient's brain were immunostained with an anti α-syn antibody. Before measurements, these samples were dried at room temperature. Brain sections were scanned with an X-ray microbeam at BL40XU beamline. An X-ray microbeam was obtained using a pinhole with a diameter of 5 μm. The sections were scanned in the X and Y directions with a step size of either 3 or 5 μm. Scans with 10, 20, or 40 steps in each direction were performed. At each point of the scan, a wide-angle X-ray scattering pattern was recorded. The X-ray

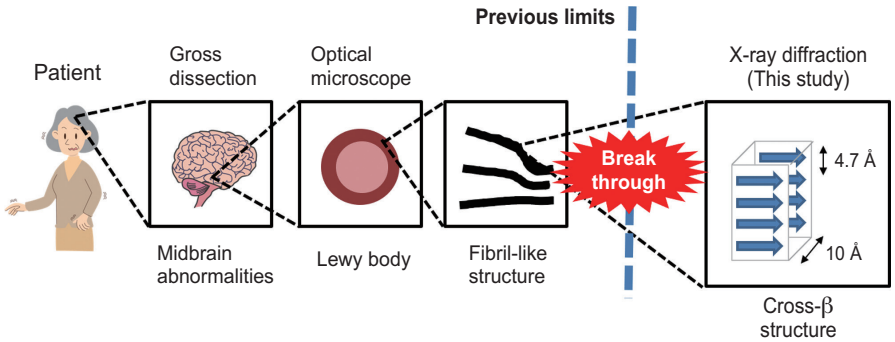

Fig. 1. Abnormal changes in the brain of Parkinson's disease patients.

wavelength was 0.083 nm with a bandwidth of about 2%. The X-ray detector was an X-ray image intensifier (V7739P, Hamamatsu Photonics, Hamamatsu, Japan) coupled with either a CCD camera (C4742-98-24ER, 1344×2018 pixels) or an sCMOS camera (C11440-22CU, 2048×2018 pixels), both from Hamamatsu Photonics. The exposure time was 0.3–0.5 s. The sample-to-detector distance was about 115 mm. No vacuum path was used.

The basic assumption in the data analysis is that LBs, which comprise aggregated amyloid fibrils with high density, should produce stronger X-ray scattering than other regions of the brain. Thus, a map of total wide-angle scattering intensity was compared with a microscopy image of stained sections. For each scan, 100, 400, or 1600 X-ray diffraction patterns were obtained. Total scattering intensity in a diffraction pattern at each point was calculated, and a 2D intensity map was constructed. If the LBs identified by chemical staining contain a high density of amyloid fibrils, a high intensity region is expected to appear in the same area of the 2D intensity map. Brain slices from the patient showed LBs identified by the antibody staining (Fig. 2(e)) and a marked peak in the 2D map of total scattering intensity (Fig. 2(d)).

Then, five points where the highest intensity was observed in the 2D map were searched. These are usually the central part of the identified peak region. The averaged diffraction pattern of the images obtained at these five points was treated as a "top" image (Fig. 2(a)). Similarly, diffraction patterns at half of the points that showed lower intensities than the other half were averaged as a "bottom" image (Fig. 2(b)). The top image was recorded from the region with aggregates of amyloid fibrils, whereas the bottom image represented the background without protein accumulation. A "difference" image obtained by subtracting the bottom image from the top image (Fig. 2(c)) represents diffraction from amyloid fibrils only. The strong rings seen in the top and bottom images are due to the Kapton sheet that was used to mount the brain section. These were completely removed by subtraction. The difference scattering pattern was obtained (Fig. 2(c)), and peaks correspond to amyloid fibrils at q = 6.1 and 13.5 nm^{-1} (d = 1.03 and 0.47 nm) were observed (Figs. 2(c) and 2(f)) in some LBs. These peaks are characteristic of the cross-β structure.

As a result, we found that some of them gave a diffraction pattern typical of a cross-β structure [5]. This finding confirms for the first time that LBs in the brain of PD patients contain amyloid fibrils with a cross-β structure and supports the validity of *in vitro* propagation experiments using artificially formed amyloid fibrils of α-syn. Notably, our finding supports the new concept that PD is a type of amyloidosis, a disease characterized by accumulation of amyloid fibrils of α-syn.

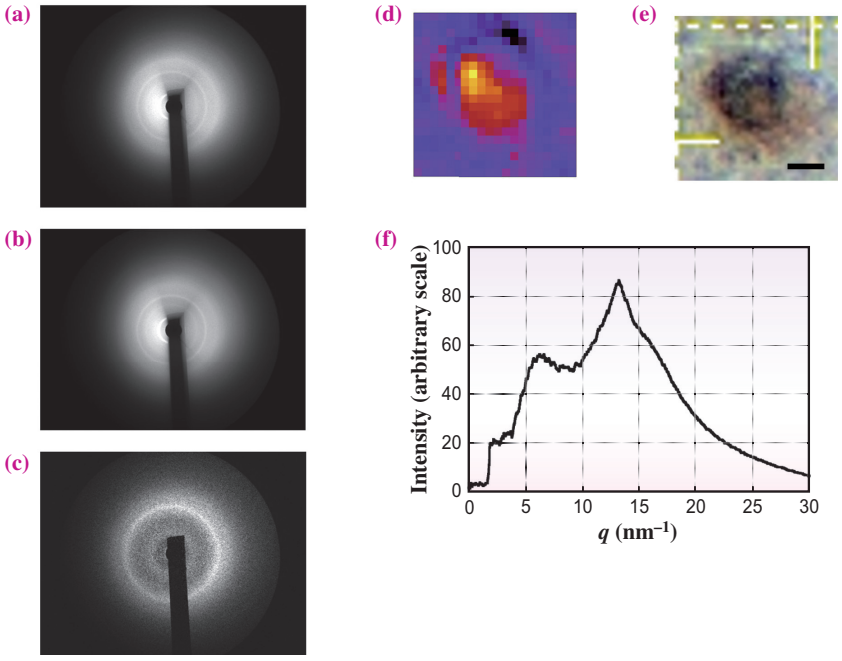

Fig. 2. Analysis of human Lewy bodies showing a sharp diffraction peak corresponding to d = 0.47 nm. **(a)** top image. **(b)** bottom image. **(c)** Difference image obtained by subtracting (b) from (a). **(d)** 2D map of total wide-angle scattering intensity. A 20×20 scan was carried out in 3 μm steps. **(e)** Micrograph of an antibody-stained brain section. Scale bar, 10 μm. **(f)** Circularly averaged X-ray scattering intensity profile of (c).

Katsuya Araki[a,*], Naoto Yagi[b] and Hideki Mochizuki[a]

[a] Department of Neurology, Osaka University Graduate School of Medicine
[b] Japan Synchrotron Radiation Research Institute (JASRI)

*Email: araki@neurol.med.osaka-u.ac.jp

References

[1] K.C. Luk *et al.*: Science **338** (2012) 949.
[2] M. Masuda-Suzukake *et al.*: Brain **136** (2013) 1128.
[3] S.B. Prusiner *et al.*: Proc. Natl. Acad. Sci. USA **112** (2015) E5308.
[4] K. Araki *et al.*: Sci. Rep. **5** (2015) 17625.
[5] *K. Araki, N. Yagi, K. Aoyama, C. Choong, H. Hayakawa, H. Fujimura, Y. Nagai, Y. Goto, H. Mochizuki: Proc. Natl. Acad. Sci. USA* ***116*** *(2019) 17963.*

Gradient of index and moduli is essential for optimal function of the eye lens

The human eye lens is a synchronized opto-mechanical structure designed to meet the dynamic focusing requirements of the visual system. It is held in place by a ring of suspensory ligaments that transmit force to control shape changes of the lens to view objects clearly over a range of distances, a process called accommodation. The major properties of the eye lens: transparency, refractive power and elasticity, determine the quality of images focused on retina. The eye lens is composed of layers of fiber cells filled with proteins called crystallins. The overall crystallin protein concentration of a human eye lens is around 65% of its weight. The relationship between protein concentrations and refractive index is linear over a wide range and this has been described by the Gladstone-Dale formula [1]. The link between biomechanical properties and the proteins, is not yet clear but a link between the refractive index and the biomechanical parameters is emerging.

The biomechanics of the human lens is neither fixed nor constant because of the inhomogeneous and variable nature of aging cells and tissues in the long term and the process of accommodation. The other complicating factor is that biomechanics can be described by a number of parameters and these have been investigated in the eye lens using a range of different techniques that have yielded a variety of results. The variations are caused by aging trends, spatial variations and assumptions inherent in the measurements. A recent study, using the only known non-invasive technique for studying biomechanics of the eye lens: Brillouin light scattering analysis, can measure mechanical modulus at a resolution of nearly 60 μm [2]. This study showed a gradient distribution of longitudinal elastic modulus along the central optical axis in *in vivo* human lenses aged from 19 to 63 years old [2]. Such a distribution resembles almost exactly the profiles of refractive index in *in vitro* human lenses of a similar age range that were measured by the X-ray Talbot interferometer located at beamline BL20B2 at SPring-8 [3]. The similarity in distributions of refractive index and mechanical modulus of elasticity (Fig. 1) suggests a potential link between biomechanics, optics and ultimately proteins in the eye lens.

Brillouin scattering analysis makes use of the interactions between optics and acoustics in two ways: a) acoustic periodical modulation of material density, which is related to refractive index, causes light scattering; b) incident light creates spatial and temporal variations in elastic strains of the material initiating acoustic waves. As a result, the incident light will either gain energy from existing acoustic waves in the medium with a frequency upshift or lose energy to induce new acoustic waves with a frequency downshift. The mechanical property of the material included in these frequency shifts can therefore be determined with a known density to refractive index ratio [4].

Experiments conducted at SPring-8 **BL20B2** use a monochromatic X-ray beam of 25 keV, which passes through the interferometer that consists of a tantalum phase grating G1 and a gold absorption grating G2 with pattern thicknesses of 2.1 μm and 16.6 μm, respectively. For both gratings the pitch is 10 μm and pattern size area is 25×25 mm^2. For phase retrieval, grating G2 is shifted using a 5-step fringe scan method with a Piezo stage. A scientific CMOS detector (ORCA Flash 4.0. Hamamatsu Photonics) is used to monitor the Moiré fringe patterns generated by X-ray beam after passing through the sample and the system. The phase shift image can be integrated using different images from the scan and the X-ray refractive index difference can be determined from the phase shifts per pixel. The protein concentration is calculated

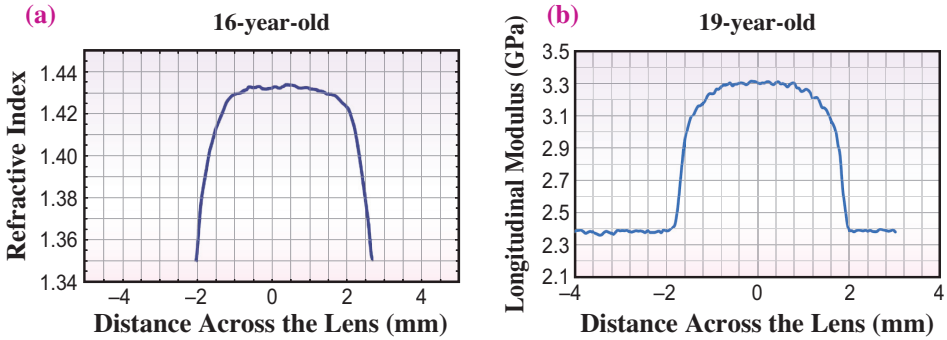

Fig. 1. **(a)** Gradient refractive index profile of a 16-year-old lens compared to **(b)** gradient profile of mechanical modulus of a 19-year-old lens.

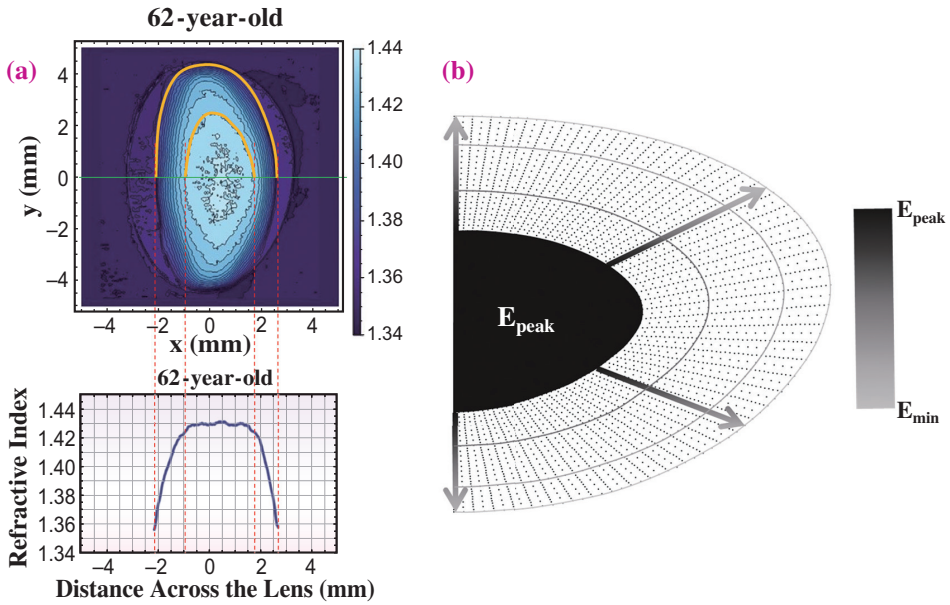

Fig. 2. **(a)** Geometry of lens nucleus and cortex from gradient refractive index profile of a 62-year-old lens measured at SPring-8 **(b)** discretized Finite Element model showing uniform Young's modulus in the nucleus and radial moduli in the cortex.

using the X-ray refractive index difference from which optical refractive index is determined according to the Gladstone-Dale formula [1].

To investigate the relationship between mechanical modulus obtained from Brillouin Light Scattering analysis and refractive index measured by X-ray Talbot interferometry, we developed computational models using a Finite Element method correlating these two parameters in lens models based on measurements made at SPring-8 at five different ages: 16, 35, 40, 57 and 62 years old (Fig. 2). Models with radial (gradient) cortical elastic moduli, following the distributions of both longitudinal elastic modulus and refractive index, were compared, in terms of deforming ability, optical power and internal stress patterns, with models that had a uniform cortical modulus [5]. Under stretching forces from zonular fibers over a range of physiologically acceptable directions, models with radial cortical elastic moduli showed similar amounts of optical power for a smaller change in thickness than did the models with a uniform cortical modulus indicating that the gradient provides a more efficient alteration of refractive power with shape change. Smooth stress changes, with no discontinuities, were found only in models with a gradient of moduli (Fig. 3) suggesting that the gradient is necessary for improved optical and mechanical function.

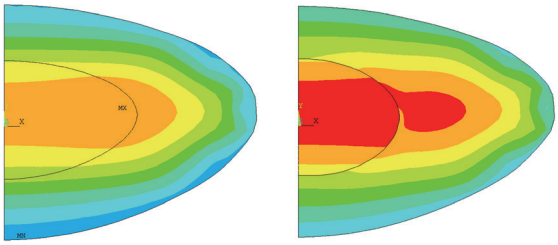

(a) radial **(b) uniform**

Fig. 3. **(a)** Uniform stress distribution in the 16-year-old model with radial cortical Young's moduli **(b)** discontinuities in stress distribution in the 16-year-old model with a uniform cortical Young's modulus (von Mises stress in MPa).

Kehao Wang[a], Masato Hoshino[b] and Barbara K. Pierscionek[a,*,†]

[a] School of Science and Technology, Nottingham Trent University, UK
[b] Japan Synchrotron Radiation Research Institute (JASRI)

*Email: barbara.pierscionek@staffs.ac.uk

[†] Present address: School of Life Science and Education, Staffordshire University, UK

References

[1] R. Barer and S. Joseph: Quart. J. Microscop. Sci. **95** (1954) 399.
[2] S. Besner *et al.*: Investig. Ophthalmol. Vis. Sci. **57** (2016) 5093.
[3] B.K. Pierscionek *et al.*: Oncotarget **31** (2015) 30532.
[4] K. Wang and B.K. Pierscionek: Prog. Retin. Eye Res. **71** (2019) 114.
[5] *K. Wang, D.T. Venetsanos, M. Hoshino, K. Uesugi, N. Yagi and B.K. Pierscionek: IEEE TBME* ***67*** *(2020) 999.*

Active pumping of ^{229}Th nuclear clock isomer by synchrotron radiation-based nuclear resonant scattering

A nuclear system is one of the ideal quantum states because it is well isolated from external disturbance by the surrounding electrons, and thus it is highly irrefrangible. If a nucleus can be operated using a coherent light source laser, one can expect to realize a research field of quantum electronics based on nuclei instead of atoms or molecules. However, the accessible laser energy is up to only ~10 electron volts (eV) and it is impossible to excite nuclei using a laser because the transition energy of nuclei is usually higher than the keV or MeV range.

The only exception is the ^{229}Th nucleus. This nucleus has a first excited state of extraordinarily low energy. This state is called an isomeric state or isomer. The energy level of the isomeric state is only ~8 eV, which corresponds to the vacuum ultraviolet (VUV) or light with ~150 nm wavelength; therefore, the transition between the ground state and the isomeric state is accessible by a laser technique. Although this fact was first pointed out in the 1970s, the existence of the isomeric state was confirmed only recently. In 2007, the isomer energy was reported to be 7.8 ± 0.5 eV on the basis of indirect gamma-ray spectroscopy [1], and in 2016, deexcitation from the isomeric state via internal conversion was observed [2]. However, the energy of the isomeric state is still ambiguous, and the lifetime of the isomeric state is also unknown. Furthermore, no optical transition between the two states has been reported.

Even though the details are not yet clear, many applications based on this laser-accessible nuclear transition have been proposed. The most famous example is the ultrahigh-precision frequency standard: the "nuclear clock." An atomic clock which is used as a current frequency standard is a base technology in both science and society. The current precision of the atomic clock is about 1 part in 10^{18}. A nuclear clock based on ^{229}Th nuclei is expected to be much more precise, 10^{19}–10^{20}. A ^{229}Th nuclear clock may provide many applications, for example, in relativistic geodesy, in the search for dark matter, and in the observation of possible variation of the fundamental constants of physics [3].

Our group aims to observe the VUV photon emission via deexcitation from the isomeric state to accurately determine the energy and lifetime of the isomeric state. Figure 1 shows the principle of our scheme. First, the X-ray beam is used to irradiate ^{229}Th nuclei in the ground state so that the nuclei undergo a transition to the second excited state

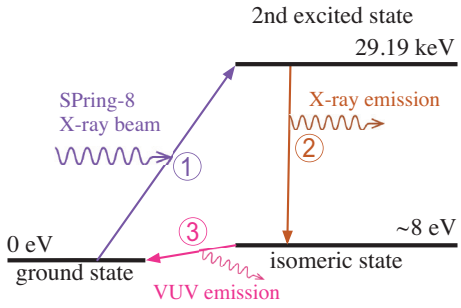

Fig. 1. Transitions used in the experiment. The three horizontal lines represent the three lowest ^{229}Th nuclear levels.

(process 1 in Fig. 1). Then, the nuclei spontaneously predominantly decay to the isomeric state; hence, the population of the isomeric state is increasing during beam irradiation (process 2). Finally, we observe the VUV photons emitted during the deexcitation from the isomeric state to the ground state (process 3).

A key point of the scheme is the preparation of the isomers. All the past experiments that reported positive results used ^{233}U α-decay as an isomer source. Since the α-decay causes radioactivity that disturbs the measurement, the ground state of ^{229}Th is preferred as an isomer source. To produce the isomers from the ground state, we need to pump up the nuclei actively. However, no attempts at active production have succeeded to date due to ambiguity of the isomeric state, such as the lack of knowledge of the precise energy and lifetime. On the other hand, our method should enable ^{229}Th nuclei to be actively pumped up to the isomer state regardless of the uncertainties. The combination of processes 1 and 2 is usually called synchrotron radiation-based nuclear resonant scattering (NRS), which is widely used in materials science.

In this work [4], we carried out the NRS measurement at SPring-8 **BL09XU** and **BL19LXU**. A schematic view of the experiment is shown in Fig. 2. The beam operation mode was A-mode in which the 203 bunches are equally spaced with a time interval of 23.6 ns. The X-ray beam was monochromatized by two silicon monochromator pairs and the bandwidth of the beam was ~0.1 eV. It was focused by a compound refractive lens array and irradiated to the target of thorium oxide. A total of 0.24 μg ^{229}Th was deposited on a thin graphite plate with a diameter of 0.4 mm. At the downstream end of the beam, we placed an

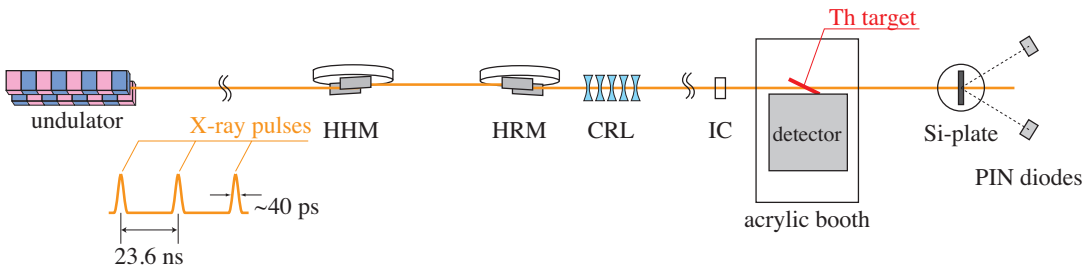

Fig. 2. Schematic of the experiment. The X-ray beam is generated at the undulator and propagates to the right side.

absolute X-ray beam energy monitor that can measure the beam energy with an accuracy of 0.07 eV.

In the NRS measurement, we scanned the X-ray beam energy and searched for the NRS peak. To confirm that NRS occurred, we detected the X-ray photons emitted via the transition in process 2 in Fig. 1. In comparison with the NRS signal rate, the background rate due to X-ray fluorescence following photoelectric absorption was 10^6–10^7 times higher; we developed a dedicated fast and energy-sensitive X-ray detection system to overcome the poor signal-to-noise ratio. This system consists of silicon avalanche photodiodes and peripheral fast circuits [5]. The energy and timing of each X-ray photon from the thorium target were measured simultaneously using this system. It also measured the pulse width of each analog pulse. The subsequent analysis based on these three parameters can increase the signal-to-noise ratio.

Figure 3 shows the NRS peak and the temporal profile of the NRS signal. Using the NRS data, we determined the accurate energy and the half-life of the second excited state to be 29,189.93 ± 0.07 eV and 82.2 ± 4.0 ps, respectively.

This work is the world's first realization of active pumping to the isomeric state. The production rate was ~25 k counts per second. This scheme provides a more efficient and cleaner method for isomer production than ^{233}U α-decay. This method also enables us to control the isomer production. It is expected to become a key technique for VUV photon detection.

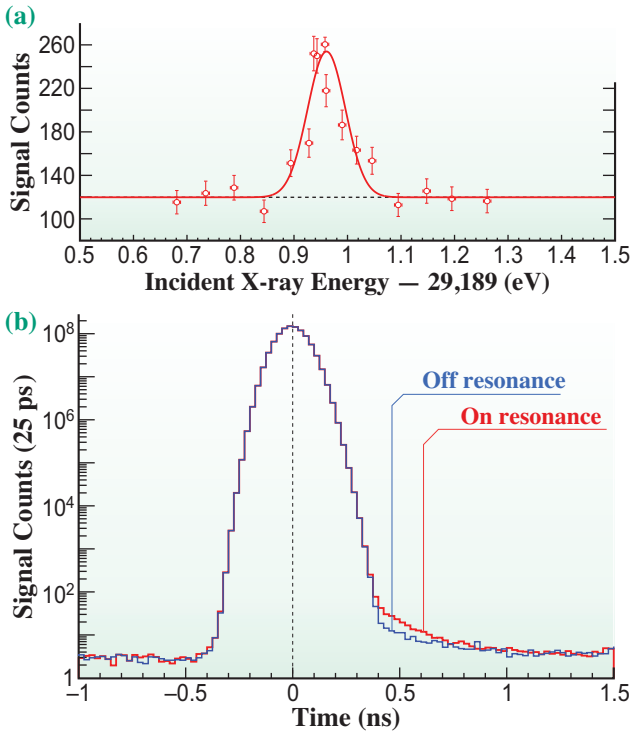

Fig. 3. **(a)** NRS peak and **(b)** temporal profile of the NRS signal.

T. Masuda*, T. Hiraki, A. Yoshimi and K. Yoshimura

Research Institute for Interdisciplinary Science, Okayama University

*Email: masuda@okayama-u.ac.jp

References

[1] B.R. Beck *et al.*: Phys. Rev. Lett. **98** (2007) 142501; B.R. Beck *et al.*: LLNL-PROC-415170 (2009).
[2] L. van der Wense *et al.*: Nature **533** (2016) 47.
[3] V.V. Flambaum: Phys. Rev. Lett. **97** (2006) 092502.
[4] *T. Masuda, A. Yoshimi, A. Fujieda, H. Fujimoto, H. Haba, H. Hara, T. Hiraki, H. Kaino, Y. Kasamatsu, S. Kitao, K. Konashi, Y. Miyamoto, K. Okai, S. Okubo, N. Sasao, M. Seto, T. Schumm, Y. Shigekawa, K. Suzuki, S. Stellmer, K. Tamasaku, S. Uetake, M. Watanabe, T. Watanabe, Y. Yasuda, A. Yamaguchi, Y. Yoda, T. Yokokita, M. Yoshimura and K. Yoshimura: Nature* ***573*** *(2019) 238.*
[5] T. Masuda *et al.*: Rev. Sci. Instrum. **88** (2017) 063105.

Pressure-induced phase transition in plastic crystal neopentylglycol with colossal barocaloric effects

Caloric effects are phase-transition thermal effects regulated by external fields [1]. In the vicinity of a ferromagnetic-to-paramagnetic transition, an applied magnetic field can effectively suppress the disorder of magnetic moments, which in turn accounts for the entropy changes—this is widely known as the magnetocaloric effect (MCE). Similarly, an electrocaloric effect (ECE) can be also found near a ferroelectric-to-paraelectric transition owing to the alignment of polarizations by electric fields. In some elastically active compounds known as ferroelastics, an external compressive or tensile stress can also modify the crystal structure, bringing out the elastocaloric effect (eCE). Unlike the three aforementioned caloric effects that are observed in ferroics, the barocaloric effect (BCE) is not system-selective and can, in principle, be achieved in any atomic system by applying hydrostatic pressure, because pressure is always factored in the free energy of a system. Caloric materials that exhibit caloric effects can be used for solid-state refrigeration through a designated cooling cycle, which is a promising alternative to the vapor compression cycle that is currently in service.

Very recently, we have discovered that a series of plastic crystals exhibits record large BCEs under very weak pressure [2]. Typical entropy changes, whose magnitude characterizes the caloric effect, are about several hundred $J{\cdot}kg^{-1}{\cdot}K^{-1}$, which is 10 times better than those in previous materials, as shown in Fig. 1. Plastic crystals (also termed 'orientation-disordered crystals') are a class of highly disordered solids in which organic molecules (sometimes also inorganic structural blocks) are oriented randomly while their mass centers form highly symmetric lattices, such as the face-centered-cubic (fcc) structure [3]. It is worthwhile to note that the largest entropy change reported is 687 $J{\cdot}kg^{-1}{\cdot}K^{-1}$, exceeding that (~520 $J{\cdot}kg^{-1}{\cdot}K^{-1}$) of the popular liquid refrigerant R134a [4].

Selecting neopentylglycol (NPG) as a model material, we collected the heat flow data using a differential scanning calorimeter (DSC) at 0.1, 15.2, 30.4, 45.0, 71.5 and 91.0 MPa. The phase-transition temperature was defined as the temperature at which the heat flow became maximum. The entropy changes under constant pressure were calculated by integrating the heat flow $Q(P,T)$, after subtracting the baseline. As shown in Fig. 2(a), for a pressure change from ambient pressure to 91.0 MPa, the directly measured entropy change is 384 J $kg^{-1}{\cdot}K^{-1}$, which is highly consistent with the value of 389 $J{\cdot}kg^{-1}{\cdot}K^{-1}$estimated using the Clausius–Clapeyron relation (Fig. 1). Actually, more than 50% of the maximum entropy changes are achieved at pressures as low as 15.2 MPa, and the entropy changes tend to be saturated at about 45.0 MPa; such low driving pressures are desirable for real applications. Shown in Fig. 2(b) is the P–T phase diagram, where there is a thermal hysteresis of about 14 K.

To understand the colossal BCEs of NPG, we conducted a structural study using synchrotron X-ray diffraction (XRD) at SPring-8. The high-resolution XRD patterns obtained at SPring-8 **BL02B2** at a wavelength of 0.9994 Å are plotted in Fig. 3(a). A phase transition is observed to take place at about 313 K, consistent with the thermal measurements (Fig. 2). Rietveld refinement analysis suggests that at room temperature, the NPG molecules are ordered on a monoclinic lattice with space group $P2_1/n$ [5]. This ordered phase transforms into an fcc lattice on heating. The lattice constants are summarized in Fig. 3(b) as a function of temperature. The high-pressure XRD data were collected at **BL04B2** using a diamond anvil cell at a

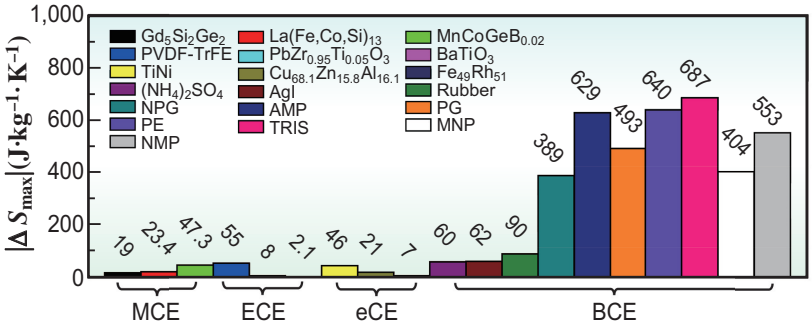

Fig. 1. Plastic crystals with colossal BCEs for next-generation solid-state refrigeration technology: NPG, pentaglycerin (PG), pentaerythritol (PE), AMP, tris(hydroxymethyl)aminomethane (TRIS), 2-methyl-2-nitro-1-propanol (MNP), 2-nitro-2-methyl-1,3-propanediol (NMP).

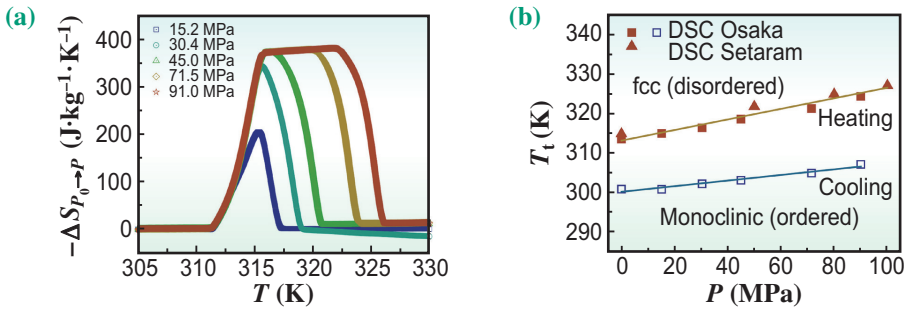

Fig. 2. **(a)** Pressure-induced entropy changes during heating for pressure change from ambient pressure to 15.2, 30.4, 45.0, 71.5 and 91.0 MPa. **(b)** *P* –*T* phase diagram determined using high-pressure DSC.

wavelength of 0.3324 Å. The pressure was determined using a ruby pressure scale. At 318 K, the compound crystallizes in the disordered phase under ambient pressure. Upon applying a pressure of 200 MPa, this phase was converted into the ordered phase, as shown in Fig. 3(c), directly indicating that applying pressure can certainly induce the phase transition.

The discovery of the colossal BCEs in plastic crystals indicates a new direction for caloric materials research. With the help of *in situ* high-pressure XRD, we are able to attribute the observed colossal BCEs to the pressure-induced disorder-to-order transition.

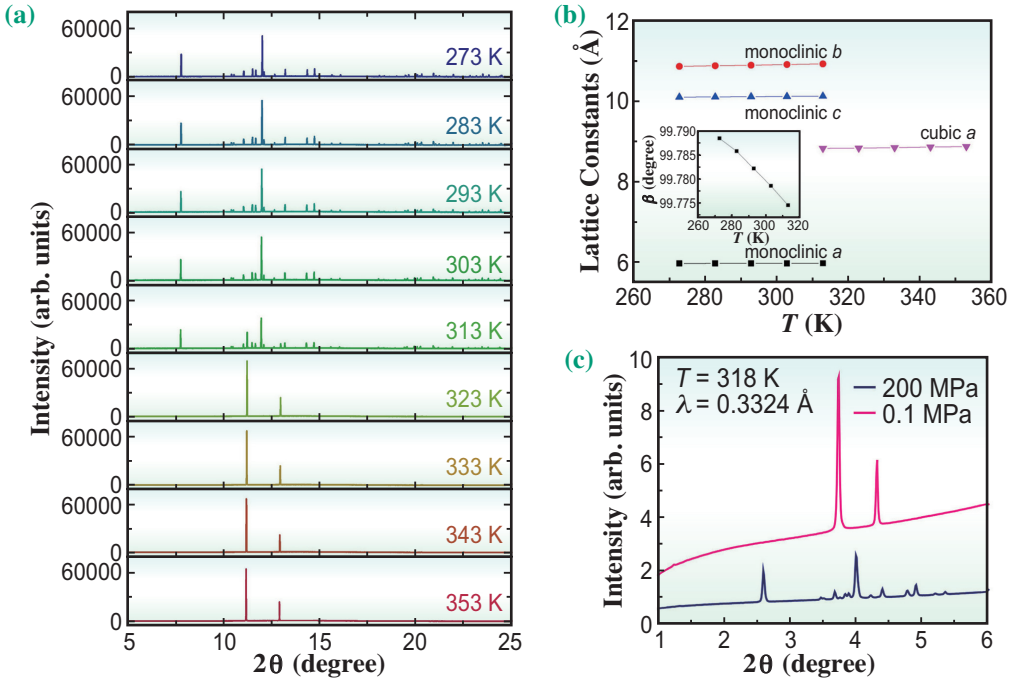

Fig. 3. **(a)** High-resolution XRD patterns obtained at BL02B2. **(b)** Lattice constants as a function of temperature. **(c)** High-pressure XRD patterns at 318 K obtained at BL04B2.

Bing Li[a,*], Takeshi Sugahara[b] and Kuo Li[c]

[a] Institute of Metal Research, Chinese Academy of Sciences, China
[b] Department of Materials Engineering Science, Osaka University
[c] Center for High Pressure Science and Technology Advanced Research, China

*Email: bingli@imr.ac.cn

References

[1] X. Moya *et al.*: Nat. Mater. **13** (2014) 439.
[2] *B. Li, Y. Kawakita, S. Ohira-Kawamura, T. Sugahara, H. Wang, J. Wang, Y. Chen, S.I. Kawaguchi, S. Kawaguchi, K. Ohara, K. Li, D. Yu, R. Mole, T. Hattori, T. Kikuchi, S. Yano, Z. Zhang, Z. Zhang, W. Ren, S. Lin, O. Sakata, K. Nakajima and Z. Zhang: Nature* ***567*** *(2019) 506.*
[3] N.G. Parsonage & L.A.K. Staveley: Disorder in Crystals (Clarendon Press, Oxford, 1979).
[4] M.O. McLinden: Thermophysical properties of refrigerants. ASHRAE Handbook: Fundamentals. (Atlanta, 2009).
[5] D. Chandra *et al.*: Powder Diffr. **8** (1993) 109.

Discovery of simple variant selection effect during stress-driven martensitic transformation

Martensitic transformations (MTs) have been found in various material systems induced by either temperature or pressure/stress, and are the basic principle for shape memory and superelastic effects. The most well-known MTs are those of Fe and its alloys: the fcc (face-centered cubic) to bcc (body-centered cubic) transition during cooling and the bcc to hcp (hexagonal close packed) transition under pressure [1]. The perovskite to post-perovskite (pPv) transition of $MgSiO_3$ in the D" layer of the Earth's deep mantle is also inferred to be martensitic and shows strong inheritance of texture [2].

In martensitic transformations, the development of transformation textures is correlated with the original orientation of the parent phase. These relationships are usually expressed by the parallelism of certain planes and directions of the parent and transformed structures. One example is the Burgers' orientation relationship in the temperature-induced $\alpha \rightarrow \beta$ transition of Ti and Zr: $(0001)_\alpha$ // $\{110\}_\beta$ where 12 variants are involved [3]. However, sometimes, some particular variants are favored more than others during the transition owing to the presence of external stress or strain. For the temperature-induced martensitic phase transition of alloys, the variant selection phenomenon has been extensively studied. In contrast, the variant selection effect in stress- and pressure-driven MTs is still much less understood because of the major technical challenge. Hence, it is of great interest to study the variant selection effect in pressure/stress-driven MTs, which are important in both multifunctional material design and geodynamics.

Using radial synchrotron X-ray diffraction at SPring-8 **BL10XU**, we study the *in situ* variant selection during the cubic-to-orthorhombic martensitic transformation of Mn_2O_3 at pressure up to 51.5 GPa and stress up to 5.5 GPa [4]. Mn_2O_3 crystallizes into a cubic structure under ambient conditions and transfers to the orthorhombic pPv structure under pressure (Fig. 1) [5]. The transition from a highly symmetric cubic structure to a less symmetric orthorhombic structure makes it a perfect sample for the investigation of variant selection under pressure and stress.

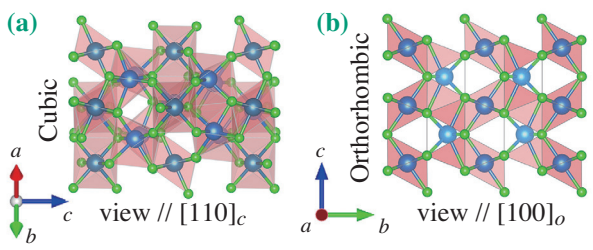

Fig. 1. Crystal structures of Mn_2O_3.

Figure 2 shows unrolled diffraction images of Mn_2O_3 at various pressures. The systematic intensity variation on each pattern represents the preferred orientation of the lattice (texture). At low pressure it is a pure cubic phase and strong texture appears at 10.3 GPa (Fig. 2(a)). Phase transition starts at 24.1 GPa, as proved by the appearance of new peak lines indicated by red arrows (Fig. 2(b)). No further phase transition can be observed up to 51.5 GPa (Fig. 2(c)). The quenched sample went back to the cubic phase with the same original preferred lattice orientation (Fig. 2(d)), indicating that this phase transformation is reversible.

Inverse pole figures (IPFs) were obtained for both phases of Mn_2O_3, and partial IPFs represent complete texture information in accordance with cubic and orthorhombic crystal symmetry (Figs. 3(a) and3(b)). The low-pressure cubic phase displayed a 110 texture, while the intensity increased with pressure and reached its highest value of 3.24 m.r.d. at ~20.2 GPa ($t \approx 3.5$ GPa) (Fig. 3(a)). Above the phase transition point, the high-pressure phase developed a very strong 100 texture with an intensity of 11.3 m.r.d. (Fig.3(b)). The texture change during the phase transition suggests a relationship of $(110)_c$//$(100)_o$, where $(110)_c$ is the lattice plane perpendicular to the stress direction. The much higher texture intensity of the high-pressure phase indicates that variant selection might occur during the phase transition. This can be more clearly presented in the pole figures (PFs) projected along the compression direction (Figs. 3(c) and 3(d)). They have axial symmetry, conforming to the geometry of the deformation experiment. For the cubic phase, it is clear that one {110} plane is in the center of the 110 PF, while four planes are at around 30° and one at 90° (Fig.3(c)). This means that only one of the six {110} planes of cubic phase, the (110) plane, is aligned perpendicular to the compression direction. For the orthorhombic phase, there is only one maximum at the center of the 100 PF, indicating that $(100)_o$ lattice planes are preferentially oriented perpendicular to the compression direction (Fig.3(d)). Because of the orientation relationship $\{110\}_c$//$(100)_o$, all $\{110\}_c$ planes have a chance to became $(100)_o$. However, with stress there is obviously variant selection and the orthorhombic phase selects one of the cubic

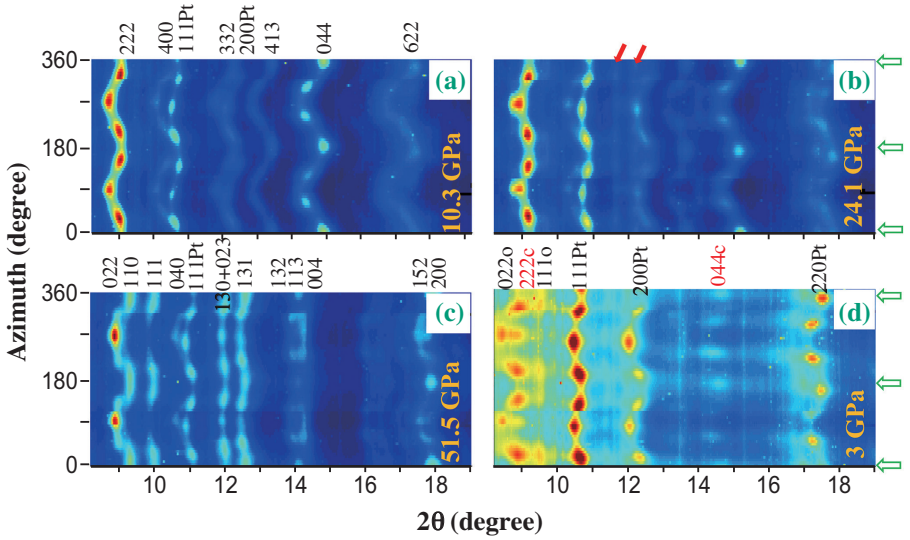

Fig. 2. Unrolled diffraction patterns of Mn_2O_3 under pressure: **(a)** cubic; **(b)** two-phase mixture; **(c)** orthorhombic; **(d)** two-phase mixture during decompression.

{110} planes that is closest to perpendicular to the compression direction.

Our study provides an example of almost perfect variant selection during a phase transition under stress. For Mn_2O_3, similarities in atomic arrangements of the cubic {110} and orthorhombic (100) lattice planes can explain the texture transfer of $(110)_c$ to $(100)_o$ during the phase transition. In addition, the axial stress applied in our experiments will lead to stronger strain of lattice planes perpendicular to the compression direction than in other directions. Thus, these planes will more easily transfer to the high-pressure phase and consequently result in the variant selection during the phase transition.

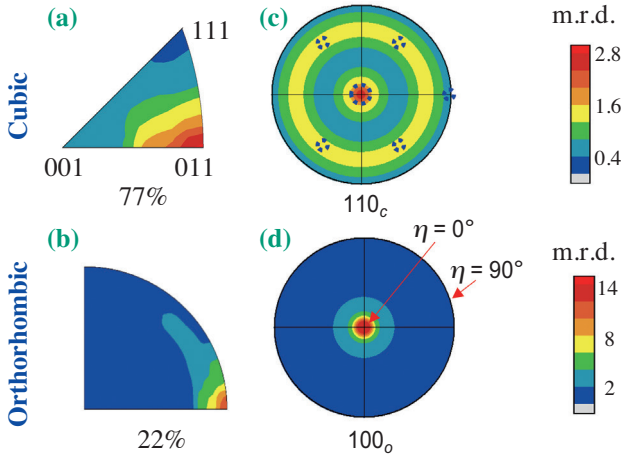

Fig. 3. Orientation relationship and variant selection during phase transition of Mn_2O_3. Inverse pole figures of **(a)** cubic and **(b)** orthorhombic phases. Pole figures of **(c)** cubic and **(d)** orthorhombic phases. Pressure is 24.1 GPa. An equal area projection is shown.

Binbin Yue*, Fang Hong and Bin Chen

Center for High Pressure Science and Technology Advanced Research, Shanghai, China

*Email: yuebb@hpstar.ac.cn

References

[1] L. Miyagi *et al.*: J. Appl. Phys. **104** (2008) 103510.
[2] D.P. Dobson *et al.*: Nature Geosci. **6** (2013) 575.
[3] W.G. Burgers: Physica **1** (1934) 561.
[4] *B. Yue, F. Hong, N. Hirao, R. Vasin, H.-R. Wenk, B. Chen, and H.-K. Mao: Proc. Natl. Acad. Sci.* ***116*** *(2019) 14905.*
[5] J. Santillán *et al.*: Geophys. Res. Lett. **33** (2006) L15307.

Studying ultrafast dynamics of temperature-dependent dislocation in Fe-0.1mass%C using femtosecond X-ray diffraction

In the iron and steel industry, the development of new alloys and the improvements in manufacturing processes have resulted in the commercialization of several new materials systems. Specifically, the process control during steel production has attracted significant attention in the automobile industry. In the steel manufacturing process, the heat treatment plays an extremely important role. During heat treatment, nonequilibrium states may be produced as a result of ultrafast microstructural changes directly affecting the final properties of the metal, resulting in new alloys [1]. However, the difficulty of observing atomic diffusion and dislocation recovery during such ultrafast microstructural changes hinders the physical and kinetic understanding of these processes. The martensitic transformation is an extremely important phenomenon in physical metallurgy. Many studies have focused on the rapid heating of low-carbon steel, and improved ductility and strength by the refinement of crystal grains has been reported [1]. However, a complete understanding of the phenomenon remains elusive owing to a lack of an operand measurement. To the best of our knowledge, the microstructural changes under ultrafast heating rates greater than 10^4 °C·s^{-1} have not been observed directly in steel.

To observe these ultrafast and irreversible changes in the steel microstructure, single-shot X-ray diffraction (XRD) measurements are highly effective. Generally, high intensity X-rays obtained from synchrotron radiation require a very short exposure time (10 ms) for recording the XRD patterns [2]. However, this exposure time is far greater than the temporal resolution of the target (which is less than 1 μs) required for the direct observation of the microstructural changes in iron and steel. Therefore, X-ray beam with an intensity four orders of magnitude higher than that of synchrotron X-rays is required. X-ray free-electron laser (XFEL) is capable of producing such high intensity X-rays. In this study, time-resolved XRD measurements were carried out to clarify the changes in the dislocation density and carbon concentration during the martensitic transformation of steel at ultrafast heating rates of 10^3–10^4 °C·s^{-1}. The experiments were carried out at SACLA **BL3**. The influence of the ultrafast heating on the formation of the microstructure is discussed within the context of the dislocation migration [3].

Figure 1 shows the experimental setup of XRD measurements using femtosecond XFEL pulses. For a steel sample under ultrafast heating, a two-dimensional XRD pattern was recorded using a multiport charge-coupled device (MPCCD) detector. The ultrafast electrical heating, the temperature measurement, and the X-ray detection were synchronized with a trigger signal from the XFEL source. Both edges of the sample (15 mm×5 mm×0.5 mm) were affixed to copper electrodes to facilitate resistive heating. The sample had a known mass composition of 0.1 mass%C-2 mass%Mn-bal.Fe with a martensitic microstructure, and it was cold-rolled for a 50% reduction in thickness. The XRD line profiles were obtained by integrating the diffraction images in the circumferential direction. Ungár *et al.* proposed that the X-ray line profiles could be analyzed by considering the effects of anisotropic lattice strains along the crystallographic directions, and the strength of the lattice strains around the dislocations [4]. These characteristics are used to deduce the optimal relationship between the dislocation density and the X-ray line profiles.

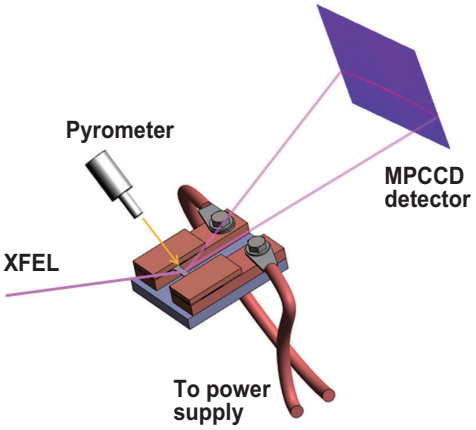

Fig. 1. Experimental setup of femtosecond XFEL.

Figure 2 shows the temperature dependence of the screw and edge components of the dislocation densities for a heating rate of 1.2×10^4 °C·s^{-1}. In the α' phase, the total dislocation density is approximately constant below 500°C. However, it is noted that in this temperature region (100–500°C), the edge dislocations are decreased while the screw dislocations are increased along with the increase in the temperature. This behavior is attributed to the migration of the high mobility edge dislocations towards the deformed dislocation loop, indicating that the edge dislocations are unstable below 500°C. Furthermore, the edge dislocation component decreases drastically above 600°C, while the screw dislocation component decreases insignificantly above 600°C. Therefore, the screw dislocations are predominant dislocations

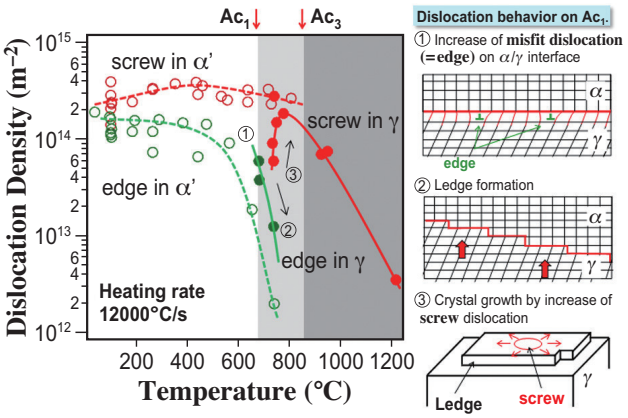

Fig. 2. Temperature dependence of the dislocation densities of the screw and edge dislocations at 1.2×10^4 °C s^{-1}.

in the α' phase at temperatures above the perlite transformation (Ac_1). On the other hand, the edge dislocations are predominant in the γ phase around Ac_1 region. As the temperature increases, the dislocation type immediately changes from the edge dislocations to the screw dislocations. The screw dislocation component in the γ phase decreases rapidly in 100% austenite structure above austenitizing temperature (Ac_3). It is seen that, the edge dislocation which are unstable at the high temperature, fall in number and the screw dislocations are introduced in the lattice for promoting the three-dimensional screw growth. The dislocation multiplication in the γ phase of the steel, thus results in the crystal growth of the γ phase.

Figure 3 shows the microstructure formation mechanism. In this study, the dynamic changes in the carbon concentration and the dislocation densities were successfully observed for a timescale shorter than 0.1 s. These changes indicate the precipitation of fine particles of θ-Fe_3C and a delay in dislocation recovery. At the heating rate of 10^4 °C·s^{-1}, the diffusion distance of carbon is extremely short and thus, the growth of θ-Fe_3C particles is restricted before the α' to γ phase transformation takes place.

The dislocation density is one of the key factors in producing high-strength steel. Fine grains of γ phase with high dislocation densities result from the transformation of the α' phase with a high dislocation density, at a high heating rate. The dislocation density is further multiplied by a martensitic transformation with rapid cooling. This study shows that the direct observation of a dynamic change in the dislocation density enables our understanding of kinetics in the microstructure, under steep thermal gradients, and contributes to the further development of the functional steels and new manufacturing processes.

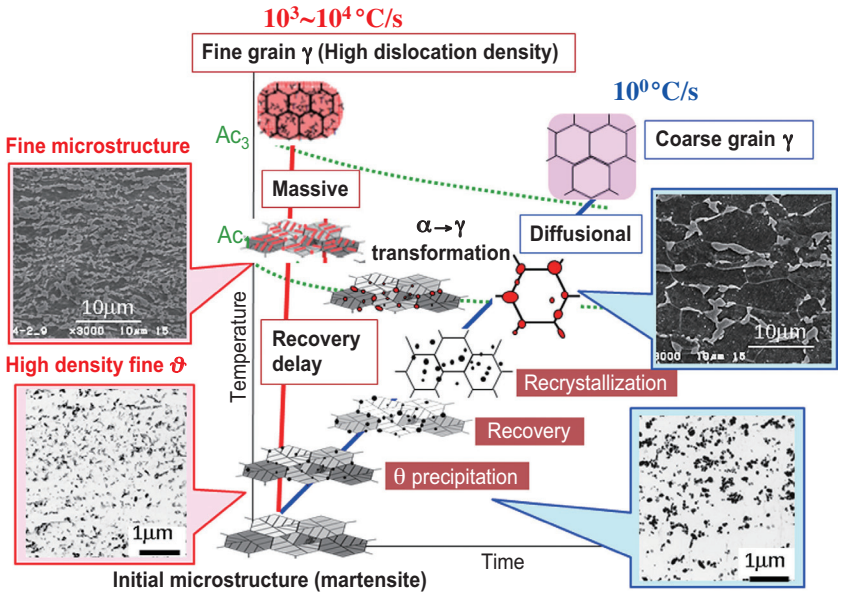

Fig. 3. Microstructure formation mechanism.

Mitsuharu Yonemura

Advanced Technology Research laboratories,
Nippon Steel Corporation

Email: yonemura.4k8.mitsuharu@jp.nipponsteel.com

References

[1] T. Lolla *et al.*: Mater. Sci. Technol. **27** (2011) 863.
[2] M. Yonemura *et al.*: Mater. Trans. **47** (2006) 2292.
[3] *M. Yonemura, H. Nishibata, T. Nishiura, N. Ooura, Y. Yoshimoto, K. Fujiwara, K. Kawano, T. Terai, Y. Inubushi, I. Inoue, K. Tono and M. Yabashi: Sci. Rep.* ***9*** *(2019) 11241.*
[4] T. Ungár *et al.*: J. Appl. Cryst. **32** (1999) 992.

Direct evidence of Co-3*d* orbital change associated with spin crossover in $LaCoO_3$ obtained by X-ray Compton scattering

Trivalent Co oxides exhibit exotic physical and chemical properties, which are attributed to the multiple degrees of freedom on the spin, orbital and lattice arising from the $3d^6$ electronic configuration of Co^{3+}. One of the examples, $LaCoO_3$, has been attracting widespread interest from researchers because of its unusual spin crossover phenomena. The substance shows broad magnetic anomalies at around 100 and 500 K [1]. The magnetic anomaly at around 500 K is accompanied by an insulator-to-metal transition (IMT). This phenomenon is considered to be the temperature-induced spin crossover from the nonmagnetic low-spin (LS) ground state to magnetic excited states on the basis of the ligand-field theory premising the local Co-3*d* under a six-coordinated crystalline electric field. Despite the decades of research history and the extensive efforts of researchers, there is still controversy as to what the magnetic excited state induced around 100 K is: intermediate spin (IS) with $S = 1$ or high spin (HS) with $S = 2$. The IS state, which has one degree of freedom on e_g orbitals, is strongly supported by experiments exhibiting Jahn-Teller distortion and/or fluctuation, although an IS first excited state is contradictory to ligand-field theory. Several pieces of spectroscopic evidence support the HS state, which is inconsistent with the magnitude of the measured magnetization and the ferromagnetic correlation among Co-spins revealed by neutron scattering experiments. Thus, neither spin-state model can comprehensively explain all the important experimental findings, leaving us with unsolved riddles and controversy. Very recently, experimental results suggesting the collective character of spin crossover and the necessity of the models to take into account a nonlocal electronic structure have been suggested. Therefore, detailed experimental research on the electron-orbital states of Co-3*d* responsible for the spin crossover is desirable for understanding the spin crossover phenomena of $LaCoO_3$.

To investigate the characteristics of Co-3*d* electron-orbital states in $LaCoO_3$, such as the symmetry and distribution, we have conducted X-ray Compton scattering experiments using SPring-8 **BL08W** [2,3]. The X-ray Compton scattering experiments enable the imaging of the electron density distribution in the momentum space. The technique is bulk-sensitive and measurements can be obtained at high temperatures and under high magnetic fields, which are advantages over angle-resolved photoemission spectroscopy (ARPES). The Compton profiles $J(p_z)$ obtained by Compton scattering experiments reflect the projection of the three-dimensional electron momentum density $\rho(p_x, p_y, p_z)$ onto the z axis [4], which lies along the scattering vector

$$J(p_z) = \iint \rho(p_x, p_y, p_z)\, dp_x dp_y \quad (1)$$

The electron momentum density (EMD) can be reconstructed from $J(p_z)$ measured along several crystallographic directions [4]. Comparison of EMDs below and above the temperature of the spin crossover of $LaCoO_3$ reveal the Co-3*d* electron-orbital states responsible for its spin crossover phenomena.

Figure 1(a) shows the reconstructed difference 2D-EMD between 10 and 270 K across the 100 K spin crossover. The experiments across the 500 K spin crossover also yielded a similar result. These findings

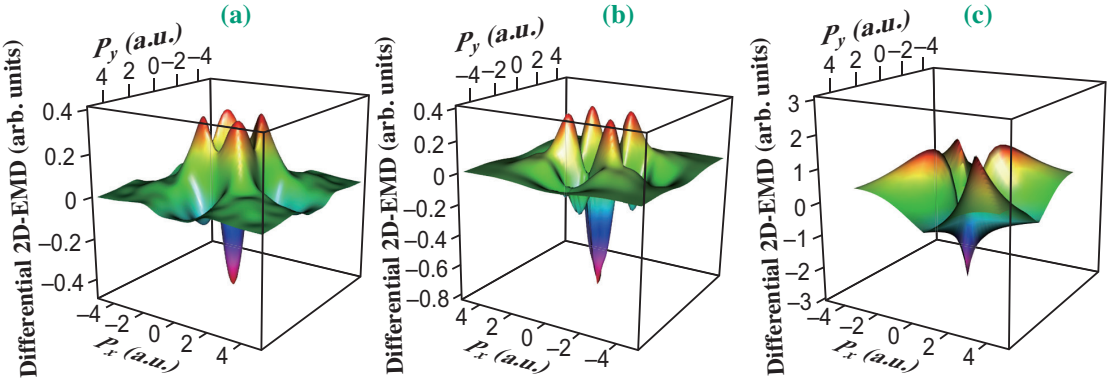

Fig. 1. Aerial views of the difference two-dimensional electron momentum density (2*d*-EMD) of Co-3*d* in $LaCoO_3$ between 10 and 270 K for **(a)** measured and **(b)** calculated molecular orbitals (MO) and **(c)** calculated atomic orbitals (Atom).

unambiguously demonstrate that the symmetry change due to electron transfer between t_{2g} and e_g orbitals is responsible for both the spin crossovers at around 100 and 500 K [2,3].

As shown in Fig. 2, a difference $J(p_z)$ increases with increasing temperature, showing that a larger number of electrons are excited to e_g orbitals at higher temperatures. The magnitude of t_{2g}-e_g electron transfer can be estimated from the area intensity of difference $J(p_z)$. Figure 3 shows the temperature dependence of the area intensity of the difference $J(p_z)$. Below 300 K, a thermal-activation-like increment with increasing temperature was observed. On the other hand, a steep increment is shown at around 500 K, suggesting the cooperative character of the 500 K spin crossover [3].

The shape of $J(p_z)$ and the 2D-EMD also provide important information. The difference $J(p_z)$ shown in Fig. 2 exhibits an oscillation at approximately p_z = 2–4 atomic units (a.u.). The oscillation is characteristic of the molecular orbitals (MO) constructed by the hybridization of Co-e_g and O-2p [2,3]. The calculated 2D-EMD and the difference $J(p_z)$ are reproduced much better for the MO than for localized atomic orbitals (Atom), as shown in Figs. 1 and 2. The oscillatory behavior in the difference $J(p_z)$, which occurs above 100 K (not shown), develops with increasing temperature and becomes very prominent above 500 K (see Fig. 2). This finding indicates further development of the MO formation resulting from the progress of hybridization between Co-e_g and O-2p through the 500 K spin crossover, which might be related to the itineracy of the electrons above the IMT.

The present Compton scattering experiments demonstrate that the MO resulting from covalent bonding between Co-3d and O-2p plays an important role in the spin crossover of $LaCoO_3$. This finding strongly indicates a collective character of the spin crossover phenomena in $LaCoO_3$; i.e., the nonlocal electron-orbital states are essential for the spin crossover phenomena. Detailed theoretical analyses, such as the first-principles calculations of MO, are indispensable for further progress in the research of the spin crossover phenomena in this substance.

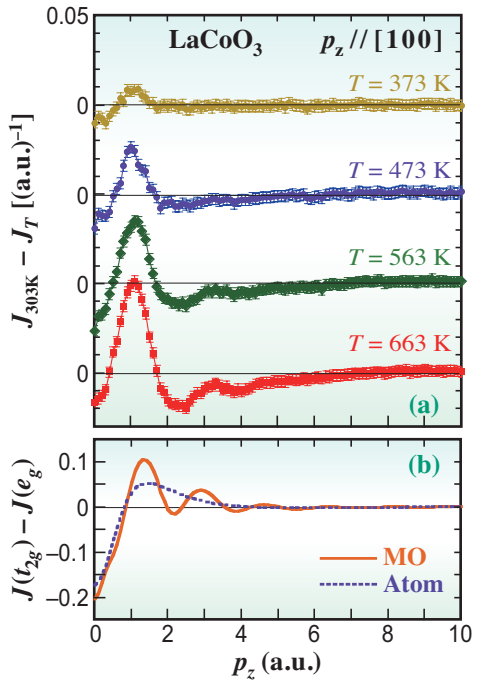

Fig. 2. **(a)** Temperature dependence of the difference Compton profiles ($J_{303\,K}$ - J_T ; T = 373 – 663 K) for $[100]_c$ direction of the pseudocubic unit cell, along with **(b)** the calculated difference Compton profiles for molecular orbitals (MO) and localized atomic orbitals (Atom).

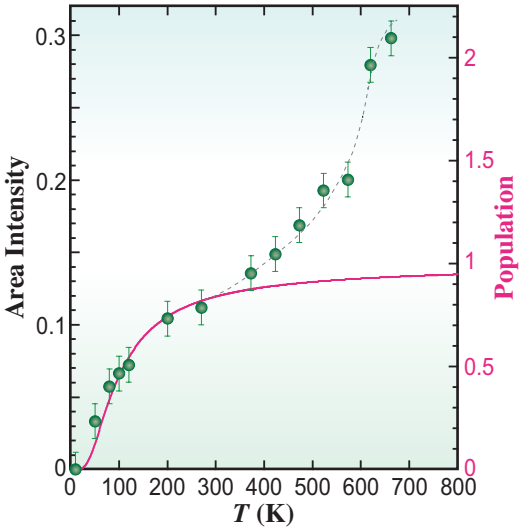

Fig. 3. Temperature dependence of the area intensity of the difference Compton profiles.

Yoshihiko Kobayashi

Department of Physics, Tokyo Medical University

Email: koba@tokyo-med.ac.jp

References

[1] J.B. Goodenough and J.M. Longo, Landolt-Börnstein (Springer, Berlin, 1970), Vol. 4a, Chap. 3, and references therein.
[2] Y. Kobayashi *et al.*: J. Phys. Soc. Jpn. **84** (2015) 114706.
[3] *Y. Kobayashi, Y. Sakurai, N. Tsuji, K. Sato and K. Asai: Phys. Rev. B* ***98*** *(2018) 115154.*
[4] M.J. Cooper *et al.*: X-ray Compton Scattering (Oxford University Press, Oxford, 2004).

Oxygen *K*-edge X-ray Raman spectroscopy for solid oxygen up to 140 GPa with hard X-rays

Oxygen is one of the most familiar materials to us as it is essential to sustain life. In the ground state, one O_2 molecule has two unpaired electrons, making this molecule a magnet. The magnetic and van der Waals interactions between O_2 molecules cause four solid phases with different structures up to ~10 GPa. Above this pressure, in contrast, four O_2 molecules form an O_8 cluster. The two unpaired electrons are thought to play a role in combining the four O_2 molecules. The epsilon phase of oxygen, which has O_8 clusters as structural units, has been reported to have no long-range magnetic order but stable up to ~96 GPa. At this pressure, oxygen exhibits a structural phase transformation and metallic electrical conductivity [1]. Note that the crystal structure of metallic oxygen has not yet been solved completely. Although the epsilon phase is considered to be stable between 10 and 96 GPa, some experimental studies have reported anomalies at 20–40 GPa. The phase transitions and anomalies are expected to involve changes in the electronic structure.

X-ray spectroscopy is a tool for studying the electronic structures of matter. Soft X-rays are usually used to measure the electronic structure of oxygen, e.g., in X-ray absorption spectroscopy. However, it is extremely difficult to collect oxygen *K*-edge absorption spectra of dense solid oxygens under high-pressure conditions even with the present synchrotron sources. The oxygen *K*-edge is located at around 530 eV. Soft X-rays of approximately this energy are absorbed by the surrounding materials compressing the sample oxygen, and hardly penetrate to or pass through the materials. Inelastic X-ray scattering enables us to collect such spectra using hard X-rays as a probe and signals. X-ray Raman scattering (XRS) is one form of the inelastic X-ray scattering related to the core-electron excitation. XRS spectra, similar to those of X-ray absorption spectroscopy, can be obtained only by tuning the energy difference of the incident and scattered X rays to the absorption edge energy, even if the absorption edge energy is in the soft X-ray region. A study in which this technique was applied to oxygen has revealed the change in the electronic structure when the structural unit changes from O_2 to O_8 [2]. We have applied this technique to dense solid oxygen having O_8 structural units over the range of pressures at which it is insulator (17 GPa) to metal (137 GPa) and have interpreted these spectra based on theoretical calculations [3].

XRS spectra of solid oxygen were measured at SPring-8 **BL12XU**. The incident X-ray energy and the typical energy resolution were 9.9 keV and 1.4 eV, respectively, using the spectrometer with the Si(111) double-crystal monochromator and the Si(555) analyzers. At several pressures, the generated pressure and the crystal structure of the existing phase were confirmed by X-ray diffraction at SPring-8 **BL10XU**. An XRS spectrum contains two components: a sharp π^* band and a broad σ^* band (Fig. 1). The π^* band corresponds to the lowest unoccupied orbital of an O_2 molecule and the σ^* band corresponds to an antibonding orbital along the molecular axis. Their positions are shifted to higher energies and the widths become broader with increasing pressure. At 67 GPa, the π^* band has a side band on the higher energy side.

The positions of these two bands generally shift to higher energies with increasing pressure. However, the positions shifted to lower energies in the pressure region where oxygen becomes a

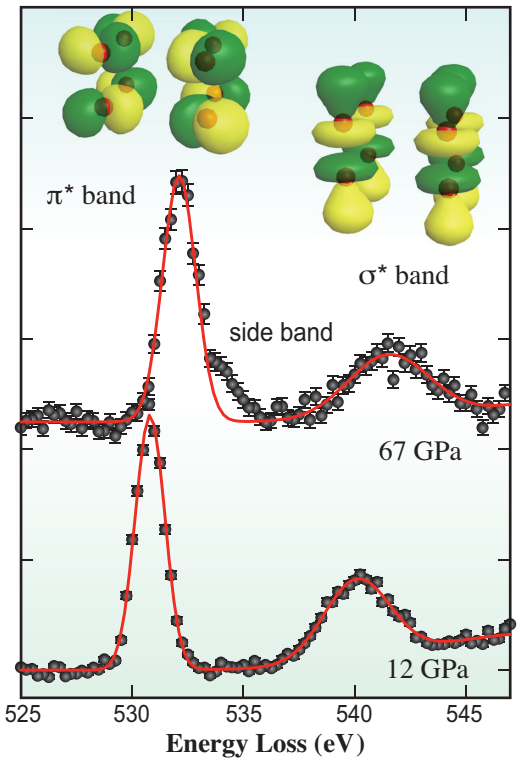

Fig. 1. Typical X-ray Raman scattering spectra of solid oxygen. Red lines indicate fitting of two Gaussians and one linear line to the spectra. (Inset) O_8 cluster with examples of π^* and σ^* orbitals. Red balls indicate oxygen atoms.

metal (between 94 and 115 GPa), and then shifted to higher energies after metallization (Fig. 2). Electrons belonging to the σ* and π* bands are considered to be distributed along and off the O_2 molecular axis, respectively (Fig. 1). Therefore, the change in σ* and π* is related to the change in bonding between the two oxygens in an O_2 molecule and between the four O_2 molecules in an O_8 cluster, respectively. The negative shift of the π* band position was qualitatively reproduced in the calculation, indicating closure of the direct bandgap during metallization and delocalization of electrons in a plane perpendicular to the O_2 molecular axes. In contrast, the negative shift of the σ* band, which was not reproduced in the calculation, indicates weakening of O_2 intramolecular bonding. This is consistent with the softening of the Raman active O_2 vibron mode [4].

Another notable point is the appearance of the π* side band (Fig. 1). By comparison with the theoretical calculation, it is concluded that this is most probably because of semi-metallization of epsilon oxygen [3] and may be related to the reported anomalies at around 30 GPa. The pressure dependences of the σ* and π* band positions also seem to change at this pressure (Fig. 2). Microphotographs of the sample chamber exhibit three different conditions of the dense solid oxygen, i.e., insulator, semimetal, and metal (Fig. 2). Further detailed comparisons with theoretical studies would be helpful in understanding what occurs in the electronic structure at around 30 GPa. Measurements with higher energy resolution are imperative.

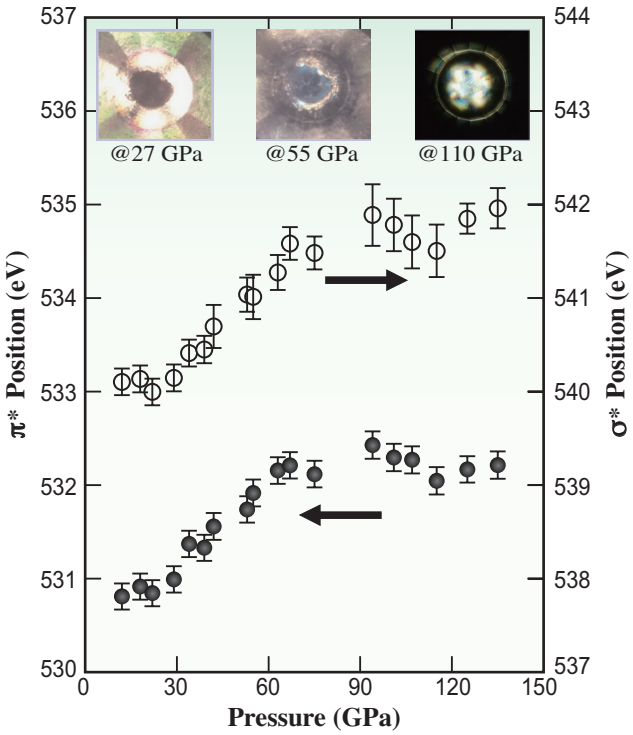

Fig. 2. Pressure dependence of the π* and σ* band positions shown by closed and open circles, respectively. (Inset) Microphotographs of the sample chamber at the pressures indicated.

Hiroshi Fukui

Graduate School of Material Science, University of Hyogo

Email: fukuih@sci.u-hyogo.ac.jp

References

[1] Y.A. Freiman: Low Temp. Phys. **41** (2015) 847.
[2] Y. Meng *et al.*: Proc. Natl. Acad. Sci. USA **105** (2008) 11640.
[3] *H. Fukui, L.T. Anh, M. Wada, N. Hiraoka, T. Iitaka, N. Hirao, Y. Akahama, and T. Irifune: Proc. Natl. Acad. Sci. USA **116** (2019) 21385.*
[4] A.F. Goncharov *et al.*: Phys. Rev. B **68** (2003) 100102(R).

The magnetic anisotropy of graphene-covered cobalt on silicon carbide

One of the remarkable properties of graphene is its high spin diffusion length that is due to a weak spin-orbit coupling. This makes graphene a promising spin-transport material to be implemented in spintronic devices [1]. Besides that, graphene has an impact on the magnetic anisotropy of thin magnetic films and can lead to chiral spin textures [2,3]. Due to effects like these, the magnetic properties of graphene-containing systems have become an active field of research. The interfaces of graphene with room-temperature ferromagnets are particularly interesting. Of these, Ni(111) and Co(0001) are highlighted due to their well-matched lattice constants with respect to the graphene lattice. Here, we investigate the graphene-cobalt interface on a silicon carbide (SiC) substrate, with emphasis on the magnetic anisotropy of the graphene-covered cobalt film.

We chose SiC as a substrate since it is the most promising for the implementation of graphene applications, due to its established use in semiconductor industry. Furthermore, pure SiC is semi-insulating, which overcomes the need to transfer the prepared graphene to an insulating substrate. Graphene on SiC can be prepared by high-temperature annealing of the SiC crystal, which leads to preferential evaporation of the silicon atoms since their vapor pressure with respect to that of carbon is higher by orders of magnitude. The remaining carbon atoms then rearrange into a graphene lattice depending on the preparation conditions.

In this study, we prepared graphene-covered cobalt by means of intercalation. We started with a $(6\sqrt{3}\times6\sqrt{3})R30°$ reconstructed SiC(0001) surface, which is the precursor layer of graphene on SiC [4]. Subsequently, cobalt films were deposited on the $6\sqrt{3}$ reconstructed SiC surface and subjected to a controlled annealing procedure. During annealing, a chemical reaction of the cobalt and the SiC surface converts the $6\sqrt{3}$ structure into a graphene film, which is subsequently intercalated by the cobalt atoms. The intercalation temperature is in the range of 300°C to 600°C depending on the cobalt film thickness, as described in detail in reference [5]. In order to get insight into the magnetic properties, photoemission electron microscopy (PEEM) was employed. The PEEM experiments were carried out at SPring-8 **BL17SU** beamline using the SPELEEM apparatus. The intercalation was verified by photoelectron spectroscopy (XPS) using a spherical sector analyzer (CLAM IV, VG Microtech) located at beamline BL11 at the synchrotron radiation source DELTA, Germany.

Figure 1 shows a PEEM image of a $6\sqrt{3}$ reconstructed SiC sample before cobalt deposition. Since the image was recorded during excitation with ultraviolet light from an Hg lamp, the contrast is dominated by local variations of the sample work function. The wide bright stripes correspond to $6\sqrt{3}$ reconstructed SiC terraces whereas the narrow dark stripes correspond to monolayer graphene inclusions at the step edges.

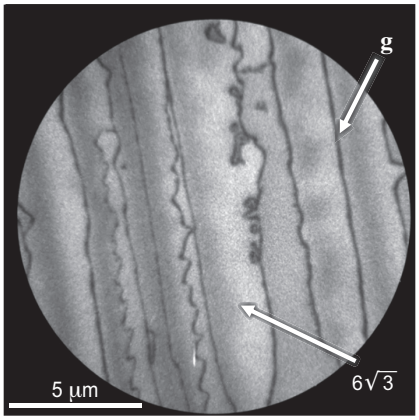

Fig. 1. Ultraviolet-excited PEEM image recorded before cobalt deposition. (g = monolayer graphene)

Figure 2(a) shows an XPS spectrum recorded before cobalt deposition. It consists of four chemically shifted components, which correspond to the $6\sqrt{3}$ reconstructed terraces (components S1 and S2), to the graphene monolayer inclusions at the step edges (component G), and to the bulk SiC bonding (component SiC). After deposition and annealing of a 0.4 nm thick cobalt film, the XPS spectrum is significantly changed, as shown in Fig. 2(b). In particular, the G-component is increased which relates to a partial transformation of the $6\sqrt{3}$ reconstructed surface into a graphene-covered surface. Figure 2(c) shows the XPS spectrum recorded after the deposition and annealing of 3.0 nm cobalt. Here, only one asymmetric graphene-related component remains. Therefore, at high film thickness the $6\sqrt{3}$ reconstruction is fully converted into a graphene-covered surface.

The magnetic properties of the cobalt-intercalated samples with different film thicknesses were investigated using PEEM images with magnetic contrast, obtained by utilizing the X-ray magnetic circular dichroism (XMCD) at the Co L_3-edge. For

each film thickness, two images corresponding to 90°-rotated synchrotron radiation incidence direction are shown. Comparing the two images, the preferred magnetization axis can be determined. In particular, it can be determined whether a perpendicular or in-plane magnetic anisotropy is present. For a perpendicular magnetization, no significant contrast change is expected upon sample rotation, whereas the opposite is expected for an in-plane magnetization.

Figures 3(a) and 3(b) show the resulting images for a 1.1 nm thick cobalt film. Clearly, only the regions near the step edges are magnetic. In contrast, for 1.5 nm and 3.0 nm thick cobalt films, the whole surface is magnetic, as shown in Figs. 3(c—f). In both cases, the contrast change upon sample rotation indicates that the magnetization is mostly in the sample plane. Furthermore, it becomes clear that the magnetic domains favorably align parallel or anti-parallel to the substrate step edges, as visible in Figs. 3(c) and 3(e). Therefore, the step edges introduce a significant magnetic anisotropy forcing the magnetization in the sample surface. It is expected that the magnetic anisotropy can be tuned by a modification of the step heights, which is viable through changes to the SiC heating process.

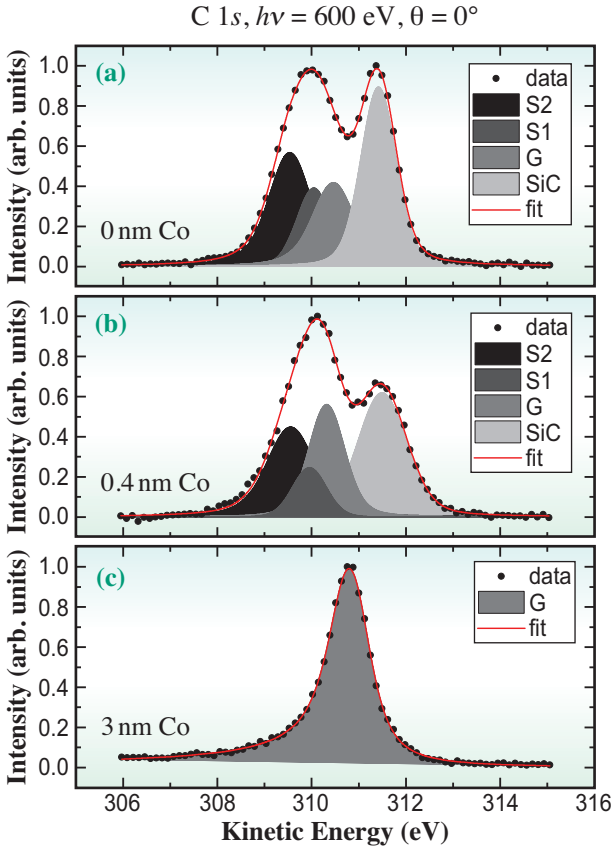

Fig. 2. XPS spectra taken at normal emission: before cobalt deposition **(a)**, after deposition and annealing of 0.4 nm **(b)**, and 3.0 nm **(c)** thick cobalt films.

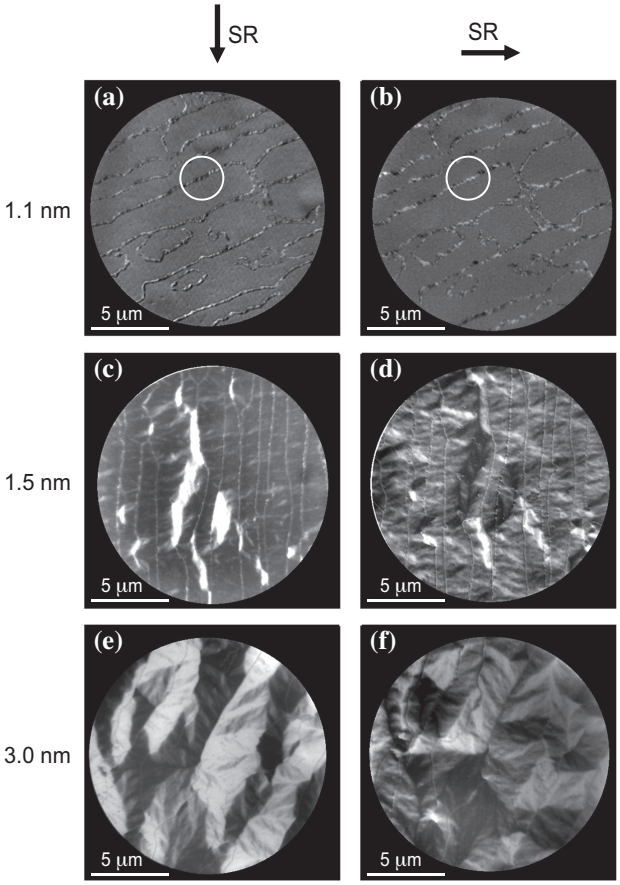

Fig. 3. XMCD-PEEM images with magnetic contrast recorded after cobalt intercalation. The arrows indicate the incidence direction of the synchrotron radiation (SR).

Richard Hönig[a,*], Takuo Ohkochi[b] and Carsten Westphal[a]

[a] TU Dortmund University, Dortmund, Germany
[b] Japan Synchrotron Radiation Research Institute (JASRI)

*Email: richard.hoenig@tu-dortmund.de

References

[1] W. Han *et al.*: Nat. Nanotechnol. **9** (2014) 794.
[2] A.D. Vu *et al.*: Sci. Rep. **6** (2016) 24783.
[3] H. Yang *et al.*: Nat. Mater. **17** (2018) 605.
[4] C. Riedl *et al.*: J. Phys. D: Appl. Phys. **43** (2010) 374009.
[5] *R. Hönig, P. Roese, K. Shamout, T. Ohkochi, U. Berges and C. Westphal: Nanotechnology* ***30*** *(2019) 025702.*

Magnetoelectric-effect-driven antiferromagnetic domain motion revealed by scanning soft X-ray magnetic circular dichroism microscopy

Magnetic materials are classified roughly into ferromagnets and antiferromagnets. Ferromagnets have spontaneous magnetization and have been a major player in both magnetic research and various magnetic devices. By contrast, in antiferromagnets, magnetic moments are fully compensated and no net magnetization emerges. Because of this inherent characteristic, antiferromagnets have long been regarded as useless materials. However, once the antiferromagnetic (AFM) spin, especially in micro/nanosize devices, can be controlled by some external field, we can enjoy various functionalities such as the ultrafast AFM spin/domain dynamics, which yield novel phenomena such as THz emission. Owing to the recent development of spintronics, spin-torque and magnetoelectric (ME) effects are expected to become a key to the control of the AFM spin/domain. The ME effect is referred to as magnetization (***M***) induction by an electric field (***E***) and electric polarization (***P***) by a magnetic field (***H***) through the ME susceptibility α :: $\boldsymbol{M} = \alpha' \cdot \boldsymbol{E}$ and $\boldsymbol{P} = \alpha \cdot \boldsymbol{H}$. Cr_2O_3 is a prototypical ME-AFM material known since the middle of the1950s. In 2005, Borisov *et al*. demonstrated that the ME-controlled AFM domain state in Cr_2O_3 was detectable through the exchange bias polarity, which was induced by the interfacial exchange coupling between the AFM Cr_2O_3 and ferromagnetic (FM) layers [1]. In this scenario, it is assumed that the Cr_2O_3 AFM domain, or at least the interfacial Cr spin, FM domain, couples with Cr_2O_3 and exchange bias polarity are connected mutually; this has been believed but is unproven. We prove that direct evidence to support this hypothesis can be obtained through magnetic domain observation using the scanning soft X-ray magnetic circular dichroism (XMCD) microscope equipped at SPring-8 **BL25SU** [2] by taking advantage of the element-specific feature. In this instrument, the circularly polarized soft X-ray is focused on the sample using the Fresnel zone plate, and the sample is scanned two dimensionally to maintain the focused state. During scanning, the soft X-ray absorption intensity is collected. By subtracting the obtained image collected with the opposite helicity of the incident soft X-ray, two-dimensional mapping of the XMCD intensity can be accomplished.

Figure 1 shows the two-dimensional map of the XMCD intensity measured at H = 0 T with the incident photon energy of the (a) Co L_3-edge (778.6 eV) and (b) Cr L_3-edge (576.1 eV) for a Pt 1.5 nm/Co 0.4 nm/Au 1.0 nm/Cr_2O_3 150 nm/Pt 20 nm thickness multilayer film [3]. Upward and downward Co FM domains with several μm are visualized in Fig. 1(a). Similar contrast is observed in Fig. 1(b), indicating that a significant XMCD signal can be obtained from the interfacial Cr spin. It is noteworthy that the two-dimensional distribution is spatially coupled with the Co FM domain. Additionally, the H-dependence of XMCD intensity measured on an individual domain (not shown) revealed that the sign of exchange bias polarity is opposite for oppositely directed domains. In the following (Figs. 2 and 3), on the basis of this finding, the (quasi-) static AFM domain wall motion is explored through the magnetic domain observation of FM Co, i.e., XMCD imaging at the Co L_3-edge.

Other important but difficult issues are the switching process [3] and dynamics [4]. The switching process of magnetic materials is either coherent rotation or magnetic domain wall propagation. In a general FM substance, either switching mode can occur, depending on the size of the magnetic substance; below and above the characteristic size, which is on the order of the magnetic domain wall width, coherent rotation or magnetic domain wall propagation occurs, respectively. In the case of the AFM substance, it is not established whether a similar switching process occurs, although this is widely believed. We address this issue by directly observing the change in the magnetic domain pattern on applying a ME field. For such observation, there are many technical requirements, e.g., high magnetic field (> a few T), temperature controllability, and *in situ* E application, all of which are met by the aforementioned instrument.

Figure 2 shows the magnetic domain pattern in the remanent state, i.e., H = 0 T and E = 0 MV/m, after applying various E with constant H = +4 T. In the switching process, the newly nucleated magnetic domains are rarely observed but the expansion of the pre-existing magnetic domains are observed; the red (blue) magnetic

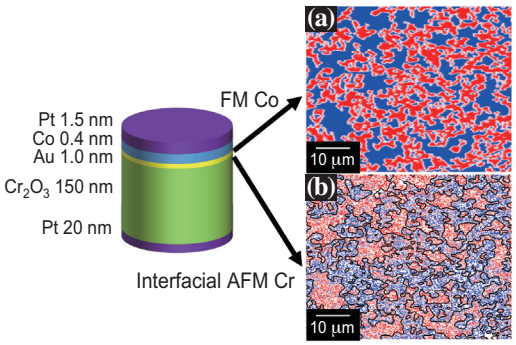

Fig. 1. Two-dimensional mapping of XMCD intensity measured at the photon energy of the Co L_3-edge (top right) and Cr L_3-edge (bottom right). Blue and red regions correspond to upward and downward magnetizations, respectively. The measurement temperature was 280 K and H during the observation was zero. In the left side of the figure, the stacking structure of the studied film is shown.

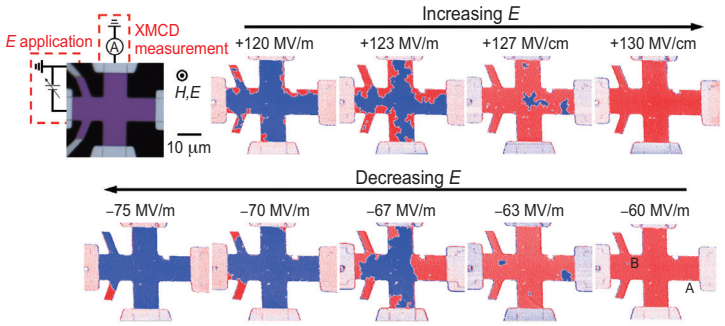

Fig. 2. Magnetic domain pattern after applying ME field, with H = +4 T and various E, showing increasing (top) and decreasing (bottom) branches of E. Observations were done at 280 K. The photon energy used for the imaging was 778.6 eV (Co L_3-edge). In the top left of the figure, an optical microscope image of the fabricated Hall device with the equivalent circuit diagram used to apply E is shown. The Hall device is 10 μm wide and 50 μm long. In this device, the 20-nm-thick Pt buffer layer and the Pt/Co/Au layer were used as the bottom and top electrodes, respectively, to apply E to the Cr_2O_3 layer. After applying E and H, both fields were removed during the XMCD measurements. A bias voltage, which is often applied to improve the signal-to-noise ratio in the TEY method, was not applied during the measurements. E and H were applied in the direction perpendicular to the film and the positive direction was defined as the direction from the substrate side to the film side.

domain expands in the increasing (decreasing) branch, which indicates that magnetic domain wall propagation is predominant. Referring to the finding in Fig. 2, we further address the ME-induced magnetic domain wall dynamics of the AFM Cr_2O_3. In contrast to the current-induced magnetic domain wall propagation in the FM materials, the propagation direction of the AFM domain wall is difficult to define by E. The direct observation of the magnetic domain pattern is a way to directly address this issue.

Figure 3 shows the evolution of the magnetic domain pattern measured at zero ME field after applying a pulsed ME field. The applied ME field condition before the domain observation is similar to that in Fig. 2 except that pulsed E with an amplitude of –133 MV/m and various widths were applied instead of DC E in the case of Fig. 2. Details of the measurement procedure can be found in our previous report [4]. Starting from the initial state, the blue magnetic domain expands with increasing pulse width. The magnetic domain wall propagation as a function of the pulse width gives the AFM domain wall velocity v driven by the ME effect: v ~22 m/s in the case of Fig. 3. v depends on the amplitude of E and the v–E relationship should yield a variety of ME-driven AFM spin/domain dynamics such as the effective Gilbert damping parameter of the AFM Cr_2O_3. To meet such growing interest, detection of the AFM order parameter without using exchange coupling with the FM moment is desirable because the low spin dynamics of the FM moment would mask the ultrafast dynamics of the AFM spin.

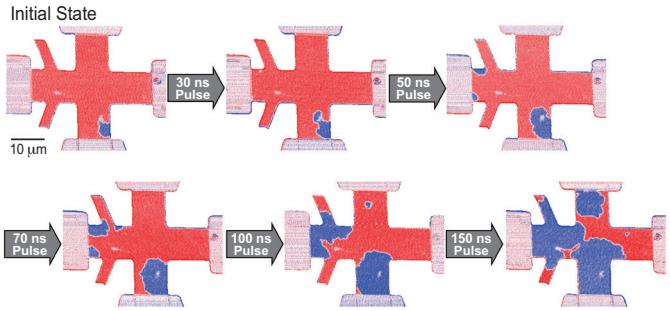

Fig. 3. Evolution of magnetic domain after applying ME field with pulse E = –133 MV/m with various pulse widths and H = +4 T. Observations were done at 280 K. The photon energy used for the imaging was 778.6 eV (Co L_3-edge). The definition of blue and red domains and the measurement sequence are similar to those of Fig. 2.

Yu Shiratsuchi

Department of Materials Science and Engineering, Osaka University

Email: shiratsuchi@mat.eng.osaka-u.ac.jp

References

[1] P. Borisov *et al.*: Phys. Rev. Lett. **94** (2005) 117203.
[2] Y. Kotani *et al.*: J. Synchrotron Rad. **25** (2018) 1444.
[3] *Y. Shiratsuchi, S. Watanabe, H. Yoshida, N. Kishida, R. Nakatani, Y. Kotani, K. Toyoki, and T. Nakamura: Appl. Phys. Lett.* ***113*** *(2018) 242404.*
[4] *Y. Shiratsuchi, H. Yoshida, Y. Kotani, K .Toyoki, T.V. A. Nguyen, T. Nakamura, and R. Nakatani: APL Mater.* ***6*** *(2018) 121104.*

Signature of rigidity transition in liquid As_2Se_3 observed by inelastic X-ray scattering

As_xSe_{1-x} is an interesting glass-forming system where the glass-forming ability is maximized for x=0.4 or As_2Se_3. This has been discussed in terms of rigidity theory, which focuses on the nearest-neighbor coordination number of the atoms, suggesting that the system will be most stable when the number of mechanical constraints per atom is equivalent to the number of spatial degrees of freedom, 3 [1], which corresponds to an average coordination number of 2.4. The idea of a rigidity transition has been used to account for the relatively high glass-forming ability of As_2Se_3, and to suggest that in the glassy state there can be a stiffness transition from inflexible to flexible structures when the average coordination number drops below 2.4.

As_2Se_3 also has interesting and typical properties as a liquid. Investigation of the local structure of liquid As_2Se_3 in a wide temperature range at high pressures [2] revealed that the average coordination number exceeded 2.4 near the melting point and *decreased* with increasing temperature, whereas, more often, the average coordination number of a liquid increases with increasing temperature. This correlates with the rather unusual semiconductor-metal transition in liquid As_2Se_3 (see the atomic configurations of crystalline and liquid As_2Se_3 in Fig.1). Usually, the semiconductor-metal transition occurs when the valence electron density increases with compression of the material at high pressures; closing the band gap and delocalization of conduction electrons are the main processes for metallization. Liquid As_2Se_3, however, acquires metallic properties during volume expansion with increasing temperature. This suggests that atomic motion induced by the thermal energy may play an important role in the semiconductor-metal transition in this liquid.

Considering these unusual properties, it is interesting to directly investigate the atomic dynamics of liquid As_2Se_3 via measurement of the dynamic structure factor, *S(Q, E)*, where *Q* and *E* are momentum and energy transfer, respectively. In particular, there was interest in the mesoscale region, corresponding to nanometer-order correlation lengths, where one may begin to see the onset of the impact of the local atomic structure.

In the present study, inelastic X-ray scattering experiments were carried out at temperatures from 1073 to 1673 K at 6 MPa and at momentum transfers *Q* from 1.6 to 11 nm^{-1} using the high-pressure apparatus installed at SPring-8 **BL35XU** [4]. Highly brilliant X-rays with high energy resolution were incident onto the sample with the scattered X-rays received by an array of analyzer crystals. The energy and momentum transfer resolutions were 1.5 meV and 0.45 nm^{-1}, respectively. The As_2Se_3 sample of 99.999% purity and 0.1 mm thickness was mounted in a single-crystal sapphire cell that was placed in a high-pressure vessel. The vessel was filled with He gas (99.999% purity) at 6 MPa to stabilize the liquid state. The background spectra were measured at 1273 K and 6 MPa using an empty cell. After background subtraction with the absorption correction and integration with respect to *E*, we deduced the normalized dynamic structure factor *S(Q,E)/S(Q)* of liquid As_2Se_3 from the observed spectra. Figure 2 shows *S(Q,E)/S(Q)* of liquid As_2Se_3 at

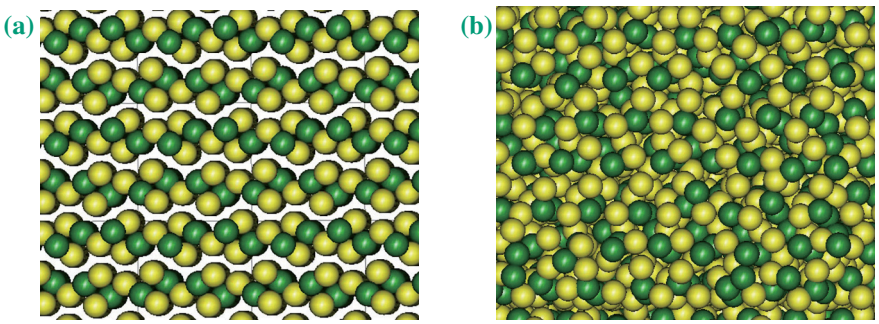

Fig. 1. Atomic configurations of As (green) and Se (yellow) in monoclinic crystalline As_2Se_3 [3] (left) and in liquid As_2Se_3 (right) near the melting point. The liquid structure was obtained by reverse Monte Carlo simulation [2].

1073 and 1473 K. At 1073 K, the inelastic excitations at 2.6 nm^{-1} merge into a broad single peak as a result of the spectrometer resolution while they are clearly separate at 2.9 nm^{-1}, indicating a discrete increase in the excitation energies between these Q values. On the other hand, the acoustic excitations at 1473 K disperse with increasing Q without such a discrete energy change. An anomaly in the acoustic mode energy at 2.7 nm^{-1} was observed below 1373 K, as shown in Fig. 3, where black circles denote the excitation energy of the model function of the damped harmonic oscillator.

The Q dependence of the excitation energy is reminiscent of an anti-crossing phenomenon in a solid. A linear chain model presenting an anti-crossing dispersion curve to the black circles is applied to describe in Fig. 3 and obtained the optimized dispersion curves indicated by the red broken lines. Comparison with structural information obtained by reverse Monte Carlo modeling of X-ray diffraction data [2] indicates that the disappearance of the anomaly at higher temperatures (>1373 K) is associated with a drop in the average coordination number, reminiscent of the threshold applicable for glass-forming in rigidity theory. Thus, the surprising jump in the dispersion in the liquid may be analogous to the stiffness transition in network glasses.

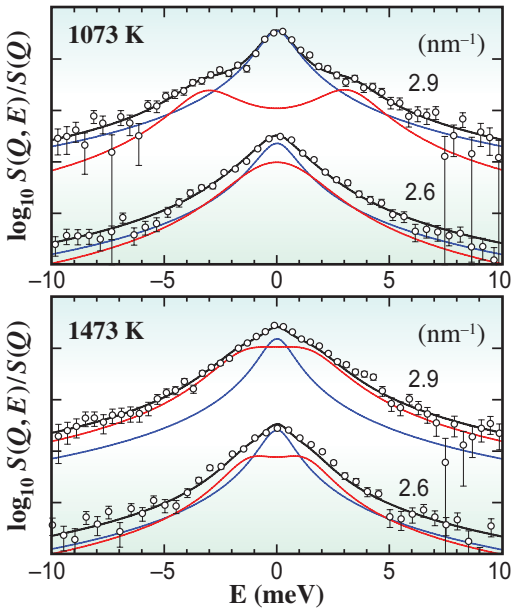

Fig. 2: $S(Q,E)/S(Q)$ of liquid As_2Se_3 at 1073 K (upper graph) and 1473 K (lower graph) at 6 MPa. Open circles and solid lines denote the experimental results and the optimized fits, respectively. Also shown are the quasielastic/Lorentzian component (blue) and inelastic excitation/damped harmonic oscillator (red) of the model function convoluted with the spectrometer resolution function.

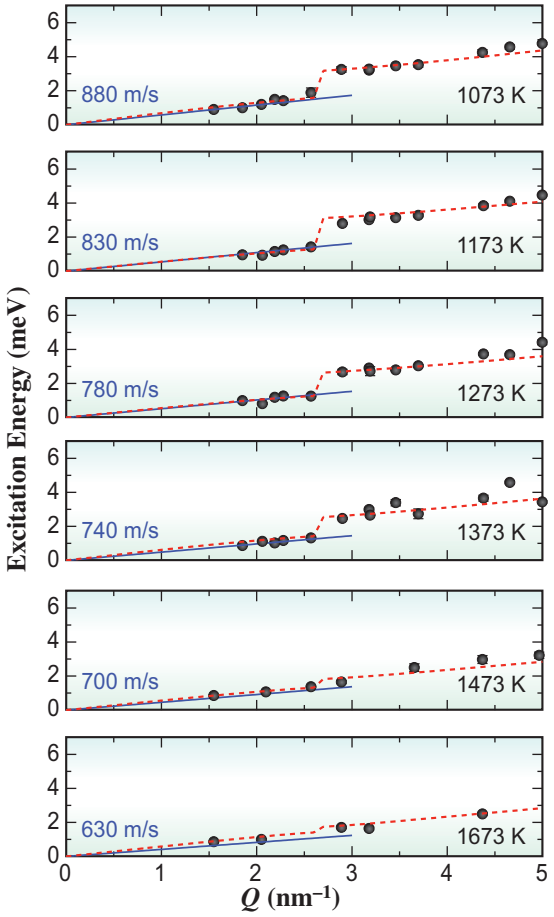

Fig. 3. Excitation energies of the acoustic mode as a function of Q at the indicated temperature. The red broken lines indicate optimized fits using a linear chain model. The energy corresponding to the ultrasonic sound speed indicated in each panel is also shown by a blue line from the origin.

Masanori Inui[a,*,†], Alfred Q. R. Baron[b] and Yukio Kajihara[a]

[a] Graduate School of Integrated Arts and Sciences, Hiroshima University
[b] Materials Dynamics Laboratory, RIKEN SPring-8 Center

*Email: masinui@hiroshima-u.ac.jp

[†] Present address: Graduate School of Advanced Science and Engineering, Hiroshima University

References

[1] J.C. Phillips: J. Non-Cryst. Solids **34** (1979) 153; M.F. Thorpe: J. Non-Cryst. Solids **57** (1983) 355.
[2] M. Inui *et al.*: J. Non-Cryst. Solids **366** (2013) 22.
[3] A.L. Renninger and B.L. Averbach: Acta Cryst. B **29** (1973) 1583.
[4] *M. Inui, A.Q.R. Baron, Y Kajihara, K. Matsuda, S. Hosokawa, K. Kimura, Y. Tsuchiya, F. Shimojo, M. Yao, S. Tsutsui, D. Ishikawa and K. Tamura: J. Phys.: Condens. Matter* ***30*** *(2018) 28LT02.*

First observation of 'superfluorescence' at extreme ultra-violet wavelengths

'Superradiance' was first introduced in 1954 [1] as arising from quantum correlations between excited atoms interacting through an electromagnetic field of wavelength λ, all located within a spatial region of dimension λ. Superradiance as initially described is difficult to realize in practice, but spontaneous emission can induce a related process in initially uncorrelated atoms, even in an extended medium (interatomic spacing comparable to λ, but excited atoms extending over a region in space much larger). This process was termed 'superfluorescence' [2]. Superfluorescence was first observed on rotational transitions in HF at microwave wavelengths [3], and subsequently at visible wavelengths following the availability of lasers [review in 4]. The initial stages of superradiance have been observed at X-ray wavelengths [5], and in diamond NV-centers [6].

In stark contrast to spontaneous emission, the peak intensity of superradiance scales as N^2, where N is the number of interacting atoms. The temporal width of the emission pulse thus scales as 1/N. N can be of the order of 10^{10}, leading to very short, intense pulsed emission. For superfluorescence, where the initial excitation is incoherent, there is a characteristic time delay for a macroscopic polarization to develop, which also scales as 1/N. Superradiant decay can completely deplete the upper level, so potentially offers a route to intense, coherent, pulsed emission with variable pulse duration and delay. However, its generation at short wavelengths presents challenges, since higher number densities are required to meet the requirement that interatomic spacing must be comparable to wavelength. Further, suitable atomic transitions are difficult to find. The lack of suitable materials for windows and optical elements at short wavelength introduces technical constraints.

We recently overcame these challenges to observe superfluorescence at vacuum ultraviolet (164 nm) and extreme ultraviolet (30.4 nm) wavelengths for the first time [7]. A suitable atomic level scheme is found in helium ions, a high density of which can be rapidly created by ionization with free-electron laser (FEL) pulses (SACLA **BL1**) at photon energies greater than the helium ionization potential of ~25 eV (Fig. 1). Since windows cannot be used, we used a pulsed valve to inject neutral helium into a small differentially-pumped gas cell with 1 mm apertures. Essentially all of the neutral helium atoms along the FEL beam's path through the gas cell could be ionized. At 24.3 nm, resonant with excitation of the 4*p* electronic state of

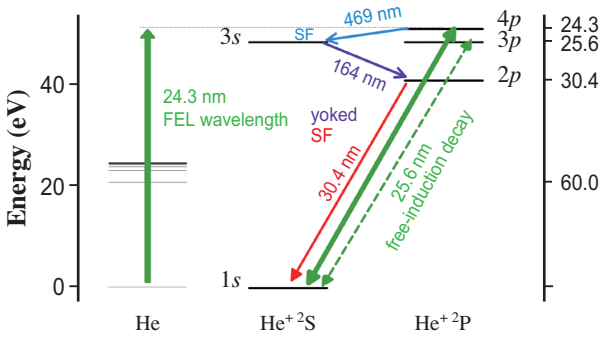

Fig.1. Partial level scheme. Helium atoms are ionized and then excited by the same FEL pulse, resonant with the 1*s*-4*p* transition in He^+. Due to the high density of excited 4*p* ions, superfluorescence occurs on the route 4*p*-3*s*-2*p*-1*s*, with the 2nd and 3rd steps 'yoked' due to the initial coherence of the 1*s*-4*p* excitation.

the ion, a high density of excited ions is created within the <100 fs pulse. This results in superfluorescent decay on the 4*p*-3*s* transition at 469 nm. Experimentally this was observed as highly-directional blue flashes of light (Fig. 2). Using a fast photodiode, it was confirmed that the pulses had temporal widths of the order of picoseconds, and picosecond delays with respect to the incident FEL pulse. This unequivocally confirms superfluorescence on this transition. Atomic population is transferred to the 3*s* state, which can undergo further superfluorescence decay (164 nm) to the 2*p* state. Observations with a grazing-incidence spectrometer (Fig. 2) confirmed highly-directional emission at this wavelength. Since superfluorescence requires a population inversion to proceed, further superfluorescence on the 2*p*-1*s* transition at 30.4 nm would not be expected. However, we also observed highly-directional emission at this wavelength (Fig. 2). Superradiant emission is only possible on this transition as *yoked* superfluorescence [8], which can occur if the initial excitation imparts sufficient coherence to the atomic system. Here, superfluorescence occurs from the 3*s* state to the 1*s* state 'through' the 2*p* state, with emission at 164 nm and 30.4 nm appearing simultaneously. While we were unable to confirm this interpretation experimentally due to the lack of detectors with both sufficient sensitivity and sufficient time resolution in the required wavelength regions, the intensity and directionality of the observed emissions strongly support our conclusions.

Further evidence is provided from semi-classical numerical simulations. We used the Maxwell-Liouville equations [9], with 16 atomic levels and time and spatial step-sizes of 6.5 as and 3.0 nm to model the propagation of 70-fs-long pulses through 50 μm of helium ions. The simulations were performed in parallel on the JAEA supercomputer. Results for a single pulse are shown in Fig. 3, where the rolling Fourier transform of the electric field at the output of the medium is plotted as a function of time. Free-induction decay is seen as a spectrally narrow tail at the 1*s*-4*p* resonant frequency. Similar emission is also seen at a wavelength of 25.6 nm, on the 1*s*-3*p* transition. Following a short delay (~3 ps), emission is seen at a wavelength of 469 nm, which can be interpreted as superfluorescence on the 4*p*-3*s* transition. Following a further delay (at t ~10 ps), emission is seen simultaneously at wavelengths of 164 nm (3*s*-2*p*) and 30.4 nm (2*p*-1*s*). This is consistent with our interpretation of yoked superfluorescence. Weaker signal can also be seen at wavelengths corresponding to four-wave mixing between the various wavelengths present in the medium, although these were not observed experimentally.

The observation of yoked superfluorescence is of particular interest since it arises due to the coherence of the exciting pulse, which for SACLA BL1 is only partial. From the point of view of applying coherent processes at short wavelengths, this is an important result. Whereas seeding technology (such as that used at FERMI) can be used to generate coherent FEL pulses at the wavelengths used here, shorter wavelength FELs still rely on the SASE process.

The extension to even shorter wavelengths presents the challenge of finding suitable level schemes and generating even higher target densities. One approach is to use nanoparticles such as clusters or superfluid liquid helium droplets, which offer number densities similar to the solid phase.

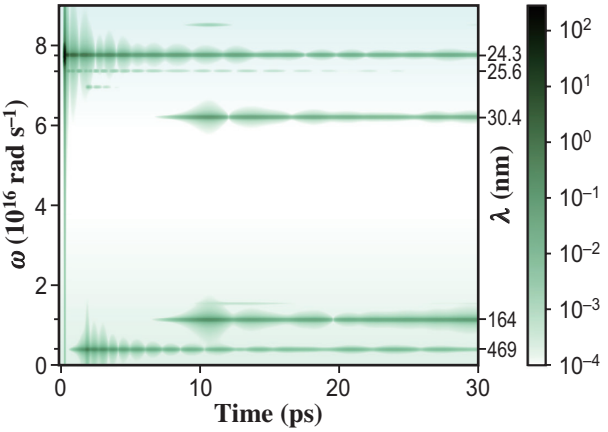

Fig. 3. Simulation results. Rolling Fourier transform (20 fs window) of the electric field at the output of the medium.

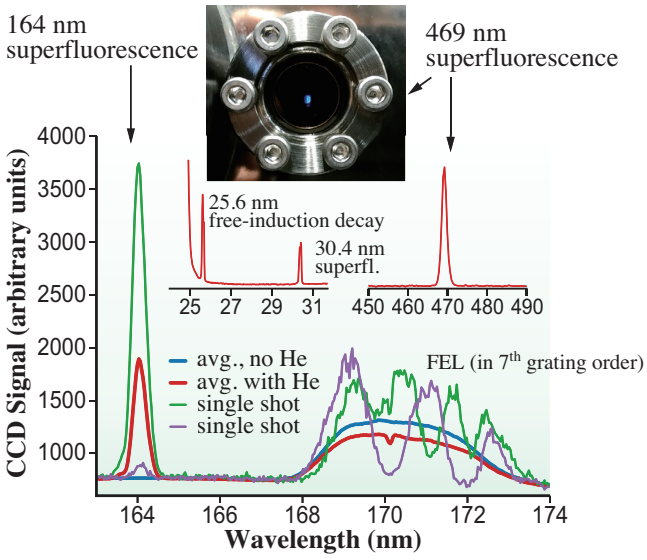

Fig.2. Overview of experimental results. Strong, highly-directional emission was observed at wavelengths of 469 nm, 164 nm, 30.4 nm, and 25.6 nm.

James R Harries[a,*], Hiroshi Iwayama[b] and Susumu Kuma[c]

[a] Synchrotron Radiation Research Centre, QST
[b] UVSOR, Institute for Molecular Science
[c] Atomic, Molecular, and Optical Physics Laboratory, RIKEN/Wako

*Email: harries@spring8.or.jp

References

[1] R.H. Dicke: Phys. Rev. **93** (1954) 99.
[2] Bonifacio and Lugiato: Phys. Rev. A **11** (1975) 1507.
[3] N. Skribanowitz *et al.*: Phys. Rev. Lett. **30** (1973) 309.
[4] Superradiance Multiatomic Coherent Emission, edited by M G Benedict (CRC Press, Bristol, Philadelphia, 1996)
[5] A.I. Chumakov *et al.*: Nat. Phys. **14** (2018) 261.
[6] A. Angerer *et al.*: Nat. Phys. **14** (2018) 1168.
[7] *J.R. Harries, H. Iwayama, S. Kuma, N. Suzuki, Y. Azuma, I. Inoue, S. Owada, T. Togashi, K. Tono, M. Yabashi and E. Shigemasa: Phys. Rev. Lett. **121** (2018) 263201.*
[8] J.H. Brownell *et al.*: Phys. Rev. Lett. **75** (1995) 3265.
[9] R. Marskar and U. Österberg: Opt. Express **19** (2011) 16784.

Object transport system mimicking the cilia of *Paramecium Aurelia*, making use of the light-controllable crystal bending behavior of photochromic diarylethene

Diarylethene derivatives are photochromic compounds whose colorless open-ring isomers undergo cyclization to the colored closed-ring isomers upon UV irradiation and revert to the original open-ring isomers by cycloreversion reaction upon visible light irradiation. The excellent thermal stability of both isomers, the high photochromic sensitivities and the ability to undergo reversible photochromic reactions even in the crystalline state [1] make them among the most promising photochromic molecules.

In 2007, the photoinduced bending phenomena of diarylethene crystals were reported in Nature [2]. The photoinduced microscopic movements, i.e., photoisomerization between open- and closed-ring isomers, induced the macroscopic movement of the bending behavior of the diarylethene crystals. In the paper, a crystal of diarylethene threw a ball upon UV irradiation.

We also reported the photoinduced bending behavior of other diarylethene derivatives the following year [3]. Single crystals of naphthyl-substituted derivative **1o** prepared by sublimation also showed

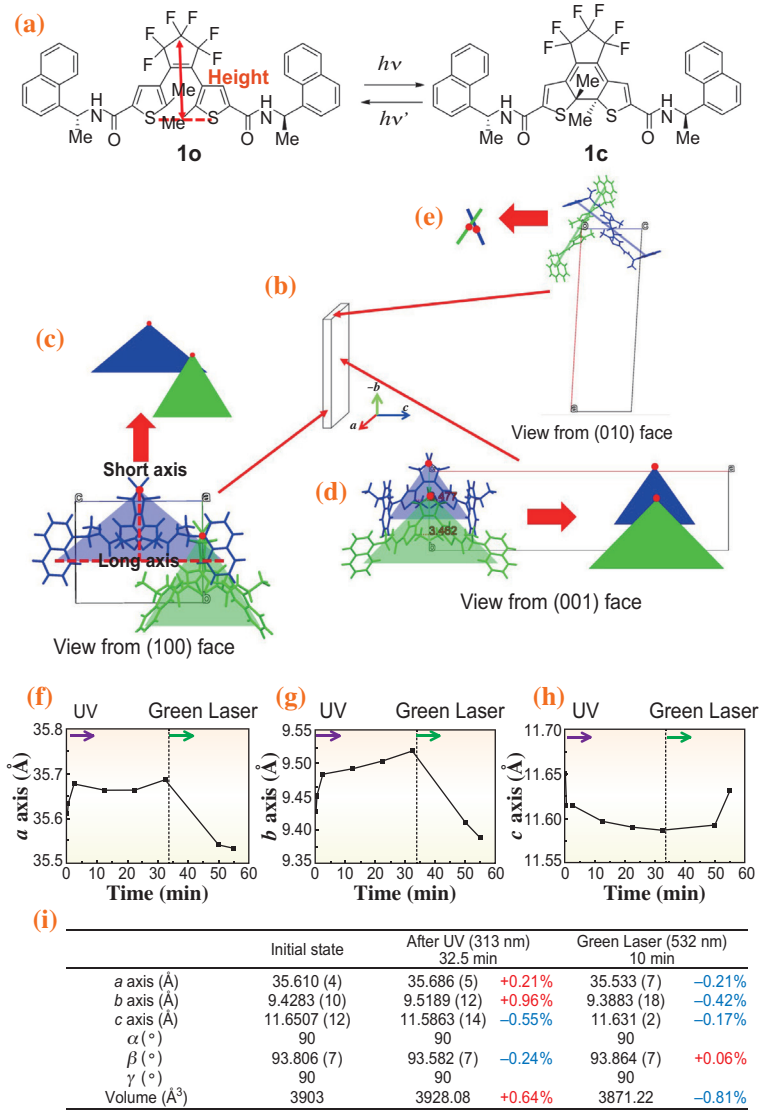

(i)

	Initial state	After UV (313 nm) 32.5 min		Green Laser (532 nm) 10 min	
a axis (Å)	35.610 (4)	35.686 (5)	+0.21%	35.533 (7)	–0.21%
b axis (Å)	9.4283 (10)	9.5189 (12)	+0.96%	9.3883 (18)	–0.42%
c axis (Å)	11.6507 (12)	11.5863 (14)	–0.55%	11.631 (2)	–0.17%
α (°)	90	90		90	
β (°)	93.806 (7)	93.582 (7)	–0.24%	93.864 (7)	+0.06%
γ (°)	90	90		90	
Volume (Å^3)	3903	3928.08	+0.64%	3871.22	–0.81%

Fig. 1. Molecular packing of diarylethene **1o** in the crystal prepared by sublimation, and the size changes of the unit cell upon alternate irradiation with UV and visible light. **(a)** Molecular structural changes of diarylethene **1o**, **(b-e)** molecular packing of two conformers (illustrated with green and blue triangles) of **1o** in the unit cell, (**f-i**) size changes of unit cell of **1o** upon alternate irradiation with UV and visible light.

reversible bending upon alternate irradiation with UV and visible light. However, the mechanism of the bending motion was unclear because the crystals prepared by sublimation were thin (thickness ~2 μm).

The thin platelet crystals of **1o** (Fig. 1(a)) were analyzed at SPring-8 **BL02B1** and **BL40XU** beamlines. The data obtained showed that the two conformers of **1o** are aligned along the long axis of the crystals, as shown in Figs. 1(b)–1(e). It is well known that when the short axis (height) of a diarylethene molecule in the crystal is parallel to the long axis of the crystal, the crystals exhibit bending motion away from the incident UV light [4] owing to the elongation of the height of the assumed triangular shape of the molecule (Figs. 1(b)–1(e)). Upon irradiation with UV light from the (001) surface, the *a* and *b* axes of the unit cell expand, inducing the bending of the crystal away from the incident UV light (Figs. 1(f)–1(i)). Then, upon irradiation with visible light, the crystal returned to the original straight shape because of shrinkage along the *a* and *b* axes (Figs. 1(f)–1(i)). The same bending behavior was observed when the light was irradiated onto the (100) surface. This behavior agrees with the molecular packing in the crystal.

We have designed an object-transport system made from vertically arranged diarylethene crystals (Fig. 2(a)) of **1o** [5]. The surface covered with bending crystals was fabricated in three steps. (1) By the sublimation of **1o**, only dot-shaped structures were formed on the substrate. (2) To make nucleation sites for crystal growth, magnetron sputtering with Au-Pd alloy was performed on the dot-shaped structures. (3) Using this dotted surface covered with the Au-Pd alloy as a target substrate for sublimation, we obtained thin platelet crystals of **1o** on the substrate.

We demonstrated the transport using a polystyrene bead (PB) (average diameter 1 mm) as the target object by irradiating UV and visible light from various directions. As shown in Figs. 2(b)–2(e), the motion of the PB on the thin platelet crystals was controlled at will by changing the direction of applied UV or visible light. First, UV light (λ=254 nm) was applied from the top of the screen and the PB moved downward, as a result of the cooperative bending of the crystals (Fig. 2(b)). Upon irradiation with visible light orthogonal to the surface, the PB returned upward as the bended crystals recovered to their original straight form (Fig. 2(c)). Without light irradiation, the ball did not move (Fig. 2(d)). Then UV light was irradiated from the bottom of the screen, causing the ball to move upward, indicating that the transport direction corresponded to the direction of UV incidence (Fig. 2(e)). Consequently, we succeeded in transporting the PB in any desired direction by photoirradiation. This smart surface will be applicable to remote-controlled object transport in various environments and holds potential for the development of soft robots.

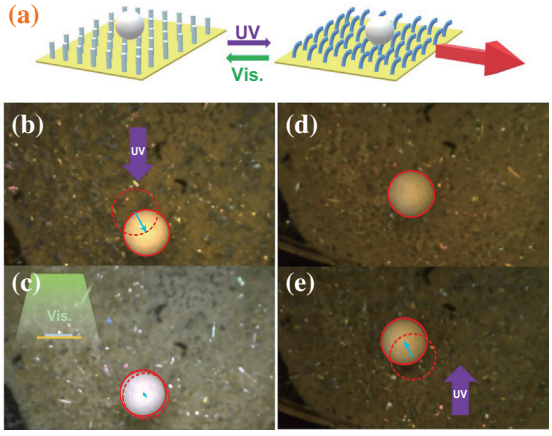

Fig. 2. **(a)** Illustration of photoinduced object transport model consisting of photoinduced bending crystals. **(b)** A polystylene bead with 1 mm diameter moved downward upon UV irradiation from the top of the screen. **(c)** Upon visible light irradiation orthogonal to the surface, the ball moved upward. **(d)** Without photoirradiation, the ball did not move. **(e)** When UV light was irradiated from below, the ball moved upward. The original position of the bead in each panel is indicated by a red dashed circle. The displacement vector is shown by a light blue arrows.

Kingo Uchida*, Ryo Nishimura and Ayako Fujimoto

Department of Materials Chemistry, Ryukoku University

*Email: uchida@rins.ryukoku.ac.jp

References

[1] M. Irie *et al.*: Chem. Rev. **114** (2014) 12174.
[2] M. Irie *et al.*: Nature **446** (2007) 778.
[3] K. Uchida *et al.*: Chem. Commun. (2008) 326.
[4] M. Morimoto, M. Irie: J. Am. Chem. Soc. **132** (2010) 14172.
[5] *R. Nishimura, A. Fujimoto, N. Yasuda, M. Morimoto, T. Nagasaka, H. Sotome, S. Ito, H. Miyasaka, S. Yokojima, S. Nakamura, B.L. Feringa and K. Uchida: Angew. Chem. Int. Ed.* ***58*** *(2019) 13308.*

Supramolecular polymerization in liquid crystalline media enables modular approach to multifunctional core–shell columnar coassembly

Supramolecular polymerization offers an enormous opportunity to develop soft materials with a dynamic, adaptive, reconfigurable, and recyclable nature [1]. These characteristics are derived from noncovalently connected monomeric units that can be associated and dissociated, reversibly triggered by external environments such as heat, light, and chemicals. While recent progress in the field of supramolecular polymerization has been mainly made in solution-phase studies, we were interested in the use of liquid crystalline (LC) phases as media for supramolecular polymerization. When a disk-shaped chiral monomer, ^{OCB}**Disk**$_{NH}$* (Fig. 1), is noncovalently polymerized in a nematic LC medium comprising rod-shaped molecules of 4-cyano-4'-pentyloxybiphenyl (5OCB) (Fig. 1), the nematic LC phase undergoes "structural order-increasing" mesophase transition into a highly elaborate, single columnar mesophase having a discrete core–shell geometry (Fig. 2(a)) [2].

^{OCB}**Disk**$_{NH}$* (Fig. 1) is the derivative of a chiral benzenetricarboxamide (BTA), which is known to form one-handed helical supramolecular polymers in solution via amide-mediated triple hydrogen bonds (H-bonds). The hydrocarbon side chains of ^{OCB}**Disk**$_{NH}$* are appended with an oxycyanobiphenyl (OCB) terminus. This terminal OCB serves as a compatibilizer with 5OCB molecules (Fig. 1), since disks and rods are generally incompatible in coassembly: the former tends to pile up in a face-to-face manner, while the latter tends to orient parallel to one another. Such compatibilizing units are the key to integrating the supramolecular polymer of ^{OCB}**Disk**$_{NH}$* with the nematic LC medium of 5OCB.

A mixture of ^{OCB}**Disk**$_{NH}$* and 5OCB (molar ratio, 1/6) was heated to its isotropic melting temperature and then allowed to cool, where 5OCB is integrated with supramolecularly polymerized ^{OCB}**Disk**$_{NH}$*. Figure 2(d) shows the synchrotron X-ray diffraction (XRD) profile obtained at SPring-8 **BL44B2**. It exhibits sharp and intense peaks in the low-angle region, while the high-angle region exhibits only a broad diffraction peak. This profile can be assigned to a columnar LC phase with a centered rectangular *c*2*mm* symmetry. Together with spectroscopic studies, we revealed that each column comprises helical stacks of H-bonded polymeric ^{OCB}**Disk**$_{NH}$* in its core, wrapped by a helical shell consisting of self-assembled 5OCB (Fig. 2(a)).

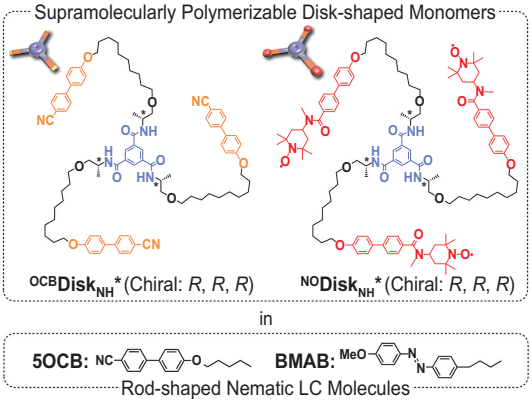

Fig. 1. Molecular structures of disk-shaped monomers and rod-shaped LC molecules.

Our core–shell columnar LC material showed unique dynamic behaviors in response to an applied electric field (E-field). In contrast to conventional single-component columnar LC phases that are rigid and barely orientable by electrical stimuli, our disk/rod multicomponent columnar LC material rapidly responded electrically, resulting in unidirectional columnar ordering (Fig. 3(a)). Despite its rapid E-field responsiveness, the unidirectional order was maintained for several days after turning off the applied

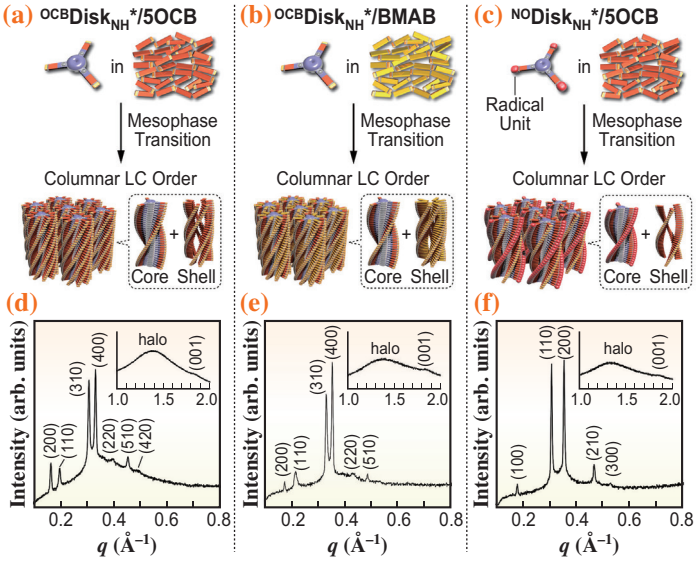

Fig. 2. **(a, b, c)** Schematic representations of the supramolecular polymerization of disk-shaped monomers in LC medium comprising rod-shaped molecules, resulting in a "structural order-increasing" mesophase transition into columnar LC phases with a helical core–shell geometry. **(d, e, f)** Synchrotron XRD profiles of columnar LC materials with core–shell geometries.

E-field. The columnar orientation could also be redirected between parallel and perpendicular to the direction of applied direct-current (DC) and alternating-current (AC) E-fields, respectively (Fig. 3(a)). Figures 3(b) and 3(c) show two-dimensional XRD profiles obtained at SPring-8 **BL45XU**, where two distinct diffraction arcs, indexed as the (200) and (400) planes of the rectangular columnar geometry, appeared in the equatorial direction under the DC E-field (Fig. 3(b)), whereas they appeared meridionally under the AC E-field (Fig. 3(c)). These profiles indicate the parallel and perpendicular orientations of the core–shell columns relative to the DC and AC E-field directions, respectively. We proposed that such rapid electrical reorganization occurs through electrical reconstruction, where the LC columns can dynamically dissociate into the core- and shell-forming molecules and reconfigure into the columns in their electrically preferred direction. Note that our core–shell columnar LC material simultaneously exhibits both high structural order and high stimuli responsiveness, which is highly desirable for sophisticated functional materials.

Furthermore, this system is flexible and adaptive enough to incorporate molecules other than 5OCB to form multifunctional core–shell columnar LCs. When this supramolecular polymerization of ^{OCB}**Disk**$_{NH}$* was carried out in a nematic LC medium composed of a rod-shaped azobenzene derivative, 4-butyl-4'-methoxy azobenzene (BMAB) (Fig. 1), a core–shell columnar LC material with a rectangular geometry, as revealed by XRD at SPring-8 BL44B2, having a photoisomerizable shell was formed (Figs. 2(b) and 2(e)). This modularly obtained columnar mesophase was responsive not only electrically but also optically; it underwent a reversible phase transition between columnar and isotropic phases when photoirradiation was turned off and on. The optoelectrically responsive columnar LC material was incorporated into an LC-based rewritable "AND" logic gate device, where the columnar structure can be quickly reorganized only when the E-field and UV light are simultaneously applied (Fig. 3(d)).

The potential of our modular synthetic approach to multifunctional core–shell columnar LC materials was further extended by utilizing a monomer of ^{NO}**Disk**$_{NH}$*, which bears a sterically bulky nitroxyl radical in its side chains (Fig. 1) [3]. Similar to the case of ^{OCB}**Disk**$_{NH}$* and 5OCB, the supramolecular polymerization of monomeric ^{NO}**Disk**$_{NH}$* in nematic 5OCB afforded a single mesophase with a core–shell columnar geometry (Figs. 2(c) and 2(f)). The columnar orientation of this single LC phase can be redirected electrically and magnetically into parallel and perpendicular directions, respectively, to the applied fields. The abovementioned examples demonstrated that we can easily replace either the core or shell part of the core–shell columnar LC coassemblies with different molecular components by simple mixing. Such a unique feature is conferred by the multicomponent coassembly of functional molecules by supramolecular polymerization in an LC medium. This design principle will shed light on the exploration of supramolecular soft materials with advanced functions and emergent properties.

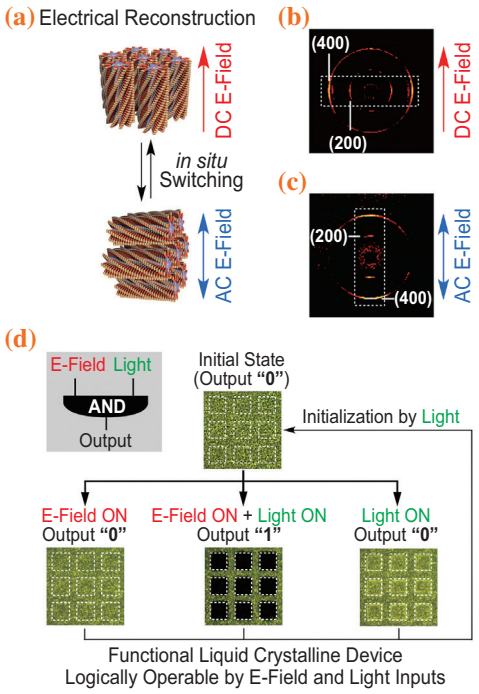

Fig. 3. **(a)** Schematic representations and **(b, c)** 2D-XRD profiles of electrical reconstruction behaviors of ^{OCB}**Disk**$_{NH}$*/5OCB, where the core–shell LC columns can be oriented parallel and perpendicular to the directions of applied DC and AC E-fields, respectively. **(d)** Polarized optical micrographs of LC-based optoelectrically rewritable "AND" logic gate operation based on ^{OCB}**Disk**$_{NH}$*/BMAB upon application of a DC E-field and/or upon irradiation with UV light with a lattice-patterned photomask. Dashed squares represent areas exposed to UV light, whereas the entire area was exposed to the E-field.

Keiichi Yano[a], Yoshimitsu Itoh[a,*] and Takuzo Aida[a,b]

[a] Department of Chemistry and Biotechnology, The University of Tokyo
[b] RIKEN Center for Emergent Matter Science/Wako

*Email: itoh@macro.t.u-tokyo.ac.jp

References

[1] T. Aida *et al.*: Science **335** (2012) 813.
[2] *K. Yano, Y, Itoh, F. Araoka, G. Watanabe, T. Hikima and T. Aida: Science **363** (2019) 161.*
[3] K. Yano *et al.*: J. Am. Chem. Soc. **141** (2019) 10033.

Single-crystal-like chiral organic droplets exhibiting unidirectional rotating sliding

Bridging the gap between the nanoscale (e.g., molecules) and macroscopic (e.g., materials that can be taken in the hand) words is a key issue in science and technology. For instance, the construction of organic materials with ultralong-range structural order on a scale of several millimeters or even several centimeters, i.e., beyond the nanometer scale that can be achieved by general molecular self-assembly, is one of the ultimate goals of soft materials science and engineering as well as thin-film device technology. Furthermore, if it becomes a reality, it might lead to discoveries of unknown behaviors of molecules in the condensed phase.

Here, we report a surprising finding of a very unique soft material that exhibits not only three-dimensional (3D) structural integrity like a single crystal but also fluidity [1]. In general, single crystals have a well-defined polyhedral shape and consist of a continuous and regular assembly of 3D unit cells [2]. However, when heated to their melting temperature and subsequently cooled, organic molecules generally solidify into polycrystals with multiple grain boundaries. Even for a liquid crystal, its macroscopic entity usually comprises many discontinuous microdomains, with the exception of a nematic phase [3]. Unlike those materials, our material can be obtained as a millimeter-size macroscopic droplet by the spontaneous assembly of a molecule upon simply heating a bulk solid sample to the melting temperature and subsequently cooling.

The structure of the obtained droplets is characterized by high positional and orientational ordering and 3D structural integrity similar to that of single crystals. One molecule that shows such a superb self-assembly property is a discotic triphenylene derivative with six chiral 2-pentyl groups as side chains (Fig. 1(a)). When a bulk sample of an enantiomerically pure molecule was placed in a glass capillary (Fig. 1(b)) and exposed to an X-ray beam at SPring-8 **BL45XU** at the mesophase temperature, regularly arranged diffraction spots clearly appeared in the resulting through-view two-dimensional (2D) XRD image (Fig. 1(b)). This molecule exhibits a single-domain mesophase in a size regime greater than 1 mm, where 2D sheets, formed by the herringbone-like packing of the triphenylene core, stack into a multilayer structure with a one-dimensional (1D) structural correlation, resulting in 3D periodic order (Figs. 1(b,c)). The mesophase was identified as the H* phase (i.e., chiral H phase), which has never been reported even for the very widely investigated rod-shaped liquid-crystalline molecules.

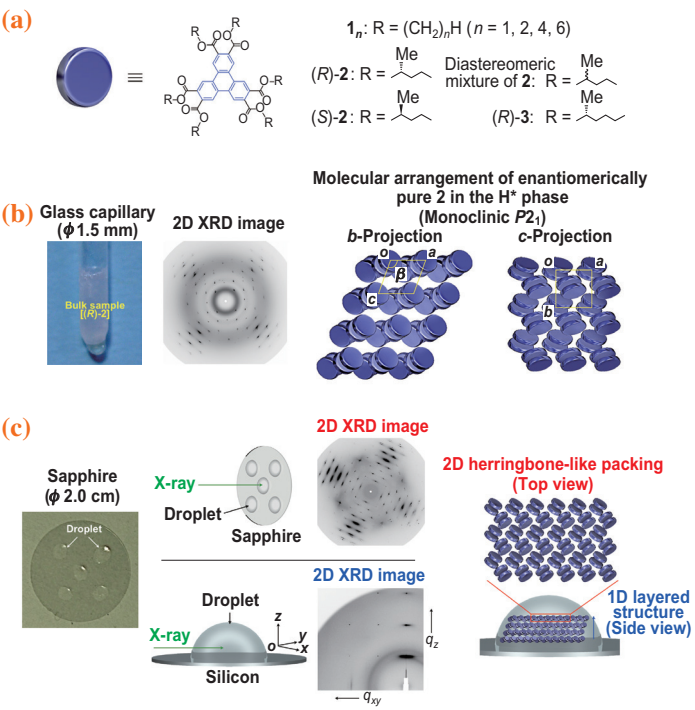

Fig. 1. **(a)** Chemical structures of triphenylenes. **(b)** Photograph, 2D XRD image, and schematic illustration of the arrangement of the triphenylene core of enantiomerically pure **2** in its H* phase with a monoclinic $P2_1$ space-group symmetry. **(c)** Photograph, 2D XRD images, and schematic illustration of the arrangement of enantiomerically pure **2** in a droplet.

Surprisingly, under the force of gravity, the droplet can flow without impairing the internal 3D structure. In common sense, crystals, in which the position and orientation of the constituent elements are rigorously determined, do not show fluidity. Plastic crystals, in which the constituent molecules are rotating but fixed at their positions, do not generally behave like a fluid. In liquid crystals that exhibit fluidity, although the constituent molecules have orientational order, their positions are not fixed owing to translational and rotational motion. According to this general notion of the phases of organic materials, the present molecular assembly is surprising: it exhibits flowability despite its well-defined positional and orientational order. X-ray imaging using a synchrotron radiation X-ray beam (beamline BL45XU) showed that under the force of gravity, droplets of this chiral triphenylene in the mesophase can flow without impairing the internal structure while unidirectionally rotating clockwise or

counterclockwise in accordance with the chirality of the side chains (Fig. 2(a), bottom).

The intriguing fluid nature allowed us to reveal the occurrence of synchronous and collective asymmetric molecular motion controlled by small molecular chirality. This result demonstrates that the "small" point chirality of a molecule can control the movement direction of the "macroscopic" molecular assembly. Rheological measurements indicated that the unidirectional rotational flow behavior originates from the difference in yield stress between the enantiomers. Furthermore, the chiral triphenylene assembly was found to possess very unusual rheological properties that exhibit comparable storage and loss elastic moduli at values greater than 10^4 Pa (Fig. 3). This delicate balance between elasticity and viscosity accounts for the unique fluid nature of the droplet.

We assume that the "2D + 1D" structure is essential for both the spontaneous formation of the single-crystal-like droplet and the macroscopic asymmetric collective motion of the molecules in the H* phase. In the past, we reported that a large-area single-crystalline order was achieved in layered materials in which constituent molecules assemble into a sheet with a 2D structural correlation [4,5]. This structural pattern holds true for the order in the H* phase of the molecules. The 1D structural correlation between the 2D sheets also plays a role in the collective molecular motion with enantiospecific unidirectional rotation (Fig. 2(b)).

The discovery of the unprecedented soft material that exhibits spontaneous ultralong-range ordering as well as synchronous and collective asymmetric movement will update the fundamental understanding of the structure formation, motility, and phase of organic materials.

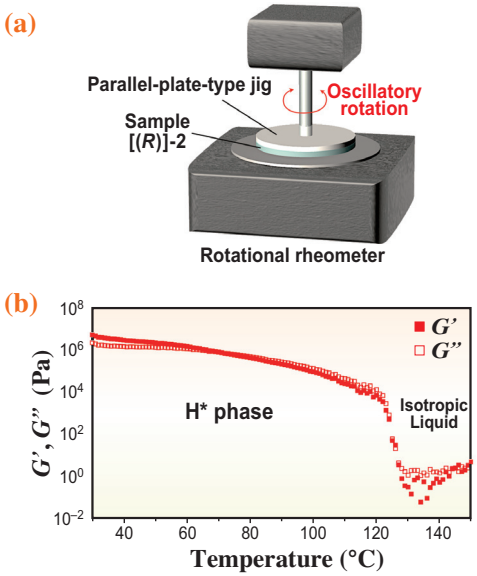

Fig. 3. **(a)** Schematic illustration of a rheometer equipped with a parallel-plate jig for the dynamic viscoelasticity measurement of (*R*)-**2**. **(b)** Temperature dependence of the storage elastic modulus (*G'*) and loss elastic modulus (*G"*) of (*R*)-**2**.

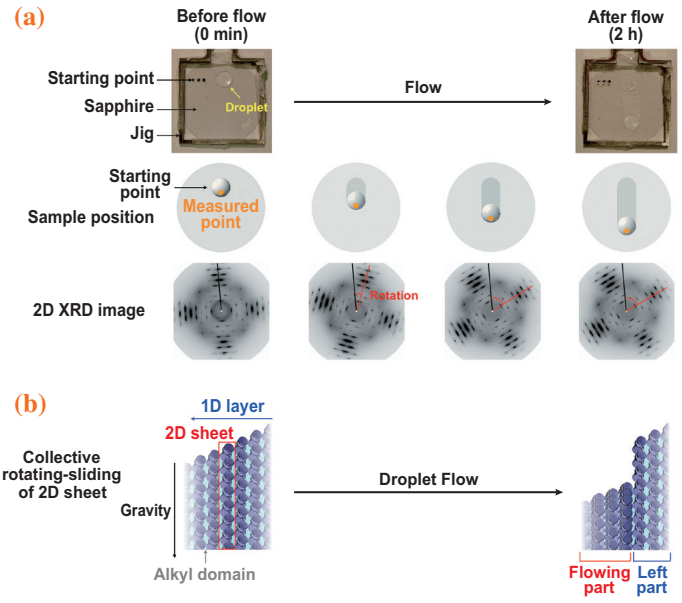

Fig. 2. **(a)** Photographs and 2D XRD images of (*R*)-**2** droplets on a vertical sapphire substrate before and after flow. **(b)** Schematic illustration of the rotating-sliding motion in a sliding droplet.

Takashi Kajitani

Suzukakedai Materials Analysis Division,
Tokyo Institute of Technology

Email: kajitani.t.ab@m.titech.ac.jp

References

[1] *T. Kajitani, K. Motokawa, A. Kosaka, Y. Shoji, R. Haruki, D. Hashizume, T. Hikima, M. Takata, K. Yazawa, K. Morishima, M. Shibayama, T. Fukushima: Nat. Mater.* ***18*** *(2019) 266.*
[2] T. Hahn: International Tables for Crystallography, Vol. A: Space-Group Symmetry 5th Ed. (Kluwer Academic, Dordrecht, 2002).
[3] I.W. Stewart: in Handbook of Liquid Crystals Vol. 1, 2nd Ed. (ed. J.W. Goodby *et al.*) Ch. 4 (Wiley, Weinheim, 2014).
[4] N. Seiki *et al.*: Science **348** (2015) 1122.
[5] T. Yokota *et al.*: Nat. Nanotechol. **13** (2018) 139.

Determination of 3D local structures of dopant in heavily phosphorus-doped diamond

Diamond is an important material not only for its beauty as a gem, but also for its excellent properties such as high hardness, high heat resistance, and good insulating performance. It is a promising material for realizing innovative devices, such as next-generation power devices and quantum sensors, because diamond becomes a high-performance semiconductor upon impurity doping. For device applications, it is necessary to introduce electron (n-type) or hole (p-type) carriers into diamond by adding other elements to make it conductive. Boron is an effective additive element for p-type diamond, whereas nitrogen has been found to be less effective owing to its high activation energy. Instead of nitrogen, phosphorus is used for obtaining n-type diamond and much effort has been devoted to improving the conducting properties of P-doped diamond [1].

When doped atoms are incorporated into substitution sites, electric conduction can be obtained. However, theoretical studies have predicted that some of the added phosphorus atoms, incorporated into the diamond crystal with an atomic arrangement, inhibit conduction [2]. Experimentally, high-resolution core-level photoemission spectroscopy demonstrated that there are two P chemical sites [3]. However, until now, the local structure of the P dopant has not been determined experimentally owing to the lack of appropriate research methods.

Photoelectron holography (PEH), performed with high-intensity/-resolution soft X-rays at SPring-8 and a high-resolution photoelectron analyzer, has made it possible to study the chemical-site-dependent local structure of impurity-doped semiconductors with low concentrations of impurity atoms. In the core-level photoelectron angular distribution, namely, the photoelectron hologram, there is an interference pattern between two types of photoelectron wave (Fig. 1): in one type, waves come directly from the atom (emitter) and in the other type, waves are scattered by neighboring atoms (scatterer). Since the photoelectron hologram reflects the local crystal structure around the atom where photoexcitation takes place, a three-dimensional (3D) atomic image can be directly reconstructed from the photoelectron hologram. This is an excellent point of PEH, making it highly superior to conventional methods of local structure study, such as EXAFS. Moreover, PEH enables the detection of the locations of dopant atoms in crystallographically inequivalent sites of elemental samples and the orientation of dopant-related complexes.

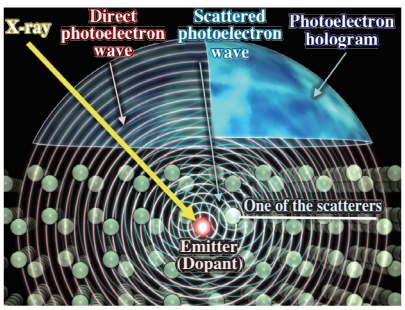

Fig. 1. Schematic illustration of photoelectron holography.

A homoepitaxial heavily P-doped (111) diamond film was fabricated by microwave-plasma-assisted chemical vapor deposition (MPCVD). The P concentration was 1×10^{20} cm^{-3} (0.06 at.%), which was determined by secondary ion mass spectroscopy. The film surface used for the PEH measurements was cleaned using H_2 plasma, thereby providing a H-terminated film. To reduce the number of adsorbed molecules on the surface, the sample was annealed *in situ* at ~500°C under ultrahigh vacuum before the measurements. PEH measurements for C 1*s* and P 2*p* were performed at SPring-8 **BL25SU** using a Scienta DA 30 electron analyzer with a photon energy of 700 eV. The energy resolution was set to approximately 200 meV. The base pressure of the PES chamber was better than 5×10^{-8} Pa. The chemical potential of the sample was determined from the Fermi edge of the molybdenum substrate in electrical contact with the sample. All measurements were performed at room temperature to prevent charging.

Figure 2 shows photoelectron holograms for two phosphorous chemical sites (components α and β) of heavily P-doped diamond (yellow), together with simulated holograms obtained using theoretical local structure models. For component α, 3D atomic images reconstructed using the scattering pattern extraction algorithm with L_1-linear regression [4] are also shown in Fig. 3. The reconstructed atomic images are located at the expected positions of the carbon atoms in the diamond crystal structure (large and small circles). This indicates that P atoms of component α are located at substitution site of the diamond crystal. Diamond crystal contains two crystallographically inequivalent sites, which we call sites A and B (see Fig. 3(c)). The observed hologram is the sum of two holograms considering sites A and B to be emitters. Expected positions of carbon atoms viewed from sites A and B are denoted with the large and small circles,

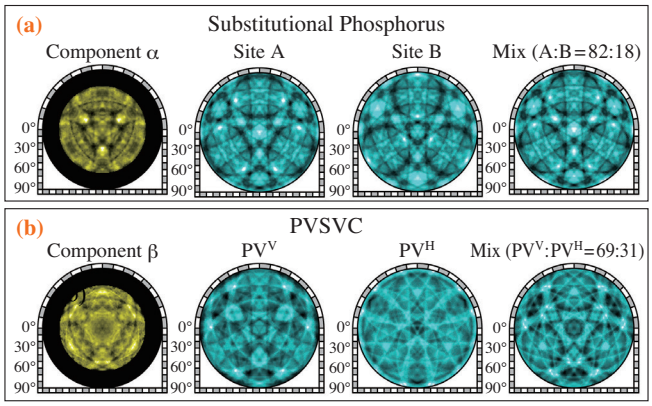

Fig. 2. Experimental (yellow) and simulated (blue) photoelectron holograms for components **(a)** α and **(b)** β of P 2*p* core level spectra of heavily P-doped diamond. For the simulated holograms of substitutional P, holograms viewed from sites A and B as well as their weighted sum are shown. For the simulated holograms of PVSVC, holograms of different orientations (PV^V and PV^H) and their weighted sum are shown.

respectively. Interestingly, the reconstructed images are observed mainly in the site A position, which is different from that in the C 1*s* reconstructed image (Fig. 3(b)). This indicates that doped P atoms are preferentially incorporated into site A of the diamond crystal (Fig. 4(a)). The ratio of site occupation can be obtained by reproducing the experimental hologram with the weighted sum of two simulated holograms for sites A and B (Fig. 2(a)). We obtained the ratio of 82:18 for sites A and B occupations. We speculate that this preferential occupation of site A stems from the CVD growth process.

For component β (Fig. 2(b)), we found that the experimental hologram looks very different from that of component α, indicating that the P atoms in this chemical site are located differently from those in component α. By considering the proposed local structure models, we found the phosphorus-vacancy (V) splitting vacancy complex (PVSVC) to be the most probable candidate. In PVSVC, a P atom is located in the middle of the bond between two adjacent carbon atoms, but the two carbon atoms are removed to form vacant sites (Fig. 4(b)). This assignment is further confirmed from the similarity of the experimental and simulated holograms. To reproduce the experimental hologram, the sum of simulated holograms of PV^V and PV^H ($=PV^{H1}+PV^{H2}+PV^{H3}$) (see Fig. 4(b) for geometrical configurations) with the ratio of 69:30 was used. This deviates from the expected value of 1:1, indicating the preferential orientation of the V-P-V direction parallel to [111].

Thus, the high-resolution PEH was used to determine the local structures of the two P chemical sites, with information on the crystal site of the substitutional P and the orientation of the PVSVC. Such information is valuable for understanding the atomistic mechanism of diamond thin-film growth during CVD and can be used to align the orientation of functional complexes.

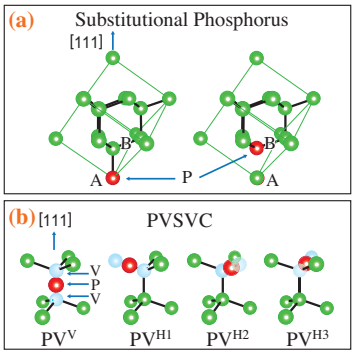

Fig. 4. **(a)** Crystal sites A and B in the diamond structure. **(b)** Local structures and orientations of PVSVC.

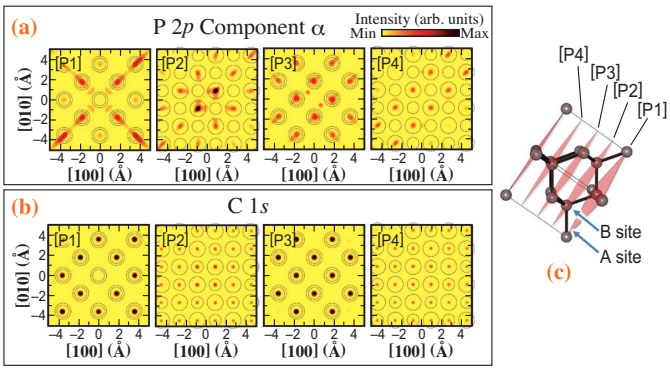

Fig.3. Cross sections of reconstructed atomic images at different z values for **(a)** component α of P 2*p* and **(b)** C 1*s*. **(c)** The diamond crystal structure and the planes of reconstructed atomic images shown in (a) and (b).

Takayoshi Yokoya[a,*], Hiromitsu Kato[b] and Tomohiro Matsushita[c,d]

[a] Research Institute for Interdisciplinary Science, Okayama University
[b] Advanced Power Electronics Research Center, National Institute of Advanced Industrial Science and Technology
[c] Japan Synchrotron Radiation Research Institute (JASRI)
[d] Division of Materials Science, Nara Institute of Science and Technology

*Email: yokoya@cc.okayama-u.ac.jp

References

[1] H. Kato *et al.*: Appl. Phys. Lett. **93** (2008) 202103.
[2] R. Jones *et al.*: Appl. Phys. Lett. **69** (1996) 2489.
[3] H. Okazaki *et al.*: Appl. Phys. Lett. **98** (2011) 082107.
[4] T. Matsushita *et al.*: Electron. Spectrosc. Relat. Phenom. **178-179** (2010) 195.
[5] *T. Yokoya, K. Terashima, A. Takeda, T. Fukura, H. Fujiwara, T. Muro, T. Kinoshita, H. Kato, S. Yamasaki, T. Oguchi, T. Wakita, Y. Muraoka and T. Matsushita: Nano Lett.* ***19*** *(2019) 5915.*

Tracking multiple components of a nuclear wavepacket in photoexcited Cu(I)-phenanthroline complex using ultrafast X-ray spectroscopy

The mixing of electronic and vibrational wavefunctions has a substantial impact on ultrafast non-adiabatic chemical reactions owing to the breakdown of the adiabatic Born-Oppenheimer approximation at the conical intersections of multidimensional potential energy surfaces. This means that one should disentangle the coupling between electronic and nuclear degrees of freedom to understand the underlying photoreaction mechanism. The coupled electronic and vibrational energy flows can be explored by tracking a nuclear wavepacket that propagates along the reaction pathway and finally dissipates the excess energy into various electronic and nuclear degrees of freedom. In the last four decades, the time evolution of the nuclear wavepacket has been studied with pump-probe optical spectroscopies. However, although these methods can capture spectral signatures arising from specific vibrational motions, it is often difficult to reveal nuclear movements of polyatomic molecules with a sub-angstrom resolution owing to the lack of atomic structural sensitivity.

Structural information at the atomic level can be obtained by time-resolved X-ray absorption near edge structure (TR-XANES). This X-ray technique is sensitive to the local structural dynamics in the close vicinity of the absorbing atom and applicable to the investigation of the ultrafast dynamics of small systems without long-range order, e.g., ligated transition metal complexes in solution phase. The recent advent of X-ray free-electron lasers (XFELs) has enabled TR-XANES to achieve both an unprecedentedly high signal-to-noise ratio and high time resolution, and consequently allows tracking of the nuclear wavepacket.

Here, we describe the femtosecond (fs) TR-XANES study [1] of a prototypical transition metal complex, $[Cu(dmphen)_2]^+$ (dmphen = 2,9-dimethyl-1,10-phenanthroline), dissolved in acetonitrile. Previous studies [2,3] revealed that after the excitation of $[Cu(dmphen)_2]^+$ into the metal-to-ligand-charge-transfer (MLCT) manifold by absorption of a visible photon, significant structural flattening occurs, so that the dihedral angle of two dimethyl-phenanthroline ligands is reduced from 90° to ~70°; this is known as the pseudo Jahn-Teller (PJT) distortion (Fig. 1). Our TR-XANES experiment performed at SACLA **BL3** successfully revealed to what extent detailed vibronic motions are observable during this PJT relaxation process.

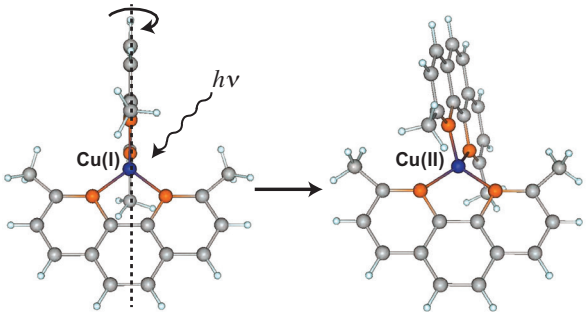

Fig. 1. Schematics of the structural change of $[Cu(dmphen)_2]^+$, known as the PJT distortion. The symmetry is reduced by the reduction of the dihedral angle between two dimethyl-phenanthroline ligands.

In the transient Cu *K*-edge XANES difference spectra (Fig. 2(a)), the pre-edge (8979.5 eV) intensity is slightly increased. This feature is associated with the $1s \rightarrow 3d$ transition and adds some dipole character to the transition by $3d$-$4p$ mixing. Consequently, the pre-edge intensity is sensitive to the molecular structural symmetry, i.e., the PJT flattening. The spectral features at 8985.0 eV and at 8986.5 eV are associated with the $1s \rightarrow 4p$ transition. The intensity decrease in this spectral region is attributed to the blueshift of the absorption edge, reflecting the oxidation of the Cu ion from d^{10} to d^9 by the MLCT excitation. The fs temporal evolutions were measured at these three probe energies (Fig. 2(b-d)). Damped oscillatory signals originating from coherent molecular vibrations were observed at 8979.5 eV and at 8985.0 eV, while no oscillatory features were found at 8986.5 eV. This difference illustrates that the selection of the X-ray probe energy is critically important for capturing the nuclear wavepacket dynamics.

The observed oscillatory signals were extracted from the large electronic backgrounds by picking up residuals after the global fitting analysis (Fig. 3). At the pre-edge (8979.5 eV), three types of oscillations were found at 83–122 cm^{-1}, 165–195 cm^{-1}, and 269–287 cm^{-1} in the time-dependent Fourier transform map (Fig. 3(c)). They are assigned to the normal modes of v_8 (the breathing mode), v_{21} (the symmetry-breaking mode), and v_{25} (the symmetry-breaking mode), respectively. In contrast, at the rise of the absorption edge (8985.0 eV), only a single band was found at 100–122 cm^{-1}, corresponding to the

breathing mode (Fig. 3(d)). The amplitude of the breathing mode corresponds to ±0.1 Å in the first half-picosecond (ps) and decays with a time constant of 0.54 ps, which is interpreted to be the time constant of the PJT dynamics. On the other hand, the symmetry-breaking modes fade at away around ~0.2 ps, indicating the redistribution of the coherent vibrational energies. This redistribution process is faster than the PJT dynamics (0.54 ps) and demonstrates that the symmetry-breaking modes are strongly coupled to the ligand flattening motion, while the breathing mode is rather irrelevant but still dominates the wavepacket dynamics.

The observed wavelength-dependent sensitivity of TR-XANES to these nuclear motions was interpreted as follows. At the pre-edge (8979.5 eV), the intensity is dominated by the dipole contribution derived from the 3*d*-4*p* mixing, which is enhanced by the symmetry-breaking of the molecule or modulated by the metal-ligand covalency. Therefore, both the symmetry-breaking modes and the breathing mode are observable at the pre-edge. On the other hand, at the rise of the absorption edge (8985.0 eV), the intensity is associated with the shift of the absorption edge, which is sensitive to the effective charge state of the Cu ion and the average Cu-N bond length. This explains why only the breathing mode is observable at the rise of the absorption edge. The capability of TR-XANES to disentangle multiple contributions to the wavepacket dynamics demonstrated here is highly advantageous in gaining a deeper understanding of ultrafast nonadiabatic chemical reactions.

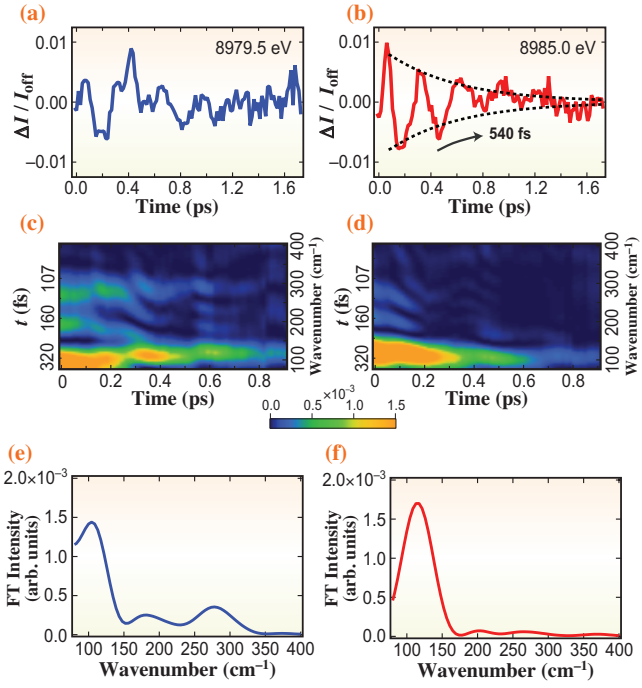

Fig. 2. Femtosecond transient Cu *K*-edge XANES. **(a)** Top: Cu *K*-edge XANES spectra of the $[Cu(dmphen)_2]^+$ ground and excited states. Middle: Difference spectrum between these two spectra. Bottom: Magnified view of the difference spectra. The blue, red, and green dotted lines indicate the photon energy positions where the fs temporal traces were measured. **(b-d)** Time dependences of the transient XANES signals measured at **(b)** 8979.5 eV, **(c)** 8985.0 eV, and **(d)** 8986.5 eV. The gray solid and dotted lines are the results of the global fitting analysis and the individual components, respectively. The arrows correspond to the signal intensities at 10 ps after photoexcitation.

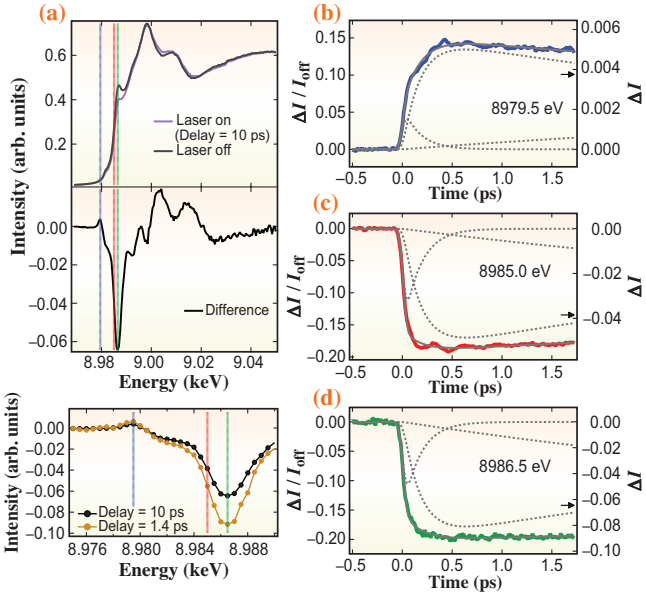

Fig. 3. Extracted coherent nuclear wavepacket. **(a,b)** Residual profiles after the global fitting analysis. **(c,d)** Time-dependent Fourier transforms of **(a,b)**. **(e,f)** Vertical projections of (c,d) with a time window of 0–0.4 ps.

Tetsuo Katayama[a,b]

[a] Japan Synchrotron Radiation Research Institute (JASRI)
[b] RIKEN SPring-8 Center

Email: tetsuo@spring8.or.jp

References

[1] *T. Katayama, Northey, W. Gawelda, C.J. Milne, G. Vankó, F.A. Lima, R. Bohinc, Z. Németh, S. Nozawa, T. Sato, D. Khakhulin, J. Szlachetko, T. Togashi, S. Owada, S. Adachi, C. Bressler, M. Yabashi & T.J. Penfold: Nat. Commun.* ***10*** *(2019) 3606.*
[2] M.W. Mara *et al.*: Coord. Chem. Rev. **282-283** (2015) 2.
[3] M. Iwamura *et al.*: Acc. Chem. Res. **48** (2015) 782.

Environmental effects on the nature of hydrogen bonding detected by synchrotron FTIR microspectroscopy

A hydrogen bond forms between a covalently bonded hydrogen atom and an atom with a high electronegativity. The range of the bonding force is wide, from the weakest van der Waals limit to the strongest covalent bond limit, centered on the well-known hydrogen bond between water molecules. Of the three forces that form hydrogen bonds (electrostatic, induction, and dispersion), it is known that the contribution of dispersive interactions such as van der Waals forces is the largest in the weak hydrogen bonds. Van der Waals forces that are easily disturbed by thermal energy around room temperature are sensitive to environmental factors such as temperature and pressure, leading to the attractive and fuzzy properties inherent in biological systems. Assessment of the van der Waals interaction is fundamental to the central quest of understanding the structure that regulates the biological function. The van der Waals interaction, named after Johannes Diderik van der Waals, who first introduced attractive interactions between neutral molecules in his equation of state, is a dispersion interaction of pure quantum physical origin and is due to quantum fluctuation. Very recently, the theoretical treatment of the van der Waals interaction has become possible.

In this research [1], we revealed the environmental effects on the nature of hydrogen bonding in a fully amorphous biocompatible zwitterionic sulfobetaine monomer, DMAPS (Fig. 1), by measurement using terahertz waves and high-intensity synchrotron radiation at SPring-8 **BL43IR** and analysis with highly accurate first-principles calculations. Biocompatible materials are in high demand for application to drug delivery and/or the coating of artificial organs to avoid the rejection of living organisms. Biocompatible zwitterionic molecules are sensitive to environmental factors such as temperature and pressure, and van der Waals forces govern the stimulus-sensitive properties. Betaine (a specific type of neutral zwitterion) contains a pair of cationic and anionic functional groups at nonadjacent positions in the molecule. A powerful means of detecting the weak interactions is vibrational absorption spectroscopy, which is applicable for many materials including biological substances.

High-intensity synchrotron radiation is useful for small amounts of samples and THz waves are useful for detecting weak hydrogen bonds. THz spectroscopic research has progressed rapidly in recent years, and signal detection and peak assignment on the basis of theoretical calculations have been established for

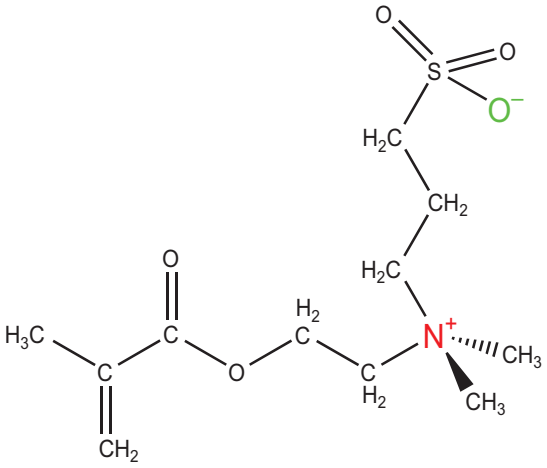

Fig. 1. DMAPS (3-[dimethyl-(2-methacryloyl oxyethyl) ammonium] propane sulfonate).

crystalline samples [2-4]. Noncrystalline amorphous samples are more informative from the biological point of view. However, the study of amorphous samples is lagging behind because of the weak signal and the difference from the gas phase and/or the crystal. To overcome the low intensity of THz absorption, we measured the sample without using a filling material such as polyethylene to dilute the sample. Furthermore, typical filling materials such as KBr in far-infrared spectroscopy are not suitable for zwitterionic molecules because of interactions between the filling materials and zwitterionic samples. It is a notable point in the present synchrotron FTIR microspectroscopy measurement that no filling material is required. Theoretically, the effect of surrounding molecules that cause the difference from the gas phase and the difficulty of the nonperiodic amorphous system is incorporated in the dielectric constants.

The complicated far-infrared spectrum of the present amorphous system was found to be well reproduced by incorporating the effect of the surrounding molecules in the dielectric constants. In this frequency region, the overall spectral profile hardly changes with temperature, except for peak sharpening and a slight peak shift to a higher frequency (Fig. 2). A strong temperature dependence was observed, however, as a peak splitting at around 300 cm^{-1}. The temperature-dependent spectral change around 300 cm^{-1} is well reproduced by changing the dielectric constant (insert of Fig. 2). A difference in the dielectric

constant negligibly affects the spectral profile in the whole range except for the region around 300 cm^{-1}. It is possible that the dielectric constant changes with temperature owing to the change in molecular mobility.

The spectral change depending on temperature is caused by the change in the nature of hydrogen bonding depending on the dielectric constant. The nature of three CH···O bonds markedly changes depending on the dielectric constant, from the typical CH···O between the CH donor and the >S=O accepter to CH···O at the van der Waals contact to no hydrogen bonding.

In summary, the environmental effect on weak intermolecular and intramolecular interactions was revealed by synchrotron FTIR microspectroscopy combined with highly accurate first-principles calculations. High-intensity synchrotron radiation makes it possible to measure small amounts of samples and is suitable for stimulus-sensitive biocompatible materials and amorphous biomolecules. The present results provide a new dimension for designing biocompatible materials with sensitivity to environmental factors such as temperature and pressure.

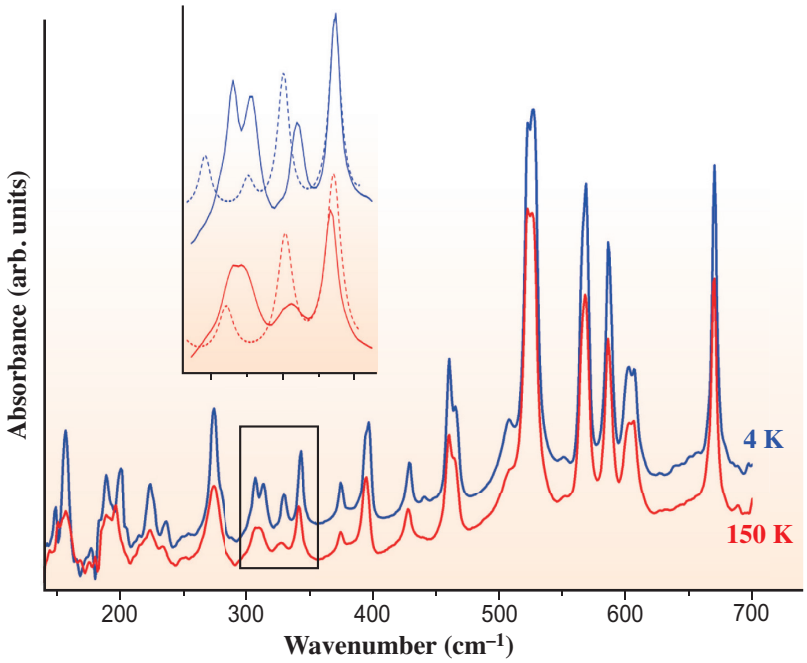

Fig. 2. Far-infrared spectra of DMAPS at 4 K (blue) and 150 K (red). The insert also shows, for comparison, calculated spectra (dashed lines) in the range indicated by the square box. Dielectric constants are 15.20 for the red dashed line and 8.33 for the blue dashed line.

Masae Takahashi

Graduate School of Agricultural Science,
Tohoku University

Email: masae.takahashi.d1@tohoku.ac.jp

References

[1] *M. Takahashi, H. Matsui, Y. Ikemoto, M. Suzuki, N. Morimoto: Sci. Rep.* ***9*** *(2019) 13104.*
[2] M. Takahashi *et al.*: Cryst. Eng. Comm. **20** (2018) 1960.
[3] M. Takahashi *et al.*: J. Phys. Chem. A **121** (2017) 2558.
[4] M. Takahashi: Crystals **4** (2014) 74.

Dynamic behavior of Rh species in Rh/Al_2O_3 model catalyst during three-way catalytic reaction: An *operando* X-ray absorption spectroscopy study

Heterogeneous catalysts have been used in various essential chemical transformations in petrochemistry, ammonia production, and environmental catalysis. Catalysts for the production of useful chemicals are usually used under ideal conditions. On the other hand, so-called catalytic converters, such as three-way catalysts (TWCs), are often exposed to nonideal conditions, such as severe time variations of oxidative and reductive atmospheres or high temperatures, which can easily induce degradation and change the structure-activity relationship during reactions. Therefore, it is essential to elucidate the dynamic behavior of structural and electronic states of a catalyst under working conditions to understand its catalysis and improve catalytic activity and stability.

Essential components of TWCs are the platinum group metals (PGMs) such as Rh, Pd, and Pt. They are vital for the purification of harmful gases in automobile exhausts, such as nitrogen oxides (NO_x), carbon monoxide (CO), and hydrocarbons (HCs). Because of the scarcity of PGMs and strict regulations on automobile exhausts, the reduction of PGM used in TWCs has been one of the urgent global issues arising in response to the trend of increasing demand for automobiles worldwide and the need to protect the global environment.

In this work [1], the dynamic behavior of Rh species in a model catalyst, 1 wt% Rh/Al_2O_3, under a TWC reaction was examined by *operando* study using conventional quick scanning X-ray absorption spectroscopy (XAS) performed at a public beamline, SPring-8 **BL01B1**, as follows. The Rh/Al_2O_3 catalyst prepared by a common impregnation method was placed into a heating XAS cell. The catalyst was pretreated under He flow at 400°C for 30 min. Immediately after the pretreatment, a model feed gas (100 $mL \cdot min^{-1}$) containing NO (1000 ppm), CO (1000 ppm), C_3H_6 (250 ppm), and O_2 (912.5–1337.5 ppm) with He balance was introduced into the XAS cell. The concentration of O_2 was varied between 912.5 and 1337.5 ppm during the reaction. The stoichiometric condition was achieved when the concentration of O_2 was set to 1125 ppm on the basis of the chemical equation shown below.

$$C_3H_6 + 4\,NO + 4\,CO + 9/2\,O_2 \rightarrow 2\,N_2 + 7\,CO_2 + 3\,H_2O$$

The dynamic behavior of Rh species during the TWC reaction was analyzed by Rh *K*-edge XAS spectra in combination with various gas analyzers, a high-sampling-rate TCD-GC, a NO_x meter, and a Q-mass spectrometer. A schematic view of the *operando* XAS setup is shown in Fig. 1.

The catalytic reaction and state of Rh profiles during the TWC reaction over 1 wt% Rh/Al_2O_3 are summarized in Fig. 2. The pretreatment with He gas induced the reduction of some of the Rh species. Initially, 80% of NO is converted to N_2 with the oxidative model feed gas, but the reduction activity declined to 60% as the Rh species was oxidized. After the first-feed-gas condition, the conversion rate of NO to N_2 increased as the feed gas was changed to the stoichiometric condition in a stepwise manner. When the feed gas was changed to a reductive gas 1 hour after the beginning, the conversion rate of model pollutant gases, CO, NO, and C_3H_6, exhibited no change, but the Rh species was rapidly reduced to its metallic state. Monitoring of the following condition variation between oxidative and reduction feed gases suggested reproducible catalytic behavior of the catalyst under the present conditions. From the findings concerning the reduction of NO of high catalytic activity under reductive and oxidative conditions in the beginning period, we confirmed the importance of the surface state of the catalytically active species. The time resolution of the NO_x meter was the highest among effluent gas analyzers and the NO_x profile can be tied to the redox state of the surface of Rh species. With the stepwise decrease in the oxygen concentration of the feed gas, the NO_x profile exhibited a discontinuous change. On the other hand, with the stepwise increase in the oxygen concentration, the NO_x profile showed a sigmoidal curve. In brief, this behavior was explained by two-step autocatalytic oxidation and simple one-step pseudo-

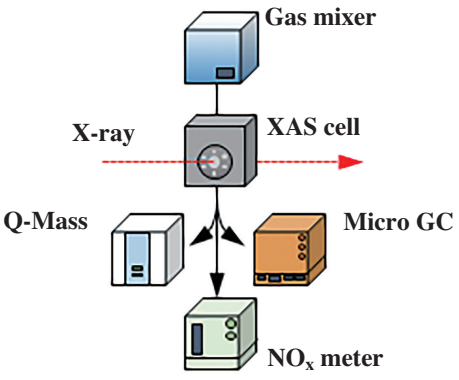

Fig. 1. Simplified view of *operando* XAS setup.

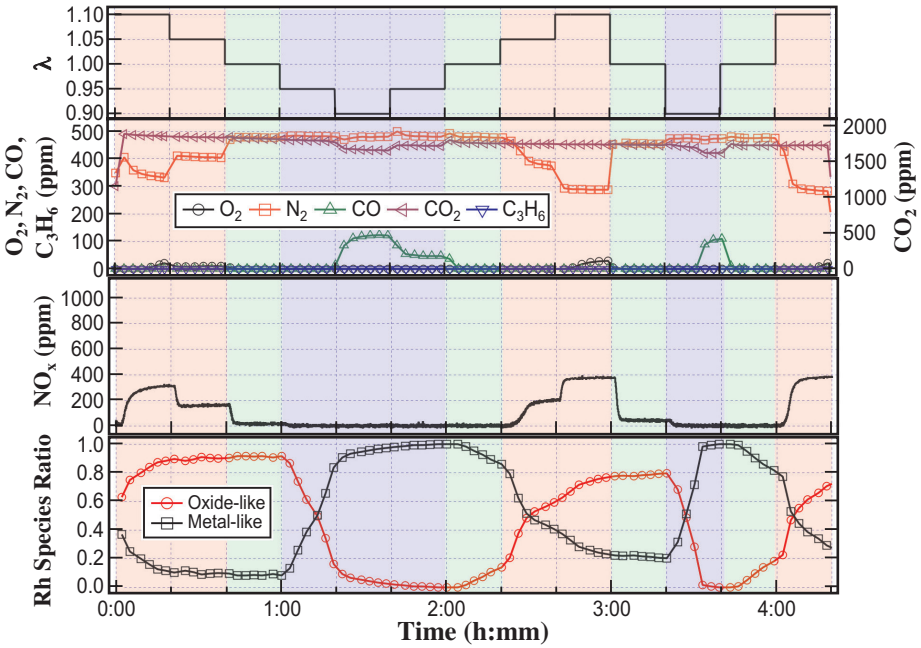

Fig. 2. GC, NO_x profiles of the effluent gases and redox behavior of Rh species during TWC reaction over 1 wt% Rh/Al_2O_3, and λ, the O_2 concentration indicator. $(\lambda = ([NO]_a+[CO]_a+[O_2]_a\times2)/([NO]_s+[CO]_s+[O_2]_s\times2)$, where $[X]_y$ is the concentration of X under the actual (y=a) or stoichiometric (y=s) condition. [1]

first-order kinetics during oxidation and reduction processes on the basis of the results of curve fitting analysis of the NO_x profiles.

The dynamic behavior of Rh species during feed gas switching is summarized in Fig. 3. We assumed that the sizes of the Rh nanoparticles were almost unchanged because the intensities of the Fourier transforms of the EXAFS spectra (not shown) were similar. Considering the reduction process of Rh species, the surface of the oxide-like Rh species was easily reduced to the metallic state swiftly and randomly. On the other hand, in the oxidation process of Rh species, surface oxidation of Rh species proceeded via random and autocatalytic growth by oxide-like Rh site generation.

In summary, we successfully performed *operando* XAS measurement of the Rh/Al_2O_3 model catalyst during TWC and found that the reaction steps of oxidation and reduction of surface Rh species involve two-step autocatalytic oxidation and simple one-step pseudo-first-order kinetics. We also demonstrated the implementation of a powerful *operando* XAS system for heterogeneous catalytic reactions and its importance for understanding the dynamic behavior of active metal species of catalysts. It is also promising that a more brilliant X-ray source will enable the clarification of the local structure and electronic states of the target elements with higher temporal, spatial, and energy resolutions, thus contributing to the further understanding of functional materials.

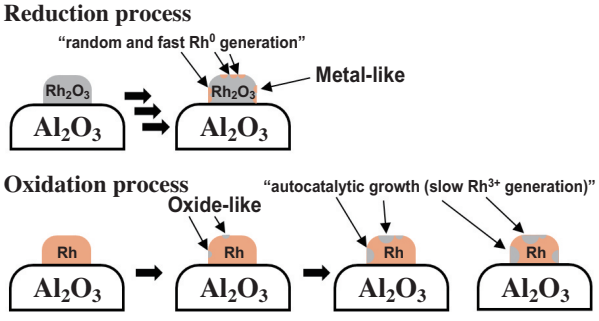

Fig. 3. Redox behavior of Rh species when the gas composition is switched. [1]

H. Asakura[a,b,*], S. Hosokawa[a,b], K. Teramura[a,b] and T. Tanaka[a,b]

[a] ESICB, Kyoto University
[b] Graduated School of Engineering, Kyoto University

*Email: asakura@moleng.kyoto-u.ac.jp

References

[1] *H. Asakura, S. Hosokawa, T. Ina, K. Kato, K. Nitta, K. Uera, T. Uruga, H. Miura, T. Shishido, J. Ohyama, A. Satsuma, K. Sato, A. Yamamoto, S. Hinokuma, H. Yoshida, M. Machida, S. Yamazoe, T. Tsukuda, K. Teramura, T. Tanaka: J. Am. Chem. Soc.* ***140*** *(2018) 176.*

Operando observation of sulfur species that poison polymer electrolyte fuel cell studied by near ambient pressure hard X-ray photoelectron spectroscopy

X-ray photoelectron spectroscopy (XPS) is a powerful tool for investigating surface physical and chemical properties of functional materials and systems. Although conventional photoelectron spectroscopy can only be operated under high vacuum, we recently succeeded in ambient pressure (10^5 Pa) XPS measurements [1] using brilliant microfocused hard X-rays from SPring-8 **BL36XU** undulator beamline. The beamline and XPS apparatus are dedicated to investigating degradation and poisoning mechanisms in polymer electrolyte fuel cells (PEFCs) and are maintained by University of Electro-Communications and supported by New Energy and Industrial Technology Development Organization (NEDO). In this work, we performed *operando* S 1*s* hard X-ray photoelectron spectroscopic (HAXPES) measurements to observe various sulfur species that poison PEFCs under working conditions.

One important methodological achievement in this work is that one can directly measure the electric potential of the electrolyte constituting the membrane-electrode assembly (MEA) as the power generation part in PEFCs. Although it is easy to measure the electrode voltage using a tester probe, the electrolyte voltage is difficult to obtain because the insertion of the tester probe induces the appearance of an electric double layer (EDL) at the electrolyte-probe interface, resulting in an electric potential difference at the interface. On the other hand, the technique of electric potential measurements using XPS is already well known and voltage distributions such as those of transistors have been reported. Owing to the exploitation of the (near) ambient pressure XPS technique, the electrolyte voltage in wet electrochemical cells is expected to be measurable, providing essential information for understanding electrochemical reactions at the interface between the working electrode and the electrolyte. Figure 1 shows the electric potentials of a Pt cathode and anode and a Nafion electrolyte determined, respectively, by Pt $3d_{5/2}$ and F 1*s* XPS, in which cathode-anode voltages of 0.2 and 1.2 V were applied with the cathode grounded [2]. Variation of the EDL is clearly observed; even the polarity of the EDL at the cathode changes by 1.12 V between 0.2 and 1.2 V. It is here noted that the anode-electrolyte voltage does not differ between 0.2 and 1.2 V because the anode works well as a pseudo-standard hydrogen electrode, while the cathode-electrolyte voltage drastically changes, allowing essentially different electrochemical reactions.

We have applied this novel method of electric potential measurement in electrochemical cells to sulfur species that poison PEFCs [3]. Figure 2 shows the S 1*s* XPS spectra around the cathode and anode under working conditions. Without artificial introduction of S-containing species to the MEA, we observed several kinds of S species depending on the applied cathode-anode voltage V_{CA}. Peak S1 can immediately be assigned to the sulfonic acid group ($-SO_3H$, +6 valent) of Nafion, while other peaks, S2 (+4 valent), S3 (zero valent), and S4 (–2 valent) ascribed on the basis of their binding energies (BE) to SO_3^{2-} in the electrolyte, thioether or embedded S in the C support, and anionic atomic S species adsorbed on the Pt nanoparticles, respectively. With increasing V_{CA}, the number of anionic S species adsorbed on the Pt nanoparticles at the cathode electrode gradually decreased and they completely disappear at $V_{CA} \geq 0.8$ V owing to oxidation reactions from adsorbed S to SO_3^{2-} and possibly SO_4^{2-}, but S4 reappeared again with decreasing V_{CA}. With the introduction of oxygen to the cathode electrode, no sulfur species other than the sulfonic acid group of Nafion was detected even at the lowest voltage (not shown in Fig. 2).

Figures 3(a)-3(c) respectively give the S 1*s* BE of S1, S2, and S4 as a function of V_{CA}. Note that the cathode is always grounded. The BE of S4 species in Fig. 3(c) are found to be constant at the cathode and decreasing with a slope of –1 eV/V at the anode, implying that the S4 species is S adsorbed on the Pt electrode. The S1 species (sulfonic acid group in Nafion electrolyte) exhibits similar V_{CA} dependence on the anode as in Fig. 2. The most interesting finding in Fig. 3 is that the S2 species (see Fig. 3(b)) ascribed to

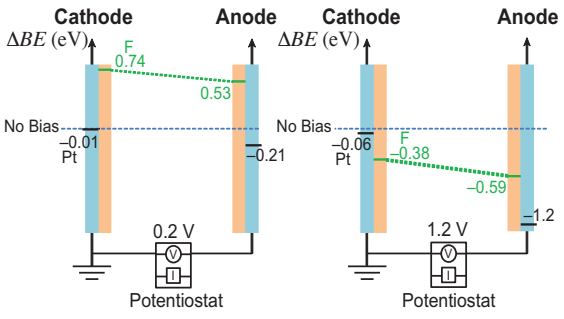

Fig. 1. Electric potential diagrams of the PEFC at the cathode-anode voltages of 0.2 V (left) and 1.2 V (right).

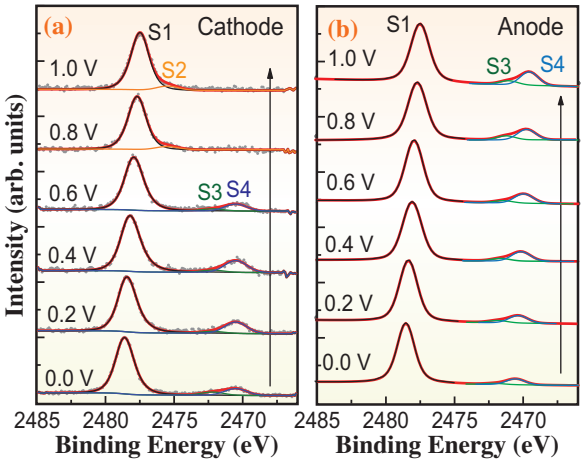

Fig. 2. S 1*s* HAXPES of **(a)** the cathode and **(b)** the anode in the PEFC with a cathode-anode voltage V_{CA} of 0.0–1.0 V. The cathode was always grounded.

tetravalent SO_3^{2-} also shows similar V_{CA} dependence to S1 in Fig. 3(a), clearly indicating that SO_3^{2-} is not adsorbed on the Pt or C electrode but is dissolved in the electrolyte. Consequent redox reactions concerning sulfur species are depicted in Fig. 3(d).

The present work has successfully demonstrated that the measurements of electric potentials of chemical species in electrochemical cells, such as PEFCs, using ambient pressure HAXPES allow us to identify the locations of the phase (cathode, anode, or electrolyte) of the chemical species of interest, thus paving the way to new useful methodologies that can be applied to electrochemical cells such as fuel cells and batteries.

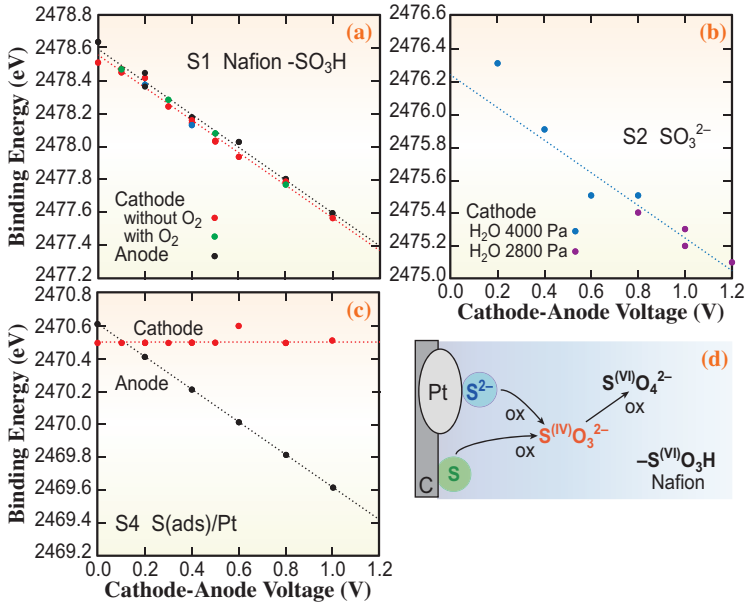

Fig. 3. S 1*s* binding energies of **(a)** S1, **(b)** S2, and **(c)** S4 species near the cathode or anode. The cathode was always grounded. **(d)** Schematic redox reactions of S species around the electrode. The SO_4^{2-} species was not detected in this work because of overlap of its peak with the Nafion sulfonic acid peak S1.

Toshihiko Yokoyama[a,*] and Yasuhiro Iwasawa[b]

[a] Institute for Molecular Science, National Institutes of Natural Sciences
[b] Innovation Research Center for Fuel Cells, The University of Electro-Communications

*Email: yokoyama@ims.ac.jp

References

[1] Y. Takagi *et al.*: App. Phys. Exp. **10** (2017) 076603.
[2] L. Yu *et al.*: Phys. Chem. Chem. Phys. **19** (2017) 30798.
[3] *L. Yu, Y. Takagi, T. Nakamura, T. Sakata, T. Uruga, M. Tada, Y. Iwasawa, S. Masaoka and T. Yokoyama: J. Phys. Chem. C* ***123*** *(2019) 603.*

Operando three-dimensional imaging of distribution and degradation process of Pt-Co cathode catalyst in polymer electrolyte fuel cell

The membrane electrode assembly (MEA) of a polymer electrolyte fuel cell (PEFC) is a heterogeneous device for clean energy production, and the visualization of the heterogeneous structure of an MEA is crucial to the understanding of chemical events proceeding in a practical PEFC device. In particular, the migration and degradation of electrocatalysts in an MEA are key issues of PEFC performance, and we have performed the *operando* imaging of the three-dimensional distribution and degradation event of a Pt-Co cathode catalyst in an MEA under PEFC operating conditions [1].

Computed-tomography XAFS (CT-XAFS) combining CT imaging and XAFS spectroscopy at the Pt L_{III}-edge and Co *K*-edge was performed at SPring-8 **BL36XU** beamline. Monochromatized hard X-rays (Pt L_{III}-edge: E = 11.386–11.697 keV, Co *K*-edge: E = 7.517–7.849 keV) were irradiated to the MEA with the Pt-Co cathode catalyst enclosed in an *in situ* PEFC cell designed for CT-XAFS measurements. The cell was operated at 353 K with N_2 flow of 600 mL·min^{-1} at the cathode and H_2 flow of 150 mL·min^{-1} at the anode, and electrochemical performances were investigated during a series of *operando* measurements. The recorded X-ray transmission images of the sample (I) and X-ray intensity images (I_0) were converted to absorption coefficient images (μt), and a fitting analysis of the obtained XANES spectra was conducted on 2D images. Finally, the three-dimensional matrices of extracted XANES fitting parameters were reconstructed into the three-dimensional images of morphology, Pt density, Co density, and Pt valence state in real space (Fig. 1). The *operando* CT-XAFS measurements were performed before and after a PEFC accelerated degradation test (ADT) (voltage cycling between 0.6 V and 1.0 V for each 3 s).

The *operando* CT-XAFS measurements provided the distribution and degradation images of the cathode catalyst in the MEA, as shown in Fig. 1. The visualized morphology images of the MEA clearly suggested the structures of domains and cracks in the cathode catalyst layer, and similar patterns in the morphology images before and after the ADT process showed that the *operando* measurements successfully visualized the same parts in the MEA before and after the ADT process. The distributions of Pt and Co in the cathode catalyst layer were obtained by analyzing Pt L_{III}-edge and Co *K*-edge XANES spectra, respectively, and suggested different degradation manners of the Pt and Co species in the Pt-Co bimetallic catalyst in the MEA. The aggregation of Pt was observed in the observation area, but the migration to the depth direction of the MEA was negligible. This was considerably different from the behavior of an MEA with a Pt cathode catalyst. In contrast, a significant amount of Co was dissolved and migrated in the depth direction of the MEA, changing the Pt valence state of the Pt-Co catalyst (Fig. 1).

The CT-XAFS analysis provides huge experimental data sets of the structural parameters, and data

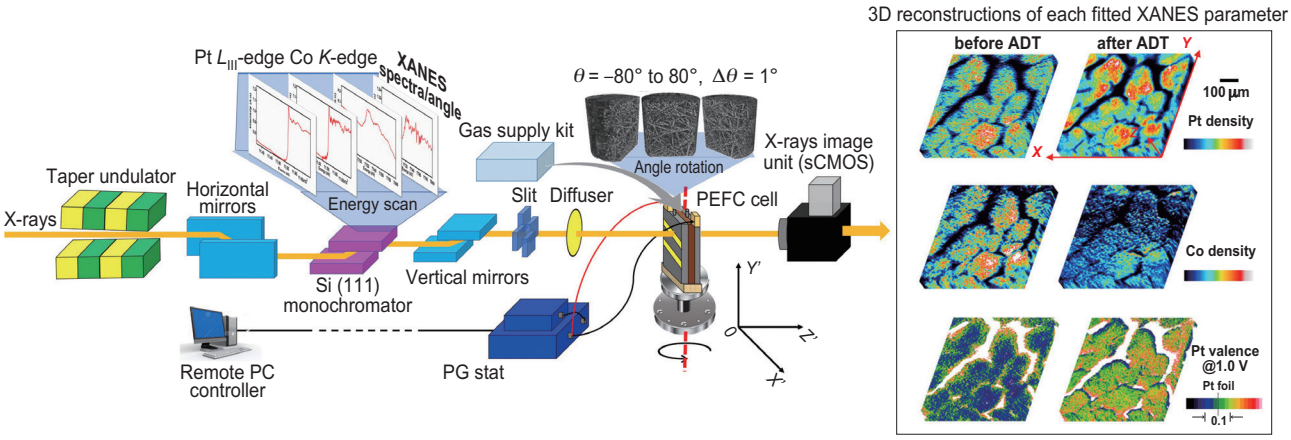

Fig. 1. Schematics of *operando* CT-XAFS measurements of PEFC MEA under operating conditions and the reconstructed 3D images of Pt density, Co density, and Pt valence state of the cathode catalyst layer at 1.0 V before and after 34,000 cycles of ADT. [1]

mining is essential to extract key parameters in the imaging data. We conducted unsupervised learning of the obtained structural parameters, e.g., morphology, Pt density, Co density, Pt valence state, geometrical distance from the surface of cracks in the MEA, loss of Pt (ΔPt), and loss of Co (ΔCo), and investigated correlations between parameters. Figure 2 shows the Pearson plots of ΔPt or ΔCo (changes in the Pt or Co density by the ADT process) and the geometrical distance from the surface of cracks formed in the cathode catalyst layer, calculated using the morphology images. The Gaussian mixture model of the Pearson plots suggested the existence of four groups (G_1–G_4) in Fig. 2: a group with an increase in the density (G_4), a group with negligible changes in the density (G_3), and two groups with decreasing density (G_2 and G_1). In the case of Co, all four groups were widely distributed from the surface to the domains, as shown in Figs. 2(c) and 2(d). On the other hand, the G_3 component of Pt was found to be localized at the surface near cracks in the cathode catalyst layer Figs. 2(a) and 2(b). These results suggest that the morphological factors of the cathode catalyst layer depend on catalyst degradation. The present infographic approach combining three-dimensional imaging and unsupervised learning is promising for extracting essential parameters related to material functions.

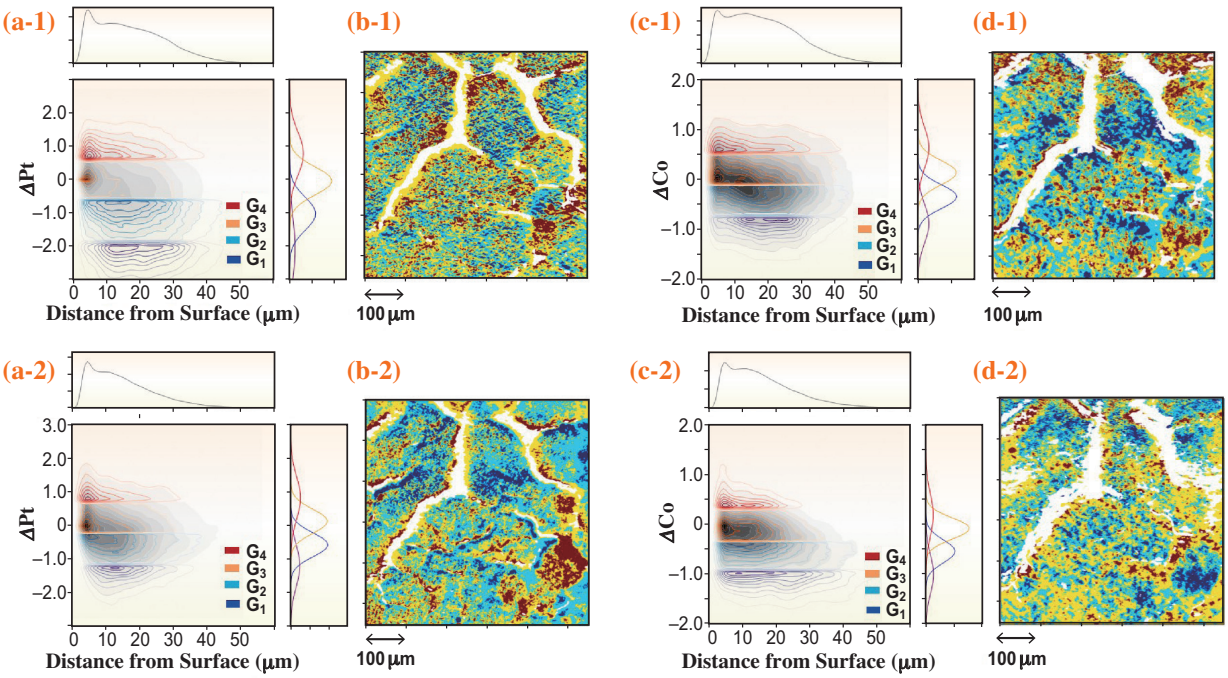

Fig. 2. Pearson plots of ΔPt **(a)** and ΔCo **(c)** and calculated geometrical distance from crack surface. **(1)** Differences in the densities after 21,000 cycles of ADT from those before ADT. **(2)** Differences in the densities after 34,000 cycles of ADT from those after 21,000 cycles of ADT. G_1–G_4: Groups classified by the Gaussian mixture model of the Pearson plots. **(b, d)** Spatial distribution maps of G_1–G_4 of each Pearson plot. [1]

Hirosuke Matsui, Yuanyuan Tan and Mizuki Tada*

Graduate School of Science & Research Center for Materials Science/Institute for Advance Science, Nagoya University

*Email: mtada@chem.nagoya-u.ac.jp

References

[1] *Y. Tan, H. Matsui, N. Ishiguro, T. Uruga, D.-N. Nguyen, O. Sekizawa, T. Sakata, N. Maejima, K. Higashi, H.C. Dam, M. Tada: J. Phys. Chem. C* ***123*** *(2019) 18844.*

Electrical double layer structure that activates the oxygen reduction reaction

The reduction of electrocatalyst usage in polymer electrolyte fuel cells (PEFCs) is an urgent issue for realizing the widespread use of fuel cell vehicles. Currently, mainstream research on PEFC catalysts is aimed at reducing the overpotential of the oxygen reduction reaction (ORR) using Pt alloy electrocatalysts such as PtNi [1]. However, non-precious metals in the catalyst are easily dissolved by the fluctuations of electrode potential during the start-stop operation of the fuel cell. Therefore, the catalytic durability of commercial fuel cell vehicles is maintained by the overloading of Pt alloy catalyst. Recently, we have focused on the properties of the ionic species in the electrical double layer (EDL) formed at the solid electrode-electrolyte solution interface [2]. We found that the hydrophobicity of organic cations in the EDL extraordinarily enhances the ORR activity in acidic solutions, which is the same as the condition in the PEFC. The high hydrophobicity of the tetraalkylammonium cation with a longer alkyl chain enhances the ORR activity. The activity on Pt(111) in the presence of the tetra-*n*-hexylammonium cation is eight times as high as that without this cation, and is comparable to the activities on Pt_3Co(111) and Pt_3Ni(111) electrodes [3]. Although this study was performed using well-defined model surfaces of single-crystal electrodes, the modification by organic cations on fuel cell catalysts for practical use can be easily introduced into the process of catalyst preparation. Determination of the detailed interfacial structure is important for the elucidation of the appropriate reaction field in the EDL of a fuel cell catalyst. In this study, three-dimensional structural determination at the atomic level using *in situ* X-ray diffraction revealed the activation factor of the ORR and the abnormal structural displacement of substrate Pt atoms.

X-ray diffraction was measured using SPring-8 **BL13XU** with an X-ray energy of 20 keV. Structural analyses along the surface normal direction were performed using X-ray specular crystal truncation rod (CTR) scattering. The CTR profiles were obtained at 0.9 V *vs* RHE where the ORR activity was estimated. Figure 1 shows the specular CTR and normalized CTR profiles of Pt(111) in 0.1 M $HClO_4$ with and without 10^{-6} M THA^+. The CTR clearly changes with the electrode potential and the addition of THA^+. Since THA^+ is composed of nitrogen, carbon, and hydrogen, the electron density at the interface is significantly lower than that of Pt. Therefore, the main origin of this change in the CTR is the structural change in the substrate Pt. The initial model used for structural optimization comprises three Pt layers and one layer of oxygen of water molecules or an OH_{ad} layer. The vertical atomic position, occupancy factor, and Debye-Waller factors for the Pt and oxygen layers were optimized by the least-squares method. The electron density profiles and schematic models of the interfacial structure are shown in Fig. 2.

Compared with the structural data at the double layer potential of 0.50 V at which water adsorbed on the Pt(111) surface, the distance between the layers of oxygen and the first Pt ($d_{O\text{-}1stPt}$) in 0.1 M $HClO_4$ without THA^+ decreased from 2.47 to 2.14 Å. This distance of 2.14 Å corresponds to the Pt-O bond length of OH_{ad} on Pt(111) proposed on the basis of low-energy electron diffraction and *in situ* X-ray diffraction measurements. Potential-dependent coadsorbed structures of water and OH_{ad} were also suggested to exist from the results of DFT calculations and Monte Carlo simulations. Previous XPS measurements indicate the coadsorption of water and OH_{ad}, hence the oxygen coverage at 0.90 V (θ_O = 0.78) includes adsorbed water and OH species. The surface relaxation of the Pt layer is promoted by electron donation from an oxygen

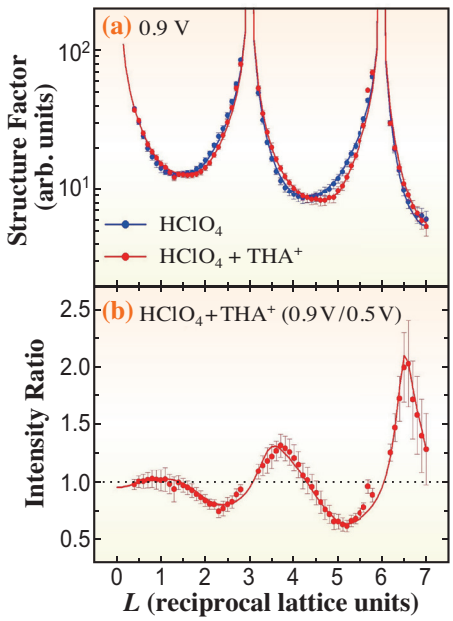

Fig. 1. **(a)** Specular crystal truncation rod (CTR) profiles of Pt(111) in 0.1 M $HClO_4$ with and without 10^{-6} M tetra-*n*-hexylammonium cation (THA^+) saturated with Ar at 0.90 V *vs* RHE. The dots are the data points and the solid lines are the structure factors calculated using the optimized model. **(b)** Specular CTR profiles at 0.90 V normalized to the data at 0.50 V.

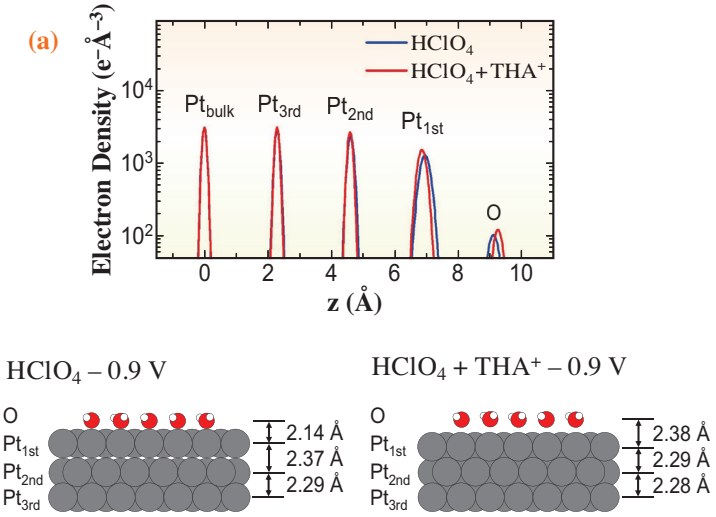

Fig. 2. **(a)** Electron density profiles of the optimized model at 0.90 V. **(b)** Schematic models estimated from structural optimization.

lone pair of the OH_{ad} as well as adsorbed water. Therefore, the distance between the first and second Pt ($d_{1stPt–2ndPt}$) layers does not change compared with that at the double layer potential of 0.50 V. Conversely, in the presence of THA^+, $d_{O\text{-}1stPt}$ was 2.38 Å, which indicates that adsorbed water is dominant instead of OH_{ad}. It is notable that the surface relaxation was eliminated ($d_{1stPt\text{-}2ndPt}$ = 2.29 Å) even though the water and OH_{ad} were adsorbed on Pt. This result indicates that the interaction between the oxygen species and Pt is decreased by the presence of THA^+.

In acidic solution, the hydration water around H^+ is linked with OH_{ad} through a hydrogen bond, as shown in Fig. 3(a). H^+-H_2O-OH_{ad} formation stabilizes the OH_{ad} layer and inhibits the ORR. According to studies on the Pt(111) surface under an ultrahigh vacuum condition, the coadsorption of OH_{ad} and H_2O forms a well-defined 3×3 honeycomb structure because the symmetry and OH•••O distance in the coadsorbed layer fit well with the Pt(111) lattice. The approach of the hydration shell around THA^+ to the Pt surface disrupts the stabilization effect between the hydration water and the OH_{ad} layer (Fig. 3(b)). The coverage of OH_{ad} is decreased by this destabilization effect, inducing the disruption of the stable hydrogen bonding network in the coadsorbed layer. These multiple effects are enhanced by the hydrophobicity of the cation and promote the access of oxygen molecules to the Pt(111) surface.

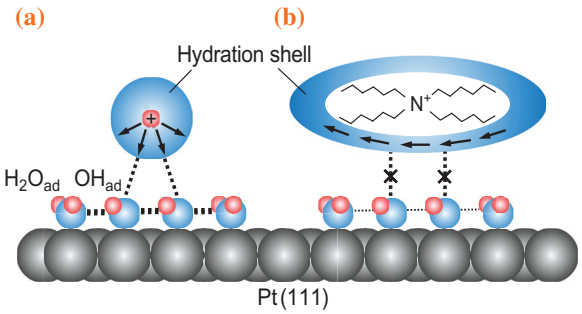

Fig. 3. Schematic model of interfacial hydrated cations and adsorbed hydroxide species on Pt(111): **(a)** hydrophilic cation and **(b)** hydrophobic cation. Arrows indicate the direction of the water dipole within the hydration shell.

Tomoaki Kumeda[a], Osami Sakata[b] and Masashi Nakamura[a,*]

[a] Graduate School of Engineering, Chiba University
[b] Synchrotron X-ray Station at SPring-8, National Institute for Materials Science (NIMS)

*Email: mnakamura@faculty.chiba-u.jp

References

[1] V.R. Stamenkovic *et al.*: Science **315** (2007) 493.
[2] M. Nakamura *et al.*: Chem. Phys. Chem. **12** (2011) 1430.
[3] *T. Kumeda, H. Tajiri, O. Sakata, N. Hoshi, M. Nakamura: Nat. Commun.* ***9*** *(2018) 4378.*

Oxygen-diffusion-driven oxidation behavior and tracking areas visualized by X-ray spectro-ptychography with unsupervised learning

Three-way exhaust catalysis is a key reaction in automobile systems, and cerium-containing mixed oxides have been widely used as the support for exhaust catalysts. The oxygen storage and release capacity (OSC) of cerium-containing mixed oxides associated with the reversible oxidation and reduction of Ce^{3+} and Ce^{4+} ions enables widening of the operation window of three-way catalysts. In particular, $Ce_2Zr_2O_x$ (denoted CZ-x, where x = 7–8) solid solutions with an ordered arrangement of Ce and Zr atoms exhibit high OSCs. The reversible oxygen storage and release processes erase the oxygen diffusion track in the bulk of the CZ-x particles, and consequently, the details of the oxygen storage pathways in the CZ-x particles remain unclear.

X-ray spectro-ptychography (XSP), a combination of XAFS spectroscopy and X-ray ptychography, is a promising tool for visualizing both the structures and chemical states of bulk materials at the nanoscale beyond the limitation of an X-ray lens. Recently, 2D XSP in the hard X-ray region has been reported, which provided 2D maps of the Ce density and valence state, suggesting the existence of several 2D domains with different oxygen storage behavior in Pt-supported CZ-x (Pt/CZ-x) catalyst particles [1]. However, significant ambiguities, especially regarding the 3D oxygen-diffusion-driven Ce oxidation tracking areas in individual CZ-x particles during the heterogeneous oxygen storage process, remain in the 2D images derived from the projection of the structure and valence state along the optical axis.

In this study, we propose the approach of 3D hard X-ray spectro-ptychography (HXSP) imaging coupled with unsupervised learning [2]. The 3D HXSP method combined with computed tomography (CT) allowed the realization of 3D nanoscale imaging of the structure and valence state inside individual Pt/CZ-x solid solution particles during the oxygen storage process. Unsupervised data mining of the visualized 3D nanoscale chemical maps then successfully revealed the concealed heterogeneous oxygen-diffusion-driven 3D nanoscale Ce oxidation tracking areas inside the individual mixed-oxide particles during the oxygen storage process.

3D HXSP (5.708–5.770 keV, which includes the Ce L_{III}-edge) was conducted at SPring-8 **BL29XUL**. For the CT measurement, the sample was rotated from –75 to 75° via 61 evenly spaced angles at each X-ray energy. The projected amplitude and phase images at each angle were reconstructed. Then, 3D image reconstruction was accomplished using the filtered back projection algorithm at each X-ray energy. The voxel size of the reconstructed 3D HXSP images in real space was as low as 14 nm, in contrast to the size of single CZ-x particles of ~500 nm to 1 μm, enabling the determination of the 3D oxidation reaction tracking areas in individual catalyst particles during the oxygen storage process.

Figure 1(a) shows the isosurface rendering of the reconstructed 3D HXSP phase images of six CZ-x particles in the field of view. The facet structures on the surfaces of the CZ-x particles can be clearly visualized in the 3D HXSP image. The Ce L_{III}-edge ptychographic-XAFS spectra allowed discrimination of Ce^{3+} and Ce^{4+}, whose linear combination fitting at each voxel afforded a 3D map of the Ce oxidation state in (x,y,z) real space. The resulting 3D cross-sectional images of the Ce valence are presented in Fig. 1(b),

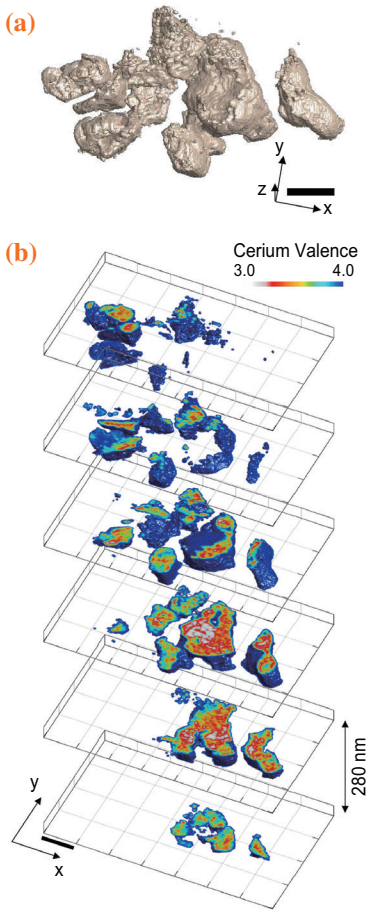

Fig. 1. **(a)** Isosurface rendering of the reconstructed 3D phase map of partially oxidized Pt/CZ particles. **(b)** Series of slices of the 3D Ce valence image along the z direction. Scale bars correspond to 700 nm.

showing the heterogeneous variation of the Ce oxidation state inside individual CZ-x particles where oxygen storage partially proceeded via the oxidation of CZ-7 with O_2 at 423 K for 1 h. The surfaces of the solid particles appeared blue (Ce^{4+}) and wide color variation inside the solid particles was observed in a heterogeneous manner.

The 3D HXSP imaging results provided a 3D nanoscale Ce valence map of the solid particles with 452×450×136 voxels. To characterize each voxel, we considered the surrounding binning of 3×3×3 voxels (42×42×42 nm^3) in the 3D map and used the local mean ($m(x,y,z)$) and local standard deviation ($sd(x,y,z)$) of the Ce valence state in each binning domain as descriptors. Note that $m(x,y,z)$ corresponds to the degree of oxygen storage ($Ce^{3+} \rightarrow Ce^{4+}$) and $sd(x,y,z)$ corresponds to the variation of oxygen storage in the local domains. Using these descriptors, we observed a volcano-type correlation between $m(x,y,z)$ and $sd(x,y,z)$, as shown in Fig. 2(a). By minimizing the Bayesian information criterion, a Gaussian mixture model approximating the 2D plot of (m, sd) revealed that the actual distribution was a mixture of four Gaussian components denoted G_1, G_2, G_3, and G_4. The volcano-type pattern was related to the course of the oxygen storage process during Ce oxidation from Ce^{3+} to Ce^{4+} via the G_1, G_2, and G_3 domains in the CZ-x particles concealed in the bulk. The Ce oxidation in the G_1 domains proceeds in the CZ-7 phase with a pyrochlore structure, whereas the Ce oxidation in the G_2 domains is considered to occur in the disordered (mixed) phases accompanied by the transformation of the pyrochlore phase to the CZ-8 κ-phase with a fluorite structure and showing a larger sd. Further oxygen storage proceeds in the Ce oxidation states above +3.7 and forms the G_3 domains with a maximum Ce valence population. The G_3 domains, considered to be nearly a fluorite phase, readily converge to the Ce^{4+} valence state in the G_4 domains and the final CZ-8 phase. We classified the locations of the four groups in (x,y,z) real space and present a 3D map and cross-sectional images in Fig. 2(b). This figure clearly shows that the locations of the four groups were dependent on the morphological characteristics of the particles: the domains belonging to G_4 (blue) were observed at the outermost surfaces of the particles, whereas those belonging to G_1 (red) were predominantly located in the cores of the particles.

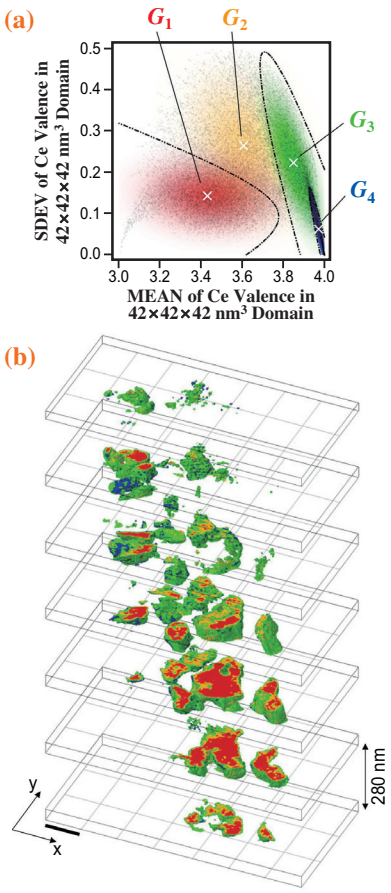

Fig. 2. **(a)** Scatter plot of mean Ce valence (m) and its standard deviation (sd) for 42×42×42 nm^3 (3×3×3 voxels) domains of partially oxidized Pt/CZ-x particles, and classification of correlation trends using a Gaussian mixture model. **(b)** Series of slices showing the 3D distributions of the four correlation groups along the z direction. The scale bar corresponds to 700 nm.

3D HXSP is expected to be an indispensable tool for determining reaction tracking areas and the relationships between the structure and function of heterogeneous functional materials. In particular, in next-generation synchrotron facilities where fluxes with much higher coherence will be achieved, the present approach will be applied to *in situ* 3D measurements, which can be expected to significantly accelerate progress in chemistry and materials science.

Yukio Takahashi[a,b,c,*], Hieu Chi Dam[d] and Mizuki Tada[e]

[a] Institute of Multidisciplinary Research for Advanced Materials, Tohoku University
[b] Department of Engineering, Osaka University
[c] RIKEN SPring-8 Center
[d] Japan Advanced Institute of Science and Technology
[e] Department of Chemistry, Nagoya University

*Email: ytakahashi@tohoku.ac.jp

References

[1] M. Hirose *et al.*: Angew. Chem. Int. Ed. **130** (2018) 1490.
[2] *M. Hirose, N. Ishiguro, K. Shimomura, D.-N. Nguyen, H. Matsui, H.C. Dam, M. Tada, Y. Takahashi: Commun. Chem.* ***2*** *(2019) 50.*

Speciation of phosphorus and zinc in soils receiving swine manure compost for nearly a quarter of a century

The accumulation of phosphorus (P), zinc (Zn), and copper (Cu) is a common issue in farmland soils receiving a large amount of swine manure (SM) compost from pig production. The SM contains relatively high levels of Zn and Cu owing to the extensive use of veterinary medicinal products in pig production [1]. Therefore, the continual application of SM in the farmland results in the elevation of these elements in the soil. The mobility and potential bioavailability of an element in soil depend on their oxidation states and chemical species. It is largely unknown how the chemical species of elements in SM have been altered in the soil over a decade or an even longer time span. The objective of this study was to investigate the concentration and chemical species of Zn and P in soil collected from a field where SM compost has been continuously applied for 23 years. Long-term field experiments are essential for revealing the changes in the accumulation and speciation of manure-derived metals and P in the soil.

The experimental plots were located at Western Region Agricultural Research Center, NARO, Kyoto, Japan and were established in 1993. The plots had been treated twice a year with chemical fertilizer (CF) and SM compost for 23 years. Air-dried soil samples were analyzed by XAFS. P *K*-edge XANES measurements were conducted at Aichi Synchrotron Radiation Center using beamline BL6N1, equipped with an InSb (111) monochromator, at ambient temperature under He atmosphere. References for P compounds and mineral-adsorption phases were also analyzed. Zn *K*-edge XAFS measurements were conducted at SPring-8 **BL01B1** and **BL14B2** beamlines, equipped with a Si(111) monochromator, at ambient temperature. References for Zn compounds and mineral-adsorption phases were also analyzed [2].

The continual application of SM compost notably increased the soil P concentration to about three times greater (SM soil, 4.5 $g \cdot kg^{-1} \cdot yr^{-1}$) than that in the chemical-fertilizer-applied soil (CF soil, 1.6 $g \cdot kg^{-1} \cdot yr^{-1}$) after 23 years of field application (Fig. 1(a)). The Zn concentration in the SM soil in the 23rd year of the field trial reached 224 $mg \cdot kg^{-1}$ (Fig. 1(b)). In contrast, the concentration of Zn remained virtually unchanged with CF application for 23 years.

The P *K*-edge XANES spectra of soils were characterized by the pre-edge at around 2145 eV (Fig. 2), indicating the presence of PO_4 associated with Fe minerals. The XANES spectrum of SM-compost-applied soil collected in 2015 (SM2015) was similar to that of the hydroxyapatite reference and exhibited a distinctive feature of a shoulder on the high-energy side of the whiteline peak. Because of the high similarity in XANES spectra even among the reference compounds, linear combination fitting (LCF) of soil XANES spectra using reference standards was reported as a group of PO_4 associated with Fe (Fe–P), Ca (Ca–P), and Al (Al–P) [3]. The original soil (Soil1992) contained 55% Al–P (0.67 $g \cdot kg^{-1}$) and 39% Fe–P (0.47 $g \cdot kg^{-1}$) as major species. The continual application of CF for 23 years (CF2015) did not induce any notable change in Al–P concentration, but an increase in the Fe–P concentration from 39% to 49% of the total P was observed. In contrast, the continual application of SM compost for 23 years (SM2015) rapidly increased the concentrations of Fe–P to 3.4 $g \cdot kg^{-1}$ (76%) and Ca–P to 0.86 $g \cdot kg^{-1}$ (19%) with a concomitant decrease in Al–P to 0.23 $g \cdot kg^{-1}$ (5%). The accumulation of these P species in the SM2015 soil corresponded to the P species in SM itself, which is enriched with Fe–P (59%) and Ca–P (41%).

The overall structure of the Zn EXAFS spectrum for the original soil (Soil1992) and CF-applied soil (CF2015) was similar to that of Zn associated with kaolinite (Fig. 3). These soils exhibited marked

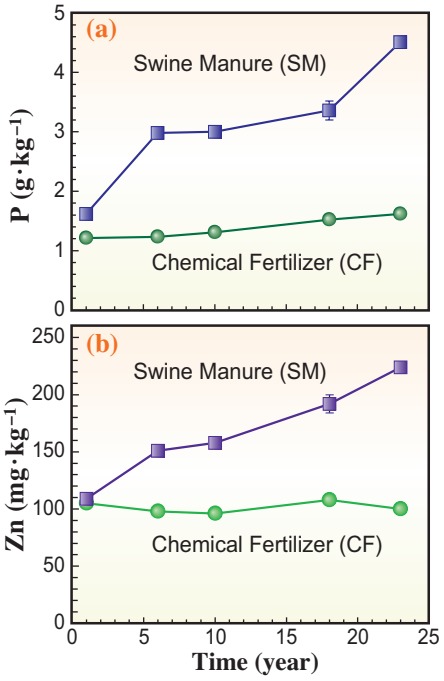

Fig.1. Concentrations of P **(a)** and Zn **(b)** in soils treated with chemical fertilizer (CF, circles) and swine manure (SM) compost (squares) for 23 years.

splitting in the first oscillation of their EXAFS spectra at 3.7 Å^{-1}, corresponding to the reference Zn associated with kaolinite. The original soil (Soil1992) contained 95% Zn associated with phyllosilicates (99 mg·kg^{-1}), which included kaolinite and hydroxyl-interlayered montmorillonite. The continual application of CF to the soil (CF2015) essentially did not change the distribution of these Zn species. In contrast, the continual application of SM compost for 23 years (SM2015) induced the accumulation of hopeite (60 mg·kg^{-1}, 27%) and Zn associated with humus (72 mg·kg^{-1}, 32%) in addition to the inherent species of Zn associated with phyllosilicates (78 mg·kg^{-1}, 35%).

Our study revealed that the continual application of SM compost to soils significantly increases the concentrations of Zn and P. Agricultural soils receiving a large amount of SM from swine production can be a primary source of Zn in the environment. In soils receiving repeated land applications of SM and pig slurry, the concentration and speciation changes of Zn and P over time are critical in predicting the long-term fate and potential mobility of these elements. Our study suggests that in the long-term land application of SM, the accumulation and speciation of Zn and P over time should be monitored to minimize the environmental loss of these elements.

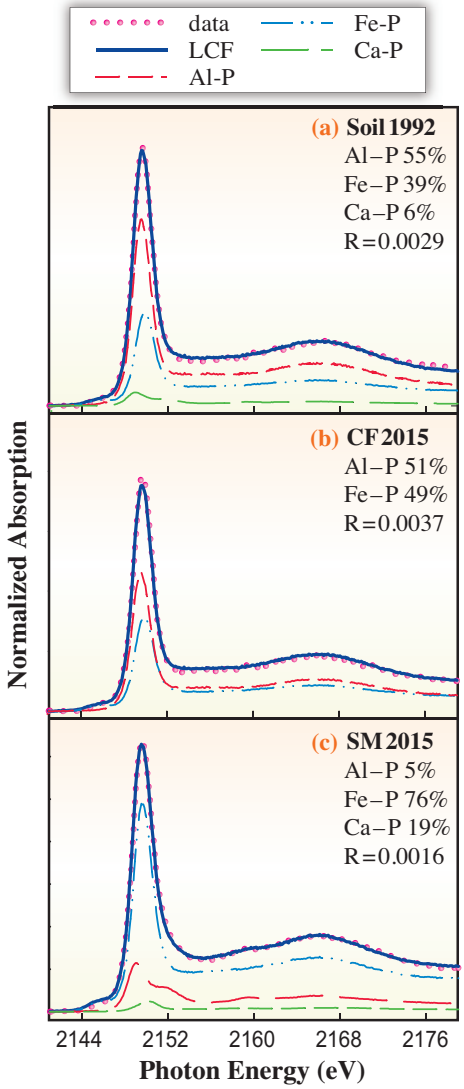

Fig. 2. P *K*-edge XANES spectra for **(a)** original soil (Soil1992), **(b)** soil treated with chemical fertilizer (CF2015), and **(c)** soil treated with swine manure compost (SM2015) and their linear combination fits using P reference spectra. Al–P, Fe–P and Ca–P represent P associated with Al, Fe, and Ca, respectively.

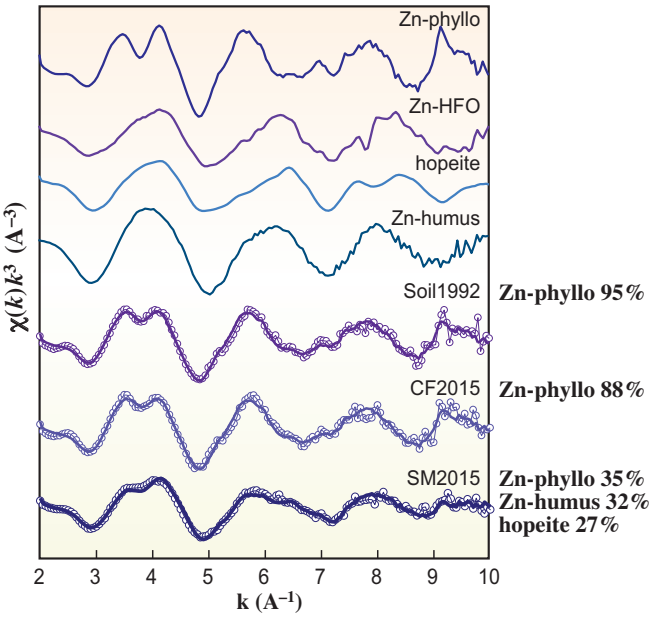

Fig. 3. Spectra of Zn *K*-edge EXAFS of selected references relative to original soil (Soil1992), soils treated with chemical fertilizer (CF2015) and swine manure (SM2015), and their linear combination fits using reference spectra (solid lines). The best results of LCF are shown on the right side of each panel. The sum of components of LCF on each sample is not adjusted to 100%. Zn phyllo: sum of Zn associated with kaolinite and montmorillonite. Zn-humus and Zn-HFO represent Zn associated with humus and ferrihydrite, respectively.

Yohey Hashimoto[a,*], Kosuke Yamamoto[a] and Jihoon Kang[b]

[a] Tokyo University of Agriculture and Technology
[b] University of Texas Rio Grande Valley, Texas, USA

*Email: yhashim@cc.tuat.ac.jp

References

[1] J. Jensen *et al.*: Environ. Int. **114** (2018) 181.
[2] *K. Yamamoto, Y. Hashimoto, J. Kang, K. Kobayashi: Environ. Sci. Technol. **52** (2018) 13270.*
[3] K. Yamamoto *et al.*: J. Environ. Quality **46** (2017) 461.

Sharp 660-km seismic discontinuity explained by extremely narrow binary post-spinel transition

The 660-km seismic discontinuity (D660) is the globally observed boundary between the Earth's upper and lower mantles. Geophysical observations characterize D660 as follows. (a) The global average depth is 660±10 km, corresponding to 23.4±0.4 GPa in pressure. (b) The changes in compressional and shear velocities at the boundary are both 6%. (c) The strong reflection of short-period P waves suggests that the thickness of D660 is less than 2 km (0.1 GPa in pressure), which is in striking contrast to the 7-km-thick 410-km discontinuity [1]. (d) The topography of the discontinuity up to ±20 km has been locally observed. (e) Seismic tomography mappings show high-velocity anomalies around the D660 beneath subduction zones, some of which seem to indicate stagnation of subducted slabs (e.g., [2]). From the above features, D660 is considered one of the most important boundaries in the mantle, especially in terms of mantle dynamics.

It has been suggested that the Earth's upper mantle consists of *ca.* 60 atom% $(Mg_{0.9}Fe_{0.1})_2SiO_4$ polymorphs (olivine, wadsleyite, and ringwoodite) coexisting with *ca.* 40 atom% pyroxene and garnet. In contrast, most parts of the lower mantle are constituted of *ca.* 70 atom% $(Mg,Fe)SiO_3$ bridgmanite with *ca.* 20 atom% ferropericlase and *ca.* 10 atom% calcium perovskite. At a pressure near that at D660, ringwoodite decomposes to bridgmanite + ferropericlase, which is called the post-spinel transition. Because of the agreement of the post-spinel transition pressure with the D660 pressure (e.g., [3]) and the high elastic wave velocities of the post-spinel phase against those of ringwoodite, it is usually considered that the post-spinel transition is the cause of the formation of D660. Whether or not the post-spinel transition can explain D660 will determine the chemical structure of the mantle (homogeneous *vs* chemically layered mantle) and the type of mantle convection (whole-mantle *vs* layered-mantle convection). If the D660 is due to the post-spinel transition, slabs could be subducted to the lower mantle because the mantle would be homogenous across D660, leading to whole-mantle convection. However, if the D660 is not due to the transition, compositionally distinct upper and lower mantles are required to explain the sharp D660, which should imply layered-mantle convection.

If the thickness of D660 primarily corresponds to the pressure interval of the three-phase coexistence of ringwoodite + bridgmanite + ferropericlase in the Mg-Fe binary post-spinel transition, this binary loop must be extremely narrow and have a pressure interval of less than 0.1 GPa. However, such a narrow binary loop has never been demonstrated by high-pressure experiments owing to the following experimental difficulties. (a) The experimental uncertainties in pressure are larger than 0.1 GPa, indicating there is no pressure resolution suitable for evaluating the pressure interval. (b) Sample pressures drop by 0.5–2.0 GPa despite a constant press load and temperature. Such a pressure drop may have led to serious overestimation of the pressure interval [3] because the post-spinel phase remains even in a ringwoodite-stability field owing to the sluggish reversal reaction. Thus, these reasons have made the precise estimation of an extremely narrow pressure interval impossible. An experimental approach with pressure precision better than 0.1 GPa and precise control of a target pressure is essential to examine whether the binary loop is narrow enough to account for the sharp D660.

We determined the phase relations in the system Mg_2SiO_4–Fe_2SiO_4 at around 23 GPa and 1700 K with a combination of advanced multianvil techniques and *in situ* X-ray diffraction using the Kawai-type

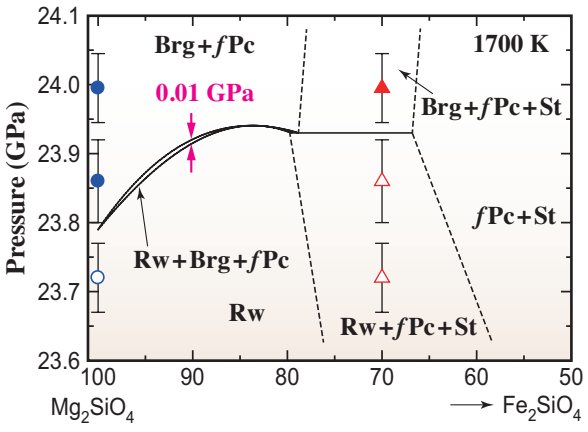

Fig. 1. Phase relations in the system Mg_2SiO_4–Fe_2SiO_4 at 1700 K. The compositions of the three phases (Rw, Brg, and *f*Pc) are shown by solid lines. Dashed lines are rough drawings of the phase boundaries in this system. Open and solid circles indicate the stable phases are Rw and Brg + Pc, respectively. Open and solid triangles indicate that stable phases are Rw + *f*Pc + St and Brg + *f*Pc + St, respectively. Pressures were calculated with the MgO scale using the equation of states reported in Ref. 5. Brg: bridgmanite, *f*Pc: ferropericlase, Rw: ringwoodite, St: stishovite.

multianvil press SPEED-Mk.II at SPring-8 **BL04B1** [4]. We improved the pressure precision to 0.05 GPa by obtaining a wide X-ray path to samples. We also suppressed a pressure decrease by increasing the press load during heating. Two samples with bulk compositions of Mg_2SiO_4 and $(Mg_{0.7}Fe_{0.3})_2SiO_4$ were loaded in a single-cell assembly to simultaneously determine their transition pressures. Since the binary loop of ringwoodite + bridgmanite + ferropericlase ends near the $(Mg_{0.7}Fe_{0.3})_2SiO_4$ composition, this procedure constrains both ends of the binary loop. In combination with thermochemical calculation, we estimated the entire shape of the binary loop to estimate the pressure interval at $(Mg_{0.9}Fe_{0.1})_2SiO_4$.

The binary phase relations determined at 1700 K are shown in Fig. 1. A striking feature is that the difference between the transition pressures in Mg_2SiO_4 and the four-phase coexistence (ringwoodite, bridgmanite, ferropericlase, and stishovite) boundary is 0.14 GPa. The geometry of the phase diagram shows that the pressure interval of the binary loop at $(Mg_{0.9}Fe_{0.1})_2SiO_4$ should be much smaller than this pressure difference. The pressure intervals at $(Mg_{0.9}Fe_{0.1})_2SiO_4$ were quantitatively estimated at 1700 K using compositions of the three phases (bridgmanite, ferropericlase, and ringwoodite) between the Mg endmember and the four-phase coexistence boundary calculated with available thermodynamic data. The pressure interval was found to be 0.012±0.008 GPa at a bulk composition of $(Mg_{0.9}Fe_{0.1})_2SiO_4$ at 1700 K (Fig. 1). This pressure interval corresponds to a depth interval of only 100–500 m, which is one order of magnitude smaller than the observable thickness of D660 (less than 2 km). The pressure interval at an expected mantle temperature (2000 K) was evaluated by the same procedure. We obtained a pressure interval of 0.003±0.002 GPa at 2000 K, which is even smaller than that at 1700 K. Thus, the seismically observed sharpness of D660 is in excellent agreement with our experimental results. This circumstance does not require chemical stratification of the upper and lower mantles, supporting a compositionally homogenous mantle throughout the present-day mantle and whole-mantle convection.

Using available thermodynamic data, we also estimated the possible expansion of the binary post-spinel transition interval up to 7 km owing to the latent heat of the phase transition when mantle flow crosses D660 (Fig. 2). We suggest that global mapping of the sharpness of D660 should be carried out to assess the presence of vertical flows that are faster than thermal diffusion. The present study encourages global seismologists to revisit this topic to obtain new insights into mantle dynamics.

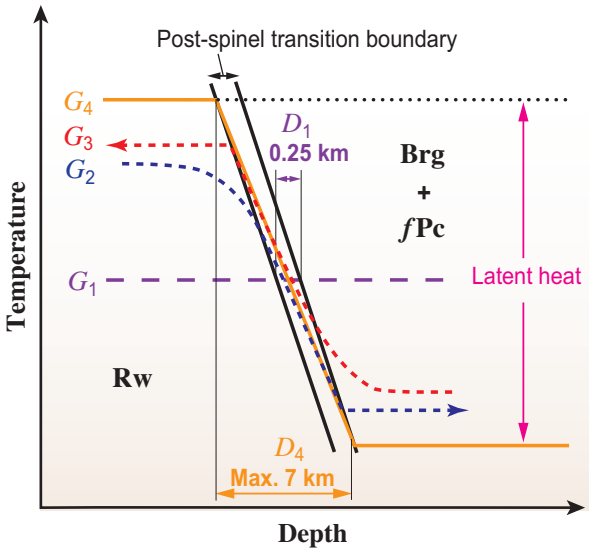

Fig. 2. Expansion of discontinuity thickness of the post-spinel transition boundary owing to latent heat of post-spinel transition. The black solid line is the phase boundary of the post-spinel transition. The isothermal geotherm is shown as G_1 (dashed line), providing a transition thickness of D_1 (0.25 km). The complete adiabatic geotherm is shown as G_4 (yellow solid line), forming D_4 (7 km at most) owing to latent heat (30–90 K). If the geotherm is under intermediate conditions (G_2 and G_3 dashed curves), the latent-heat effect should be smeared out and provide the D660 thickness between D_1 and D_4 (D_2 and D_3) depending on the flow direction. Brg: bridgmanite, fPc: ferropericlase, Rw: ringwoodite.

Takayuki Ishii* and Tomoo Katsura

Bayerisches Geoinstitut (BGI), Universität Bayreuth, Germany

*Email: Takayuki.ishii@Uni-Bayreuth.de

References

[1] F. Xu *et al.*: J. Geophys. Res. **108** (2003) 2024.
[2] Y. Fukao & M. Obayashi: J. Geophys. Res. **118** (2013) 5920.
[3] T. Ishii *et al.*: Sci. Rep. **8** (2018) 6358.
[4] *T. Ishii, R. Huang, R. Myhill, H. Fei, I. Koemets, Z. Liu, R. Myhill, F. Maeda, L. Yuan, L. Wang, D. Druzhbin, T. Yamamoto, S. Bhat, R. Farla, T. Kawazoe, T. Noriyoshi, E. Kulik, Y. Higo, Y. Tange, T. Katsura: Nat. Geosci.* ***12*** *(2019) 869.*
[5] Y. Tange *et al.*: J. Geophys. Res. Solid Earth **114** (2009) B03208.

Laboratory measurements of sound velocities of $CaSiO_3$ perovskite reveal the fate of subducted oceanic crust into the Earth's deep interior

Laboratory measurements of sound velocities of minerals at high pressures and high temperatures play an important role in enabling scientists to interpret seismic data in terms of chemical and mineralogical compositions of the Earth's mantle by direct comparison with global seismic models. Previous studies have demonstrated that velocities of pyrolite, a hypothetical rock derived as a mixture of mid-ocean ridge basalts (MORB) and peridotite, agree well with those of geophysical observations at depths down to ~560 km [1]. There is, however, still no unique interpretation of seismic data at depths below 560 km where pyrolite sound velocities fail to explain the high seismic gradients observed at the bottom of the mantle transition region (MTR; 410–660 km in depth), as well as the low-velocity zones beneath the 660-km discontinuity. Recent seismic tomography studies revealed that the oceanic lithosphere descend into the deep mantle at subduction zones [2], forming at these depths, gravitationally stable layers of chemically distinct materials such as MORB or harzburgite, which constitute the main bodies of the subducted slab. However, what exactly happens to those slab components as they remain deep into the mantle remains relatively unknown.

Calcium silicate perovskite (CaPv) constitutes 7–10 vol% pyrolite and up to 30 vol% MORB below a depth of ~560 km and therefore is an important constituent mineral in both the peridotitic mantle and basaltic crust in the MTR and lower mantle. Despite this importance, measurements of its sound velocity under the corresponding P, T conditions have never been performed because this phase is unquenchable to atmospheric pressure and adequate samples for such measurements are unavailable. This lack of constraints leads to unresolved debates as to whether pyrolite and MORB can reproduce seismic velocity profiles throughout the mantle.

We measured simultaneously the sound velocity and density of CaPv using ultrasonic interferometry combined with synchrotron X-ray techniques and the multianvil apparatus at SPring-8 **BL04B1** [3] (Fig. 1). Starting from a $CaSiO_3$ glass rod, a polycrystalline sintered body of CaPv was first synthesized *in situ* at 21 GPa and 1300 K. Once the transformation is confirmed from the diffraction peaks of CaPv (Fig. 1(d)), the travel times of P- and S-waves (Fig. 1(b)), sample length (Fig. 1(c)), and density (Fig. 1(d)) are measured following the procedures described in [3]. Five independent experiments were carried out at pressures up to 23 GPa and temperatures of 700–1700 K in the stability field of the cubic CaPv. The thermoelastic properties (e.g., K_S: adiabatic bulk modulus, G: shear modulus) were determined using our experimental P- and S-wave velocities and densities (Fig. 2). We found that cubic CaPv has a

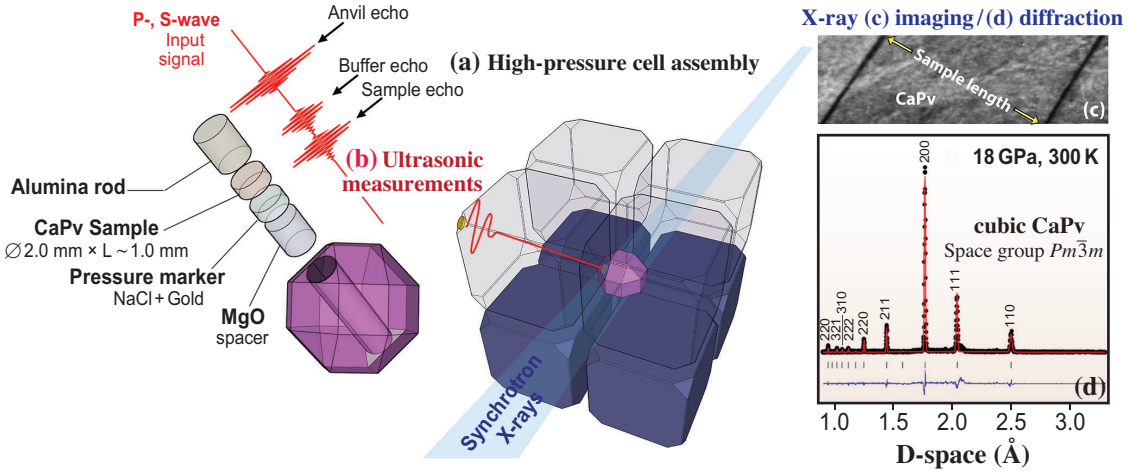

Fig. 1. Schematic diagram of the ultrasonic measurements at BL04B1. **(a)** Eight WC anvils are used to compress the cell assembly to the target pressure. **(b)** Travel times of P- and S-waves were measured by recording arrival times of the acoustic echoes at the buffer rod and sample interfaces. **(c)** Sample length was determined by X-ray imaging techniques. **(d)** CaPv density and pressure were determined *in situ* from the X-ray diffraction pattern of the sample and the gold pressure marker, respectively.

shear modulus G_0 = 126(1) GPa, which is about ~26% lower than theoretical predictions (~171 GPa) [4], leading to substantially lower shear velocities in CaPv-bearing compositions than those predicted under the *P*, *T* conditions of 660–770 km depths.

Our CaPv elasticity data, combined with those from previous experimental studies show that shear velocity increments due to the formation of CaPv in pyrolite and MORB are insufficient to explain the high shear-wave velocities below a depth of ~560 km [3] and suggest the presence of a nearly pure harzburgite region (Fig. 3) at the bottom of the MTR. The basaltic crust in the remaining part of the stagnated slab would descend to the lower mantle where it should remain trapped owing to the density contrast between MORB and the pyrolitic mantle changing at a depth of ~780 km. Our results show that the discrepancy between the velocities of pyrolite and those of seismological models at depths of 660–780 km can be reconciled if ~20–30 vol.% MORB is globally present in this region (Fig. 3), which is consistent with the recent discovery of CaPv in natural diamond [5]. Our results also provide further evidence for the presence of oceanic crust materials in the uppermost lower mantle. Basalt enrichment below 660 km would stabilize regimes of slab stagnation above this depth of 660 km, in the MTR, and down to a depth of ~1000 km in the lower mantle, as predicted by global-scale geodynamics calculations [6]. CaPv, which has velocities substantially lower than those of bridgmanite, should greatly contribute in tracing the existence and recycling of the former oceanic crust in the Earth's lower mantle.

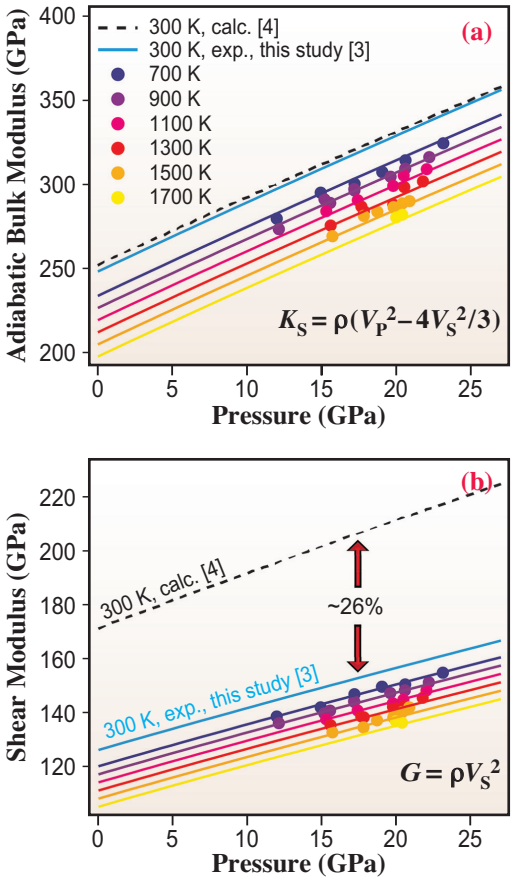

Fig. 2. **(a)** Adiabatic bulk and **(b)** shear moduli of CaPv as functions of pressure and temperature determined in our experimental study, compared with those determined in a previous theoretical study [4]. Cubic CaPv has a shear modulus that is about ~26% lower than theoretical predictions [3,4].

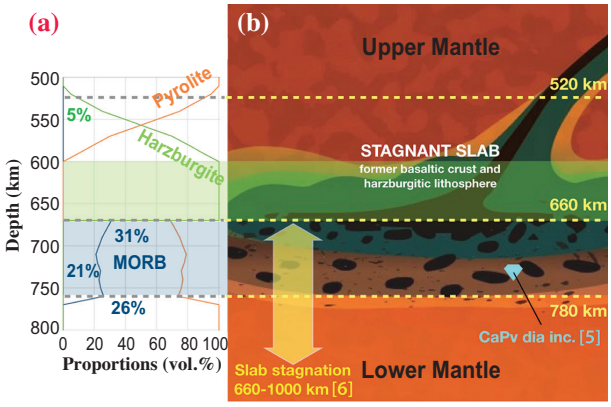

Fig. 3. **(a)** Estimates of mineralogical proportions of harzburgite and MORB relative to that of pyrolite, on the basis of shear wave velocity model. **(b)** Schematic of mantle regions beneath subduction zones. The high seismic velocities above a depth of 660 km is explained by the gradual increase of harzburgite components from ~500 to 600 km, below which a nearly pure harzburgite region should be formed. The basaltic crust, which is denser than pyrolite and harzburgite in the MTR but less dense than those two in the lower mantle, is likely to remain trapped at depth between 660 and 780 km.

Steeve Gréaux[a,b,*] and Tetsuo Irifune[a,b]

[a] Geodynamics Research Center, Ehime University
[b] Earth-Life Science Institute, Tokyo Institute of Technology

*Email: greaux@sci.ehime-u.ac.jp

References

[1] T. Irifune *et al.*: Nature **451** (2008) 814.
[2] Y. Fukao & M. Obayashi: J . Geophys. Res. **118** (2013) 5920.
[3] *S. Gréaux, T. Irifune, Y. Higo, Y. Tange, T. Arimoto, Z. Liu and A. Yamada: Nature **565** (2019) 218.*
[4] L. Stixrude *et al.*: Phys. Rev. B **75** (2007) 024108.
[5] F. Nestola *et al.*: Nature **555** (2018) 237.
[6] M.D. Ballmer *et al.*: Sci. Adv. **1** (2015) e1500815.

Earth's cooler core inferred from new resistance-heated diamond-anvil-cell experiments

The center core of the Earth is mainly composed of metallic iron. Since the liquid core coexists with the solid at the inner core boundary (ICB), the melting temperature of iron at ICB of 5100 km depth provides us an important constraint of the temperature of the Earth. Many researchers have conducted experiments to determine the melting temperature of the iron under high-pressure conditions corresponding to those at the ICB. A pioneering ultrahigh-pressure laser-heated diamond anvil cell (DAC) experiment performed by Boehler [1] showed the melting temperature of iron up to 200 GPa, in which melting was judged visually as the onset of convective motion. Extrapolation of Boehler's melting curve gives the melting point of iron to be 4850±200 K at 330 GPa corresponding to the pressure at ICB. The melting curve of iron has then been repeatedly examined by laser-heated DAC studies (e.g., Anzellini *et al.* [2]), but the results have been markedly different from each other. Anzellini and others found the melting point of iron to be 6230±500 K at 330 GPa by extrapolating their results from 200 GPa. These conflicting results are likely to be due to large spatial and temporal temperature variations, especially in the direction parallel to the compressional axis, in laser-heated DAC samples. Another source of the discrepancy may be the difference in the melting criterion employed in previous studies. Furthermore, the previous DAC experiments were carried out only up to 200 GPa and thus required long extrapolation to 330 GPa, which is another source of a large uncertainty. Here we employed internal-resistance-heated DAC techniques, which stabilize the sample temperature during heating compared with conventional laser heating [3]. Experiments were carried out up to 290 GPa and 5360 K, far beyond the pressure and temperature (*P*–*T*) rrange ever achieved in earlier internal-resistance-heated DAC studies (<100 GPa, <2000 K) (e.g., Komabayashi *et al.* [4]). The melting temperature of iron was determined on the basis of the change in the voltage–temperature relation to 290 GPa, close to the pressure at the ICB.

High-pressure melting experiments were conducted using an internal-resistance-heated DAC (Fig. 1). Pure iron foil with a thickness of 1 μm was fabricated with a focused ion beam system (FEI Versa 3D DualBeam); the central part of the foil was narrowed to locate a hot spot and generate temperature high enough to melt iron. The foil was loaded between the Al_2O_3 thermal insulation layers and connected to an electrode several millimeters away from the culet. After compression to a desired pressure, direct electrical current was applied to the iron foil for heating. Ramp rates were typically several hundred millivolts per second. One-dimensional temperature profiles were obtained parallel to the view given in Fig. 1 by a spectroradiometric method [5]. Synchrotron XRD measurements were conducted at SPring-8 **BL10XU** (Fig. 2) [5]. A monochromatic X-ray beam with a wavelength of 0.413–0.415 Å was collimated to 6 μm at full width of half maximum (FWHM) in runs performed below ~150 GPa and to 2 μm at higher pressures. Angle-dispersive XRD patterns were collected on a flat panel detector (PerkinElmer XRD 0822) with a typical exposure time of 1 sec.

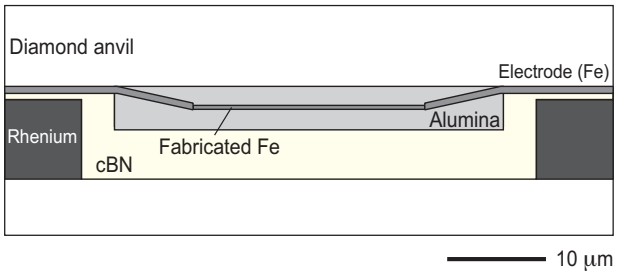

Fig. 1. Sample configurations for internal-resistance-heated DAC experiments.

We obtained the voltage–temperature relationship for the iron sample during heating by applying electricity. The sample temperature increased with increasing applied voltage; however, after reaching a certain temperature, the temperature started fluctuating. At the same time, we observed an anomaly in the voltage–resistance curve. In addition, the voltage–resistance relationship became no longer identical during the temperature increase and decrease (note the same voltage–resistance path during increasing and decreasing voltage unless such temperature fluctuation occurred at some point). Seventeen separate runs were performed between 6 and 290 GPa to determine the melting temperature of iron (Fig. 3) on the basis of the applied voltage–sample temperature relationship. In a run at around 90GPa, when we heated hcp Fe, the fcc phase appeared above 2770 K at 92 GPa, consistent with the result of an earlier experiments on the fcc–hcp boundary. The

XRD peaks corresponding to fcc then diminished with further temperature increase to 3030 K, coinciding with the onset of sample temperature fluctuation. After the high *P–T* experiment, we recovered this sample from the DAC and observed a clear melting texture in its cross section. The melting temperature of iron should therefore be 3030±150 K at 97 GPa. Even at higher pressures, we successfully observed the onset of fluctuation in the voltage–temperature relationship and obtained the melting point of iron to 290 GPa, which is well above the pressure range examined in previous DAC studies (< 200 GPa).

The melting point of pure iron, 5500±220 K at 330 GPa (Fig. 3), gives the upper limit for the temperature at ICB, since the liquid outer core includes light elements that depress the melting temperature. The combination of 2 wt% Si and 3.6 wt% O (or 0.7wt% H) indeed gives the least depression of the outer core liquidus temperature by 380 (±170) K, although an Fe–Si–O liquid core is also unlikely [6]. Therefore, the ICB temperature should be lower than 5120±390 K. These values also give the upper bound for the temperature at core-mantle boundary (CMB) to be 3760±290K by employing the outer core density profile and the Grüneisen parameter $\gamma = 1.5$. It is certainly lower than the dry solidus temperature of ~4150 K for a pyrolitic/chondritic mantle at the CMB, consistent with the fact that the bottom of the mantle is presently not molten globally. The recent core energetics modeling by Hirose *et al.* [6] demonstrated that maintaining a geodynamo with 1 TW ohmic dissipation requires a core cooling rate of as low as 100 K/Gyr when we consider SiO_2 crystallization at the CMB. If the current CMB temperature is ≥4000K, the minimum core cooling rate of 100 K/Gyr leads to the global melting of the lowermost mantle at least 1.5 Gyr ago.

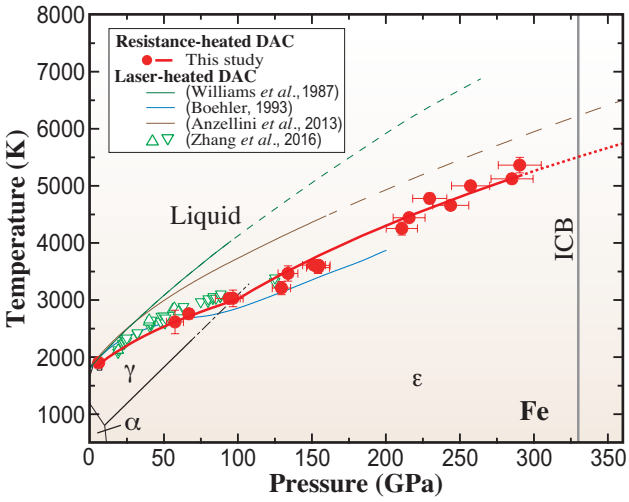

Fig. 3. Melting curve of iron at high pressure. Red closed circles are the onset of melting and the red line is the fitted melting curve (this study). Melting curves from previous reports are shown for comparison.

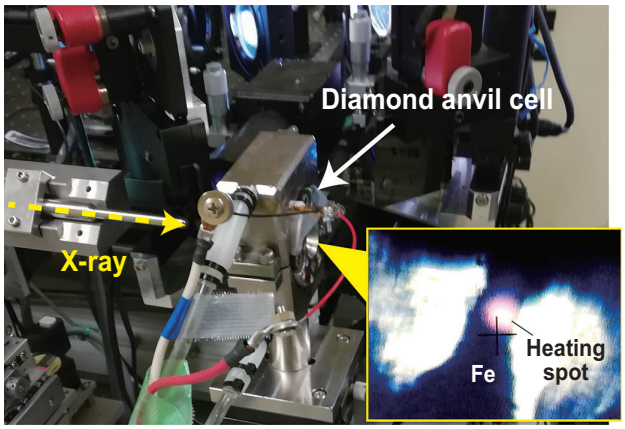

Fig. 2. Overview of the experimental setup at BL10XU, SPring-8. Inset shows an optical microscopy image during heating.

Ryosuke Sinmyo[a,b,*], Kei Hirose[a,b] and Yasuo Ohishi[c]

[a] Earth-Life Science Institute, Tokyo Institute of Technology
[b] Department of Earth and Planetary Science, The University of Tokyo
[c] Japan Synchrotron Radiation Research Institute (JASRI)

*Email: sinmyo@meiji.ac.jp

References

[1] R. Boehler: Nature **363** (1993) 534.
[2] S. Anzellini *et al.*: Science **340** (1993) 464.
[3] *R. Sinmyo, K. Hirose, Y. Ohishi: Earth Planet. Sci. Lett.* ***510*** *(2019) 45.*
[4] T. Komabayashi *et al.*: Phys. Chem. Miner. **39** (2012) 329.
[5] Y. Ohishi *et al.*: High Pres. Res. **28** (2008) 163.
[6] K. Hirose *et al.*: Nature **543** (2017) 99.

Imaging fossil asteroidal ice in primitive meteorite by synchrotron radiation-based X-ray computed nanotomography

In the early Solar System, dust grains accreted to form planetesimals, and subsequent collisions and coalesce of planetesimals formed large planets. Some planetesimals that formed in the outer cold region are considered to have contained some ice upon formation. There are many meteorites showing evidence of aqueous alteration caused by ice melting in their parent bodies. However, researchers have yet to discover how the primordial ice was distributed in the meteorite parent bodies. This is largely due to complex secondary processes (e.g., aqueous alteration, brecciation) that affect most meteorites and destroy primordial information. Recently, we performed X-ray nano-computed tomography (XCT) of the Acfer 094 meteorite, which has been little affected by such modification, to determine the ice distribution in its parent body [1].

XCT was performed at SPring-8 **BL47XU**. We prepare two microsamples (~25×25×30 μm) from Acfer 094 meteorite chips by a focused ion beam technique. The samples were analyzed by two different XCT methods: dual energy tomography (DET) [2] and scanning imaging X-ray microtomography (SIXM) [3]. In the DET method, we obtained three-dimensional (3D) images with X-ray linear attenuation coefficients (LACs) at two different X-ray energies, one above and one below the *K*-absorption edge energy of iron: 7 and 8 keV, respectively. The images at 7 keV correspond closely to the compositional (*Z*) contrast, and those at 8 keV clearly show Fe-rich materials. In the SIXM method, we simultaneously obtained 3D images of both X-ray absorption contrast with LACs and X-ray phase contrast with refractive index decrements (RIDs), where the refractive index = 1−RID and RID corresponds to material density. These XCT images (Fig. 1) revealed three extremely porous regions in the two samples at a ~10 μm scale. We call these regions "ultraporous lithology (UPL)." The nondestructive observations ensure that the UPLs were originally present in this meteorite. 2D histogram plots of LAC and RID values indicate that the samples consist mainly of hydrous amorphous silicates (Fig. 2), which was confirmed by transmission electron microscopy observation of thin sections extracted from the CT samples. These suggest that the meteorite underwent aqueous alteration.

We performed scanning electron microscopy observation of polished surfaces of meteorite chips to search for more UPLs and found numerous UPLs. UPLs with abundant pores are fragile. Nevertheless, the UPLs showed no evidence of pore compaction, which was expected to have occurred during the parent body accretion. This suggests that the pores in UPLs were originally filled with some solid material(s). It is reasonable to consider that some ice, a major component in the early Solar System, once filled the pore spaces and subsequently disappeared owing to its evaporation and/or melting. That is, UPLs represent fossils of ice in the meteorite parent body. Melting of the ice is expected to have caused hydration of amorphous silicates. The ice abundance estimated on the basis of the pore fraction in UPLs is, however, too low to justify the observed aqueous alteration. This suggests that the distribution of ice was heterogeneous and that ice was much more abundant elsewhere in the parent body.

We propose that the inhomogeneous ice distribution originated during the meteorite parent body formation by dust agglomeration during radial migration from the outer to inner regions of the early Solar System

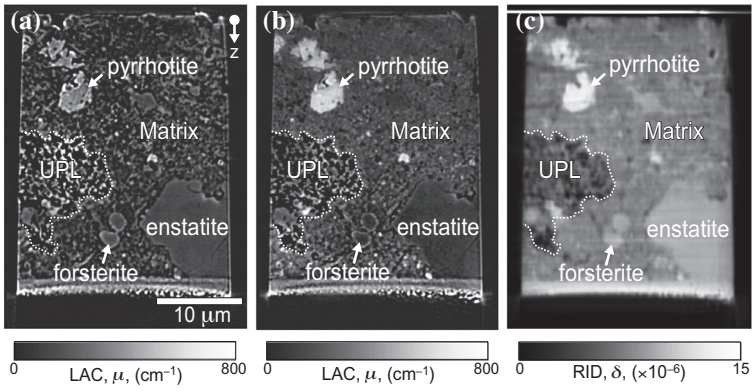

Fig. 1. XCT slice images of a microsample of the Acfer 094 meteorite. Absorption XCT images at 7 **(a)** and 8 keV **(b)**, and a phase XCT image **(c)** showing a UPL embedded in the matrix. Mineral names and compositions: pyrrhotite ($Fe_{1-x}S$); forsterite (Mg_2SiO_4); enstatite ($MgSiO_3$).

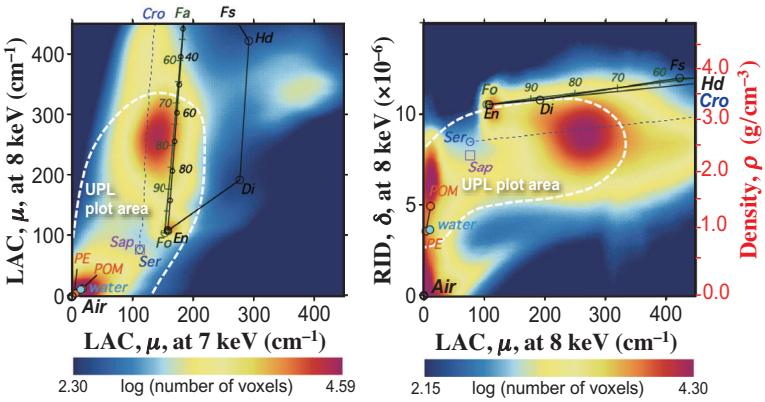

Fig. 2. 2D histograms of LAC and RID values of a microsample of the Acfer 094 meteorite at 7 and 8 keV. The histograms show peaks around air, resin, forsterite (Fo: Mg_2SiO_4), enstatite (En: $MgSiO_3$), and serpentine (Ser: $Mg_3Si_2O_5(OH)_4$) – cronstedtite (Cro: $Fe_2((Si,Fe)_2O_5)$). Other mineral names and compositions: Sap, saponite [$Ca_{0.25}(Mg,Fe)_3((Si,Al)_4O_{10})(OH)_2{\cdot}nH_2O$]; Fa, fayalite ($Fe_2SiO_4$); Di, diopside ($MgCaSi_2O_6$); Hd, hedenbergite ($FeCaSi_2O_6$); Fs, ferrosilite ($FeSiO_3$); PE, polyethylene [$(C_2H_4)_n$], POM, polyacetal [$(CH_2O)_n$].

across the H_2O snow line (SN). Recent theoretical studies [4] suggest that planetesimals and planets underwent such radial migration in the early stage of Solar System evolution. In the outer region beyond the SN, ice-rich dust accreted into the parent body first; subsequently, in the inner region, ice-free dust accreted. This process would produce a radial variation of ice abundance in the parent body.

On the basis of the above discussion, we propose the following model (Fig. 3). (i) The meteorite parent body grew from fluffy silicate dust with and without ice through radial migration from the outer to inner regions of the early Solar System across the SN. "Fluffy dust" denotes the general model of dust that formed the planets [5]. (ii) Around the SN, solid ice-silicate aggregates, which were formed by the sintering of ice in the fluffy dust, were incorporated into the meteorite parent body. The aggregates correspond to UPL precursors (ice-bearing UPLs). (iii) Subsequently, an aqueous alteration induced by ice melting took place in the parent body. A major part of the water was supplied from the ice-rich core.

The radial migrations of ice-bearing asteroids could have supplied some water to the inner forming region of the Earth. Therefore, our findings would be important to the understanding of not only icy asteroid formation but also the origin of water on the Earth.

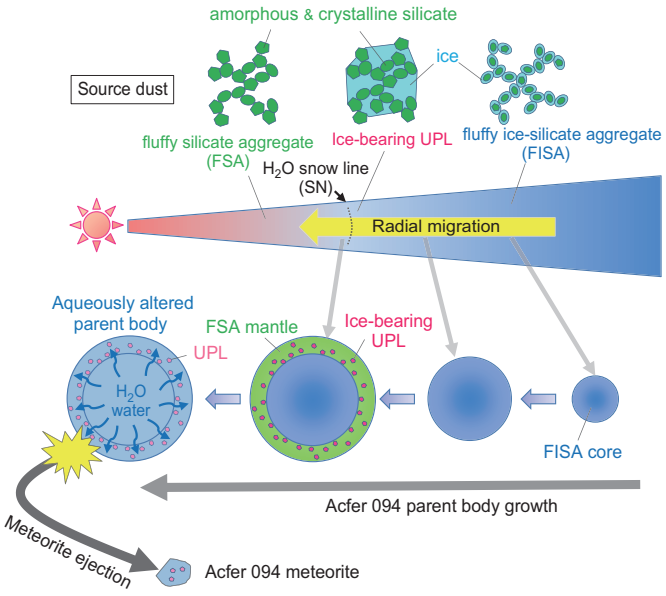

Fig. 3. Schematic illustration of the Acfer 094 meteorite parent body formation model. The parent body grew by agglomeration of fluffy dust with and without ice through its radial migration from the outer to inner regions of the solar nebula across the SN. The process produced a layered structure inside the parent body, with an ice-rich core and an ice-poor mantle. Around the SN, ice-bearing UPLs formed by sintering of ice were incorporated into the mantle. Subsequently, the melting of ice, mainly in the core, induced an aqueous alteration in the parent body.

Megumi Matsumoto

Department of Earth and Planetary Materials Science, Tohoku University

Email: m_matsumoto@tohoku.ac.jp

References

[1] *M. Matsumoto, A. Tsuchiyama, A. Nakato, J. Matsuno, A. Miyake, A. Kataoka, M. Ito, N. Tomioka, Y. Kodama, K. Uesugi, A. Takeuchi, T. Nakano and E. Vaccaro: Sci. Adv.* ***5*** *(2019) eaax5078.*
[2] A. Tsuchiyama *et al.*: Geochim. Cosmochim. Acta **116** (2013) 5.
[3] A. Takeuchi *et al.*: J. Synchrotron Rad. **20** (2013) 793.
[4] K.J. Walsh *et al.*: Meteorit. Planet. Sci. **47** (2012) 1941.
[5] A. Kataoka *et al.*: Astron. Astrophys. **557** (2013) 4.

Investigation of crystallographic deformation by converse piezoelectric effect of piezoelectric thin films

Piezoelectric materials, such as lead zirconate titanate Pb(Zr,Ti)O_3 (PZT), can convert mechanical energy to electrical energy, and vice versa, through direct and converse piezoelectric effects. For PZT, it is known that the morphotropic phase boundary (MPB) composition, which is the interface between the tetragonal (*P*4*mm*) and rhombohedral (*R*3*m*) phases, provides superior dielectric and piezoelectric properties [1]. PZT thin films have been widely developed for use in microelectromechanical systems (MEMS) such as sensors, actuators, and energy harvesters [2]. The piezoelectric properties of PZT thin films are different from those of their bulk ceramic counterparts because they are affected by many factors, including crystal quality, crystal orientation, and internal stresses from substrates [3]. Therefore, investigation of the fundamental properties of piezoelectric thin films is of great significance to improve MEMS devices.

Continuous efforts have been made to evaluate the origin of piezoelectric effects by *in situ* characterization methods. Recently, we have developed a simple and precise method to measure the effective piezoelectric coefficients ($e_{31,f}$) of PZT thin films using unimorph cantilevers [4]. Their piezoelectric properties are considered to arise from intrinsic and extrinsic contributions. Intrinsic contributions are associated with crystal lattice deformation (such as elongation and shrinkage), whereas extrinsic contributions originate from collective lattice distortions caused by domain rotations or phase transitions. Our previous study demonstrated that the piezoelectric properties of polycrystalline PZT thin films are better than those of epitaxial PZT thin films, probably because of the large extrinsic contributions to such films.

In this study, we investigated the crystallographic deformation of PZT thin films by *in situ* X-ray diffraction (XRD) measurements using synchrotron radiation to clarify the crystallographic factors contributing to their piezoelectric properties. We evaluated both epitaxial and polycrystalline PZT thin films with MPB compositions. Our study demonstrated the change in the crystal structure under applied direct current (DC) voltage, which is consistent with the polarization-electric field (*P*-*E*) hysteresis loop [5].

We prepared epitaxial PZT thin films on (001) Pt/MgO substrates and polycrystalline PZT thin films on (111)Pt/Ti/SiO_2/Si substrates. Both films were approximately 3 μm thick and were fabricated by rf-magnetron sputtering. The Zr/Ti ratio was approximately 52/48, which is same as to the MPB composition. *In situ* XRD measurements were carried out using synchrotron radiation (λ = 0.1 nm) at SPring-8 **BL19B2** and **BL46XU**. Figure 1 shows a schematic illustration of the experimental setup for *in situ* XRD measurements in the surface normal (out-of-plane) direction and the vertical (in-plane) direction. Here, specimens were not subjected to electrical poling treatments before measurement. Figure 2(a) shows the PZT *004* peak at various DC voltages and the variation in the *c*-axis lattice parameter determined from the observed peak positions. The diffraction peaks shifted toward lower angles with increasing negative voltage and vice versa. The relative changes in the *c*-axis lattice parameter as a function of electric field represent the reversible elongation and contraction of the crystal structure along the electric field bias magnitude and direction. We also ascertained the reversible in-plane peak shifts in Fig. 2(a). The reversible contraction and elongation behavior of the *a*-axis lattice parameter was confirmed, as shown in Fig. 2(b). The electric field dependence

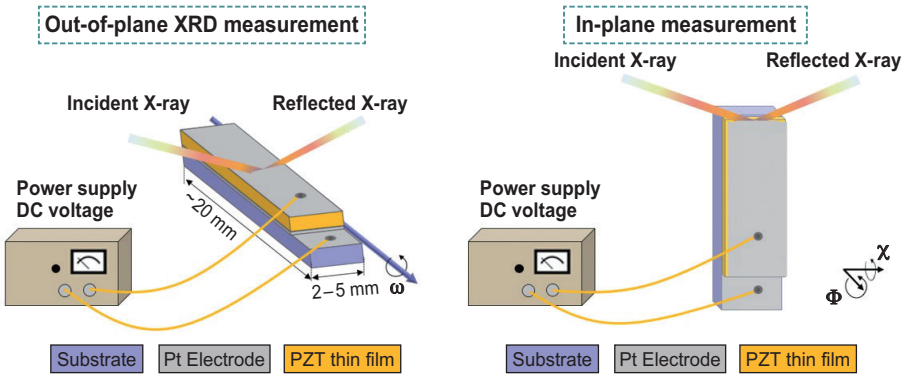

Fig. 1. Schematic illustration of the experimental setup for out-of-plane and in-plane XRD measurements under DC voltages.

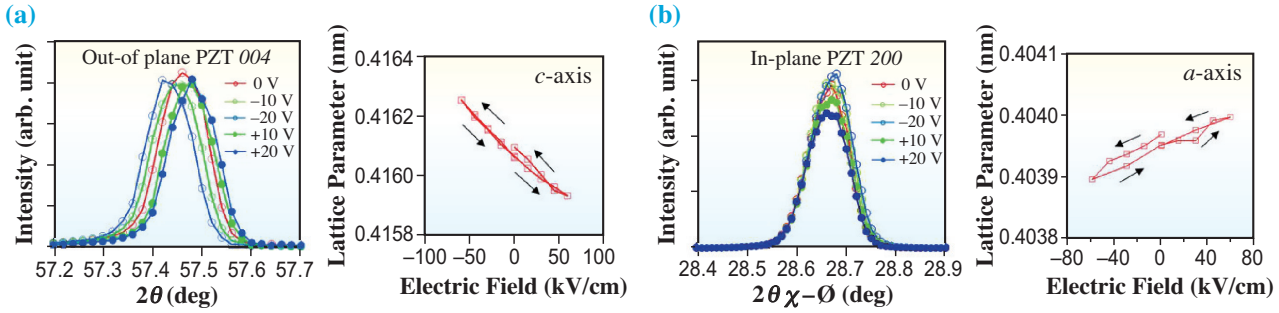

Fig. 2. (**a**) Out-of-plane XRD patterns of the epitaxial PZT thin film obtained at the PZT *004* peak at various DC voltages and *c*-axis lattice parameters as functions of electric field. (**b**) In-plane XRD patterns obtained at the PZT *200* peak at various DC voltages and *a*-axis lattice parameters as functions of electric field.

of the in-plane lattice parameter indicates behavior opposite to that of the out-of-plane case. This result is consistent with the observation that when the out-of-plane crystal lattice is stretched along the forward electric field, the in-plane crystal lattice shrinks and vice versa.

We then investigated the polycrystalline PZT thin film on a Si substrate. Figure 3(a) shows a synchrotron XRD θ–2θ pattern around the PZT *004* peak at various applied DC voltages. The polycrystalline PZT *004* peak is much broader than the epitaxial PZT peak (Fig. 2(a)). This broad peak is successfully decomposed into a rhombohedral *004* and tetragonal *400* and *004* peaks, as shown in the right graph of Fig. 3(a), indicating a slight amount of the tetragonal phase coexists. Figure 3(a) shows a clear shift in the diffraction peak for both positive and negative biases, and the peaks are shifted toward higher angles only when a voltage of +5 V is applied. Figure 3(b) shows the field-induced variation of the *c*-axis lattice parameter superimposed with the *P*–*E* hysteresis loop measured at 1 kHz. The *c*-axis lattice parameter exhibits a butterfly curve that arises from the inverse polarization effect. This behavior is consistent with the coercive electric field determined from the *P*–*E* hysteresis loops. Note that the coercive electric field of the polycrystalline PZT thin film is much smaller than that of the epitaxial PZT thin film. It was also confirmed that the field-induced strain of the polycrystalline PZT thin film was much larger than that of the epitaxial PZT thin film. This was probably due to the large extrinsic effects such as a crystalline phase transition and domain reorientation. These large extrinsic effects are considered to enhance the macroscopic piezoelectric properties. Our direct observation of crystallographic deformation paves the way to improving the piezoelectric properties of piezoelectric thin films for the application of novel piezoelectric MEMS devices.

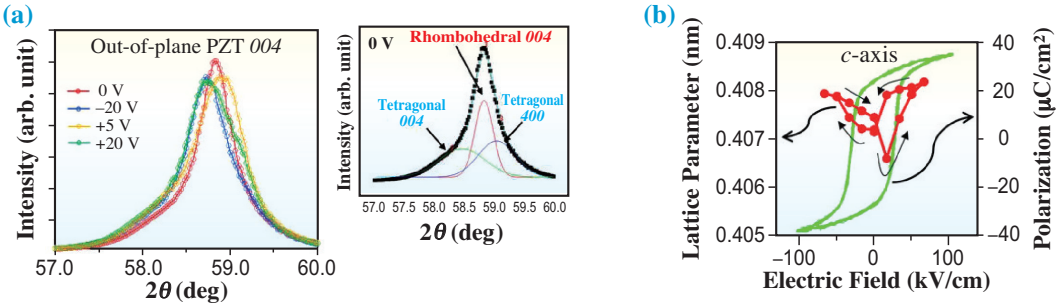

Fig. 3. (**a**) Out-of-plane XRD patterns of the polycrystalline PZT thin film at the PZT *004* peak at various DC voltages. The right graph shows fitted curves of PZT peaks of rhombohedral and tetragonal phases. (**b**) Variation in *c*-axis lattice parameter as a function of electric field, superimposed with the *P*-*E* hysteresis curve measured at 1 kHz.

Goon Tan and Isaku Kanno*

Department of Mechanical Engineering,
Kobe University

*Email: kanno@mech.kobe-u.ac.jp

References

[1] X. Du *et al.*: Appl. Phys. Lett. **72** (1998) 2421.
[2] P. Muralt *et al.*: MRS Bull. **34** (2009) 658.
[3] I. Kanno *et al.*: J. Appl. Phys. **93** (2003) 4091.
[4] *Y. Tsujiura, S. Kawabe, F. Kurokawa, H. Hida and I. Kanno: Jpn. J. Appl. Phys. **54** (2015) 1.*
[5] G. Tan *et al.*: Scientific Rep. **9** (2019) 7309.

Revealing interfacial chemistry between metal and polymer by hard X-ray photoelectron spectroscopy

The interfacial chemistry between metals and polymers has been one of the most important topics in materials science and engineering because of its broad applications based on metal/polymer junctions. Polyimide (PI) has been widely used in various applications including automobiles and semiconductors because of its excellent heat resistance and mechanical strength. Fabrication process for metal/PI junctions can be classified into two main categories. Process A involves the formation of a metal layer on a PI substrate. Process B involves the use of a PI precursor, polyamide acid (PAA), and its subsequent imidization onto the metal substrate. To investigate the chemistry of materials, X-ray photoelectron spectroscopy (XPS) is the most effective method. The nondestructive use of XPS with a conventional X-ray source (e.g., Al-$K\alpha$) requires the fabrication of samples with an interface with a depth of several nanometers from the sample surface because of the analysis depth of XPS. One approach involves the formation of several atomic layers of metal on PI by vapor deposition (VD); the interface can be analyzed by conventional XPS together with other analytical techniques [1]. This approach simulates Process A. On the other hand, the study of interfaces formed by Process B is extremely limited [2]. This is due to the lack of fabrication techniques to simulate Process B and produce samples suitable for surface analyses, including XPS. We proposed a new fabrication technique for a metal/PI bilayer structure [3]. This technique is considered for Process B. Figure 1 shows a schematic illustration of the technique: 1. A SiO_2 layer is deposited on a GaAs wafer by plasma-enhanced chemical vapor deposition (PECVD). 2. A metal layer is deposited on the SiO_2 layer by resistance heating vacuum deposition (RHVD). 3. A PAA coating solution is applied to the metal layer by the doctor-blade method and then imidized by heat treatment to obtain a PI film. A PI/metal/SiO_2/GaAs layer structure can thus be obtained. 4. The sample is turned upside down. 5. The GaAs wafer is peeled from the SiO_2 film (the GaAs/SiO_2 interface can be very easily exfoliated). 6. The SiO_2 layer is selectively removed by reactive ion etching (RIE), thus obtaining the metal and PI bilayer. We emphasize that the metal layer thickness in Step 2 can be accurately tuned in 1 nm increments by controlling the deposition conditions. We fabricated a Cu (of 30 nm thickness) and PI bilayer sample by this technique. A sample was also fabricated by a conventional VD: a PI film was prepared on a similar GaAs substrate, followed by RHVD of a Cu layer (30 nm) directly on the PI film. These samples are denoted as A-30 (conventional technique) and B-30 (proposed technique).

To investigate elemental distributions and chemical states around the Cu/PI interface, time-of-flight secondary ion mass spectrometry was performed for PI without Cu, A-30, and B-30. Figure 2 presents intensity depth profiles of secondary ions for the three samples. Cu_3 is derived from the 30-nm-thick Cu layer, and C_6 and C_3N originate from the PI layer. Here, we can observe differences in the C_6 and C_3N profiles between A-30 and B-30. The counts of C_6 and C_3N secondary ions detected in the depth range of 0–50 nm from the top of the Cu layer were calculated as follows. The C_6+C_3N intensity of A-30 (3.2×10^5) was almost equal to that of B-30 (3.3×10^5), the C_6 intensity of B-30 (1.6×10^5) was larger than that of A-30 (1.1×10^5), and the C_3N intensity of A-30 (2.1×10^5) was larger than that of B-30 (1.7×10^5). This is attributed to PI decomposition with the concentration of nitrogen-related chemical species in the A-30 Cu/PI interface region. Indeed, Miyamura suggested that the PI decomposes after heat treatment of a Cu/PI sample fabricated by conventional VD [4]. Here we found that PI decomposes during the deposition of Cu on the PI layer at room temperature, i.e., high-kinetic-energy evaporated Cu atoms can decompose PI.

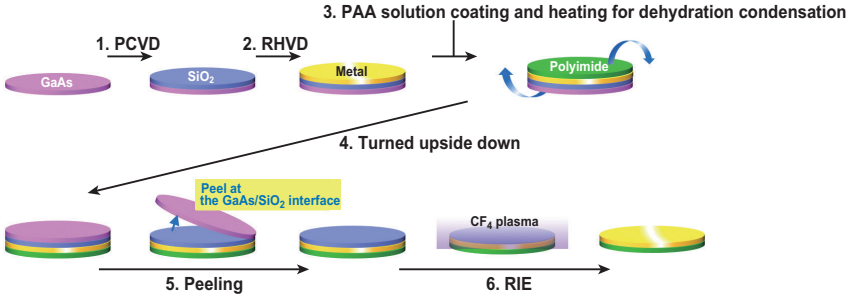

Fig. 1. Schematic of the procedures for the fabrication of a sample modeled on Process B.

For the oxygen-related secondary ions in Fig. 2, Cu_3O, Cu_2O_3H, and Cu_4O_4 originating from Cu_2O, Cu hydroxides, and CuO, respectively, could be detected. The amounts of the three fragments at the Cu/PI interface are larger for A-30 than for B-30, which is attributed to the suppression of interfacial oxidation for B-30. These results are consistent with those of scanning transmission electron microscopy [3,5]. For A-30, the Cu/PI interfacial oxidation is mainly induced by O_2 gas that permeates through the PI layer after interface formation. For B-30, the PI film is formed in Step 3 (Fig. 1) on the Cu layer, the surface of which was atmospherically oxidized after Step 2. O_2 gas permeates through the PI layer, which then oxidizes the Cu layer after formation of the interface in B-30; therefore, it is reasonable to consider that the interfacial oxidation of B-30 progresses to an equal or greater extent than that of A-30. However, opposite was observed in experimental observations. Accordingly, we can deduce that the chemical bonding between Cu and PI suppresses the oxidation of the interface.

Hard X-ray photoelectron spectroscopy (HAXPES) measurements of A-30, and B-30 were performed at SPring-8 **BL16XU** and **BL46XU**. The XPS spectrum of the PI surface was obtained using commercial Al-$K\alpha$ XPS equipment. Figure 3 shows the N 1*s* spectra of PI, A-30, and B-30. The spectrum of PI consists of a single component, C-N in PI (400.8 eV), whereas the N 1*s* spectrum of A-30 consists of two components, one at 400.8 eV and the other at *ca.* 398.6 eV. For B-30, peaks were confirmed at around 403.5 eV, 400.0 eV, and 398.6 eV. We postulate that the 398.6 eV peak is attributable to the ionic bonding between Cu and N in the open-ring part of PI. The strong interaction between Cu and N probably hinders the subsequent formation of the interfacial oxidation layer by O_2 gas that permeates through the PI layer.

This analysis protocol can also be broadly utilized for the investigation of various interfaces fabricated by metal deposition on a polymer or polymer coating on a metal, which are significant in a wide range of engineering fields.

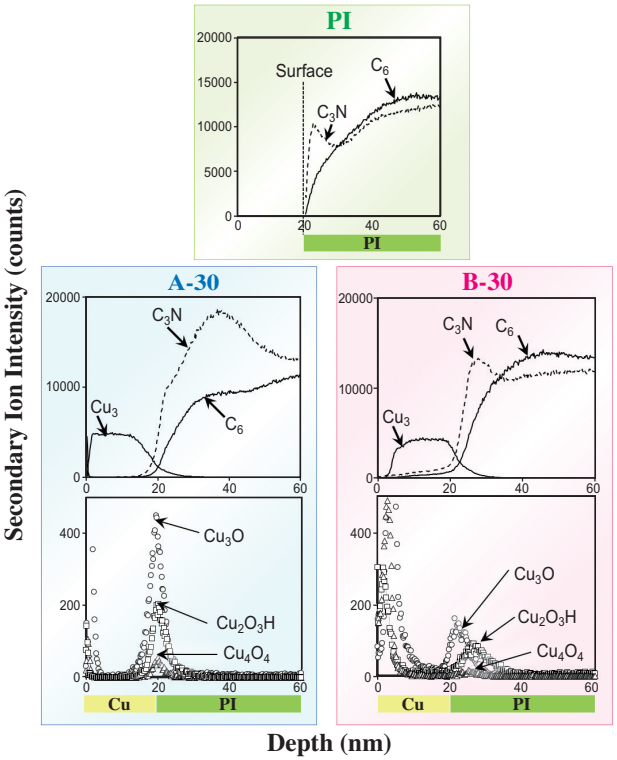

Fig. 2. Time-of-flight secondary ion mass spectrometry depth profiles of the secondary ion intensities for PI, A-30, and B-30. The profiles of secondary ions related to carbon, nitrogen, and copper (upper) and oxygen (lower) are shown separately in the A-30 and B-30 profiles for clarity.

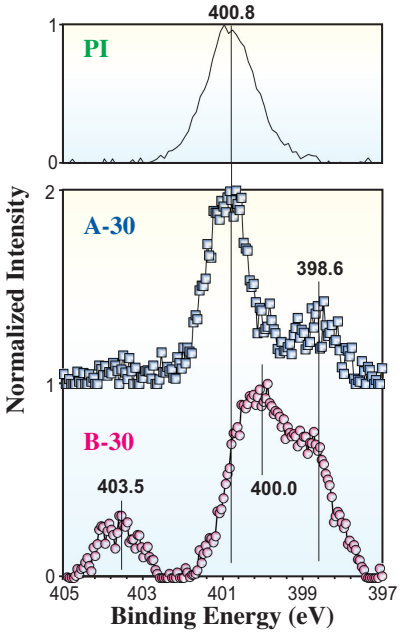

Fig. 3. Normalized Al-$K\alpha$ XPS ($h\nu$=1.5 keV) and HAXPES ($h\nu$=8.0 keV) spectra for N 1*s* of PI, A-30, and B-30.

Yugo Kubo

Analysis Technology Research Center,
Sumitomo Electric Industries, Ltd.

Email: kubo-yugo@sei.co.jp

References

[1] R. Haight *et al.*: J. Vac. Sci. Technol. A **6** (1988) 2188.
[2] S.A. Chambers *et al.*: J. Vac. Sci. Technol. A **8** (1990) 875.
[3] *Y. Kubo, H. Tanaka, Y. Saito and A. Mizoguchi: ACS Appl. Mater. Interfaces* ***10*** *(2018) 44589.*
[4] T. Miyamura: Ph.D. Dissertation, Tohoku University, 2009 (in Japanese).
[5] Y. Kubo *et al.*: Anal. Chem. **88** (2016) 5225.

Accelerators & Beamlines Frontiers

SPring-8 Beam Performance

Recent update on accelerators

Orbit fluctuations excited by pulsed kicker magnets at ID23 and ID25 have been observed for years. At the beamlines, there are twin helical undulators and pulsed kickers so that the optical helicity can be switched at the repetition rates of 0.1 – 1 Hz (or 10 Hz in some cases) by making orbit bumps between kickers. Ideally, an orbit bump is supposed to be closed within the kickers without orbit fluctuations out of the kickers (Fig. 1). However, owing to hardware imperfections, the orbit bump is not perfectly closed, which results in orbit fluctuations at other beamlines. Our basic strategy to suppress such orbit fluctuations is to use correction magnets in ID sections that are composed of iron- and air-core magnets, and drive them based on feedforward tables. Nevertheless, it has been observed for years that the orbit fluctuations become gradually larger, i.e., the feedforward correction gradually deteriorates, as time elapses even after the feedforward tables are optimized. Typically, users start to see the fluctuations in a couple of weeks after the optimization. For this reason, we have developed the so-called adaptive feedforward orbit correction system. The new system monitors orbit distortions every hour, for instance, so that the feedforward tables are updated before users detect the fluctuation. In fiscal year 2019, the new system was operated manually and the reliability was verified. We plan to start user operations with the new feedforward system presumably in spring of the year 2020.

A full-energy direct beam injection from the SACLA linac to the SPring-8 storage ring has been developed. This new injection setup is beneficial in that (i) the 1 GeV linac and the 8 GeV booster synchrotron that are currently used for the injection to the storage ring can be shut down, (ii) the new injection setup with the low-emittance beam will eventually be inevitable after the major upgrade of the storage ring, and (iii) an experience with the new setup is invaluable when next-generation light sources become available, such as the new 3 GeV light source in Tohoku where a full energy injection from a linac is employed. For a year or so, we have developed a new timing system that can smoothly switch between the direct injection from the SACLA linac and the conventional injection from the booster, and simultaneously modified the beam transport hardware configurations. After several test runs in beam study times, we finally started user time operations with the new set up for full-energy direct injection from SACLA in February 2020. It worked as expected without a significant problem; stable lights were delivered to users without any deterioration of beam quality. Unfortunately, the injection with this new set up needed to be stopped just after 24 hours of user operation because of an independent problem with the electron gun of the SACLA linac. We aim to restart the new injection set up early in fiscal year 2020.

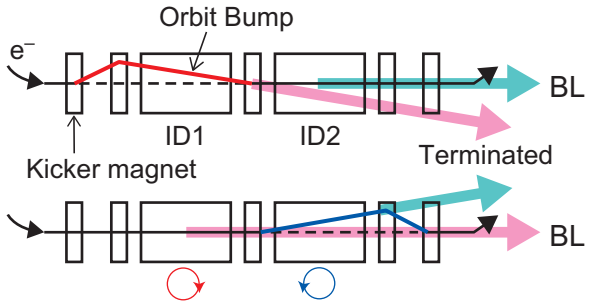

Fig. 1. The twin helical undulators at BL25SU. It consists of two helical undulators and five kicker magnets. The kicker magnets are used to generate bumped electron orbits at the undulators.

Shiro Takano and Takahiro Watanabe*

Japan Synchrotron Radiation Research Institute (JASRI)

*Email: twatanabe@spring8.or.jp

New highly efficient and fully automatic MX at SPring-8 BL45XU beamline

Recently, high flux and microfocus X-rays have enabled structural analysis from tiny (less than 20 μm) protein crystals, such as LCP crystals of membrane proteins, at macromolecular crystallography (MX) beamlines. However, there still remains demand for highly efficient data collection from relatively large crystals (crystal size: 50 μm or more) obtained by soaking chemical compounds aimed at, for example, drug discovery. Thus, SPring-8 **BL45XU**, operated as the SAXS beamline, was redesigned and reconstructed as a high-throughput automatic MX beamline with high flux and microfocus X-rays.

The new BL45XU was designed on the basis the undulator beamlines BL41XU and BL32XU [1], at each of which an in-vacuum undulator and double crystal monochromator with Si (111) were installed. Available wavelengths range from 0.775 Å to 1.9 Å (Fig. 1(a)). The size of the focused X-rays at the sample position can be changed from 5 (H)×5 (V) to 50 (H)×50 (V) μm^2 by adjusting the aperture of the virtual source slit and the glancing angles of vertical and horizontal focusing mirrors with a photon flux of 5.2×10^{12} – 1.8×10^{13} photons/s at 1.0 Å (Fig. 1(b)). The diffractometer in the experimental hutch was designed to enable high-speed and fully automatic measurement. The pixel array detector Pilatus 3 6M was installed to enable high-frame-rate measurement. The automatic sample changer with twin arms, SPACE-II [2], enables high-speed sample exchange (Fig. 1(c)). All the motorized axes are controlled by the beamline control software BSS [3]. The automated data collection system *ZOO* [4] has achieved automation for all goniometer-based data collection schemes in protein crystallography via communication with BSS. *ZOO* can estimate the absorbed dose in implemented schemes to mitigate severe radiation damage that may interfere with precise structure analyses (Table 1). The system has enabled 'unattended' automatic measurements. Users can obtain good datasets simply by sending their crystals without the need to visit the SPring-8 site. The automatic and unattended measurements, the so-called "mail-in" service, started at the end of May 2019.

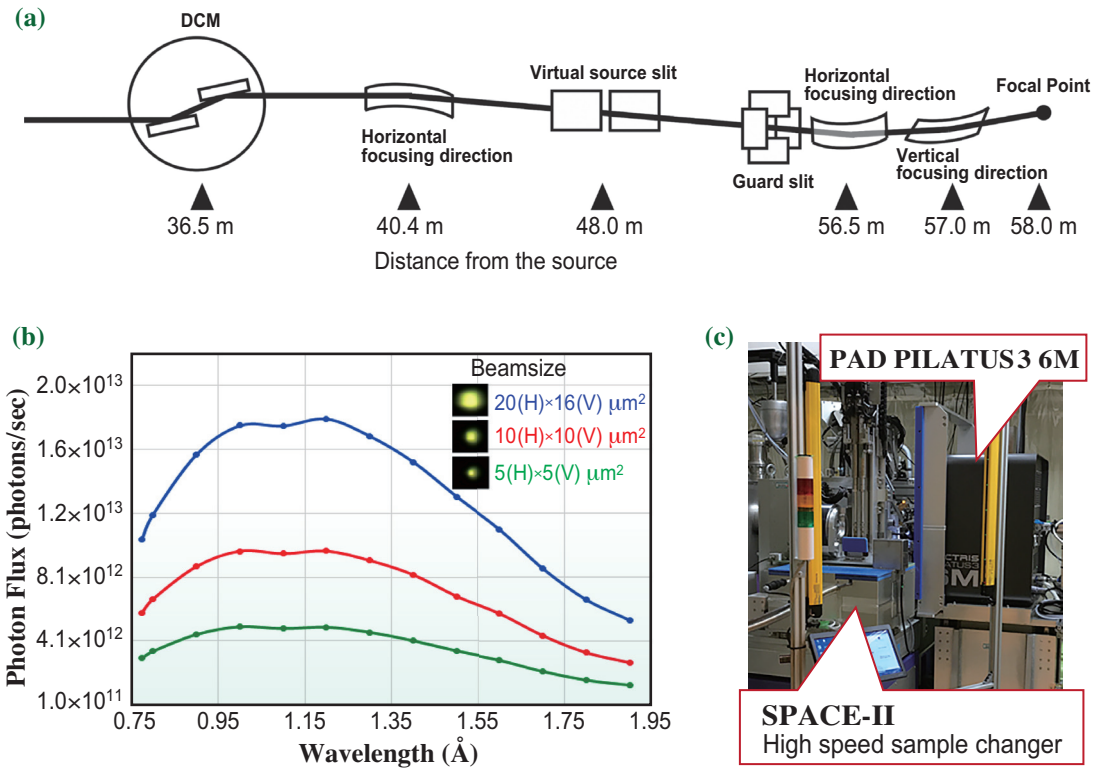

Fig. 1. Overview of BL45XU. **(a)** Layout of the optics. **(b)** Photon flux and beam profiles at the sample position. **(c)** Photograph of BL45XU experimental hutch showing diffractometer (sample changer and pixel array detector (PAD)).

Table 1. Experimental results of automatic measurements using *ZOO* system in BL45XU

Type	Single crystal		Multiple crystals	
Number of Sample	128 pins/8 pucks		73 pins/6 pucks	
Experimental time	8 h 13 min		11 h 19 min	
Ave. exp. Time	3 min 51 s		8 min 23 s	
Beam size	20 (H) × 16 (V) μm^2		20 (H) × 16 (V) μm^2	
(Photon flux)	(1.73×10^{13} photons/sec)		(9.75×10^{12} photons/sec)	
Crystal size	50 – 150 μm		5 - 20 μm (Membrane protein - LCP)	
Data collection by *ZOO*				
Data Collect	121 pins: Single point (102 pins) Helical (9 pins) Total Φ = 360°, (Dose = 10 MGy)		64 pins: Multiple small wedge Total Φ = 10° (Dose = 10 MGy)	
Data processing by KAMO (XDS)				
Processed	121 data (Indexing failed: 5 set)		64 pins, 940 data	Resolution, Completeness, I_0/σ [outer shell]
	Completeness > 94% : 116 data		**Sample A:** (30 pins, 287 data)	1.92 Å , 99.6%, 1.56
	Beyond 2.0 Å	33 data	**Sample B:** (23 pins, 446 data)	2.04 Å , 99.8%, 1.42
	3.0 – 2.0 Å	25 data	**Sample C** (9 pins 190 data)	4.78 Å , 99.8%, 1.94
	Below 3.0 Å	58 data (9.17 – 3.03 Å)	**Sample D** (2 pins, 17 data)	Failed to a small number of data

S. Baba[a,*], K. Hirata[b], N. Mizuno[a] and T. Kumasaka[a]

[a] Japan Synchrotron Radiation Research Institute (JASRI)
[b] RIKEN SPring-8 Center

*Email: baba@spring8.or.jp

References

[1] K. Hirata *et al.*: J. Phys. Conf. Ser. **425** (2013) 012002.
[2] H. Murakami *et al.*: Acta Crystallogr. D **76** (2020) 155.
[3] G. Ueno *et al.*: J. Synchrotron Rad. **12** (2005) 380.
[4] *K. Hirata, K. Yamashita, G. Ueno, Y. Kawano, K. Hasegawa, T. Kumasaka and M. Yamamoto: Acta Cryst. D **75** (2019)138.*

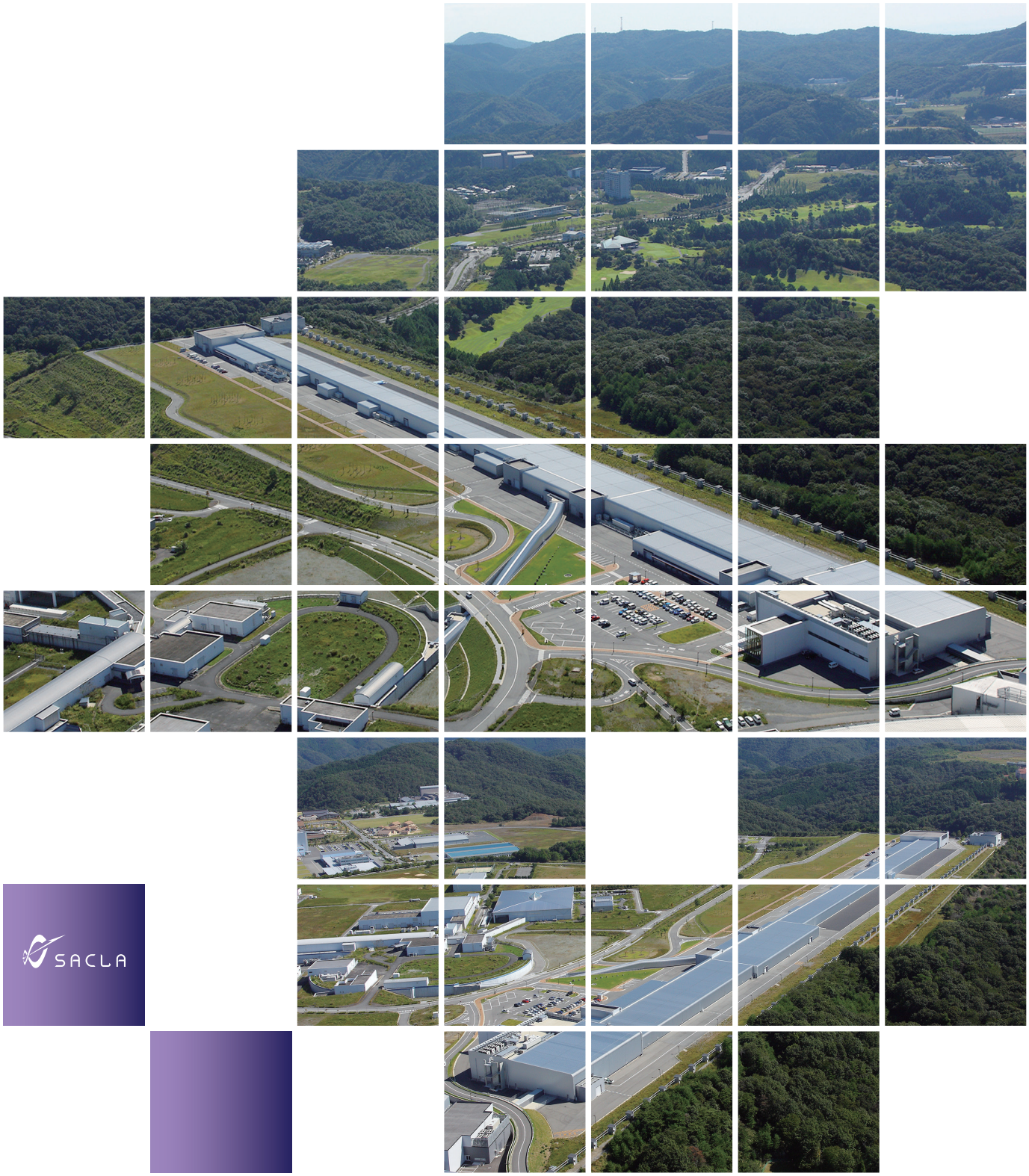

SACLA Beam Performance

Multiple-beamline operations enabling the simultaneous use of three FEL beamlines (BL1, BL2, and BL3) have been standard for user experiments. This operation scheme has provided stable and high-performance soft and hard XFELs for user experiments throughout the year. The net user time in FY2019 across user shifts for these beamlines is expected to exceed 6400 hours, with high levels of laser performance and availability. Self-seeded XFELs have been open for user experiments since the middle of FY2019. On the other hand, aiming at the full system integration of SACLA and SPring-8 towards a sustainable facility upgrade, an innovative system has been developed for enabling timesharing use of the SACLA linac as an injector for the current SPring-8 storage ring. The upgraded accelerator control system allows arbitrary switching patterns of multiple-beamline, e.g., 1 pps for BL2 and 59 pps for BL3. The beam test has also been intensively carried out to check the operational performance and evaluate the system completeness from the viewpoint of beam injection to the ring and XFEL utilization. The final system check at the user time is scheduled in February 2020. Figure 1 shows variations in the stored current and beam injection efficiency during the beam test. The beam injection rate was 1 Hz during the test, which will be increased to up to 10 Hz in the actual beam injection.

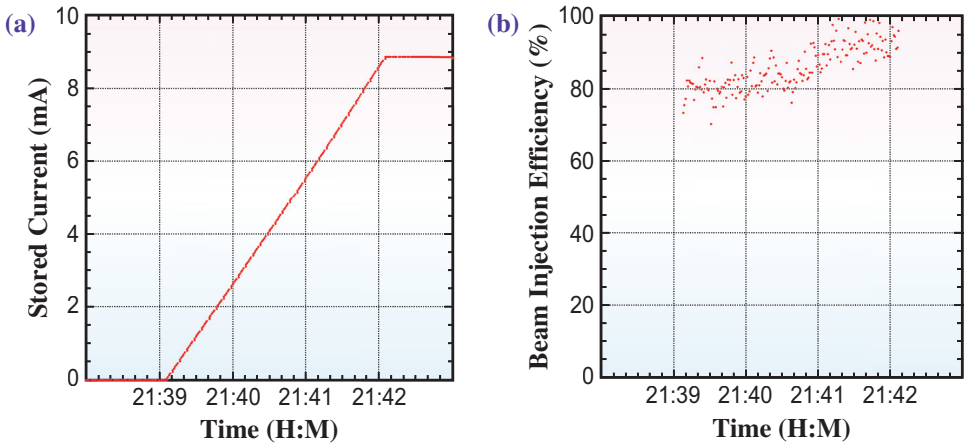

Fig. 1. Variations in stored current **(a)** and beam injection efficiency **(b)** during the beam injection test on February 4, 2019. The beam injection rate was 1 Hz.

Hitoshi Tanaka

RIKEN SPring-8 Center

Email: tanaka@spring8.or.jp

Generation of high-intensity narrowband X-ray Free Electron Laser through reflection self-seeding

Current X-ray Free Electron Lasers (XFELs) are operated mostly on the basis of self-amplified spontaneous emission (SASE) scheme, where spontaneous radiation originating from density modulations in the electron beam is exponentially amplified along periodic magnetic fields in undulators. Although the SASE scheme is effective in producing intense X-ray beams, the stochastic starting-up processes cause poor temporal coherence and a large fractional bandwidth (~0.3%). To perform specific kinds of experiments, such as wide-angle X-ray scattering and spectroscopy, one must monochromatize XFEL beams at the cost of considerable loss of photon flux. For example, photon flux after the monochromator is only ~3% of that before the monochromator when a silicon (Si) (111) double-crystal monochromator is applied for monochromatization. Narrowing the bandwidth of XFEL beams while retaining the high intensity would boost the throughputs of current XFEL experiments and help open up new field of X-ray sciences.

To realize high-intensity narrowband XFEL beams, a self-seeding scheme using a diamond crystal [1] was proposed and demonstrated at the Linac Coherent Light Source and SACLA. In this scheme, a thin diamond crystal is placed in the middle of the undulators. The SASE radiation from the upstream undulators is monochromatized with the crystal in the Bragg forward diffraction geometry, producing a delayed monochromatic X-ray beam, called the wake pulse, in addition to the transmitted XFEL beam with a broad bandwidth. By achieving a spatiotemporal overlap between the monochromatic wake and the electron bunch in the downstream undulators, one can increase the intensity of the monochromatic component. However, we could not achieve stable operation of this seeding scheme at SACLA, possibly owing to an insufficient signal-to-noise ratio for the seeding intensity as a result of the contamination of the transmitted SASE beam.

As an alternative approach to generating narrowband XFEL pulses, we developed a new self-seeding scheme, called reflection self-seeding, at SACLA **BL3** (Fig. 1) [2]. In this scheme, a Si channel-cut crystal monochromator is used in the reflection geometry for monochromatizing XFEL beams generated by upstream undulators. The X-ray beam injected to the downstream undulators is purely monochromatic in this case. Thus, one could produce a brilliant X-ray beam with a narrow bandwidth by amplifying the seed pulse in the downstream undulator section.

Although reflection self-seeding seems to be a simple approach to producing narrowband XFEL beams, its realization is not straightforward. When we use a conventional Si channel-cut crystal with a gap of ~10 mm, the optical delay caused by the crystal becomes several tens of picoseconds. In this case, a very long (~100 m) magnetic chicane is required to achieve a temporal overlap between the electron bunch and the seed in the downstream undulators. To suppress the optical delay, we developed a Si

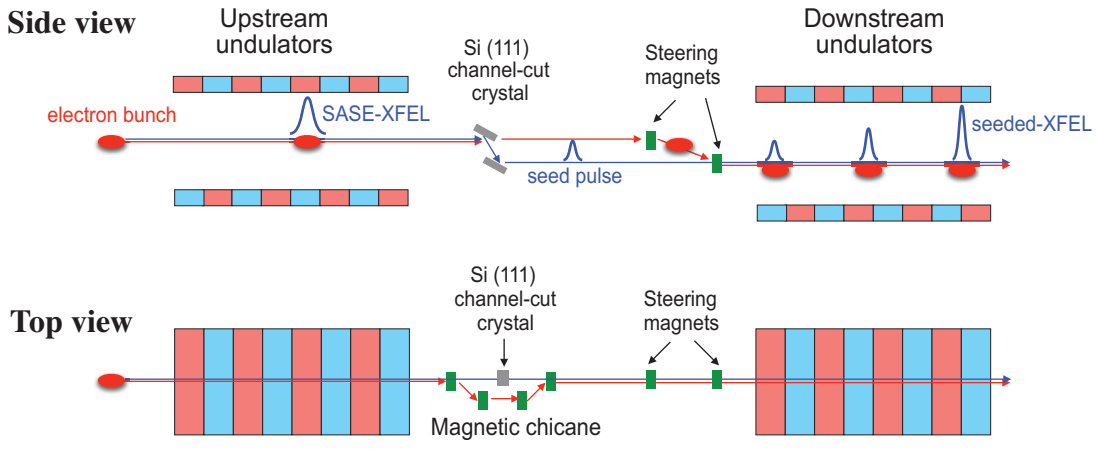

Fig. 1. Schematic illustration of reflection self-seeding at SACLA.

channel-cut crystal with a gap of a few hundred micrometers, which we call a micro-channel-cut crystal [3]. With this new optical device, the optical delay can be reduced to a few hundred femtoseconds, which can be readily compensated by electron beam delay due to the magnetic chicane.

Figure 2 shows the averaged spectra of SASE-XFEL in the normal operating mode and the seeded-XFEL for a central photon energy of 9.85 keV. It is clearly seen that the injection of the seed drastically narrowed the bandwidth of the XFEL beam. The intensity at 9.85 keV of the seeded-XFEL greatly exceeds that of SASE-XFEL, which corresponds to an increase in spectral brightness by a factor of six with respect to the normal SASE mode.

The self-seeded XFEL has been promoted to the normal operation mode of SACLA and used in a wide variety of user experiments. There is, however, still some room to further increase spectral brightness by narrowing the bandwidth of the seeded-XFEL. The use of higher order reflection in the channel-cut crystal is a straightforward approach to achieving higher spectral brightness. In fact, we are currently developing a reflection self-seeding scheme using a Si (220) channel-cut crystal.

The reflection self-seeding is based on a simple and robust principle. So far, our new seeding scheme has been operating stably at SACLA. We anticipate that the seeded-XFEL beam from SACLA will be a strong driving force for opening new frontiers of X-ray sciences, such as the exploration of nonlinear X-ray optical phenomena and the imaging of tiny objects at atomic resolution, as well as for reducing the measurement time in experiments.

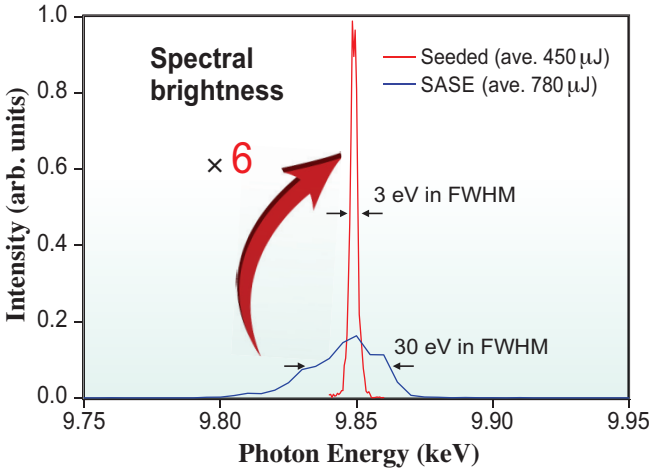

Fig. 2. Averaged spectra of seeded- and SASE-XFEL with central photon energy of 9.85 keV.

Ichiro Inoue[a,*], Taito Osaka[a] and Makina Yabashi[a,b]

[a] RIKEN SPring-8 Center
[b] Japan Synchrotron Radiation Research Institute (JASRI)

*Email: inoue@spring8.or.jp

References

[1] J. Amann *et al.*: Nat. Photonics **6** (2012) 693.
[2] *I. Inoue, T. Osaka, T. Hara, T. Tanaka, T. Inagaki, T. Fukui, S. Goto, Y. Inubushi, H. Kimura, R. Kinjo, H. Ohashi, K. Togawa, K. Tono, M. Yamaga, H. Tanaka, T. Ishikawa & M. Yabashi: Nat. Photonics* ***13*** *(2019) 319.*
[3] T. Osaka *et al.*: J. Synchrotron Rad. **26** (2019) 1496.

FACILITY STATUS

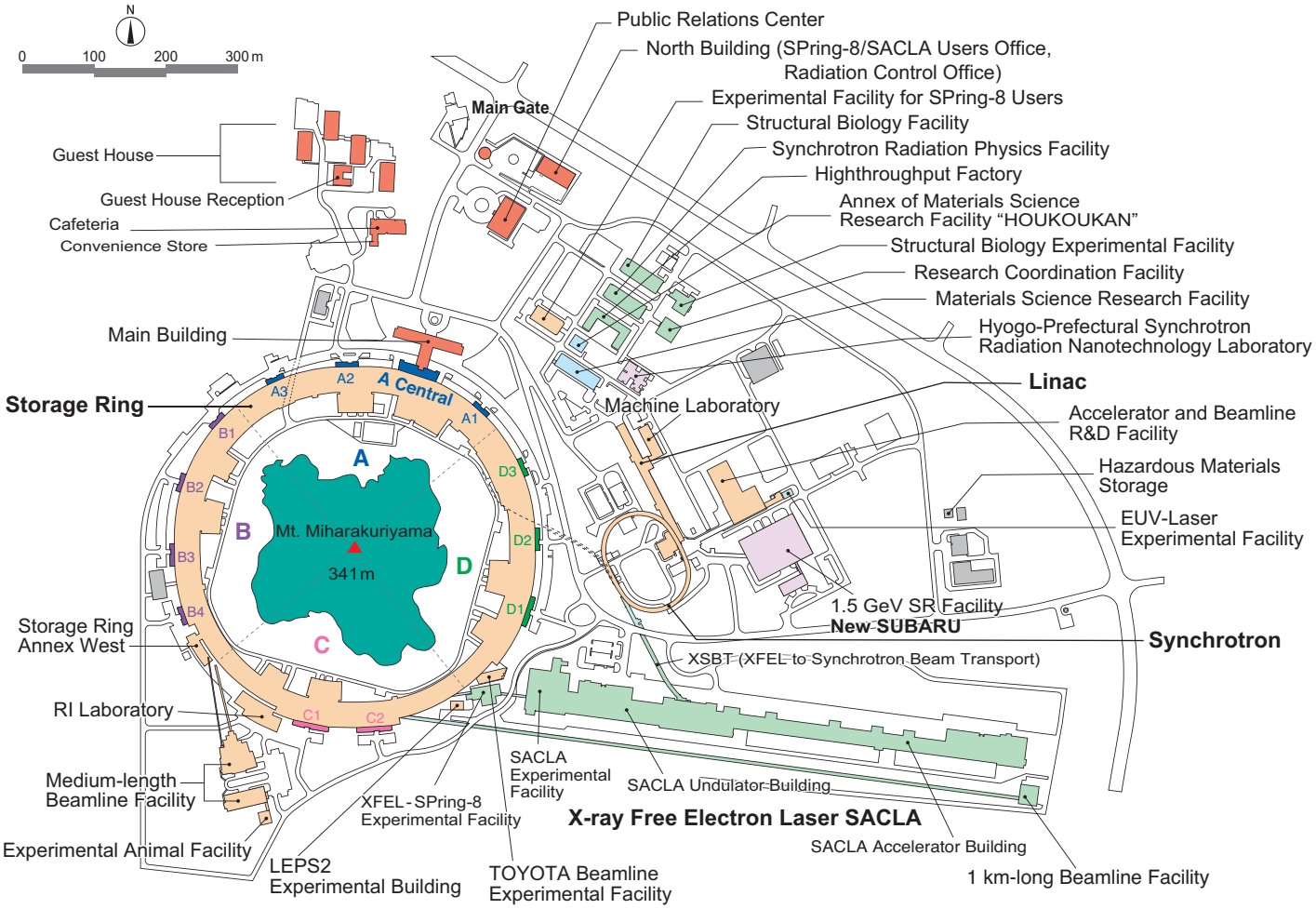

SPring-8

I. Introduction

SPring-8 was stably operated throughout FY2019 with a total operation time of the accelerator complex and the total user beam time of 5162.6 h and 4537.6 h, respectively, and a total downtime of 40.3 h. SPring-8 had to complete all its operations by the middle of February 2020.

In 2019, an automatic data collection using the *ZOO* system developed by RIKEN and JASRI was newly made available. The PX-BL Automatic Data Collection system was introduced in 2019B, and now users only need to send samples to SPring-8 to obtain data (no visit required).

Concerning the contract beamlines, there were four interim reviews conducted for WEBRAM (BL15XU, National Institute for Materials Science), Advanced Softmaterial (BL03XU, Advanced Softmaterial Beamline Consortium), NSRRC ID (BL12XU, National Synchrotron Radiation Research Center), and NSRRC BM (BL12B2, National Synchrotron Radiation Research Center), and the projects were authorized to continue.

At present, there are as many as 15,000 SPring-8 users, all of whom are members of the SPring-8 User Community (SPRUC). It is important for SPring-8 to jointly organize scientific events with SPRUC, such as the SPring-8 Symposium, to facilitate dialogue between users and the facility staff. The SPring-8 Symposium was held at Okayama University (mainly Kanemitsu Hall) on August 30–31, 2019, with 359 participants. SPring-8 also facilitates communication between users and industry. The Joint Conference on Industrial Applications of SPring-8 was held in Kawasaki City on September 5-6, 2019, with 299 participants. As part of its continuous effort towards fostering human resources in synchrotron sciences, SPring-8 organized the 19th SPring-8 Summer School with 90 students of graduate schools nationwide, in cooperation with Hyogo University, Kwansei Gakuin University, The University of Tokyo, Okayama University, Osaka University, Japan Atomic Energy Agency, National Institutes for Quantum and Radiological Science and Technology, and RIKEN. Furthermore, SPring-8 and SPRUC organized the 3rd SPring-8 Autumn School with 62 participants, which included undergraduate to doctoral students and company researchers.

II. Machine Operation

The operation statistics for the last five fiscal years are shown in Fig. 1. In FY2019, the total operation time of the entire SPring-8 accelerator complex was 5285.7 h. The operation time of the storage ring was 5271.2 h, 86.1% of which (4537.9 h) was devoted to SR experiments. This excellent figure for the user time represents a storage ring availability of 99.0%. The total downtime caused by failures amounted to 40.5 h, accounting for 0.89% of the total user time. For 99.5% of the user time in FY2019, the stored beam current was maintained at 100 mA by the top-up operation wherein the stored beam was filled up on demand at any time. The extreme stability of the light source intensity better than 0.1% was provided by the top-up operation.

The variety of operation modes for SR experiments is one of the characteristics of SPring-8. The operation modes are classified into two types, the several-bunch and hybrid-filling modes. The several-bunch mode consists of equally spaced bunches or trains of bunches such as 203 bunches or 29 trains of 11 bunches. The hybrid-filling mode is composed of a long train of bunches and isolated single bunches. The isolated bunch current is kept constant within 1% through the top-up operation. The isolated bunch impurity is routinely maintained better than 10^{-8} by the bunch cleaning system in the booster. The operation modes of SPring-8 are listed in Table 1 with the share of each operation mode in FY2019. Table 2 summarizes the beam parameters of the storage ring.

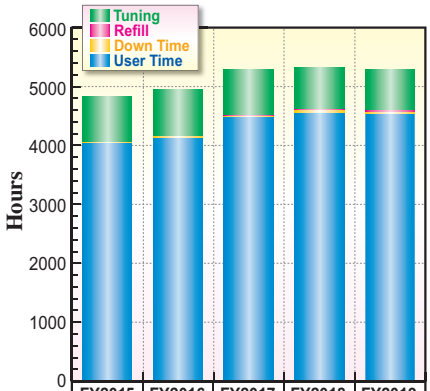

	FY2015	FY2016	FY2017	FY2018	FY2019
Accelerator Operation Time	4817.9	4951.7	5281.6	5329.8	5285.7
Storage Ring Operation Time	4804.8	4941.1	5270.4	5316.7	5271.2
Tuning & Study (Acc. & BL)	767.2	803.1	769.6	721.8	701.7
Refill	5.3	3.4	4.6	5.3	5.6
Down Time	16.8	23.1	28.7	43.1	40.5
Mean Time Between Failures	202.8	229.2	194.7	168.9	206.3
Achieved User Time	4033.9	4125.5	4478.7	4559.6	4537.9
Planned User Time	4056.0	4152.0	4512.0	4608.0	4584.0
Availability (%)	99.5	99.4	99.3	98.9	99.0

Fig. 1. Operation statistics for last five fiscal years.

Table 1. Operation modes in FY2019

	Single bunch current (mA)	Share of operation time (%)
203 bunches		31.4
4 bunch-train × 84		3.1
11 bunch-train × 29		22.5
1/7-filling + 5 single bunches	3	7.3
2/29-filling + 26 single bunches	1.4	3.1
1/14-filling + 12 single bunches	1.6	9.4
4/58-filling + 53 single bunches	1.0	2.1
11/29-filling + 1 single bunch	5	20.9

Table 2. Beam parameters of SPring-8 storage ring

Energy [GeV]	8
Number of buckets	2436
Tunes (ν_x / ν_y)	41.14 / 19.34
Current [mA]:	
single bunch	12
multi bunch	100
Bunch length (σ) [psec]	13
Horizontal emittance [nm·rad]	2.4*
Vertical emittance [pm·rad]	4.8*
Coupling [%]	0.2
RF Voltage [MV]	14.4** ~ 16
Momentum acceptance [%]	3.2 (~256 MeV)
Beam size (σ_x / σ_y)* [μm]	
Long ID section	333 / 7
ID section	316 / 5
BM1 section	94 / 12
BM2 section	100 / 12
Beam divergence (σ_x' / σ_y')* [μrad]	
Long ID section	8 / 0.7
ID section	9 / 1.0
BM1 section	58 / 0.5
BM2 section	68 / 0.5
Operational chromaticities (ξ_x / ξ_y)	+2 / +2***
Lifetime [hr]:	
100 mA (multi bunch)	~250
1 mA (single bunch)	~30
Horizontal dispersion [m]:	
Long ID section	0.153
ID section	0.146
BM1 section	0.039
BM2 section	0.059
Fast orbit stability (0.1 – 200 Hz) [μm]:	
horizontal (rms)	~4
vertical (rms)	~1

* Assuming 0.2% coupling
** Power saving mode
*** With bunch-by-bunch feedback

III. Beamlines

The SPring-8 storage ring can accommodate up to 62 beamlines: 34 insertion devices, 4 long undulators, and 24 bending magnets. At present, 57 beamlines are in operation, covering a wide variety of research fields involving synchrotron radiation science and technology. The beamlines are classified into the following three types:

(1) Public Beamlines (26 beamlines operating),
(2) Contract Beamlines (18 beamlines operating), and
(3) RIKEN Beamlines (13 beamlines operating).

There are now 26 public beamlines in full operation. The beamlines that were proposed and constructed by external organizations, such as universities, research institutes, private companies, and consortiums, are called contract beamlines and exclusively used by contractors for their own research purposes. At present, 18 contract beamlines are in operation. The beamlines constructed by RIKEN except for public beamlines are called RIKEN beamlines and mainly used for RIKEN's own research activities, with partial availability for public use. RIKEN is now operating 13 beamlines.

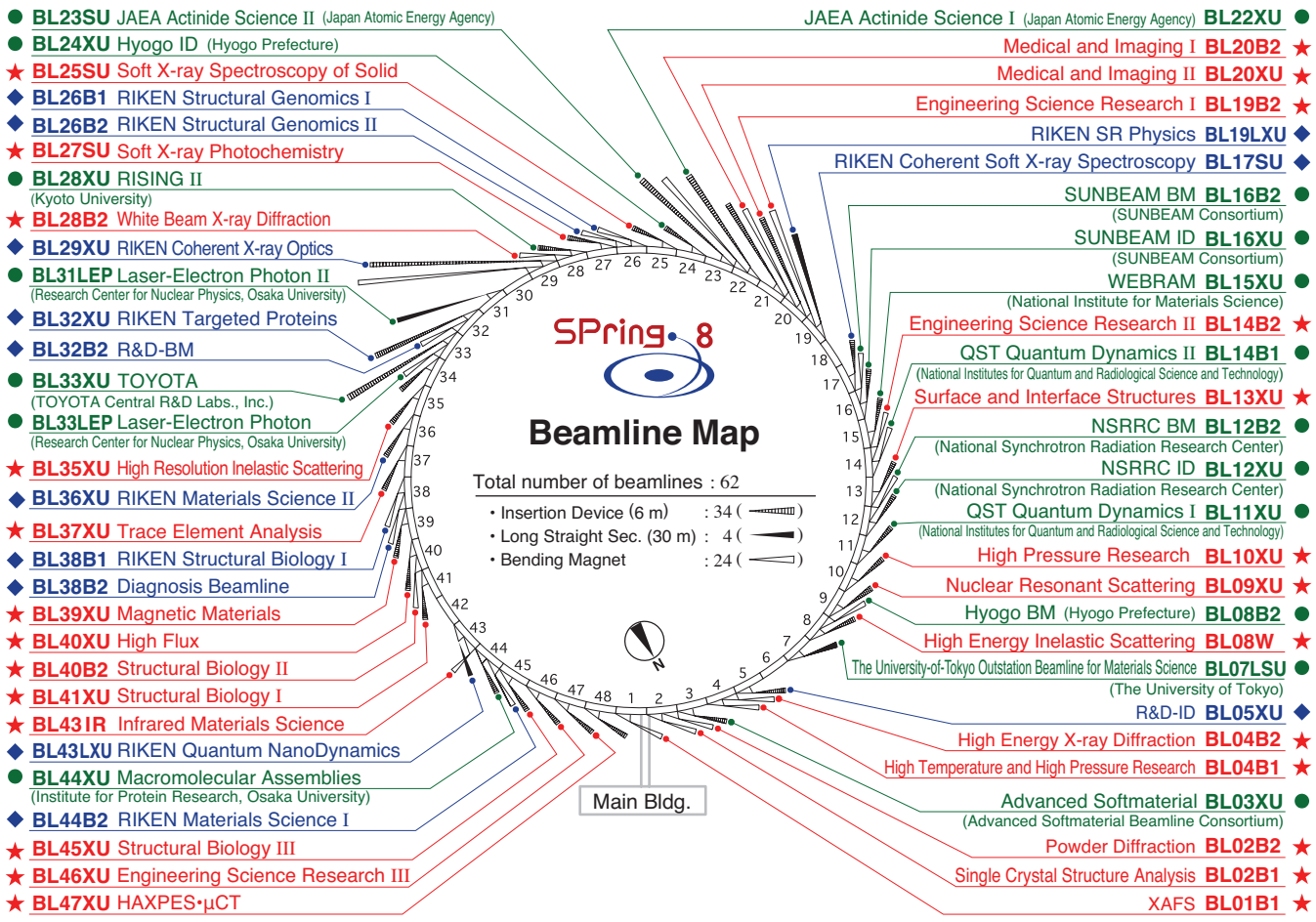

BL: Beamline
B1, B2: Bending Magnets
XU: X-ray Undulator
SU: Soft X-ray Undulator
W: Wiggler

IR: Infrared Radiation
LEP: Laser-Electron Photon
LXU: Long-length X-ray Undulator
LSU: Long-length Soft X-ray Undulator

★ : Public Beamlines
● : Contract Beamlines
◆ : RIKEN Beamlines

WEBRAM: Wide Energy Range Beamline for Research in Advanced Materials
NSRRC: National Synchrotron Radiation Research Center, Taiwan
RISING: Research & Development Initiative for Scientific Innovation of New Generation Batteries

Fig. 2. Beamline map.

Table 3. List of beamlines

BL #	Beamline Name	(Public Use) or (First Beam)	Areas of Research and Available Techniques
★ Public Beamlines as of April 2020			
BL01B1	XAFS	(Oct. 1997)	XAFS in wide energy region (3.8 to 113 keV). XAFS of dilute systems and thin films. Quick XAFS with a time resolution of seconds to tens of seconds.
BL02B1	Single Crystal Structure Analysis	(Oct. 1997)	Charge density study and crystal structure analysis from single crystal X-ray diffraction. (X-ray energy range: 8 – 115 keV)
BL02B2	Powder Diffraction	(Sept. 1999)	Charge density study and phase identification of crystalline materials from accurate powder diffraction measurements. (X-ray energy range: 12.4 – 35 keV)
BL04B1	High Temperature and High Pressure Research	(Oct. 1997)	High temperature and high pressure research with the multi-anvil press by powder X-ray diffraction, radiography and ultrasonic measurement.
BL04B2	High Energy X-ray Diffraction	(Sept. 1999)	Pair distribution function analysis for glass, liquid, and amorphous materials. High-energy X-ray total scattering. Containerless levitation.
BL08W	High Energy Inelastic Scattering	(Oct. 1997)	Magnetic Compton scattering. High-resolution Compton scattering. High-energy Bragg scattering. High-energy fluorescent X-ray analysis.
BL09XU	Nuclear Resonant Scattering	(Oct. 1997)	Lattice dynamics using nuclear inelastic scattering. Mössbauer spectroscopy, especially for the surface/interface study and under the extreme conditions. Hard X-ray photoelectron spectroscopy (HAXPES). Depth analysis of HAXPES with high flux and energy resolution.
BL10XU	High Pressure Research	(Oct. 1997)	Structure analysis and phase transitions under ultra high pressure (DAC experiment). Earth and planetary science.
BL13XU	Surface and Interface Structures	(Sept. 2001)	Atomic-scale structural analysis of surfaces and interfaces of crystalline materials, ultra-thin films, and nanostructures. Surface X-ray diffraction (SXRD). Microbeam diffraction.
BL14B2	Engineering Science Research II	(Sept. 2007)	X-ray Imaging. XAFS in wide energy region (3.8 to 72 keV). XAFS of dilute systems and thin films.
BL19B2	Engineering Science Research I	(Nov. 2001)	Residual stress measurement. Structural analysis of thin film, surface, interface. Powder diffraction. X-ray topography. Ultra-small angle X-ray scattering.
BL20XU	Medical and Imaging II	(Sept. 2001)	Microimaging. Micro-/nano-tomography, phase-contrast microtomography, X-ray diffraction tomography (XRD-CT), hard X-ray microbeam/scanning microscopy, imaging microscopy, coherent X-ray optics, and other experiments on X-ray optics and developments of optical elements. Refraction-enhanced imaging. Ultra-small angle scattering.
BL20B2	Medical and Imaging I	(Sept. 1999)	Microimaging: microtomography, phase-contrast microtomography with grating interferometer for biological specimen and other kinds of specimen. Evaluation and development of various kinds of optical elements for novel imaging techniques. Large field X-ray topography.
BL25SU	Soft X-ray Spectroscopy of Solid	(Apr. 1998)	Study of electronic state of solids by soft X-ray photoemission spectroscopy (PES) including angle-resolved PES (ARPES). Atomic arrangement analysis of surfaces by photoelectron diffraction (PED) technique using two-dimensional photoemission analyzer. Magnetic state analysis by magnetic circular dichroism (MCD) of soft X-ray absorption and its element-specific magnetization curve measurements.
BL27SU	Soft X-ray Photochemistry	(May 1998)	Ambient atmospheric pressure soft X-ray photoabsorption spectroscopy. Chemical state analysis of light elements in dilute samples (NEXAFS). Elemental and chemical mapping using micro soft X-ray beam. Soft-X-ray emission spectroscopy.
BL28B2	White Beam X-ray Diffraction	(Sept. 1999)	White X-ray diffraction and topography. Time-resolved energy-dispersive XAFS (DXAFS) for studies of chemical and/or physical reaction process. Biomedical imaging and radiation biology studies. High energy X-ray microtomography.
BL35XU	High Resolution Inelastic Scattering	(Sept. 2001)	Materials dynamics on ~meV energy scales using inelastic X-ray scattering (IXS).
BL37XU	Trace Element Analysis	(Nov. 2002)	X-ray spectrochemical analysis using micro/nano beam: Scanning X-ray microspectroscopy. X-ray spectroscopic imaging: Projection type spectroscopic tomography and Imaging type spectroscopic tomography. Ultra trace element analysis. High energy X-ray fluorescence analysis.
BL39XU	Magnetic Materials	(Oct. 1997)	X-ray magnetic circular dichroism (XMCD) spectroscopy and element-specific magnetometry under multiple-extreme conditions. XMCD/XAS using a 100 nm focused X-ray beam. X-ray emission spectroscopy.
BL40XU	High Flux	(Apr. 2000)	Time-resolved diffraction and scattering experiments. Microbeam X-ray diffraction and scattering experiments. X-ray photon correlation spectroscopy. Fluorescence analysis. Quick XAFS. Submicrometer-scale single crystal structure analysis with high flux and zone plate focused X-ray beam. Single shot imaging with X-ray choppers. Laser pump-X-ray probe experiment.
BL40B2	Structural Biology II	(Sept. 1999)	Noncrystalline small and wide angle X-ray scattering.
BL41XU	Structural Biology I	(Oct. 1997)	Structural biology. Macromolecular crystallography. Microcrystallography. High resolution data collection.
BL43IR	Infrared Materials Science	(Apr. 2000)	Infrared microspectroscopy.
BL45XU	Structural Biology III	(Apr. 2019)	Structural biology. Macromolecular crystallography. Automation & High throughput data collection. Microcrystallography.
BL46XU	Engineering Science Research III	(Nov. 2000)	Structural characterization of thin films by X-ray diffraction and X-ray reflectivity measurement. Residual stress measurement. Time resolved X-ray diffraction measurement. Hard X-ray Photoemission Spectroscopy. X-ray Imaging.
BL47XU	HAXPES·μCT	(Oct. 1997)	Hard X-ray photoelectron spectroscopy (HAXPES). Depth analysis of angle resolved HAXPES with wide acceptance lens. Projection type microtomography. Imaging type microtomography. Hard X-ray microbeam/scanning microscopy.

BL #	Beamline Name	(Public Use) or (First Beam)	Areas of Research and Available Techniques
	● Contract Beamlines	as of April 2020	
BL03XU	**Advanced Softmaterial** (Advanced Softmaterial Beamline Consortium)	(Nov. 2009)	Structural characterization of softmaterials using small- and wide-angle X-ray scattering. Grazing-incidence small- and wide-angle X-ray scattering for thin films. X-ray diffraction and reflectivity measurements for softmaterials.
BL07LSU	**The University-of-Tokyo Outstation Beamline for Materials Science** (The University of Tokyo)	(Oct. 2009)	Time-resolved soft X-ray spectroscopy, nano-beam photoemission spectroscopy, ultra high-resolution soft X-ray emission spectroscopy, and any methods requiring the highly brilliant soft X-ray beam.
BL08B2	**Hyogo BM** (Hyogo Prefecture)	(Jun. 2005)	XAFS in a wide energy region. Small angle X-ray scattering. X-ray topography. Imaging. X-ray diffraction for multipurpose.
BL11XU	**QST Quantum Dynamics I** (National Institutes for Quantum & Radiological Science & Technology)	(Oct. 1998)	Synchrotron radiation Mössbauer spectroscopy. XAFS. Resonant inelastic X-ray scattering spectroscopy. *In situ* X-ray diffraction during molecular-beam epitaxial growth.
BL12B2	**NSRRC BM** (National Synchrotron Rad. Res. Center)	(Oct. 2000)	X-ray absorption spectroscopy. Powder X-ray diffraction. High resolution X-ray scattering. Protein crystallography.
BL12XU	**NSRRC ID** (National Synchrotron Rad. Res. Center)	(Dec. 2001)	Non-resonant or resonant inelastic X-ray scattering. Hard X-ray photoemission spectroscopy.
BL14B1	**QST Quantum Dynamics II** (National Institutes for Quantum & Radiological Science & Technology)	(Dec. 1997)	Materials science under high-temperature and high-pressure. Energy-dispersive XAFS. X-ray stress/strain measurements.
BL15XU	**WEBRAM** (National Institute for Materials Science)	(Jan. 2000)	Hard X-ray photoelectron spectroscopy. High-precision X-ray powder diffraction. Structural analysis of thin film, surface and interface.
BL16B2	**SUNBEAM BM** (SUNBEAM Consortium)	(Oct. 1998)	Characterization of secondary battery related materials, semiconductors, fuel cells, catalysts, and several industrial materials with using X-ray absorption fine structure measurements, X-ray diffraction (including X-ray reflectivity technique), X-ray topography and computed tomography/laminography.
BL16XU	**SUNBEAM ID** (SUNBEAM Consortium)	(Oct. 1998)	Characterization of secondary battery related materials, semiconductors, fuel cells, catalysts, and structural materials using X-ray diffraction, X-ray microbeam based evaluation techniques (including X-ray magnetic circular dichroism), hard X-ray photoelectron spectroscopy and fluorescence X-ray analysis.
BL22XU	**JAEA Actinide Science I** (Japan Atomic Energy Agency)	(May 2002)	HAXPES. XAFS. Residual stress/strain distribution analysis. Materials science under high-pressure. Resonant X-ray scattering. Speckle scattering. Surface X-ray diffraction. High-energy X-ray diffraction.
BL23SU	**JAEA Actinide Science II** (Japan Atomic Energy Agency)	(Feb. 1998)	Surface chemistry with supersonic molecular beam. Biophysical spectroscopy. Photoelectron spectroscopy. Magnetic circular dichroism. STXM.
BL24XU	**Hyogo ID** (Hyogo Prefecture)	(May. 1998)	Microbeam small- and wide-angle X-ray scattering for local structure analysis. Scanning and imaging microscope, micro-tomography, coherent diffraction. Microbeam X-ray diffraction and bright field X-ray topography for electronic device materials. Near-ambient pressure hard X-ray photoelectron spectroscopy.
BL28XU	**RISING II** (Kyoto University)	(Apr. 2012)	Characterization of rechargeable battery reactions and battery related materials by resonance X-ray diffraction, X-ray absorption spectroscopy (XAS), X-ray diffraction spectroscopy (XDS), and hard X-ray photoemission spectroscopy (HAXPES).
BL31LEP	**Laser-Electron Photon II** (RCNP, Osaka University)	(Oct. 2013)	Production of high intensity GeV photon beam by laser-backward Compton scattering. Hadron physics via photonucleon and photonuclear reactions. Test and calibration of detectors with GeV gamma-ray and converted electrons/positrons.
BL33LEP	**Laser-Electron Photon** (RCNP, Osaka University)	(Jun. 1999)	Meson photoproduction from nucleon and nucleus. Photoexcitation of hyperons, nucleon resonances, and other exotic states. Photonuclear reactions. Beam diagnoses. Test and calibration of detectors with GeV photon beam.
BL33XU	**TOYOTA** (TOYOTA Central R&D Labs., Inc.)	(Apr. 2009)	Time-resolved XAFS. Characterization of industrial materials, such as catalysts, secondary batteries, fuel cells.
BL44XU	**Macromolecular Assemblies** (IPR, Osaka University)	(May 1999)	Crystal structure analysis of biological macromolecular assemblies (e.g., membrane protein complexes, protein complexes, protein-nucleic acid complexes, and viruses).
	◆ RIKEN Beamlines	as of April 2020	
BL05XU	**R&D-ID**	(Mar. 2004)	Structural and dynamical research using small and wide angle scattering, R&D of SR instruments.
BL17SU	**RIKEN Coherent Soft X-ray Spectroscopy**	(Sept. 2003)	High resolution photoemission spectroscopy. Soft X-ray emission spectroscopy. Soft X-ray diffraction spectroscopy. Soft X-ray microspectroscopy.
BL19LXU	**RIKEN SR Physics**	(Oct. 2000)	SR science with highly brilliant X-ray beam.
BL26B1	**RIKEN Structural Genomics I**	(Apr. 2002)	Structural biology research based on single crystal X-ray diffraction.
BL26B2	**RIKEN Structural Genomics II**	(Apr. 2002)	Structural biology research based on single crystal X-ray diffraction.
BL29XU	**RIKEN Coherent X-ray Optics**	(Dec. 1998)	X-ray optics, especially coherent X-ray optics.
BL32XU	**RIKEN Targeted Proteins**	(Oct. 2009)	Protein microcrystallography.
BL32B2	**R&D-BM**	(May 2002)	X-ray computed tomography, X-ray diffraction, X-ray absorption fine structure, R&D of SR instruments.
BL36XU	**RIKEN Materials Science II**	(Mar 2020)	Time resolved XAFS and X-ray diffraction, 2D/3D scanning XAFS imaging, 3D computed tomography/laminography XAFS imaging, X-ray emission spectroscopy, ambient pressure hard X-ray photoelectron spectroscopy, pink beam experiment.
BL38B1	**RIKEN Structural Biology I**	(Oct. 2000)	Time-resolved and static structures of non-crystalline biological materials using small-angle scattering and diffraction techniques.
BL38B2	**Diagnosis Beamline**	(Sept. 1999)	Accelerator beam diagnostics.
BL43LXU	**RIKEN Quantum NanoDynamics**	(Oct. 2011)	High resolution inelastic X-ray scattering for investigating atomic and electronic dynamics.
BL44B2	**RIKEN Materials Science**	(Feb. 1998)	Structural materials science research using powder X-ray diffraction.

IV. User Program and Statistics

SPring-8 calls for public use proposals twice a year, in principle. Since 1997, SPring-8 has accepted a variety of proposals as shown in Fig. 3. In FY2019, JASRI designated the field of Industrial Application Proposals Using Advanced Technology. This field is intended to promote problem-solving and the discovery of needs for new applications in various industries by utilizing advanced measurement techniques that are new to the project leader. The submitted proposals are reviewed by the SPring-8 Proposal Review Committee (SPring-8 PRC) and about 1400 proposals were approved in FY2019 (Fig. 5). Industrial Application Proposals account for approximately 16–20% of the total number of proposals conducted at the public beamlines.

The mail-in measurement service is currently provided by BL14B2 (XAFS), BL19B2 (powder diffraction and small-angle scattering), BL46XU (hard X-ray photoemission spectroscopy and thin film analysis), BL45XU, and BL32XU (protein crystallography). Figures 4 to 13 show the information on user programs.

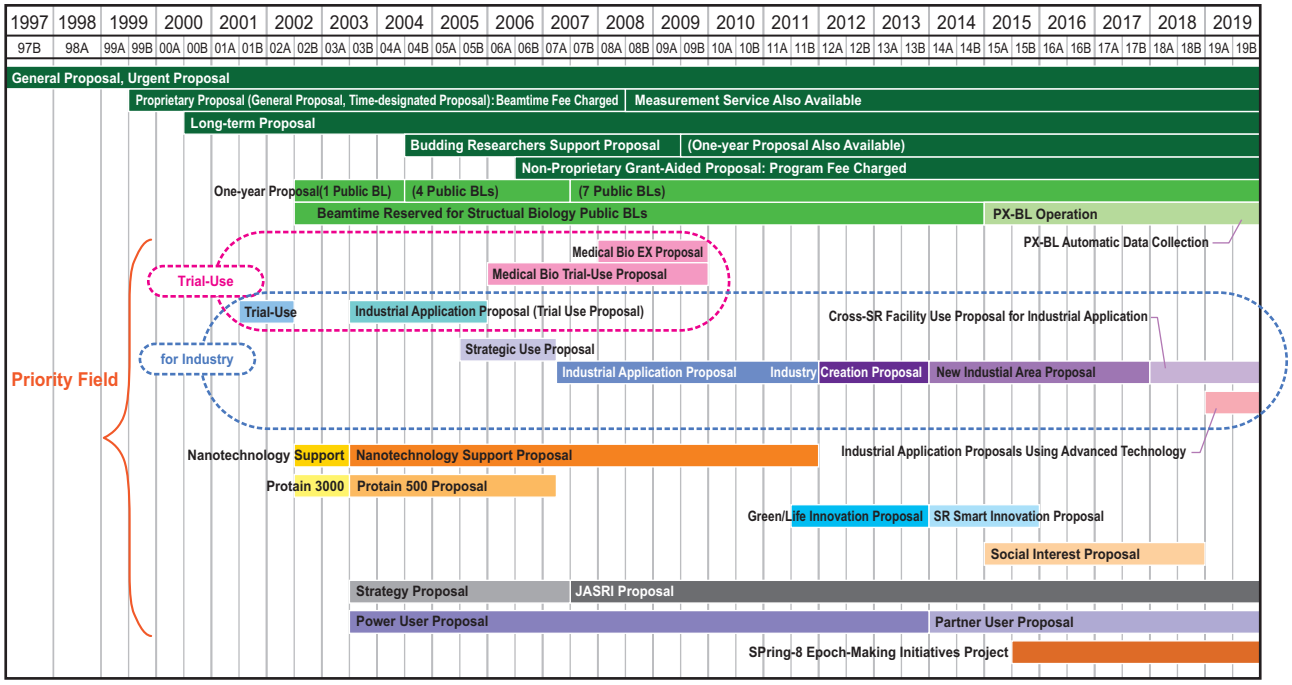

Fig. 3. Categories of proposals for the public beamlines.

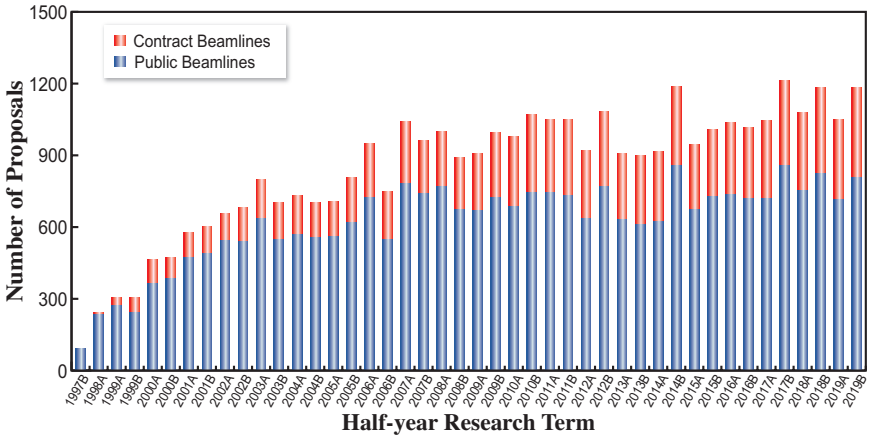

Fig. 4. Numbers of conducted experiments.

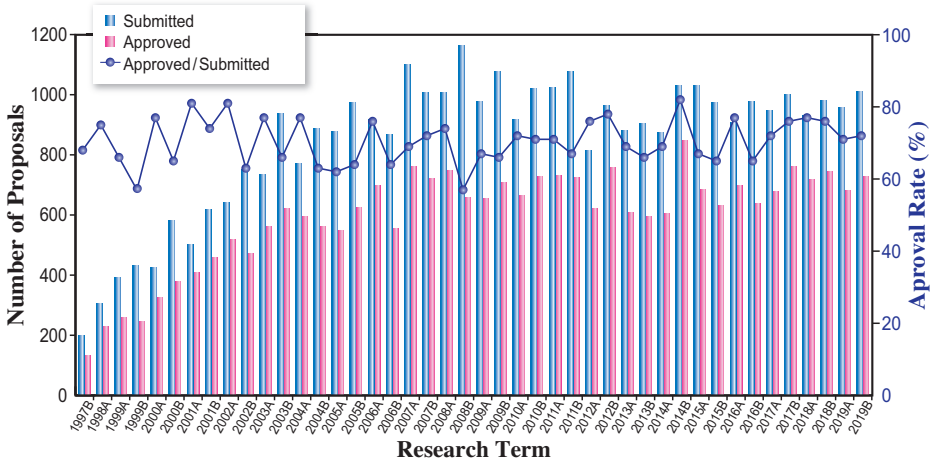

Fig. 5. Numbers of submitted proposals and approved proposals by research term (public beamlines).

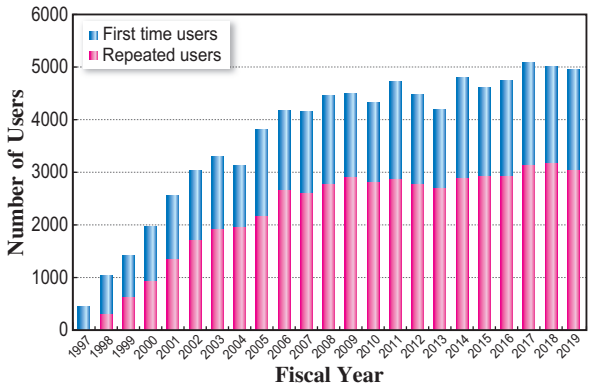

Fig. 6. Numbers of users by fical year.

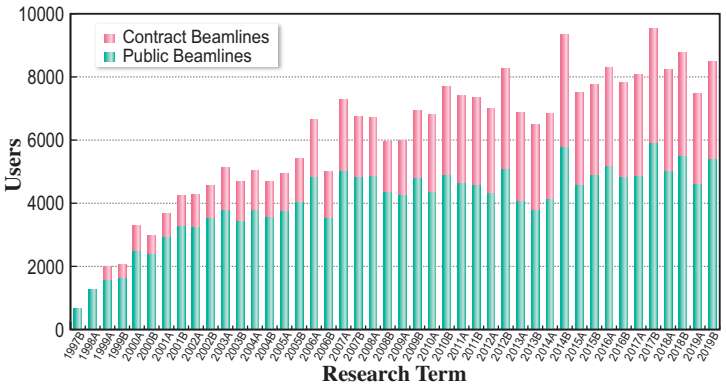

Fig. 7. Numbers of users visits by research term.

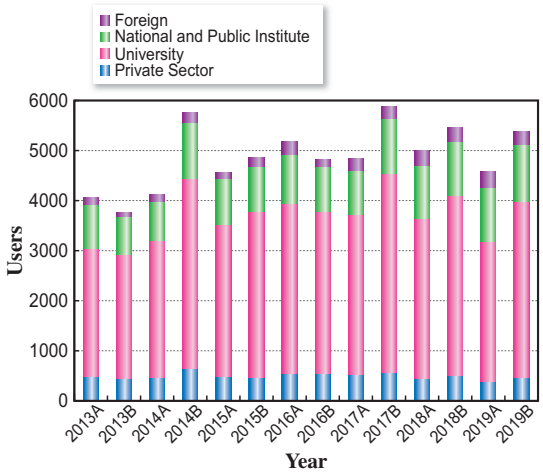

Fig. 8. Numbers of users by affiliation categories (public beamlines).

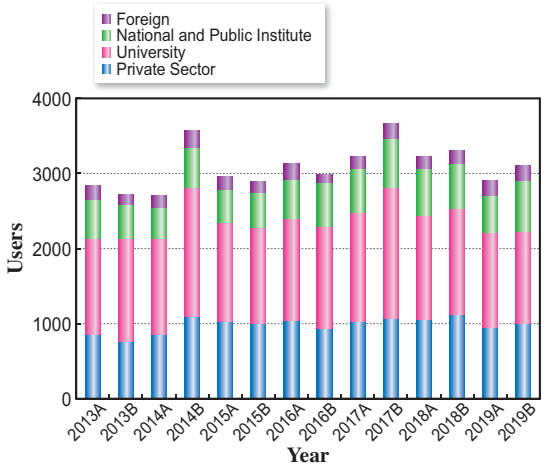

Fig. 9. Numbers of users by affiliation categories (contract beamlines).

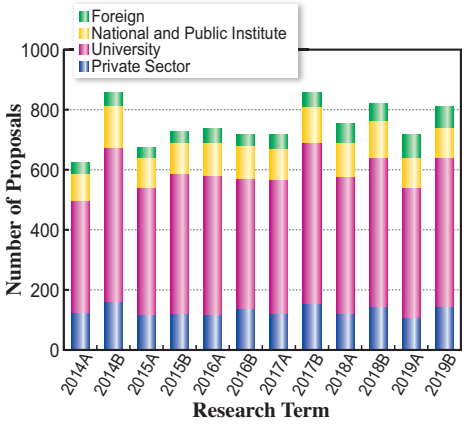

Fig. 10. Numbers of conducted proposals by affiliation (public beamlines).

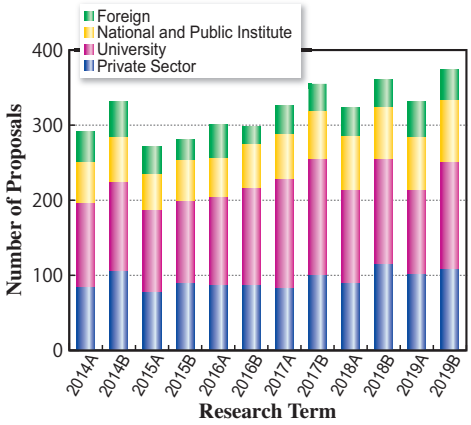

Fig. 11. Numbers of conducted proposals by affiliation categories (contract beamlines).

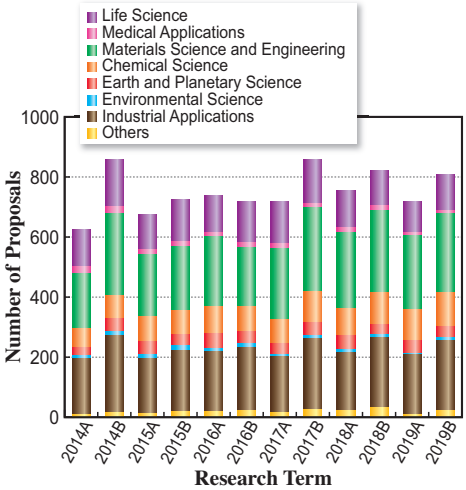

Fig. 12. Numbers of conducted proposals by research area (public beamlines).

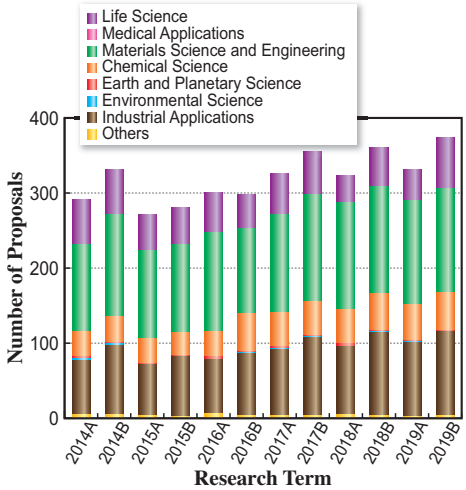

Fig. 13. Numbers of conducted proposals by research area (contract beamlines).

V. Research Outcome

As of March 2020, the total number of registered refereed papers that involved the use of SPring-8 was 16,500. Figure14 shows the annual statistics of refereed papers.

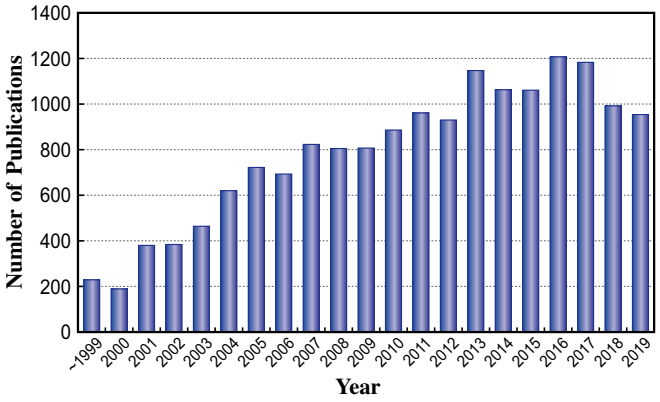

Fig. 14. Number of refereed publications.

VI. Budget and Personnel

The total budget for the operation of SPring-8 in FY2019 was about 9.3 billion yen. As of October 2019, RIKEN and JASRI have a total of 440 staff members. Figure 15 shows the annual budget allocated to operations, maintenance, and promotion of SPring-8. Figure 16 shows the number of staff at of RIKEN and JASRI.

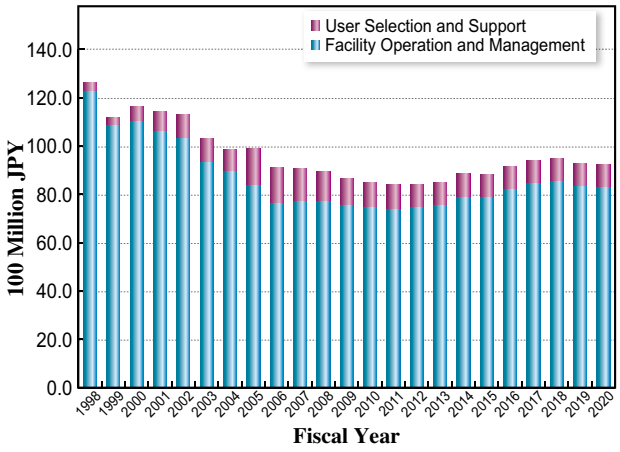

Fig. 15. SPring-8 budget.

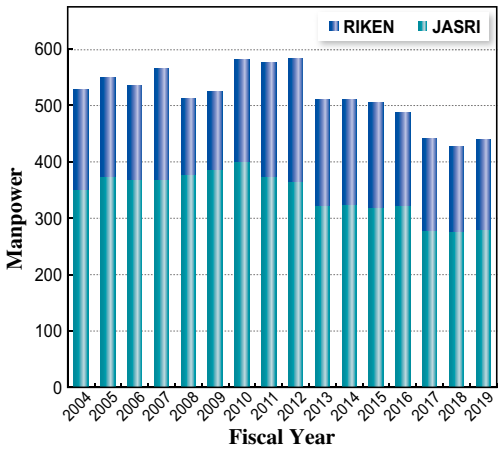

Fig. 16. Personnel at SPring-8: JASRI and RIKEN.

VII. Research Complex

The facilities of SPring-8, SACLA, and NewSUBARU form the Center of Excellence (COE) at the SPring-8 campus where JASRI, public beamline users, the contractors of contract beamlines, RIKEN, and the University of Hyogo work in close cooperation, forming a research complex where each member has its own role in delivering high-quality results to the field of synchrotron radiation science and technology. The organizational charts of RIKEN and JASRI, which are at the center of this research complex, are shown in Fig. 17 and Fig. 18, respectively.

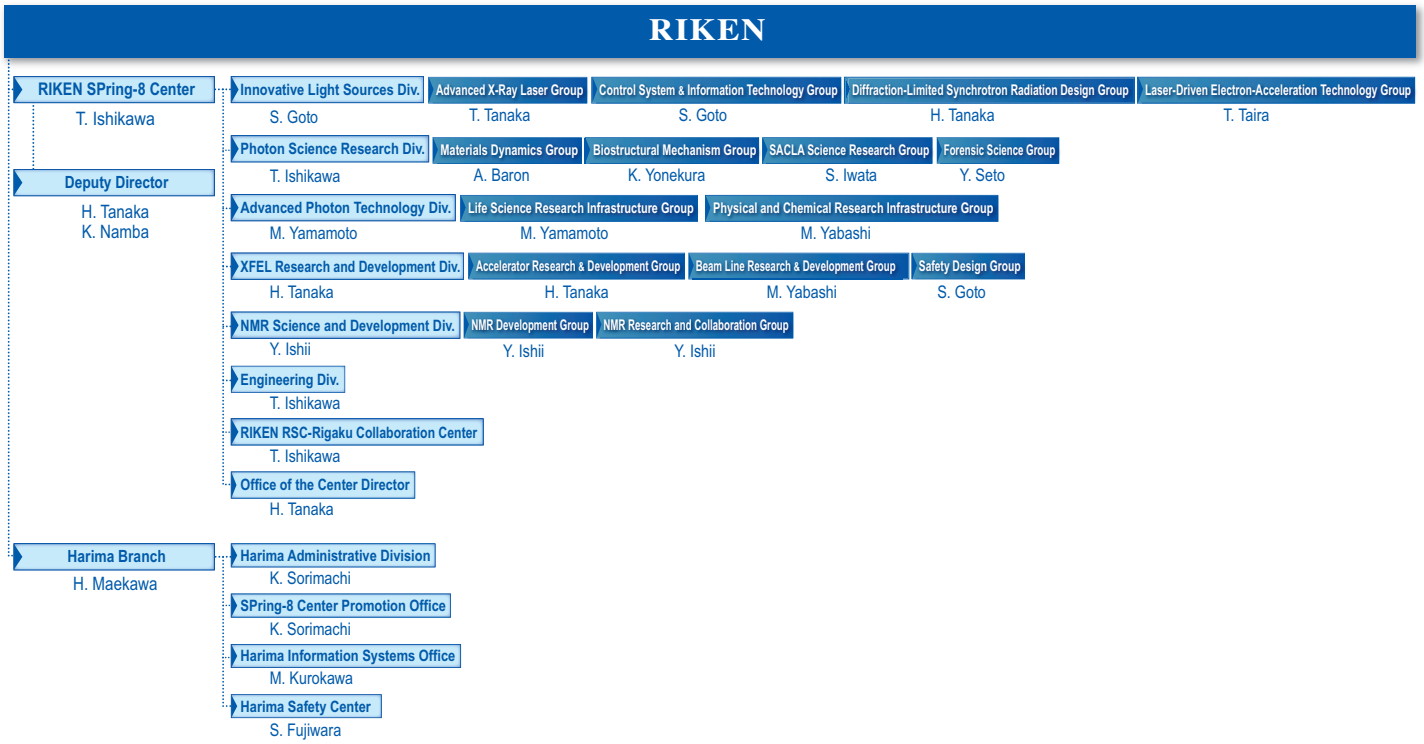

Fig. 17. RIKEN Harima Branch chart as of April 2020.

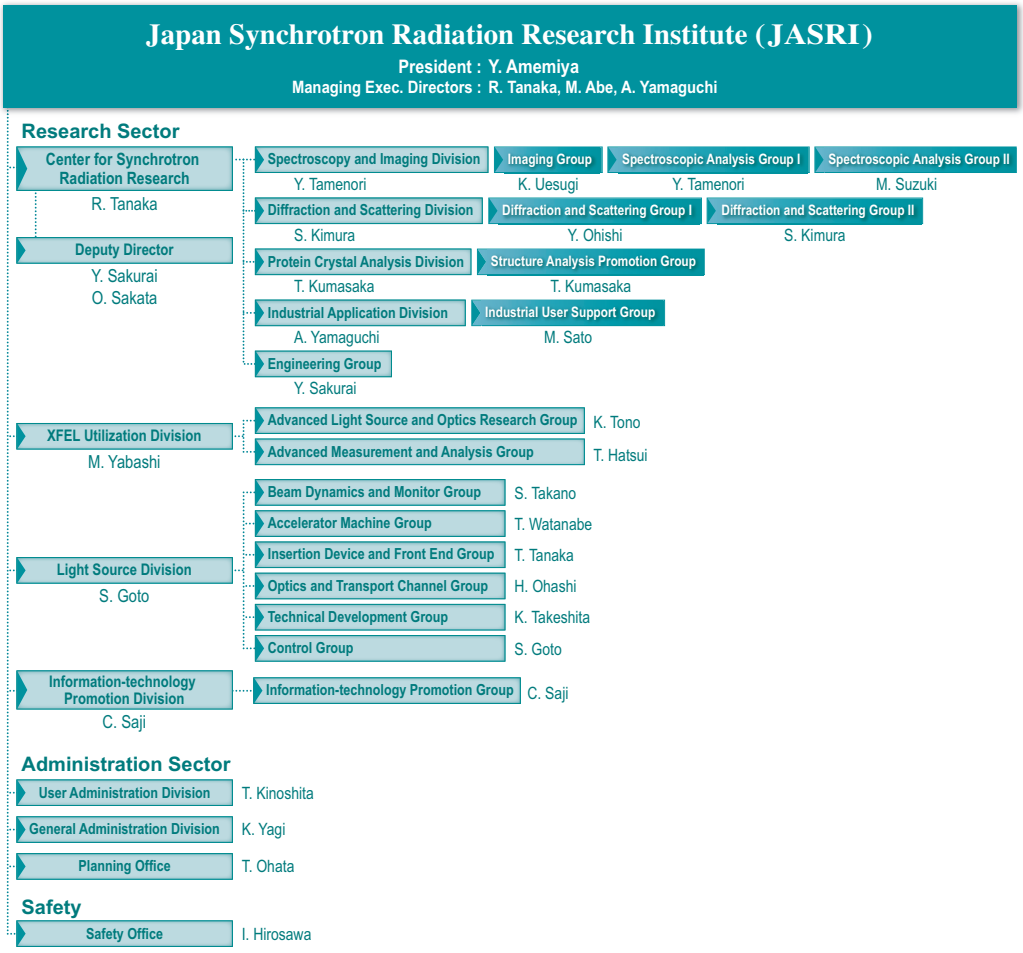

Fig. 18. JASRI chart as of April 2020.

VIII. SPring-8 Users Community (SPRUC)

Prof. J. Mizuki
Kwansei Gakuin University
SPRUC Chairman FY2019

The SPring-8 Users Community (SPRUC) is a user society consisting of all users of SPring-8/SACLA. In addition to individuals, representative organizations from 26 institutes (i.e., principal universities, national/international research institutes, industries, and beamline consortiums) participate in SPRUC to discuss further promotion of the utilization of SPring-8 from strategic and perspective viewpoints.

As one of the key activities of SPRUC, the SPring-8 Symposium is held annually at the site of one of the representative organizations jointly with RIKEN and JASRI. SPring-8 Symposium 2019 with the theme "One step for the coming two decades" was held at 50th Anniversary Hall, Okayama University on August 30–31. As indicated by the theme, a major aim of the symposium was to form a consensus on a future plan of SPring-8 through a discussion and share practical ways to realize the plan. The award ceremony of the SPRUC 2019 Young Scientist Award, which was conferred on Dr. Wataru Shihoya, The University of Tokyo, and Dr. Yuya Kubota, JASRI, was also held. SPring-8 Symposium 2020, jointly hosted by SPRUC, RIKEN, JASRI, NIMS, and University of Tsukuba, is scheduled to be held on September 18–19 at International Congress Center EPOCAL TSUKUBA.

SPRUC co-hosted the 2nd Beamlines Upgrade Workshop (February 21–22) with RIKEN and JASRI. The workshop was planned to enrich information exchange between members of SPRUC and the facility side. The facility side presented the latest situation of beamline reorganization, future prospect, and relatied problems, and the members discussed their requirements and gave suggestions for the beamline upgrade.

SPRUC has continued to promote the activities of SPRUC multidisciplinary research groups in order to develop the use of SPring-8 in new areas that will be important to future science and technology. Owing to the successful termination of the research period of the research group for nanodevice science, the research group for applied science, led by Dr. Masatoshi Takao (program officer) and Dr. Akihiko Fujiwara (project director), is the only remaining multi-disciplinary research group active at the end of the fiscal year. As an activity of the Science Promotion Board, as a subsidiary board in the SPring-8 utilization committee, SPRUC started a survey of research fields that should be promoted to generate new science. On the basis of this activity, the formation of new multidisciplinary research groups is expected.

The 4th-term SPRUC research groups were voluntarily organized in each research field, and each research group conducted research meetings actively. At the call for the 5th-term SPRUC research group,

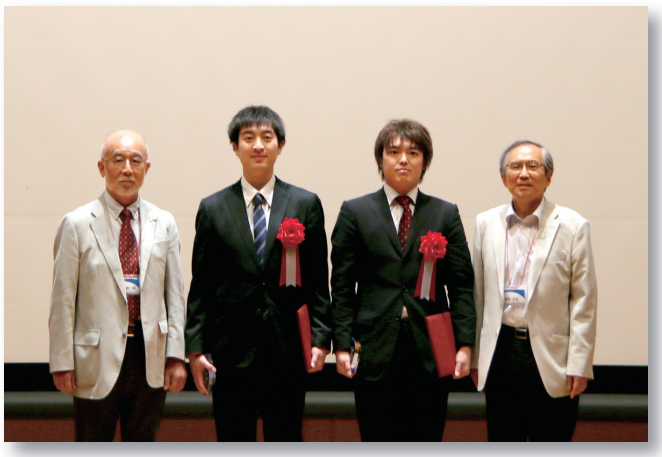

SPRUC2019 Young Scientist Award
Prof. J. Mizuki, Dr. W. Shihoya, Dr. Y. Kubota, and Prof. M. Oshima

the SPring-8 utilization committee requested that the 5th-term SPRUC research group should carry out some activities that contribute to a vision for beamline reorganization, future beamline technology, new application fields, and recruiting new users.

SPRUC supported the SPring-8 Summer School to enhance user research competency and also hosted the SPring-8 Autumn School with JASRI to acquire new users and for human resource development. The SPRUC research group contributed to planning the lectures in both schools.

Finally, modifications of the SPRUC organization and rules are described. SPRUC established the Science Promotion Board with the purpose of making practical plans toward realizing forthcoming cutting-edge science that SPring-8 should tackle. The rule for recommending councilor candidates was changed to make it possible to recruit a much broad range of candidates. The early election of the next president was introduced, and the next president from April 2020 will be Prof. Akio Kimura from Hiroshima University. The terms describing the valid period of the membership were changed to those with a much clear description. The rule for filling a vacancy for a councilor was established. These changes should contribute to the efficient and powerful operation of SPRUC.

SPring-8 Symposium 2019

IX. Outreach Activities

To recruit new users in unexplored fields of application, SPring-8 holds a series of seminars named "Workshop on Advanced Techniques and Applications at SPring-8". Here are some representatives.

- 40th: Social science and SPring-8
  May 21, 2019 • Campus Innovation Center Tokyo (Tokyo)

- 41st: Practical use of SPring-8 in Earth science field
  May 28, 2019 • Makuhari Messe (Chiba)

- 42nd: Current status and future prospects of protein structural biology research at SPring-8
  September 9-10, 2018 • Osaka University (Osaka)

- 49th: Prospects for the element-selective electric state studies with high sensitive X-ray emission spectroscopy and inelastic X-ray scattering measurement
  January 9, 2020 • Nagoya University (Aichi)

- 50th: Future prospect for room temperature superconductivity in hydride research with SPring-8
  December 24, 2019 • SPring-8 site (Hyogo)

SACLA

I. Machine Operation & Beamlines

Our eighth year of operations proceeded without any significant issues. Operation statistics are summarized in Table 1. The ratio of downtime to user time was kept below 5%, a reasonably low rate for linac-based light sources.

Table 1. Operation Statistics for FY2019

	Time (h)
Total operation time	6135.4
User time	
BL1	1188
BL2	2022
BL3	3228
Total	6438
Facility tuning time	732
Downtime	312

In 2012, two beamlines, BL3 for XFEL and BL1 for broadband spontaneous light, were opened for users, while all experiments were conducted at BL3. As the newest beamline, construction of BL2 was completed during the summer shutdown of 2014, and first laser amplification was achieved on October 21. An upgraded beamline for soft X-ray FEL, BL1, which combines the prototype accelerator of SACLA (SCSS), started operation in 2016. Parallel user operation of BL2 and BL3 started in 2018.

II. User Program and Statistics

SACLA calls for public user proposals twice per year.

In FY2016, JASRI introduced the proprietary research of General Proposals and the Proprietary Time-Designated Proposals. The project leaders of these proprietary proposals are not required to publish their research results, but required to pay each beamtime fee. In addition, to apply for the proprietary research the project leaders should be affiliated with a corporate enterprise located and registered in Japan.

Figures 1 and 2, and Table 2 provide statistics on proposals, users, and beamtime.

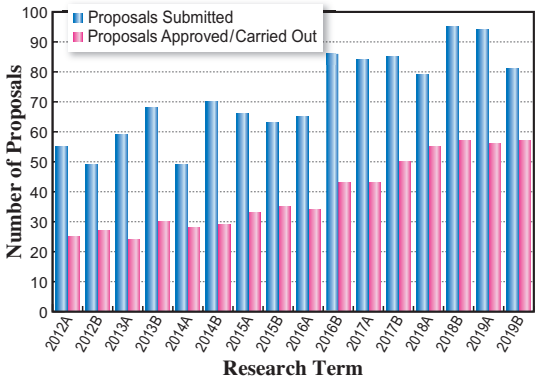

Fig. 1

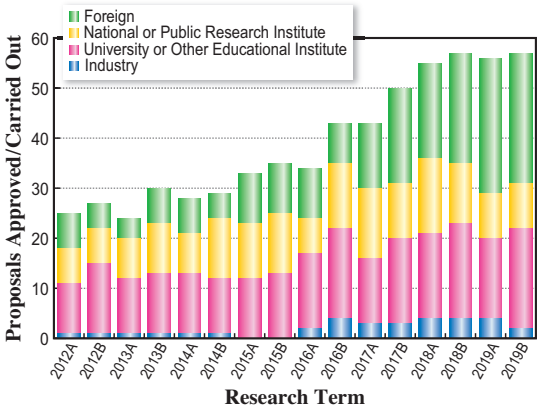

Fig. 2

Table 2. Number of proposals submitted, proposals approved/carried out, cumulative users, and beamtime available by research term

Half-year Research Term	Proposals Submitted	Proposals Approved / Carried Out					Cumulative Users	Beamtime Carried Out (Shifts)
			Priority Strategy Proposals	Non-proprietary	Proprietary			
				General Proposals	General Proposals	Time-Designated Proposals		
2012A	55	25	(12)	(13)	–	–	297	126
2012B	49	27	(19)	(8)	–	–	461	154
2013A	59	24	(15)	(9)	–	–	268	117
2013B	68	30	(19)	(11)	–	–	410	139
2014A	49	28	(20)	(8)	–	–	400	147
2014B	70	29	(17)	(12)	–	–	430	140
2015A	66	33	(23)	(10)	–	–	527	144
2015B	63	35	(23)	(12)	–	–	552	152
2016A	65	34	(21)	(12)	(1)	–	538	158
2016B	86	43	(21)	(20)	(1)	(1)	650	197
2017A	84	43	–	(43)	(0)	(0)	577	210
2017B	85	50	–	(50)	(0)	(0)	642	244
2018A	79	55	–	(55)	(0)	(0)	643	257
2018B	95	57	–	(56)	(0)	(1)	653	264
2019A	94	56	–	(55)	(0)	(1)	564	259
2019B	81	57	–	(56)	(0)	(0)	650	266

One shift = 12 hours at SACLA beamlines

Editor
Naoto Yagi
Japan Synchrotron Radiation Research Institute (JASRI)

Editing, Design & Layout
Marcia M. Obuti-Daté
Japan Synchrotron Radiation Research Institute (JASRI)

Printing
Hokuoh Printing Co.

JASRI
Information & Outreach Section
Users Administration Division

1-1-1 Kouto, Sayo-cho, Sayo-gun
Hyogo 679-5198 • JAPAN
Tel: +81-(0)791-58-2785 Fax: +81-(0)791-58-1869

Email: frontiers@spring8.or.jp
http://www.spring8.or.jp/

August 2020

SPring-8 SACLA

http://www.spring8.or.jp

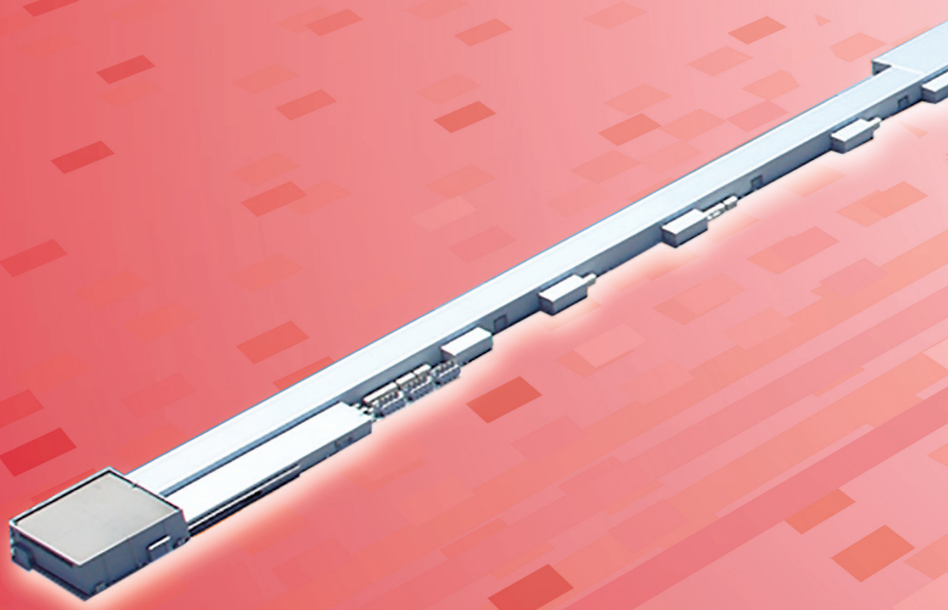

Japan Synchrotron Radiation Research Institute (JASRI)
1-1-1 Kouto, Sayo-cho, Sayo-gun, Hyogo 679-5198, Japan